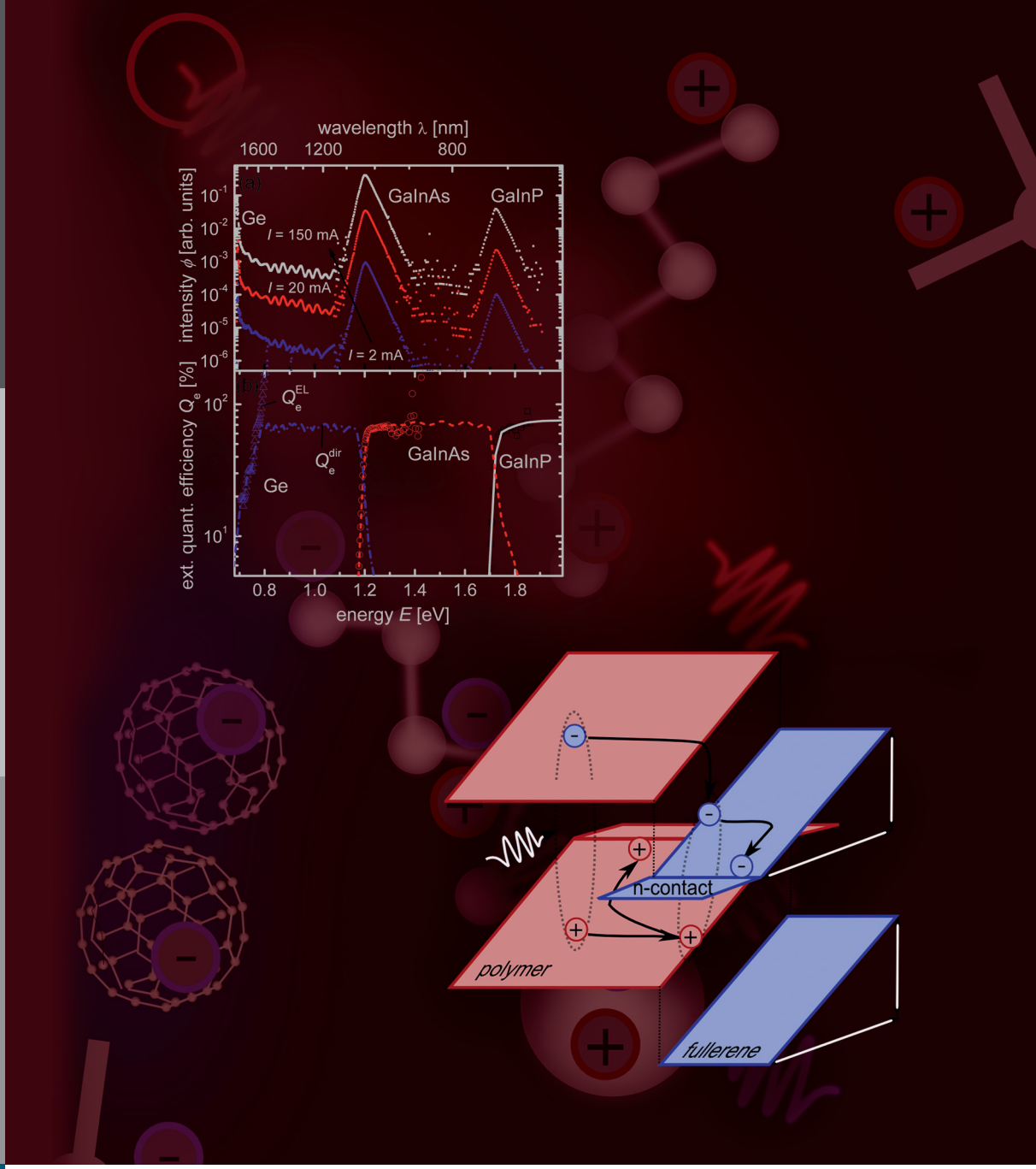

Generalized detailed balance theory of solar cells

Thomas Kirchartz

Mitglied der Helmholtz-Gemeinschaft

JÜLICH
FORSCHUNGSZENTRUM

Schriften des Forschungszentrums Jülich
Reihe Energie & Umwelt / Energy & Environment Band / Volume 38

Forschungszentrum Jülich GmbH
Institute of Energy Research (IEF)
Photovoltaics (IEF-5)

Generalized detailed balance theory of solar cells

Thomas Kirchartz

Schriften des Forschungszentrums Jülich
Reihe Energie & Umwelt / Energy & Environment Band / Volume 38

ISSN 1866-1793 ISBN 978-3-89336-573-9

Bibliografische Information der Deutschen Nationalbibliothek.
Die Deutsche Nationalbibliothek verzeichnet diese Publikation in der
Deutschen Nationalbibliografie; detaillierte Bibliografische Daten
sind im Internet über <http://dnb.d-nb.de> abrufbar.

Herausgeber und Vertrieb:	Forschungszentrum Jülich GmbH Zentralbibliothek, Verlag D-52425 Jülich Telefon (02461) 61-5368 · Telefax (02461) 61-6103 e-mail: zb-publikation@fz-juelich.de Internet: http://www.fz-juelich.de/zb
Umschlaggestaltung:	Grafische Medien, Forschungszentrum Jülich GmbH
Druck:	Grafische Medien, Forschungszentrum Jülich GmbH
Copyright: Forschungszentrum Jülich 2009

Schriften des Forschungszentrums Jülich
Reihe Energie & Umwelt / Energy & Environment Band / Volume 38

D 82 (Diss., RWTH Aachen, University, 2009)

ISSN 1866-1793
ISBN 978-3-89336-573-9

Vollständig frei verfügbar im Internet auf dem Jülicher Open Access Server (JUWEL)
unter http://www.fz-juelich.de/zb/juwel

Alle Rechte vorbehalten. Kein Teil des Werkes darf in irgendeiner Form (Druck, Fotokopie oder in einem anderen Verfahren) ohne schriftliche Genehmigung des Verlages reproduziert oder unter Verwendung elektronischer Systeme verarbeitet, vervielfältigt oder verbreitet werden.

Contents

Abstract

The principle of detailed balance is the requirement that every microscopic process in a system must be in equilibrium with its inverse process, when the system itself is in thermodynamic equilibrium. This detailed balance principle has been of special importance for photovoltaics, since it allows the calculation of the limiting efficiency of a given solar cell by defining the only fundamental loss process as the radiative recombination of electron/hole pairs followed by the emission of a photon. In equilibrium, i.e. in the dark and without applied voltage, the absorbed and emitted photon flux must be equal due to detailed balance. This equality determines the radiative recombination from absorption and vice versa. While the classical theory of photovoltaic efficiency limits by Shockley and Queisser considers only one detailed balance pair, namely photogeneration and radiative recombination, the present work extends the detailed balance principle to any given process in the solar cell. Applying the detailed balance principle to the whole device leads to two major results, namely (i) a model that is compatible with the Shockley-Queisser efficiency limit for efficient particle transport, while still being able to describe non-ideal and non-linear solar cells, and (ii) an analytical relation between electroluminescent emission and photovoltaic action of a diode that is applied to a variety of different solar cells.

This thesis presents several variations of a detailed balance model that are applicable to different types of solar cells. Any typical *inorganic* solar cell is a mainly bipolar device, meaning that the current is carried by electrons and holes. The detailed balance model for pn-type and pin-type bipolar solar cells is therefore the most basic incorporation of a detailed balance model. The only addition compared to the classical diode theory or compared to standard one-dimensional device simulators is the incorporation of photon recycling, making the model compatible with the Shockley-Queisser limit and the classical diode theory. For *organic* solar

cells, exciton binding energies are sufficiently high, so that purely bipolar models are no longer applicable. Instead, excitonic transport has to be included. Thus, the inclusion of exciton transport into the bipolar detailed balance model leads to a generalized detailed balance model that simulates solar cells with predominantly bipolar transport, with predominantly excitonic transport and with every combination of both. Due to low exciton diffusion lengths, organic solar cells are usually combined with a specific device geometry, the bulk heterojunction. In a bulk heterojunction device, the whole bulk of the absorber is made up of distributed heterojunctions, where the exciton is transferred to a bound pair at the interface, which is then split into free electron and hole. The assumption that exciton transport is only relevant towards the next heterointerface allows to develop also a version of the detailed balance model that is applicable to bulk heterojunction cells. The last variation of the detailed balance model includes the process of impact ionisation as a means to generate more than one exciton from a single high energy photon. The model for multiple exciton generating absorbers identifies possible bottlenecks as well as maximum efficiencies of future solar cells that use this concept.

Another direct consequence of the principle of detailed balance is a reciprocity theorem between electroluminescence and solar cell quantum efficiency. The theoretical part of this thesis discusses the validity range of this reciprocity and checks for each version of the model, whether the relation between electroluminescence and quantum efficiency is still applicable. The main result shows that voltage dependent carrier collection as encountered in low mobility pin-junction devices leads to deviations from the reciprocity, while it still holds for most pn-junction solar cells.

The experimental part of this thesis uses this reciprocity theorem to better interpret electroluminescence measurements of crystalline silicon, Cu(In,Ga)Se_2 and GaInP/GaInAs/Ge triple-junction solar cells. The investigation of crystalline silicon focusses on the quantification of recombination and light trapping using both spectral as well as spatial electroluminescence measurements. Temperature dependent measurements of Cu(In,Ga)Se_2 devices characterize the solar cells in terms of their compositional inhomogeneity, which would lead to inhomogeneous band gaps. However, the electroluminescence measurements reveal that the highly efficient cells don't show significant lateral variations of the band gap. For multi-junction cells, electroluminescence measurements accomplish the task of measuring the internal

voltages of all individual subcells at a given injection current. From the internal voltages, information on recombination and diode ideality of each individual cell is obtained.

Zusammenfassung

Das Prinzip der detaillierten Bilanz beschreibt die Notwendigkeit, dass jeder mikroskopische Prozess in einem System im Gleichgewicht mit seinem Umkehrprozess ist, solange sich das System selbst im thermodynamischen Gleichgewicht befindet. Die detaillierte Bilanz zwischen Absorption eines Photons und strahlender Rekombination eines Elektron/Loch-Paares ist der Ausgangspunkt für die Berechnung des maximalen Wirkungsgrads einer Solarzelle durch Shockley und Queisser. Im thermodynamischen Gleichgewicht, d.h. ohne Beleuchtung oder extern angelegte Spannung, müssen der absorbierte und emittierte Photonenfluss aufgrund des Prinzips der detaillierten Bilanz identisch sein. Diese Bedingung erlaubt dann auch die Berechnung der strahlenden Rekombination aus der Absorption im Nichtgleichgewicht. Während die klassische Theorie photovoltaischer Wirkungsgradgrenzen von Shockley und Queisser allerdings nur ein einziges Paar von Prozessen berücksichtigt - Photogeneration und strahlende Rekombination - erweitert die vorliegende Arbeit das Prinzip der detaillierten Bilanz auf jeden beliebigen Prozess in der Zelle. Diese Anwendung der detaillierten Bilanz auf das gesamte Bauelement führt zu zwei grundlegenden Ergebnissen: (i) einem Modell, welches mit dem Shockley-Queisser Wirkungsgradlimit kompatibel ist, das aber auch ist nicht-ideale und nicht-lineare Solarzellen zu beschreiben und (ii) einem analytischen Zusammenhang zwischen der Elektrolumineszenz und der photovoltaischen Quantenausbeute einer Solarzelle.

Die vorliegende Arbeit stellt mehrere Varianten eines Modells vor, die jeweils mit dem Prinzip der detaillierten Bilanz kompatibel sind, und benützt diese Varianten zur Simulation verschiedener Solarzellentypen. Jede *anorganische* Solarzelle ist ein überwiegend bipolares Bauelement, in dem der Stromtransport über die Bewegung von Elektronen und Löchern bewerkstelligt wird. Das Modell für bipolare pn- und pin-Übergänge ist demnach die einfachste und grundlegendste Variante

eines Solarzellenmodells. Der einzige wesentliche Unterschied zu der klassischen Diodentheorie oder auch zu typischen eindimensionalen Bauelementsimulatoren ist die Berücksichtigung des Photon-Recyclings. Damit wird das Modell sowohl vereinbar mit dem Shockley-Queisser Limit als auch mit der klassischen Diodentheorie. Die Exzitonenbindungsenergien von *organischen* Solarzellen sind im Gegensatz zu denen *anorganischer* Solarzellen ausreichend groß, dass reine bipolare Modelle nicht länger ausreichend sind und exzitonischer Transport mitberücksichtigt werden muss. Die Einbindung von exzitonischem Transport in das bipolare Modell führt zu einem verallgemeinerten Modell, welches eine Simulation von Zellen mit überwiegend bipolarem Transport, mit überwiegend exzitonischem Transport oder mit jeder Kombination aus diesen beiden möglich macht. Aufgrund der niedrigen Exzitonendiffusionslängen werden organische Halbleiter üblicherweise mit einer speziellen Bauelementgeometrie kombiniert - der *bulk heterojunction*. In diesem Bauelement besteht der gesamte Absorber aus einem verteilten Heteroübergang. Das photogenerierte Exziton wird am Heteroübergang zu einem gebundenen Elektron/Loch-Paar, welches dann in freie Elektronen und Löcher aufgespalten wird. Die Annahme, dass Exzitonentransport nur in Richtung der nächsten Grenzfläche relevant ist, ermöglicht die Entwicklung eines Modells, das auch auf *bulk heterojunction* Bauelemente anwendbar ist. Die letzte Variante des Modells berücksichtigt zusätzlich den Effekt der Stoßionisation, der in der Lage ist aus einem hochenergetischen Photon mehr als ein Elektron/Loch-Paar oder Exziton zu erzeugen. Das Modell für Absorber, die mehr als ein Exziton pro Photon erzeugen können, erlaubt sowohl die Identifikation möglicher Problempunkte als auch die Berechnung von maximalen Wirkungsgraden für zukünftige Solarzellenkonzepte, die dieses Konzept auszunutzen versuchen.

Eine weitere Konsequenz aus dem Prinzip der detaillierten Bilanz ist ein Reziprozitätstheorem zwischen der Elektrolumineszenz und der photovoltaischen Quantenausbeute. Im theoretischen Teil der Arbeit wird zunächst für die verschiedenen Varianten des Modells geprüft, ob das Reziprozitätstheorem gültig ist. Das wesentliche Resultat ist dabei, dass spannungsabhängige Ladungsträgersammlung, wie sie in pin-Solarzellen mit niedrigen Ladungsträger-Beweglichkeiten auftritt, immer zu Abweichungen von der Reziprozität führen, während es für die meisten pn-Solarzellen gültig bleibt.

Der experimentelle Teil dieser Arbeit verwendet dieses Reziprozitätstheorem,

um damit Elektrolumineszenzmessungen an kristallinem Si, Cu(In,Ga)Se_2 und GaInP /GaInAs/Ge Tripelzellen besser interpretieren zu können. Im Falle des kristallinen Siliziums liegt der Schwerpunkt auf der Untersuchung von Rekombination und optischer Wegverlängerung sowohl mithilfe von spektral aufgelösten als auch ortsaufgelösten Elektrolumineszenzmessungen. Temperaturabhängige Messungen an Cu(In,Ga)Se_2 charakterisieren die Solarzellen hinsichtlich der Inhomogenität ihrer Zusammensetzung, die in diesem Materialsystem zu einer ungewollten lateralen Inhomogenität der Bandlücke führen kann. Die Elektrolumineszenzmessungen zeigen jedoch, dass die hocheffizienten Zellen keinerlei signifikante laterale Variationen der Bandlücke zeigen. Im Fall der Stapelzellen erlauben Elektrolumineszenzmessungen den Zugang zu den internen Spannungen der Einzelzellen. Durch die Variation des Injektionsstroms ermöglicht diese Methode die Bestimmung der Menge an nichtstrahlender Rekombination und des Dioden-Idealitätsfaktors jeder einzelnen Zelle.

Chapter 1

Introduction

More than fifty years after the introduction of the first photovoltaic device [1], solar cells and solar modules contribute an increasing and more and more sizeable share to the world's demand for clean and renewable electrical energy. More than 90% of the actual solar module production uses silicon-based pn-junction solar cells, i.e. the same type as the pioneer device from 1954. Within these years, our understanding of the device, its working principles, and its processing has obviously achieved a high degree of maturity [2, 3]. In recent years, research has expanded [4, 5] from pn-junction type silicon solar cells to completely different materials and working principles of the photovoltaic device like organic [6–16] or dye sensitized [17–21] solar cells. The evolutionary process of solar cell research leading to state-of-the-art solar cells had economic success while creating a wish for revolutionary progress in research. No longer are only those technologies pursued that seem to work nearly immediately. Instead, theoretical concepts are sought after and materials and devices are designed [22] that may provide the basis for future solar cell generations.

Initial efficiencies of many devices using new concepts are rather low, while the number of scientific disciplines involved and the number of scientific aspects to be considered is fairly high. Since many of the new concepts in photovoltaics use e.g. electrolytes, semiconductor nano-particles [23–26], organic dyes [27], and/or organic semiconductors as functional elements, the basic physics underlying light absorption, charge separation, and energy generation differs considerably from what is well established for classical pn-junction solar cells made from inorganic semiconductors. Recently, it has been proposed [28, 29] to distinguish between two different

concepts of solar cells, namely the classical inorganic solar cells and the excitonic solar cells usually made from organic absorber materials. However, since the overall functionality in all solar cells, namely the generation of electrical power from solar light, is identical, there should be a common theory that is valid for all devices on a certain level of abstraction from physical details.

Obviously, the detailed balance theory of the maximum photovoltaic energy conversion efficiency by Shockley and Queisser (SQ) [30] is an approach that accounts for all types of (single junction) solar cells as a limiting situation. The generality of the SQ approach results from the fact that only the detailed balance pair light absorption and light emission is considered. This restriction implies that all details of excitation, charge separation, and transport inside the device are neglected by the postulate that all absorption of light leads to generation of charge carriers that, in addition, are all collected by the electrical terminals of the device. The principle of detailed balance then ensures that such a perfect solar cell is also a perfect light emitting diode (LED) and the balance between light absorption and emission defines the radiative efficiency limit. Thus, the SQ theory essentially looks at the solar cell from the outside. This neglect of internal details makes up the elegance of the SQ approach but, at a first glance, disconnects this theory from any model designed to describe the internal operation of the solar cell.

This thesis uses the basic concept behind the SQ-theory - the principle of detailed balance [31] - to develop a generalized model of solar cells that also includes the internal details of energy transport via photons, excitons and free carriers. Apart from the classical pn-junction solar cell, where collection of photogenerated minority carriers is the main process crucial for achieving a high photocurrent, I also investigate pin junction solar cells as well as transport of electrons, holes and excitons. The model is designed in a way that in the limit of high mobilities of carriers and excitons and purely radiative recombination, the efficiency is always given by the Shockley-Queisser limit. In the limit of predominantly non-radiative recombination, the model is equivalent to standard one-dimensional device simulators with the only exception that excitons are added to the system. The range in between these two limits, i.e. the case of low mobility solar cells close to the radiative limit, is a situation neither covered by Shockley-Queisser [30] nor by Shockley's diode [32] theory and most standard device simulators. The feature required for covering the

radiative limit of low mobility devices is the inclusion of generation terms caused by emission of photons in the device itself - a process usually designated as photon recycling [33]. This inclusion of photon recycling makes the model selfconsistent and allows the calculation of both the photovoltaic characteristics of a device as well as the light emitting characteristics.

Starting with a general introduction into the concept of detailed balance and the Shockley-Queisser limit, **chapter 2** defines several properties of an optoelectronic device with a special focus on reciprocity relations [34, 35] that connect the light absorbing with the light emitting situation for arbitrary values of the mobility.

The first incorporation of a detailed balance model is presented in **chapter 3** and serves for the simulation of pn and pin-junction solar cells with purely bipolar transport, i.e. without contributions from excitons. As an application for this model, we calculate the efficiency limits of SiO_2/Si quantum well solar cells. The input parameter for these simulations are the result of first principles calculations of the band structure, the density of states, the absorption coefficient and the mobility that were carried out by project partners at the Universität Jena [36].

Chapter 4 introduces the full detailed balance model including excitonic transport, which includes the excitonic (i.e. organic solar cells) and the bipolar inorganic solar cells as special cases.

In addition to excitonic transport, most organic solar cells have a distinct device geometry that is considerably different from that of inorganic solar cells. The heterointerface seperating the exciton is distributed over the whole volume of the absorber, which therefore consists of a blend of two materials. **Chapter 5** therefore extends the model to also cover these so called bulk heterojunction solar cells. I also present a possibility to incorporate our model into a commercial device simulator.

The final extension of my model includes the effect of multiple exciton generation and thereby presents simulations for solar cells, which are not limited by the Shockley-Queisser limit. Nevertheless, **chapter 6** shows that the calculation of detailed balance limits that include the internal kinetics of the charge separation process is still possible.

The reciprocity relations connecting the light absorbing with the light emitting situation are applied experimentally in **chapter 7** to solar cells made from crystalline silicon, Cu(In,Ga)Se_2 and GaInP/GaInAs/Ge-multijunction cells.

Chapter 2

Fundamentals

Starting with a general introduction into the concept of detailed balance and the Shockley-Queisser limit, this chapter defines several properties of an optoelectronic device with a special focus on reciprocity relations [34, 35] that connect the light absorbing with the light emitting situation for arbitrary values of the mobility. In addition I discuss the working principle of a solar cell in two rather simple environments: a discrete two state model and the one sided pn-junction.

2.1 The principle of detailed balance

A sample is said to be in thermodynamic equilibrium, when the temperature of the sample is the same as the temperature of its environment, when there is no change of temperature in time and when there are no external forces acting on the sample as for instance an applied voltage or excess illumination from a light source. If a sample is in thermal equilibrium, then all microscopic processes in the sample are exactly compensated by their respective inverse process. This principle is known since the first quarter of the 20th century under various names, like "The Law of Entire Equilibrium" [37], "The Principle of Microscopic Reversibility" [38], "The Hypothesis of the Unit Mechanism" [39] and "The Principle of Detailed Balancing" [40].

On first sight, the detailed balance principle, as I want to call it in the remainder of this thesis, may seem nearly trivial or at least an obvious prerequisite to maintain thermal equilibrium. On second sight, one might however argue that

the condition of equilibrium merely requires zero net change in time anywhere in the system. For instance the requirement of zero net change in e.g. particle concentration could be realized by optical generation processes counterbalanced by e.g. non-radiative recombination processes thereby violating the detailed balance principle.

To definitely show the validity of the detailed balance principle, Bridgman [41] formulated a definition that directly shows that the detailed balance is a consequence of the second law of thermodynamics. The definition reads: "No system in thermal equilibrium in an environment at constant temperature spontaneously and of itself arrives in such a condition that any of the processes taking place in the system by which energy may be extracted, run in a preferred direction, without a compensating reverse process." This definition can be proven by assuming the opposite, namely an unidirectional process. Following Bridgman's definition, we could extract energy from the system, let the system come to equilibrium with its surroundings again and then repeat the process infinitely, which is obviously forbidden by the second law of thermodynamics.

In the following, I discuss the implications of the principle of detailed balance for the calculation of photovoltaic efficiency limits but also for any device model as well as for the basic symmetry or reciprocity relationships in optoelectronic devices.

2.2 The Shockley-Queisser limit

To derive the maximum efficiency and the current/voltage(J/V)-curve of an idealized solar cell, only few considerations have to be made. The basic ingredients to calculate this limit are the detailed balance principle [31] and Planck's law [42]. The assumptions defining a cell in the SQ-limit are perfect absorption with each photon creating exactly one electron/hole pair, perfect collection of carriers and radiative recombination as the only allowed recombination mechanism. The term *perfect collection* means that every photogenerated electron travels to the collecting junction faster than it can recombine and thus that the number of generated electron/hole pairs equals the number of collected electron hole pairs. In an extended semiconductor volume, this would require infinite carrier mobility. The only properties to describe the idealized SQ-cell are its bandgap and its temperature. The bandgap

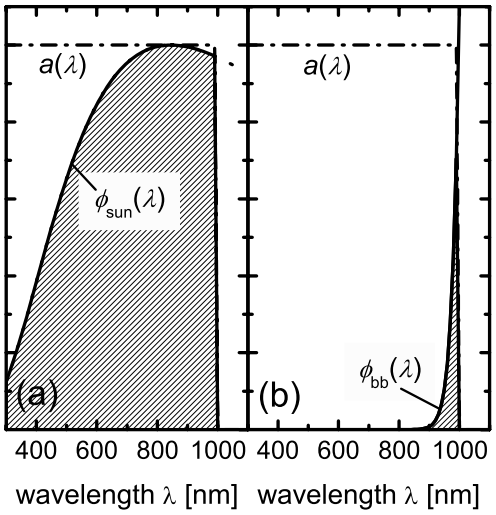

Fig. 2.1: *Photon flux that is (a) absorbed and (b) emitted by a solar cell with an absorptance a(E) and a perfect collection. The scale for the photon emission (b) depends on the applied voltage. The open circuit voltage in the SQ-limit is the voltage where the hatched regions are equal in area.*

E_g defines the threshold for absorption of light, which is assumed to be perfectly abrupt, i.e. no light is absorbed below the bandgap and every photon is absorbed above the bandgap. The photogenerated current density J_{sc} under illumination with the photon flux ϕ_{sun} is therefore

$$J_{sc} = q \int_0^\infty \phi_{sun}(E) a(E) dE = q \int_{E_g}^\infty \phi_{sun}(E) dE, \tag{2.1}$$

where E is the photon energy and q is the elementary charge. The absorption is defined by the absorptance $a(E)$, which is zero below and unity above the bandgap. Figure 2.1a illustrates this situation. Absorptance multiplied with the spectrum gives the photocurrent (hatched region) in the idealized cell.

In thermodynamic equilibrium, every process within the solar cell has to be in equilibrium with its inverse process. A violation of this law - the detailed balance

principle - would cause a net flux of energy, which contradicts the assumption of thermodynamic equilibrium. From detailed balance of the radiative microscopic processes follows that the macroscopically observable photon fluxes in and out of a device are equal in equilibrium. The amount of black body radiation that is absorbed equals the amount that is emitted if environment and device have the same temperature. Hence, Kirchhoff's law [43] follows, equating absorptance and emissivity of a body as a function of energy and angle.

Planck's law [42] allowed the description of thermal radiation emitted by a black body with the temperature T. Non-thermal radiation, as encountered in a semiconductor under non-equilibrium, is described with a generalization of Planck's law that was introduced by Würfel [44]. Non-equilibrium radiation is accounted for by a non-zero chemical potential μ_γ of radiation, which is equal to the quasi-Fermi-level splitting at the position where radiation is emitted. Würfel's generalized Planck law together with Kirchhoff's law allows the calculation of the emission of an ideal diode with flat quasi-Fermi levels. The emitted photon flux ϕ under the applied bias voltage V is

$$\phi(V,E) = \frac{2\pi E^2}{h^3c^2}\frac{a(E)}{[\exp\left((E-qV)/kT\right)-1]}, \tag{2.2}$$

where h is the Planck constant, c the velocity of light in vacuum, $a(E)$ is the absorptance and emissivity of the solar cell, and kT is the thermal energy. For voltages that are small compared with the emitted photon energies, i.e. $E - qV >> kT$, the Bose-Einstein [45, 46] term in Eq. (2.2) is well approximated by a Boltzmann distribution and we can simplify Eq. (2.2) to

$$\phi(V,E) = a(E)\phi_{\mathrm{bb}}\exp\left(qV/kT\right), \tag{2.3}$$

where the black body spectrum ϕ_{bb} is defined by

$$\phi_{\mathrm{bb}} = \frac{2\pi E^2}{h^3c^2}\exp\left(-\frac{E}{kT}\right). \tag{2.4}$$

The emission described by Eq. (2.2) and shown in Fig. 2.1 must be caused by a recombination current J_{rec}. Since in the radiative limit, there are no other possibilities to recombine, the whole recombination current must be $J_{\mathrm{rec}} = q\Phi$,

where Φ denotes the integration of $\phi(V, E)$ over energy E, i.e.

$$\Phi = \int_0^\infty \phi(V, E) dE. \tag{2.5}$$

In thermodynamic equilibrium, the total current must be zero. Thus, the recombination current has to be the same as the photocurrent, caused by absorption of the black body radiation of the environment. In this situation, the net current must be zero, i.e. $J = q(\Phi(V = 0) - \Phi(V = 0)) = 0$. Thus, the photocurrent in equilibrium must be the same than the recombination current in equilibrium. Under applied bias voltage in the dark and in the Boltzmann approximation, the total current is $J = q\Phi(0)(\exp(qV/kT) - 1)$. The prefactor for the dark current is the radiative saturation current density

$$J_{0,\mathrm{rad}} = q\Phi(0) = q \int a\,(E)\, \phi_{\mathrm{bb}} dE. \tag{2.6}$$

Under voltage bias and illumination, we have to subtract the short circuit current density and finally get

$$J = J_{0,\mathrm{rad}}(\exp(qV/kT) - 1) - J_{\mathrm{sc}}. \tag{2.7}$$

The SQ-theory produces an exponential current/voltage-curve that is mathematically already very close to the one of actual solar cells. Except for series- and parallel resistances, the major differences are the inclusion of non-radiative saturation current densities and of a diode quality factor n_{id} accounting for small deviations from the exponential slope of q/kT. The maximum attainable voltage is given by the voltage, where the solar cell emits as many photons as it absorbs. No net energy is transferred, no net current flows implying that the solar cell is in open circuit conditions. The maximum voltage is therefore usually referred to as the open circuit voltage, which results from Eq. (2.7) by setting the total current $J = 0$ and solving for V, as

$$V_{\mathrm{oc}} = kT/q \ln(J_{\mathrm{sc}}/J_{0,\mathrm{rad}} + 1). \tag{2.8}$$

The efficiency η of the solar cell follows directly from

$$\eta = \frac{\max(-JV)}{P_{\mathrm{opt}}} = \frac{J_{\mathrm{sc}} V_{\mathrm{oc}} FF}{P_{\mathrm{opt}}}, \tag{2.9}$$

where FF is the fill factor and P_{opt} is the optical power density of the incoming radiation. The current is defined by Eq. (2.7). For an unconcentrated AM1.5G spectrum [47], the maximum efficiency is around 33%. The influence of the bandgap on efficiency is rather weak in the range $1\,\text{eV} < E_g < 1.45\,\text{eV}$, while for higher bandgaps the amount of unabsorbed low energy photons becomes too high. For lower band gaps, the photocurrent increases but the lower energy per electron/hole pair leads to a net decrease in both open circuit voltage and efficiency.

2.3 Combining transport with detailed balance

2.3.1 A two state solar cell model

The Shockley-Queisser theory only looked at the solar cell as a black box and did not consider internal details of the photovoltaic process. In order to study the photogeneration process more closely, I introduce the simplest possible discrete solar cell model as depicted in Fig. 2.2. For a discrete solar cell, there are exactly two distinct states fundamentally necessary. One state that absorbs photons and creates electron/hole pairs and one state that collects the minority carrier, for instance the electron.

For the absorbing state, detailed balance between absorption and radiative recombination requires that

$$a\nu = a^*\varphi \tag{2.10}$$

holds in thermodynamic equilibrium. Here $\nu = n/n_0$ is the normalized value of the minority carrier concentration, where n is the minority carrier concentration and n_0 the equilibrium concentration of minority carriers. Correspondingly, $\varphi = \phi/\phi_{\text{bb}}$ is the normalized photon flux. The rate constants for generation and recombination are defined by a^* and a. Since normalization is carried out versus the equilibrium values, Eq. (2.10) reduces to

$$a = a^*, \tag{2.11}$$

i.e. I define one constant a for the radiative coupling between photons and electron/hole pair. The Equation (2.11) is also known as van Roosbroeck-Shockley equation [48] and is the main prerequisite for the Shockley-Queisser theory. Thus,

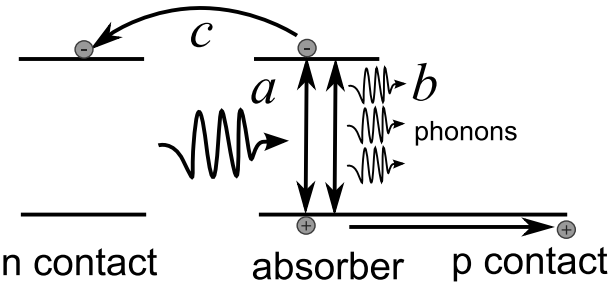

Fig. 2.2: *Scheme of a discrete solar cell model with the smallest possible number of states, namely two - one for the minority carrier contact and one for the absorber. The system is defined by the transition rates a for radiative coupling of photons and electron/hole pairs, b for the non-radiative coupling of electron/hole pairs with the phonon bath and c the coupling between the absorber and the contact. I assume that the majorities are extracted with unity efficiency and thus do not have to consider the hole contact as a separate state.*

it will also be central to the derivation of all our models in the later chapters. However, photogeneration and radiative recombination is not the only pair of processes I will discribe with detailed balance. In the same way, I define the constant b for non-radiative coupling and the constant c for the coupling of the absorber state with the normalized electron concentration in the contact ω. Then, the differential equation for the normalized concentration ν of electrons in the absorber state is

$$\frac{\partial \nu}{\partial t} = -a\nu + a\varphi - b\nu + b - c\nu + c\omega. \tag{2.12}$$

Note that in thermodynamic equilibrium, i.e. when all photon and charge carrier concentrations are one, the right hand side of Eq. (2.12) is zero. That means, as required by the definition of thermodynamic equilibrium, no concentration changes occur.

The boundary condition for the concentration of electrons in the contact is given by the ideal diode law

$$\omega = \exp\left(qV/kT\right). \tag{2.13}$$

Since both the differential equation as well as the boundary condition are defined, I can now calculate the solution for the concentration ν in the steady state $\partial\nu/\partial t = 0$.

If I allow for voltage and illumination bias, it follows

$$\nu = \frac{a\varphi + b + c\exp\left(qV/kT\right)}{a+b+c} \tag{2.14}$$

and for the normalized excess carrier concentration $\Delta\nu = \nu - 1$

$$\Delta\nu = \frac{a\Delta\varphi + c\left[\exp\left(qV/kT\right) - 1\right]}{a+b+c}, \tag{2.15}$$

where $\Delta\varphi$ is the normalized excess photon flux. As for the derivation of the Shockley-Queisser limit, I investigate now both the photocurrent and the recombination current.

The recombination current follows from the concentration of minorities in the dark, i.e. for $\Delta\varphi = 0$. The normalized excess dark carrier concentration is then

$$\Delta\nu_{\mathrm{dark}} = \frac{c}{a+b+c}\left[\exp\left(qV/kT\right) - 1\right]. \tag{2.16}$$

The concentration under illumination is

$$\Delta\nu_{\mathrm{illu}} = \frac{a\Delta\varphi}{a+b+c} \tag{2.17}$$

and the collection efficiency f_{c} of electrons, which determines the photocurrent, is

$$f_{\mathrm{c}} = \frac{c\Delta\nu_{\mathrm{illu}}}{a\Delta\varphi} = \frac{c}{a+b+c}. \tag{2.18}$$

One sees that the collection efficiency f_{c}, defined as the flux of electrons flowing from our single absorber state to the contact, normalized to the excess flux of photons being absorbed, equals the normalized dark carrier concentration $\Delta\nu_{\mathrm{dark}}/(\omega - 1)$. This relation, connecting the injection of carriers in the dark to the extraction of carriers under illumination is known as the reciprocity theorem of Donolato [34]. Just like the SQ-limit, also the Donolato theorem is a direct consequence of the principle of detailed balance [49]. It holds not only in the simplified world of our discrete solar cell model but also for continuous systems, with spatial variation of all given parameters [50–52].

Having discussed the relation between photo- and recombination current, I go one step further and discuss the case of light absorption and photocurrent generation in our discrete solar cell with the inverse case of carrier injection and light emission.

Let us assume that our single absorbing state has a certain distance to the device surface. Optically relevant is the transmittance T that depends on this distance and is defined by the requirement that the absorbed photon flux af depends on the photon flux φ_{surf} impinging on the solar cell surface via

$$a\varphi = Ta\varphi_{\text{surf}}. \tag{2.19}$$

Now, I define a quantum efficiency Q as the number of collected minorities (electrons) per photon impinging on the surface of our device as

$$Q = \frac{c\nu}{\varphi_{\text{surf}}} = \frac{c\nu}{a\varphi}\frac{a\varphi}{\varphi_{\text{surf}}} = f_{\text{c}}aT. \tag{2.20}$$

Turning now to the light emitting diode situation, we have to calculate the photon flux emitted from the surface of the device caused by radiative recombination in our single absorber state. The amount of light created by recombination follows from the rate equation (2.12) as $a\nu$. The amount of light that is emitted by the surface is damped by the factor T accounting for reabsorption of emitted photons. Thus, the emission follows as

$$\varphi_{\text{em}} = a\nu T = aT\frac{c}{a+b+c}\exp\left(qV/kT\right). \tag{2.21}$$

Using $f_{\text{c}} = c/(a+b+c)$ and Eq. (2.20), I find that the emission relates to the quantum efficiency as

$$\varphi_{\text{em}} = Q\exp\left(qV/kT\right). \tag{2.22}$$

Thus, I derived directly from the principle of detailed balance two reciprocity relations, one between the photocarrier collection and carrier injection and one between the solar cell quantum efficiency and the electroluminescence (EL).

2.3.2 The one sided pn-junction

Having discussed the solar cell in a very abstract environment, I will have a final look on a model of a solar cell, which is probably more familiar to the reader. I choose the case of an abrupt one sided pn-junction, which is a decent approximation of e.g. crystalline silicon solar cells, where the whole device consists mostly of one p-type layer, with only a thin n^+-emitter on top. This approximation has the advantage that we again only have to consider minorities – in this case electrons.

The detailed balance between radiative recombination and photogeneration in terms of commonly used quantities like lifetime τ and absorption coefficient α is given by [48]

$$\frac{n_0}{\tau} = \alpha\phi_{\mathrm{bb}}, \tag{2.23}$$

where n_0 is the equilibrium concentration of minorities. Note that Eq. (2.23) is equivalent to Eq. (2.11) with the coefficient a accounting for radiative coupling of photons and electron/hole pairs. The (energy resolved) radiative recombination rate $r_{\mathrm{rad}}(E)$ at position x follows directly from the previous Eq. (2.23) if I allow for excess minority carriers Δn as

$$r_{\mathrm{rad}}(x,E) = \frac{\Delta n(x)}{\tau} = \alpha\phi_{\mathrm{bb}}\frac{\Delta n(x)}{n_0}. \tag{2.24}$$

The electroluminescent emission depends on the rate describing radiative recombination and the probability f_{em} that the created photons are not reabsorbed and follows then from the integral

$$\phi_{\mathrm{em}}(x,E) = \int_0^d r_{\mathrm{rad}}(x,E)\, f_{\mathrm{em}}(x)\, dx \tag{2.25}$$

over the thickness d of the device. Although I don't know the emission probability f_{em} of photons, I can derive it from Würfel's generalized Planck's law (Eq. (2.2)). We know that for flat quasi-Fermi levels and thus a constant quasi-Fermi level split ΔE_{F}

$$\begin{aligned}\phi_{\mathrm{em}} &= \int_0^d \alpha f_{\mathrm{em}}(x)\, dx \phi_{\mathrm{bb}} \exp\left(\tfrac{\Delta E_{\mathrm{F}}}{kT}\right)\\ &= a(E)\,\phi_{\mathrm{bb}} \exp\left(\tfrac{\Delta E_{\mathrm{F}}}{kT}\right)\end{aligned} \tag{2.26}$$

holds. Since the absorptance

$$a(E) = \int_0^d g(x,E)\, dx \tag{2.27}$$

is the integral over the generation rate g, I find

$$\alpha f_{\mathrm{em}}(x) = g(x) \tag{2.28}$$

and finally the EL spectrum also for non-flat quasi-Fermi levels

$$\phi_{\mathrm{em}} = \int_0^d g(x)\frac{\Delta n(x)}{\Delta n_{\mathrm{j}}} dx \phi_{\mathrm{bb}} \exp\left(\frac{qV}{kT}\right). \tag{2.29}$$

Note that the voltage V is defined as the splitting of quasi-Fermi levels at the collecting junction for the minority carriers. Thus, the excess carrier concentration Δn_{j} at the junction is given by

$$\Delta n_{\mathrm{j}} = n_0 \exp\left(qV/kT\right). \tag{2.30}$$

This Eq. (2.30) is equivalent to our definition of ω in Eq. (2.13) for the discrete case. Note that the generation rate $g(x)$ is defined such that it has the unit $[\,\mathrm{cm}^{-1}]$. It relates to the commonly used generation rate G in $[\,\mathrm{cm}^{-3}\,\mathrm{s}^{-1}]$ as G normalized to the incoming photon flux ϕ_{in}, i.e. $g = G/\phi_{\mathrm{in}}$.

In order to show that the emission spectrum defined by Eq. (2.29) is identical to the result obtained for the discrete model [Eq. (2.22)], I need to define the quantum efficiency in a similar way as done in Eq. (2.20). Since the quantum efficiency describes a series connection of photocarrier generation and collection, it is useful to write the quantum efficiency as

$$Q_{\mathrm{e}}\left(E\right) = \int_0^d g\left(x, E\right) f_{\mathrm{c}}\left(x\right) dx, \tag{2.31}$$

i.e. integral over the product of two quantities: the generation rate g and the collection efficiency f_{c}. Thus, by application of Donolato's theorem [34]

$$f_{\mathrm{c}}(x) = \frac{\Delta n_{\mathrm{D}}(x)}{\Delta n_{\mathrm{Dj}}} = \frac{\Delta n_{\mathrm{D}}(x)}{n_0(x)\left[\exp(qV/kT) - 1\right]}, \tag{2.32}$$

I directly obtain the reciprocity between electro-luminescent emission and photovoltaic quantum efficiency for the continuous case [35]

$$\phi_{\mathrm{em}}(E) = Q_{\mathrm{e}}(E)\phi_{\mathrm{bb}}(E)\left[\exp\left(\frac{qV}{kT}\right) - 1\right]. \tag{2.33}$$

2.3.3 Radiative limit for arbitrary mobilities

The Shockley-Queisser theory defines the short circuit current density

$$J_{\mathrm{sc,SQ}} = q\int_0^\infty a(E)\phi_{\mathrm{sun}}(E)dE \tag{2.34}$$

as well as the saturation current density

$$J_{0,\mathrm{SQ}} = q \int_0^\infty a(E)\phi_{\mathrm{bb}}(E)dE \tag{2.35}$$

and the open circuit voltage

$$V_{\mathrm{oc,SQ}} = \frac{kT}{q} \ln\left(\frac{J_{\mathrm{sc,SQ}}}{J_{0,\mathrm{SQ}}} + 1\right) \tag{2.36}$$

only via the radiation balance. The same is possible for the radiative limit at low mobilities. This is still given by the radiation balance, however, now the emitted and absorbed portion of the light is given by the external quantum efficiency and no longer by the absorptance. Thus it follows for the radiative limit of the short circuit current density

$$J_{\mathrm{sc,rad}} = q \int_0^\infty Q_{\mathrm{e}}(E)\phi_{\mathrm{sun}}(E)dE \tag{2.37}$$

as well as of the saturation current density

$$J_{0,\mathrm{rad}} = q \int_0^\infty Q_{\mathrm{e}}(E)\phi_{\mathrm{bb}}(E)dE \tag{2.38}$$

and of the open circuit voltage

$$V_{\mathrm{oc,rad}} = \frac{kT}{q} \ln\left(\frac{J_{\mathrm{sc,rad}}}{J_{0,\mathrm{rad}}} + 1\right). \tag{2.39}$$

2.4 Solar cell and light emitting diode

The fundamentals chapter started with the SQ-limit, i.e. with the perfect solar cell. The case of perfect absorption above the band gap, infinite carrier mobilities and suppressed non-radiative recombination is also the limiting situation for a light emitting diode (LED). It seems that for less ideal devices, the requirements for LEDs and solar cells differ considerably. Organic LEDs [53] for instance have very high LED quantum efficiencies $Q_{\mathrm{LED}} \approx 15\%$ [54], while solar cells made from polymers have just reached only 5% power conversion efficiency [15]. Silicon devices, however, are among the best single junction solar cells, with efficiencies $\eta = 24.7\%$ [55, 56],

however light emission from silicon is rather inefficient with highest LED quantum efficiencies approaching $Q_{\mathrm{LED}} = 1\%$ [57]. Thus, although the reciprocity relation [Eq. (2.33)] suggests a strong link between the light emitting and light absorbing situation, there seems to be no direct relationship between LED quantum efficiency and solar cell efficiency.

However, as shown in Refs. [35, 58, 59], the photovoltaic quantity that actually relates most directly to the LED quantum efficiency is the open circuit voltage V_{oc}. In photovoltaics, a frequently used measure for the amount of recombination is to relate the V_{oc} to the band gap E_{g} either by taking the ratio $qV_{\mathrm{oc}}/E_{\mathrm{g}}$ or the difference $E_{\mathrm{g}} - qV_{\mathrm{oc}}$ [60]. If I instead relate the measured V_{oc} to its radiative limit

$$\begin{aligned} V_{\mathrm{oc,rad}} &= \tfrac{kT}{q} \ln\left(\tfrac{J_{\mathrm{sc}}}{J_{0,\mathrm{rad}}} + 1\right) \\ &\approx \tfrac{kT}{q} \ln\left(\int_0^\infty Q_{\mathrm{e}} \phi_{\mathrm{sun}} dE \Big/ \int_0^\infty Q_{\mathrm{e}} \phi_{\mathrm{bb}} dE\right) \end{aligned} \tag{2.40}$$

as defined by detailed balance, we see a direct correlation to the LED quantum efficiency. The difference of limiting and real V_{oc} gives

$$\Delta V_{\mathrm{oc}} = V_{\mathrm{oc,rad}} - V_{\mathrm{oc}} = -\frac{kT}{q} \ln\left(Q_{\mathrm{LED}}\right), \tag{2.41}$$

since the LED quantum efficiency Q_{LED} is defined as

$$Q_{\mathrm{LED}}(V) = \frac{J_{\mathrm{rad}}(V)}{J_{\mathrm{nr}}(V) + J_{\mathrm{rad}}(V)}. \tag{2.42}$$

Here, J_{rad} denotes the radiative recombination current and J_{nr} the non-radiative recombination current.

This result shows that the LED quantum efficiency and thus the amount of additional non-radiative recombination compared to the radiative one directly correlates with open circuit voltage. This provides us with the reasons for the apparent discrepancy between the requirements for good solar cell and LED materials. A high percentage of radiative recombination is the paramount requirement for efficient LEDs, while indirect semiconductors with their very long radiative lifetimes are not well suited for application in light emitting devices. Of course, they also suffer from their long radiative lifetimes compared to the non-radiative ones in terms of their V_{oc}. However, these losses only enter the V_{oc} and thus the efficiency logarithmically. For instance, a difference of radiative and non-radiative V_{oc} of only 60 meV

corresponds to a dramatic difference in Q_{LED} of one order of magnitude. The reason, why organic polymers have difficulties in becoming high efficiency solar cells is their low mobilities. Except for few special situations[1], the open circuit voltage and thus the LED quantum efficiency are independent of mobility. Thus, a low mobility is in no way an obstacle for the use of a material as LED. However, for solar cells, a low mobility leads to a low collection efficiency and photocurrent and thus is a big obstacle for high efficiencies.

To illustrate these differences, a brief look at our discrete two state device model is helpful. A low mobility is represented by a low coupling constant c of absorber and contact in this model. The open circuit situation is reached, when no current flows, i.e., when $c\nu = c\omega$. The open circuit voltage then follows from solving this equality for V as

$$V_{\mathrm{oc}} = \frac{kT}{q} \ln\left(\frac{a\Delta\varphi}{a+b} + 1\right) \tag{2.43}$$

Obviously, V_{oc} does not depend on the coupling c to the contact but only on the radiative coupling a and non-radiative coupling b of the electrons to the photons and phonons. In contrast, the collection efficiency [see Eq. (2.18)] and in turn the quantum efficiency [see Eq. (2.20)] and the photocurrent depend on c and on a low mobility. Thus, the efficiency of a solar cell is sensitive to low mobilities via the photocurrent, while the LED quantum efficiency is in this simple model totally unaffected by mobilities.

2.5 Properties of optoelectronic devices - a brief summary

Optoelectronic devices like solar cells or light emitting diodes (LEDs) are usually characterized by their parameters like the electro-optical or opto-electrical power conversion efficiency, being for both applications the decisive parameter. Apart from these parameters used to quantify the quality of a device, one can also define properties of the devices that define how they react on deviations from equilibrium. For instance the application of an external voltage to a diode usually leads to an

[1] see chapter 5.3.1 for the discussion of one exception to this rule

exponential increase in current, where the slope is determined only by the temperature. A second example is that the photocurrent is proportional to the photon flux and independent of voltage such that dark J/V and illuminated J/V only differ by a constant factor, the short circuit current. In the following, I will define five properties of optoelectronic devices that are all valid for small deviations from thermodynamic equilibrium. In the next chapters, I will then investigate under which circumstances these properties are still applicable to variable non-ideal solar cells.

Figure 2.3 summarizes these five properties of solar cells that hold for linear deviations from thermodynamic equilibrium. The current/voltage curve consists of two parts, the photocurrent caused by illumination of the sample with excess photons and the recombination current caused by injection of carriers from the contacts due to an applied voltage. For both, photocurrent and recombination current, I define an ideal situation. If the photocurrent is proportional to the photon flux and independent of voltage, the so called superposition principle holds. I define the internal voltage V_{int} as the quasi-Fermi level splitting at the collecting junction. Then the superposition principle means that the J/V_{int}-curve under illumination and in the dark differ only by a constant additive term, the photogenerated current J_{ph}, which is then equal to the short circuit current J_{sc} under illumination.

What might be the reason for a violation of the superposition principle? We already know that the quantum efficiency and thus the photocurrent depend on generation and collection of carriers via

$$J_{\mathrm{ph}} = \int_0^\infty Q_{\mathrm{e}}(E)\,\phi_{\mathrm{sun}}(E)dE = \int_0^\infty \int_0^d g(x,E)\,\phi_{\mathrm{sun}} f_{\mathrm{c}}(x)\,dxdE. \tag{2.44}$$

As long as we are far away from lasing conditions, the generation rate $g(x)$ is independent of voltage and photon flux. Thus, reasons for a violation of the superposition principle will be found in the voltage and illumination dependence of the collection efficiency. In general, Shockley-Read-Hall (SRH) [61, 62] or Auger recombination statistics lead to a minority carrier lifetime that depends on the number of electrons and holes in the device and thus on the voltage and illumination conditions. However in crystalline silicon, for instance, the influence of SRH and Auger recombination on the collection efficiency is sufficiently low that the superposition principle is hardly violated. For pin-junction solar cells, the situation is different insofar as

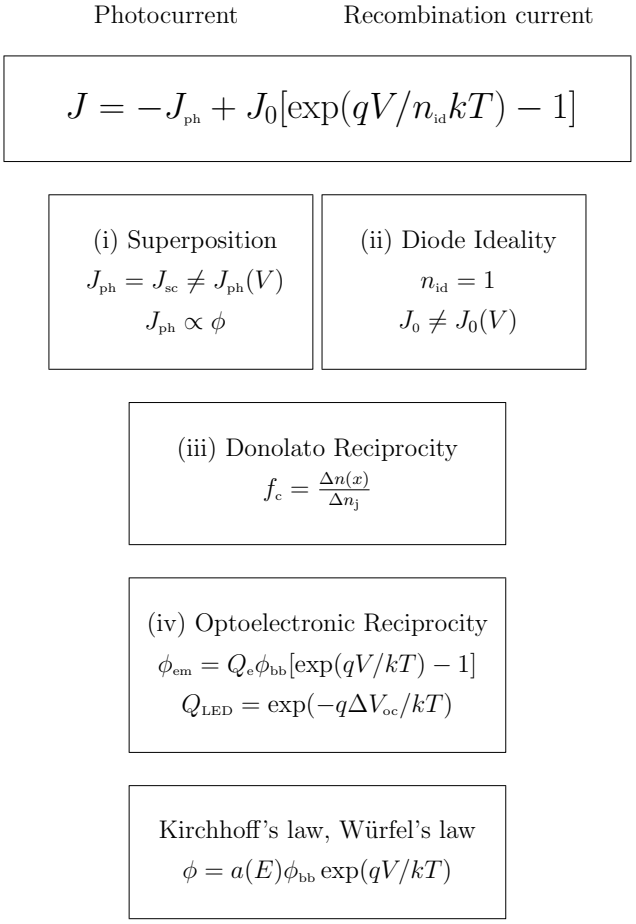

Fig. 2.3: *Summary of the properties of optoelectronic devices. Solar cells that are well described by a linear differential equation for minority carriers such as e.g. our two state model in chapter 2.3.1 for constant values of a, b and c, have (i) a photocurrent independent of voltage and proportional to the excess photon flux and (ii) a recombination current* $J_{rec} \propto \exp(qV/kT)$*. In addition, (iii) the Donolato theorem is valid as well as (iv) the optoelectronic reciprocities.*

the collection efficiency depends on the built-in field under bias, which depends by design linearly on the applied voltage.

The recombination current induced by injection of carriers at the junctions is of course always voltage dependent. For an ideal pn-junction, where only recombination of minority carriers in the neutral region takes place, the recombination current should follow the applied voltage exponentially, while the slope is only given by the inverse thermal voltage q/kT [32]. If the voltage dependence of the recombination current is either not exponential or has another slope than q/kT, usually one or several diode quality factors n_{id} are introduced. Again, we want to ask ourselves under which circumstances the recombination current is not $\propto \exp(qV/kT)$.

Let us neglect the surface recombination for a moment. Then the recombination current in an abrupt one sided pn-type device is

$$J_{\mathrm{rec}} = \int_0^d R \frac{\Delta n_{\mathrm{D}}(x)}{\Delta n_{\mathrm{Dj}}} dx \exp(qV/kT) = J_0 \exp(qV/kT). \tag{2.45}$$

The voltage dependence of the prefactor J_0 may either be caused by a voltage dependence of the recombination constant R or by a voltage dependence of the dark carrier distribution $\Delta n_{\mathrm{D}}(x)/\Delta n_{\mathrm{Dj}}$. Again, the SRH or Auger recombination statistics makes the recombination rate depend on carrier density. This directly affects R and indirectly also the dark carrier distribution $\Delta n_{\mathrm{D}}(x)/\Delta n_{\mathrm{Dj}}$.

The superposition principle and the diode ideality are fundamentally connected by the Donolato theorem [34]. I already introduced the link between photocarrier collection and dark carrier injection

$$f_{\mathrm{c}}(x) = \frac{\Delta n_{\mathrm{D}}(x)}{\Delta n_{\mathrm{Dj}}} = \frac{\Delta n_{\mathrm{D}}(x)}{n_0(x)\left[\exp(qV/kT) - 1\right]}. \tag{2.46}$$

Whenever the collection efficiency becomes voltage dependent, the superposition principle stops to hold [due to Eq. (2.44)]. If all physical quantities describing recombination - like for instance the lifetime τ and the surface recombination velocity S - only depend on voltage, the Donolato theorem will still hold. Thus the dark carrier distribution $\Delta n_{\mathrm{D}}(x)/\Delta n_{\mathrm{Dj}}$ will also be voltage dependent and the diode ideality will differ from unity. If the amount of carriers determines the value of the recombination parameters, the Donolato theorem will stop to be valid, since e.g. the diffusion length under illumination and in the dark will be different even when the

voltage is the same. Thus, a violation of the superposition principle will always induce a diode ideality $n_{\mathrm{id}} \neq 1$. However a diode quality factor $n_{\mathrm{id}} \neq 1$ may stem from either $R(V)$ or $\Delta n_{\mathrm{D}}(x)/\Delta n_{\mathrm{Dj}}(V)$. If the latter is independent of voltage, the voltage dependent recombination rate $R(V)$ may still cause $n_{\mathrm{id}} \neq 1$ without violating the superposition principle.

With the superposition, the diode ideality and the Donolato theorem, I described the interconnections between dark and illuminated current in a solar cell. What is still missing are the connections between the light absorbing and light emitting situation that have been introduced in this chapter [cf. Eqs. (2.33) and (2.41)]. The reciprocity theorem between EL and solar cell quantum efficiency bases on the detailed balance between two series connnected process: injection and radiative recombination as well as photogeneration and collection. As shown in chapter 2.3.2, Eq. (2.33) bases on the Donolato theorem [34] and Würfel's generalized Planck's law [see Eq. (2.2)] [44]. The reciprocity between open circuit voltage and LED quantum efficiency in turn depends on Eq. (2.33) and has thus the same validity range. Therefore both Eqs. (2.33) and (2.41) hold, when the Donolato theorem holds, which is the case as long as the superposition principle is valid and the photocurrent is voltage independent. In the following chapters, I will discuss these expectations derived from the basic equations (2.33), (2.41), (2.44), (2.45) and (2.46) for the case of bipolar and excitonic pin-junction solar cells as well as bulk heterojunction solar cells.

Chapter 3

Detailed balance model for bipolar charge transport

Inorganic solar cells are best described by assuming that photons directly create electron hole pairs and that excitons play no relevant role for energy transport. For this class of devices with bipolar transport, I develop a detailed balance model compatible with the Shockley-Queisser theory that is applicable also to pin-type solar cells, being the most common device geometry used for low mobility materials.

3.1 Introduction

In the fundamentals chapter, I discussed how the maximum solar cell efficiency follows from the radiation balance between emitted and absorbed photons via the so called Shockley-Queisser limit. The strict form of the Shockley-Queisser limit assumes step function like absorptances and perfect collection of carriers, implying that the absorber must be infinitely thick (step function like absorptance) and infinitely thin (perfect collection) at the same time. Relaxing the criterion of abrupt step-function like absorptances is conceptionally very simple, since the equations used for calculation of the SQ-limit [cf. Eqs. (2.34-2.36)] apply for any shape of the absorptance. Relaxing the criterion of perfect collection, however, requires a totally new model to calculate the radiative efficiency.

To include transport with finite mobilities to the detailed balance concept, the SQ-theory is based on, one needs to solve the continuity equations for electrons and

holes in a semiconductor just like any electronic device simulator does. However, to be compatible with the SQ-limit, an important ingredient has to be added to the differential equations used by most conventional device simulators. Radiative recombination inside a photovoltaic absorber leads to photons with an energy around the band gap. Of course, it is possible that these photons emitted by the solar cell itself are also absorbed at another position in the solar cell. This effect is usually termed photon recycling and has to be included for calculation of radiative efficiencies in low mobility materials. The importance of photon recycling becomes obvious, when considering an extreme case, as for instance a fluorescent collector. Here the dye molecules inside a PMMA matrix are not at all electronically coupled. Transport of energy only happens by absorption, emission and reabsorption events. A model that takes into account photon recycling describes fluorescent collectors just like a solar cell in the limit of zero mobilities.

The self consistent inclusion of photon recycling into a model of a pn-junction solar cell has already been realized by Mattheis et al. [33]. In this model, the pn-junction solar cell was discussed on an abstract level assuming the absorber to consist of the base region, while the pn-junction and the emitter region served as the boundary conditions for the differential equation in the base. Thus, the problem reduces to the solution of the diffusion equation for minority carriers in the base of the absorber. This linear differential equation has then been solved by matrix inversion.

For many thin film solar cells with rather low mobilities, however, the pn-junction is not the usually chosen device geometry. Instead, the largest part of the absorber is made up of an intrinsic (undoped) region, while the selectivity of the contacts is guaranteed by either thin, highly doped regions of different doping type or by metals or transparent conductive oxides with different work functions, as in the case of most organic solar cells.

In this chapter, I will first discuss the basic differences between pn and pin-type solar cells. Subsequently a detailed balance model for pin-type solar cells is introduced, which is capable of calculating the radiative efficiencies of low mobility materials. Since the pin-junction is an interesting case of a non-linear system, I discuss the validity of the system properties introduced in the fundamentals chapter, i.e. of the superposition principle, the diode ideality and the several reciprocity

theorems. Finally, I present an application of my detailed balance model, the calculation of mobility dependent radiative efficiencies for two materials making use of quantum effects for photovoltaic absorbers.

3.2 pn and pin type solar cells

Most solar cells are pn-junction diodes, a cell geometry that is used for crystalline silicon solar cells but also for thin film solar cells, like Cu(In,Ga)Se_2 or CdTe solar cell. However, it is by far not the only device geometry suitable for solar cells and in some cases, other device geometries perform considerably better. Any solar cell consists of a stack of different electronically active layers that may have different band gaps, doping concentrations and thicknesses. The combination of these layers, which I will term device geometry in the following, has several tasks for the photovoltaic operation. The first task of solar cells is (i) absorption of photons and creation of photogenerated carriers and/or excitons. Thus, the layer stack has to include at least one layer with an appropriate band gap and a high absorption coefficient. The carriers must then be (ii) collected, the electrons and holes each at a separate contact to achieve a net current flow. This requires merely a selectivity of contacts. The third requirement is the (iii) existence of one or several capacitive elements in the solar cell, where the externally applied voltage drops internally.

Figure 3.1 shows how three different device geometries fulfill these three tasks differently. The pn-junction solar cell usually has a thick base and a thin emitter region. Most of the light is absorbed in the base, according to requirement (i), and the pn-junction provides the necessary selectivity for electrons and holes (ii). Under applied voltage, as shown in Fig. 3.1d, the space charge region of the pn-junction also serves as capacitor (iii). Carrier collection is usually limited by diffusive transport of minority carriers to the junction. The system is therefore in first approximation linear and the collection efficiency of the minority carriers depends in a wide range not on the applied voltage.

Figure 3.1b presents another possible type of device geometry that is not used in practical solar cells but serves as a good example to understand, why efficient collection of carriers is not sufficient for high photovoltaic power conversion efficiencies [63]. In short circuit, the high band offsets at either side of the so-called

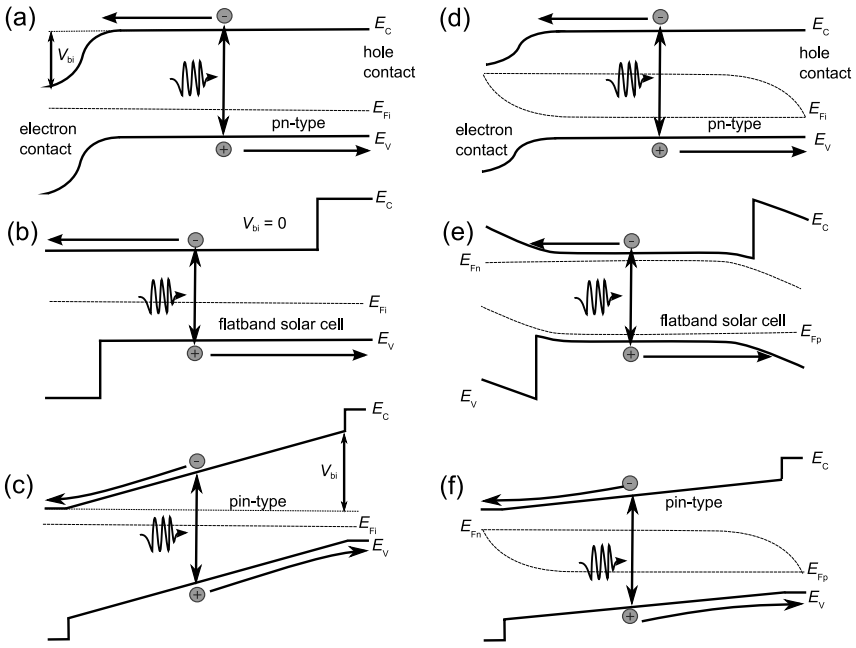

Fig. 3.1: *(a,d) A pn-type solar cell, (b,e) a flatband solar cell and a (c,f) pin-type solar cell both in short circuit and under applied voltage. Contact selectivity necessary for charge carrier collection can be achieved either by a regions with different doping concentration like for the pn and pin-type cell or with band offsets like for the flatband cell. The advantage of the pn-type solar cell is that the capacitive element (the pn-junction) is outside the main absorber region and the diffusive transport to the junction is unaffected over a large range of applied voltages. The pin-junction solar cell has a built in field in the whole absorber thereby enhancing carrier collection by an internal field. However, this field enhanced collection is voltage dependent (see f).*

flatband solar cell provide the required selectivity of contacts. However, under applied voltage (Fig. 3.1e) the flatband solar cell suffers from the fact that there is no capacitive element, where the voltage can drop without hindering charge carrier collection. At the location of the voltage drop, a potential barrier will be created leading in most cases to a low fill factor [63].

The flatband solar cell achieves charge separation merely by introducing sufficiently high band offsets. A built in voltage V_{bi} is not necessary at all, which makes clear that the open circuit voltage of photovoltaic devices in general is not limited by the built in voltage. However, an insufficiently small built-in voltage will always hinder charge carrier collection under applied voltage. Band offsets may be used in solar cells for better charge carrier collection, however they are in practical cases always combined with pn-type or pin-type structures.

The third device geometry presented in Fig. 3.1c is the pin-type solar cell. Here the absorber layer is made up of an intrinsic region, while the selectivity of contacts is realized by very thin p and n-type regions. These thin and usually highly doped regions on both sides of the absorber create a large internal field in short circuit and thus a high built in voltage. Charge transport is no longer merely diffusive but enhanced by the internal field. For low mobility and short circuit conditions, this configuration enhances therefore charge carrier collection. If a voltage is applied as shown in Fig. 3.1f, the built in field decreases. That means the field enhanced charge transport is by design dependent on applied voltage, making the pin-type solar cell a non-linear device where the collection efficiency and therefore the photocurrent are voltage dependent for insufficiently high mobilities.

From the schematic band diagrams in Fig. 3.1, we already arrived at some intuitive assumptions on the advantages and disadvantages of pn and pin-type devices. In order to provide a solid base for these assumptions, I performed simulations with the software ASA to compare pn and pin-type devices for the case of non-radiative recombination as it is usually encountered in most real devices. I assumed Shockley-Read-Hall (SRH) [61, 62] recombination with a recombination rate R_{SRH} of the form

$$R_{\mathrm{SRH}} = \frac{np - n_{\mathrm{i}}^2}{(n + n_{\mathrm{i}})\tau_{\mathrm{p}} + (p + n_{\mathrm{i}})\tau_{\mathrm{n}}} \tag{3.1}$$

with the electron and hole lifetimes given by $\tau_{\mathrm{n}} = \tau_{\mathrm{p}} = 1\mu\,\mathrm{s}$.

Figure 3.2 shows the fill factor, open circuit voltage, short circuit current density and efficiency of a pn-type (solid line) and a pin-type (dashed line) solar cell as a function of the electron and hole mobility. For high mobilities, the recombination current in the pn-type cell is smaller than in the pin-type cell, since the region with high recombination, i.e. where $n \approx p$, is larger in the pin-type cell. The fact that the recombination rate has its maximum at $n = p$ follows directly from Eq. (3.1)

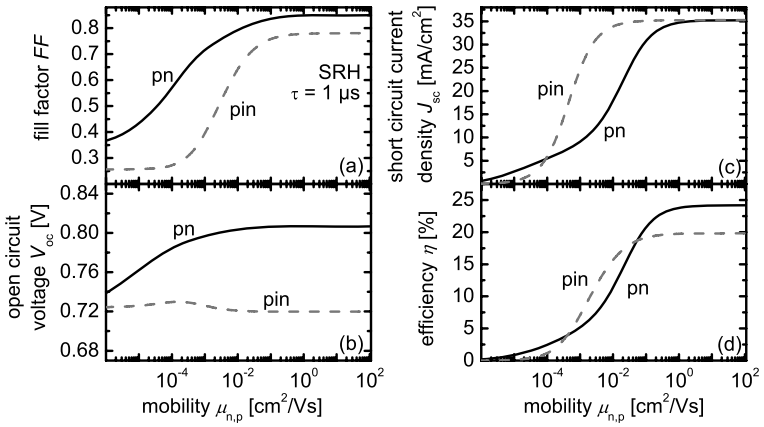

Fig. 3.2: *(a) FF, (b) V_{oc}, (c) J_{sc} and (d) efficiency η of a pn-type (solid line) and a pin-type (dashed line) solar cell as a function of the electron and hole mobility. For the recombination rate, I assumed SRH like recombination with electron and hole lifetimes $\tau_n = \tau_p = 1\mu$s. For high mobilities, the recombination current in the pn-type cell is smaller than in the pin-type cell, since the region with high recombination, i.e. where $n \approx p$ is larger in the pin-type cell. Thus, the V_{oc} and the high mobility fill factor of the pn-type cell is higher than that of the pin-type cell. For lower mobilities, the FF of the pin-type cell decreases already at higher mobilities than the one of the pn-type solar cell, since the collection of carriers is strongly voltage dependent in pin-type devices. However, the J_{sc} for the pin-type cell decreases only at much lower mobilities than for the pn-type solar cell, since the collection of charge carriers is enhanced by the built in field extending over the whole absorber width in case of the pin-type solar cell. The result for η is that for an important region of low mobilities, the pin-type solar cell is actually superior to the pn-type device.*

and from the link between electron and hole concentration, which is given by

$$np = n_{\mathrm{i}}^2 \exp(qV/kT). \tag{3.2}$$

Thus, the V_{oc} of the pn-type cell is higher and subsequently also the fill factor FF in the limit of high mobilities.

For lower mobilities, the FF of the pin-type cell decreases at higher mobilities than the FF of the pn-type solar cell. This is because the collection of carriers is strongly voltage dependent in pin-type devices leading to a decreased FF (cf. Fig. 3.1f). However, the short circuit current density J_{sc} of the pin-type cell decreases at lower mobilities than the one of the pn-type solar cell. This advantage of the pin-type cell is due to the collection of charge carriers being enhanced by the built in field extending over the whole absorber width. The final result for the efficiency η is that for an important region of low mobilities, the pin-type solar cell has actually a higher efficiency than the pn-type device.

Solar cells with pin-type geometry are mostly used for thin film silicon devices made from amorphous or microcrystalline silicon. In this case the pin-type cell has an additional advantage not covered by the simulations of Fig. 3.2. The intrinsic regions in amorphous silicon for instance have much less defects than the doped regions, which leads to the situation that the lifetimes are strongly doping dependent. The advantage of a higher V_{oc} in case of the pn-type device as shown in Fig. 3.2b would then vanish.

3.3 Superposition, ideality and reciprocity in pin-type solar cells

From Figs. 3.1c,f and 3.2a, we know that pin-type solar cells are non-linear devices with a potentially voltage dependent photocurrent. Thus, I will discuss in the following, how the device properties superposition, ideality and reciprocity, as introduced in chapter 2.5, behave in a pin-type device. To discuss all important cases, four configurations are presented in the following. The configurations are all pin-type devices and differ only by their mobility and by the recombination mechanism assumed. The two recombination mechanisms are direct band-to-band recombination and SRH-recombination, which is in general a non-linear recombination process. The two mobilities $\mu_{\mathrm{n,p}} = 10^{3}\,\mathrm{cm}^2(\,\mathrm{V\,s})^{-1}$ and $\mu_{\mathrm{n,p}} = 10^{-2}\,\mathrm{cm}^2(\,\mathrm{V\,s})^{-1}$ are chosen such that for the higher mobility transport of charge carriers is much faster than recombination (*perfect collection*) and that for the lower mobility the efficiency of carrier collection depends on the electric field and thus on the bias voltage. For

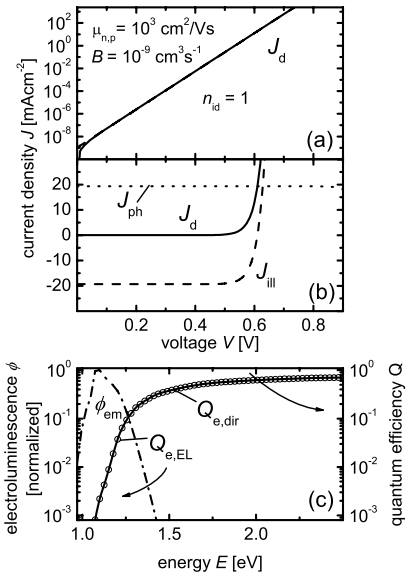

Fig. 3.3: *Comparison of the validity of three properties of photovoltaic devices: (a) ideality, (b) superposition and (c) optoelectronic reciprocity. Due to the choice of direct recombination and high mobilities, the diode ideality $n_{id} = 1$ and the superposition principle (photocurrent $J_{ph} =$ const) is valid as well as the optoelectronic reciprocity ($Q_{e,EL} = Q_{e,dir}$). The working point for the EL measurements used for $Q_{e,EL}$ is $V = 0.6\,\mathrm{V}$ throughout section 3.3.*

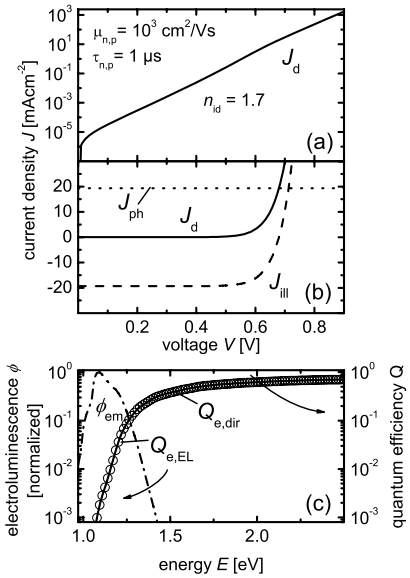

Fig. 3.4: *In spite of the choice of SRH-recombination leading to the diode ideality $n_{id} \approx 1.7$, the superposition principle is valid as well as the optoelectronic reciprocity. This is due to the case that the mobilities are high, the quasi-Fermi levels are flat and thus the collection efficiency is practically unity for any position in the device.*

all four configurations, Figs. 3.3 - 3.6 present the same types of simulations. These simulations are current/voltage curves (a) in the dark and (b) under illumination. In addition, the photocurrent $J_{\mathrm{ph}} = J_{\mathrm{d}} - J_{\mathrm{ill}}$, defined as the difference between dark current density J_{d} and the current density J_{ill} under illumination is also shown in each

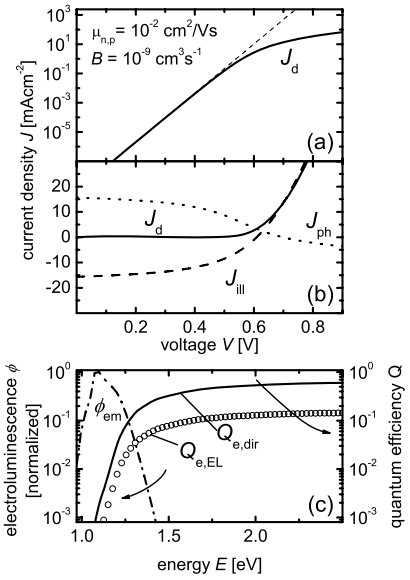

Fig. 3.5: *For direct recombination and low mobilities, (a) the ideality of the dark current (solid line) starts to differ from one (dashed line) and (b) the photocurrent becomes voltage dependent. Now, also the optoelectronic reciprocity loses its validity ($Q_{e,EL} \neq Q_{e,dir}$).*

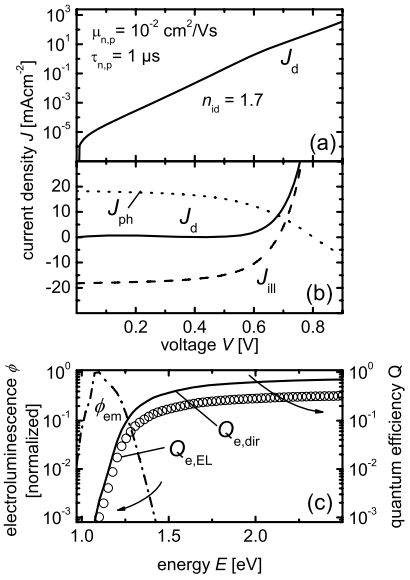

Fig. 3.6: *For SRH-recombination and low mobilities (a) the ideality of the dark current (solid line) is both higher than one and heavily voltage dependent just like (b) the photocurrent. The optoelectronic reciprocity loses its validity ($Q_{e,EL} \neq Q_{e,dir}$).*

subfigure (b). Finally, the (c) electroluminescence spectrum ϕ_{em} and the quantum efficiencies $Q_{\mathrm{e,EL}}$ and $Q_{\mathrm{e,dir}}$ are shown. For all simulations of the electroluminescence spectrum in section 3.3, a working point $V = 0.6\,\mathrm{V}$ is chosen.

Figure 3.3 shows the abovementioned simulations for the configuration with the parameters $\mu_{\mathrm{n,p}} = 10^3\,\mathrm{cm}^2(\,\mathrm{V\,s})^{-1}$ for electrons and holes (high mobility case), a direct recombination coefficient $B = 10^{-9}\,\mathrm{cm}^3\,\mathrm{s}^{-1}$, a device thickness of $d = 500\,\mathrm{nm}$ and an absorption coefficient α of crystalline silicon [64]. Figure 3.3a shows that the ideality factor n_{id} of the dark current is unity. This is due to the assumption of

direct recombination, where the recombination rate is given by $R_{\mathrm{dir}} = Bnp$. Since B is a constant and independent of voltage and since $np = \mathrm{const}$ due to the high mobility, the recombination rate is proportional to $\exp(qV/kT)$, with an ideality of one.

Figure 3.3b shows that the photocurrent, i.e. the difference between the illuminated and dark J/V-curves is constant over voltage. That means that the superposition principle [65] is valid. Figure 3.3c shows that the quantum efficiency $Q_{\mathrm{e,EL}}$ (circles) calculted from the EL spectrum (dash-dotted line) is equal to the directly measured $Q_{\mathrm{e,dir}}$ (solid line). Thus, the optoelectronic reciprocity [Eq. (2.33)] is valid.

Figure 3.4 demonstrates that for high mobilities, we can also use Shockley-Read-Hall (SRH) recombination and still obtain the same result for the superposition and the reciprocity, although the diode ideality differs from unity. This means that the recombination rate and thus the recombination current are voltage dependent and not proportional to $\exp(qV/kT)$. The voltage dependent recombination rate leads to a recombination current, which is described by $J_0(V)\exp(qV/kT)$. The voltage dependent prefactor J_0 is equivalent to an ideality $n_{\mathrm{id}} \neq 1$ [66]. Note here that the validity of the reciprocity for the high mobility limits shown in Figs. 3.3 and 3.4 is equivalent to the validity of Würfel's generalization [44] of Planck's and Kirchhoff's law.

Figure 3.5a shows that for direct recombination and low mobilities, the ideality of the dark current (solid line) starts to differ from unity (dashed line) and the photocurrent becomes voltage dependent (see Fig. 3.5b). Now, also the optoelectronic reciprocity loses its validity ($Q_{\mathrm{e,EL}} \neq Q_{\mathrm{e,dir}}$) as shown in Fig. 3.5c. This is because collection and injection are now heavily field and thus voltage dependent and thus no longer the same in the illuminated short circuit situation and in the dark situation leading to the EL emission. The difference between $Q_{\mathrm{e,EL}}$ and $Q_{\mathrm{e,dir}}$ now depends on the bias conditions. For all simulations of $Q_{\mathrm{e,EL}}$ I used $V = 0.6\,\mathrm{V}$. For higher voltages the built-in field becomes lower and thus the difference between the short circuit situation and the situation with applied bias becomes larger. For lower voltages $Q_{\mathrm{e,EL}}$ and $Q_{\mathrm{e,dir}}$ approach each other.

Figure 3.6a shows that for SRH-recombination and low mobilities the ideality of the dark current (solid line) is both higher than one and heavily voltage dependent

just like (see Fig. 3.6b) the photocurrent. For the validity of the optoelectronic reciprocity holds the same as for direct recombination with low mobilities: The voltage dependence of collection and injection leads to a difference between $Q_{\mathrm{e,EL}}$ and $Q_{\mathrm{e,dir}}$ depending on the applied voltage.

The main conclusion of the section 3.3 is that an ideality factor $n_{\mathrm{id}} \neq 1$ may have two reasons, namely a non-linear recombination process (like SRH-recombination) or voltage dependent collection as encountered in low mobility pin-type solar cells. The validity of the superposition principle as well as the validity of the optoelectronic reciprocity only depends on the question whether carrier collection is voltage dependent or not. Thus, the validities of superposition and reciprocity seem to be equivalent.

3.4 Model

After these preliminary investigations of pin-type solar cell, I introduce a model that is capable of calculating also the radiative limit for finite mobilities. To do so, I have to calculate first the carrier concentrations and then derive the current densities for electrons and holes from them. To calculate the carrier concentrations as a function of depth in the absorber, three differential equations have to be solved. The Poisson equation $\Delta\varphi = -\rho/\epsilon$ - relating the electrical potential φ to the space charge ρ and the dielectric constant ϵ - as well as the continuity equations describing transport as well as generation and recombination of carriers. The drift diffusion equations for the electron concentration n and the hole concentration p in a pin-type device are given by

$$-\frac{1}{q}\frac{dJ_{\mathrm{n}}}{dx} = -D_{\mathrm{n}}\frac{d^2n}{dx^2} - F\mu_n\frac{dn}{dx} = G - Bnp \tag{3.3}$$

$$\frac{1}{q}\frac{dJ_{\mathrm{p}}}{dx} = -D_{\mathrm{p}}\frac{d^2p}{dx^2} + F\mu_p\frac{dp}{dx} = G - Bnp \tag{3.4}$$

where J_{n} and J_{p} are the electron and the hole current densities, F is the electric field, G is the optical generation rate, $D_{\mathrm{n,p}} = \mu_{\mathrm{n,p}}kT/q$ is the diffusion constant of the electrons and holes. Due to the principle of detailed balance, the radiative recombination constant B is linked to absorption via the van Roosbroeck-Shockley

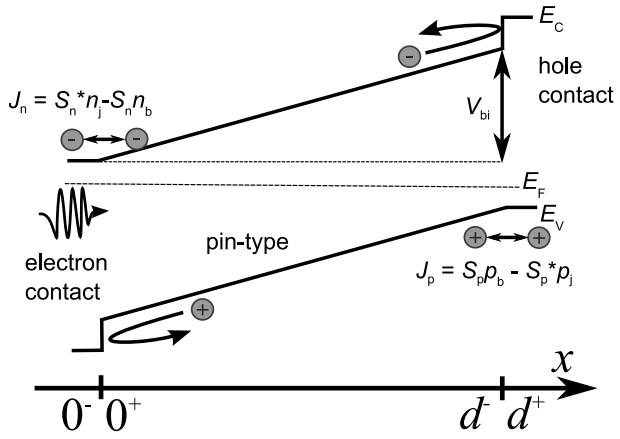

Fig. 3.7: *Schematic band diagram of the simulated pin-type solar cell highlighting the boundary conditions needed for the model in chapter 3.4. At the electron contact at $x = 0$, I allow for electron extraction and injection, while the extraction of holes which corresponds to the recombination of holes is set to zero. At the hole contact, at $x = d$, the difference between hole extraction and injection gives the net hole current. Again, minority carrier recombination is set to zero.*

equation [48]

$$Bn_{\mathrm{i}}^2 = \int \alpha(E)\phi_{\mathrm{bb}}(E)dE \tag{3.5}$$

Figure 3.7 shows the schematic band diagram of the pin-type solar cell under investigation. I only solve the continuity equations in the intrinsic region of the pin-device, while the p and the n-type layer are assumed to are infinitely thin and serve only as the boundary condition. In general, I need four extraction/injection velocities at the two contacts , i.e. two at $x = 0$ and two at $x = d$. For simplicity, I assume throughout the chapter that the electron contact is only active for electrons and the hole contact is only active for holes, meaning that surface recombination of minorities is suppressed. Thus, there are two boundary conditions left. For the electrons at the electron collecting contact ($x = 0$), I consider the possibility of extraction and injection to obtain a net electron current

$$j_{\mathrm{n}} = S_{\mathrm{n}}^{*} n_{\mathrm{j}} - S_{\mathrm{n}} n_{\mathrm{b}} \tag{3.6}$$

where the rate constants S_{n}, S_{n}^{*} have the dimension of a (collection or injection) velocity. In Eq. (3.6), the concentration of electrons on the bulk side of the contact is denoted as n_{b} and the concentration of electrons on the contact side is denoted n_{j}. Detailed balance requires now that the net current is zero in thermodynamic equilibrium thereby interlinking the two rate constants via

$$S_{\mathrm{n}}^{*} n_{\mathrm{j0}} = S_{\mathrm{n}} n_{\mathrm{b0}} \tag{3.7}$$

where $n_{\mathrm{j/b0}}$ is the equilibrium concentration of electrons in the bulk/junction. Equivalently, for the holes at the hole contact ($x = d$) holds

$$j_{\mathrm{p}} = -S_{\mathrm{p}}^{*} p_{\mathrm{j}} + S_{\mathrm{p}} p_{\mathrm{b}} \tag{3.8}$$

with

$$S_{\mathrm{p}}^{*} p_{\mathrm{j0}} = S_{\mathrm{p}} p_{\mathrm{b0}} \tag{3.9}$$

In addition to the boundary conditions for the two types of carriers, I have to define boundary conditions for the potential. In contrast to pn-junction solar cells, where applying a voltage means to inject minority carriers at the pn-junction into the base, in pin-junctions electrons are injected into the intrinsic layer at the n-contact and holes at the p-contact. This is achieved by changing the potential between the electron and hole contact via

$$V_{\mathrm{bi}} = V_{\mathrm{bi,0}} - V \tag{3.10}$$

where V is the applied voltage and $V_{\mathrm{bi,0}}$ is the equilibrium built in voltage.

3.5 Application to quantum well solar cells

3.5.1 Introduction

Theoretical calculations for estimation of efficiency limits of a given material are a two step process. The first step needs to derive material parameters theoretically. This task may be realized for instance by first principle calculations or calculations via the effective mass approximation [67] that determine the band structure of the new material. From this band structure, quantities like absorption coefficient and density of states follow, which subsequently serve to evaluate the efficiency limits of

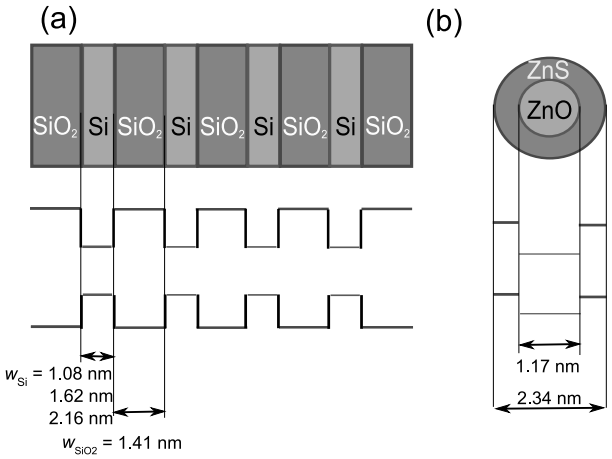

Fig. 3.8: *Scheme of the two investigated materials, (a) a SiO_2/Si superlattice and (b) a ZnO/ZnS nanowire. For both materials the schematic band diagram and the thicknesses and diameters of the geometry are given.*

the given material. A first estimate of efficiency directly follows from the band gap, by calculating the SQ efficiency limit. However, with this approach a high amount of information contained, e.g., in the absorption coefficient is lost [68].

This chapter therefore shows how to go step by step from the SQ-limit [30] to realistic efficiencies. Thereby, I am able to identify both the potential of a given concept but also the critical order of magnitude required of those parameters that are not accessible by first principle calculations [36]. For example, I show how to determine the necessary thickness and the necessary quality of the light trapping scheme to have enough absorption of photons. I also estimate the mobilities and lifetimes necessary for efficient extraction of carriers and a sufficiently high open circuit voltage.

The materials I investigate are SiO_2/Si quantum wells, which I compare to recently published theoretical data on coaxial ZnO/ZnS nanowires [22]. These materials have in common that they are possible candidates as the high band gap partner in a tandem configuration, for instance with crystalline silicon, and that the materials are abundant and non-toxic. Figure 3.8 presents a schematic drawing of the geometry and band diagram of the two materials. Finding materials with high

band gaps $E_g \approx 1.7 - 1.9\,\mathrm{eV}$ as a tandem partner is probably the most feasible way to enhance current state of the art single junction concepts considerably above their present limits. This is because up to now multijunction approaches are the only concept that has proven its ability to increase efficiencies above the SQ-limit [69]. All other concepts, like up- [70, 71] and down-conversion [72, 73], hot carrier solar cells [74–76] and multiple exciton generating absorbers [26, 77, 78] are still lacking experimental proof of efficiencies above the Shockley-Queisser limit.

A natural candidate as a tandem partner for single junction cells with band gaps around $E_g \approx 1.1\,\mathrm{eV}$ would be amorphous silicon [79]. However, although this material has an adequate band gap of around 1.8 eV, amorphous silicon is currently lacking a sufficiently high short circuit current to make current matching with high quality solar cells like c-Si possible. Therefore, superlattice absorber materials using SiO_2/Si [80–84], SiN_x/Si [85] or SiC/Si [86, 87] quantum wells or quantum dots are currently investigated experimentally by different research groups. Deposition of such stacks is possible, for instance, with plasma enhanced chemical vapor deposition of alternating layers of Si and SiO_2 followed by a rapid thermal annealing step. Confinement effects [88] in the superlattices allow band gaps to be adjusted by changing the thickness of the Si layer and the thickness and material of the surrounding dielectric. In addition, the small size of these quantum confined structures is supposed to lead to an increased oscillator strength. However, quantum confinement is in contrast to the task of charge carrier extraction, requiring highly mobile carriers. In addition, a quantum confinement implies an increase in internal interface area, which is most likely to be detrimental for non-radiative charge carrier lifetimes. Thus, the main challenge for any absorber making use of quantum effects is the achievement of sufficiently high absorption at the right band gap for example for use in tandem configuration with c-Si - but at the same time the achievement of high carrier mobilities and carrier lifetimes albeit the large band offsets and the many interfaces in the absorber.

3.5.2 Optical results

From the first principle calculations (which were carried out in Jena [36]), I derived absorption coefficients, effective densities of state and anisotropic effective masses

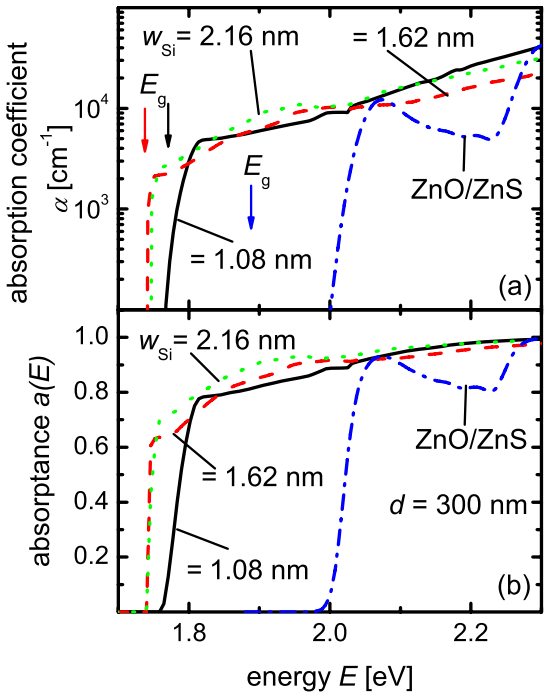

Fig. 3.9: *(a) Absorption coefficient and (b) absorptance of the three SiO_2/Si quantum wells [89] and of the ZnO/ZnS nanowire [22]. For the absorptance, I assumed a thickness $d = 300\,\mathrm{nm}$, Lambertian light trapping and zero front surface reflection as well as unity back surface reflection. The band gaps, defined as the onset of absorption are indicated by arrows ($E_g = 1.76\,\mathrm{eV}(w_{Si} = 1.08\,\mathrm{nm})$, $E_g = 1.74\,\mathrm{eV}(w_{Si} = 1.62\,\mathrm{nm}$, $w_{Si} = 2.16\,\mathrm{nm})$, $E_g = 1.88\,\mathrm{eV}$ (ZnO/ZnS nanowire))*

in transport direction. In a first step, I focus only on the optical properties of our materials, i.e. on the absorption coefficient α and the index of refraction n.

In the original Shockley-Queisser theory, the radiative limits of solar cells were calculated only from the band gap, assuming a step function like absorptance. However, in reality, solar cells will have a finite thickness and the absorptance will be

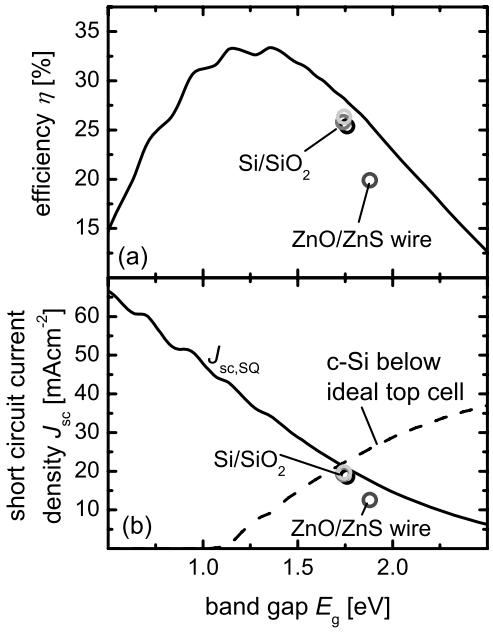

Fig. 3.10: *Efficiency as a function of band gap for step function like absorptances (solid line), an absorber temperature* $T = 300\,\mathrm{K}$ *and an AM1.5G spectrum. The radiative high mobility efficiencies calculated for the three* SiO_2/Si *quantum well configurations and for the ZnO/ZnS nanowire are indicated by open symbols. The thickness of the Si layer is* $w_{Si} = 2.16\,\mathrm{nm}$, $1.62\,\mathrm{nm}$ *and* $1.08\,\mathrm{nm}$ *from high efficiency to low efficiency. (b) Short circuit current density in the SQ-limit as a function of band gap (solid line) and short circuit current density of a 200* μm *thick c-Si solar cell in the high mobility limit and with Lambertian light trapping (dashed line). The c-Si cell is assumed to be optically below an ideal step-function like topcell with the band gap indicated by the x-axis. Thus, the intersection of the dashed and the solid line marks band gap and efficiency of the perfect top cell for c-Si. The short circuit current of the* SiO_2/Si *quantum well configurations and of the ZnO/ZnS nanowire are again indicated by open symbols.*

smeared out at the band gap. The information about increased oscillator strengths and therefore increased absorption coefficients due to quantum size effects will be lost by discussing only infinitely thick absorbers. Thus, I need to calculate the radiative limit for finite thicknesses, which requires the choice of a certain thickness of the absorber layers. For the moment, the simulations use a thickness $d = 300\,\mathrm{nm}$, which is typical for other thin film solar cells like amorphous silicon. Later (cf. Fig. 3.11), I will also discuss the thickness dependence of the photocurrent.

To calculate the upper limit of the absorptance at a given thickness, I assume zero reflection at the front surface ($R_\mathrm{f} = 0$) and unity reflection at the back ($R_\mathrm{b} = 1$) as well as one Lambertian diffuser on top of the absorber layer. Then the absorptance follows as

$$a(E) = \int_0^d 2\alpha(1 - R_\mathrm{f}) \frac{Ei_2(\alpha x) + Ei_2(\alpha(2d - x))}{1 - t_\mathrm{cell}(1 - t_\mathrm{lamb})} dx \tag{3.11}$$

with $t_\mathrm{lamb} = 1/n^2$. Equation (3.11) uses the definition

$$t_\mathrm{cell} = (e^{-2\alpha d}(1 - 2\alpha d) + (2\alpha d)^2 Ei(2\alpha d)) \tag{3.12}$$

for the angle-integrated transmission of the cell from the front with one reflection at the back side to the front, where

$$Ei(z) = \int_z^\infty \frac{e^{-t}}{t} dt \tag{3.13}$$

is the exponential integral, and

$$Ei_2(z) = z \int_z^\infty \frac{e^{-t}}{t^2} dt = e^{-z} - z Ei(z). \tag{3.14}$$

Equation (3.11) allows the calculation of the absorptance $a(E)$ from the absorption coefficient α in the limit of Lambertian light trapping. One additional requirement for the calculation of the absorptances is the knowledge of the refractive index n of the absorber material. This is due to the fact that the product of photon density of states and speed of light in a medium with refractive index n scales with n^2. Isotropically distributed photons will always have a higher density in the medium compared to air or vacuum and thus also the path length of weakly absorbed photons scales with n^2. Total internal reflection described by Snell's law guarantees that this thermodynamic requirement actually holds, by defining the transmission through a Lambertian surface as $t_\mathrm{lamb} = 1/n^2$. The refractive indices n_SL used for

calculation of the absorptances of the SiO_2/Si superlattices are estimated from the empirical refractive indices of Si and SiO_2 via

$$n_{\mathrm{SL}} = \frac{w_{\mathrm{Si}} n_{\mathrm{Si}} + w_{\mathrm{SiO2}} n_{\mathrm{SiO2}}}{w_{\mathrm{Si}} + w_{\mathrm{SiO2}}} \tag{3.15}$$

For the refractive index of silicon and SiO_2, I used $n_{\mathrm{Si}} = 3.5$ and $n_{\mathrm{SiO2}} = 1.5$ leading to the values $n_{1.08} = 2.37$, $n_{1.62} = 2.57$, $n_{2.16} = 2.71$ for the refractive indices for the cells with $w_{\mathrm{Si}} = 1.08\,\mathrm{nm}$, 1.62 nm and 2.16 nm, respectively. The refractive index n_{nw} of the ZnO/ZnS nanowire is simply unknown. Even the assumption that it may be in between the refractive indices for ZnO and ZnS seems not to be valid in this case of a type II heterojunction. The band gap of the nanowires is not in between the band gap of ZnO and ZnS but much lower, meaning that the optical properties of the nanowire are fundamentally different from either of the two bulk materials. In order to avoid big differences compared to the superlattices that are due to this unknown refractive index, I choose it to be $n_{\mathrm{nw}} = 2.5$.

With the help of the refractive indices defined above and the absorption coefficients calculated from first principles and presented in Fig. 3.9a, Eqs. (3.11-3.14) allow the calculation of the absorptances and Eqs. (2.37 - 2.39) the calculation of the radiative high mobility efficiencies of the three SiO_2/Si quantum well configurations and of the ZnO/ZnS nanowire. Figure 3.10a compares these radiative efficiencies (open circles) with the result of the Shockley-Queisser theory (solid line). Figure 3.10b presents the corresponding short circuit current densities, again in comparison to the Shockley-Queisser theory (solid line). In addition to the short circuit current densities in the SQ-limit and the radiative limit of the four cells with finite thicknesses, the dashed line represents the short circuit current density of a 200 μm thick silicon cell, again with Lambertian light trapping, that is placed optically below a step-function like top cell with the band gap as indicated by the x-axis. That means, for a two terminal tandem configuration with a very good crystalline silicon cell as the bottom cell, the intersection of dashed and solid line defines the perfect band gap and the short circuit current to be achieved. The values of this intercept are $E_{\mathrm{g}} = 1.72$ eV and $J_{\mathrm{sc}} = 21.7\,\mathrm{mA/\,cm^2}$. The values calculated for the three SiO_2/Si superlattices are quite close to this intersection, while the ZnO/ZnS nanowire has a slightly too high band gap and too low short circuit current, meaning that it would require a higher band gap bottom cell or a triple junction configuration for best

performance.

I mentioned that the thickness $d = 300\,\mathrm{nm}$ used for the calculation of the absorptances in Fig. 3.9b was an arbitrary value. Thus, Fig. 3.11 shows the evolution of short circuit current density J_{sc} versus absorber thickness for one of the three SiO_2/Si superlattices ($w_{\mathrm{Si}} = 1.08\,\mathrm{nm}$). The lines correspond to the absorptance calculated with Eq. (3.11) under the assumption of Lambertian light trapping.

This ideal case with zero reflection at the front is compared to two layer stacks consisting of a thick glass layer on top and a 100 nm thick ZnO layer between the glass and the absorber layer. Optically below the absorber are 20 nm ZnO and 300 nm Ag. The glass and the ZnO layers are assumed to be perfectly transparent and the refractive indices for ZnO and Ag are taken from Ref. [90]. For the calculation of the absorptance of the layer stack, I used a thin film transfer matrix approach able to calculate absorptances coherently. The difference between the two layer stacks is the angular distribution function of the interfaces. While the dotted line represents a layer stack with isotropically scattering surfaces, the dashed line represents flat surfaces. Thus Fig. 3.11 shows how much light is lost to reflections if a realistic layer stack is assumed. This loss is given by the difference between the solid and the dotted line. The current gain due to scattering surfaces and enhanced trapping of weakly absorbed light is given by the difference between the dashed and the dotted line. At $d = 300$ nm, the difference due to light trapping amounts to $J_{\mathrm{sc}} \approx 4\,\mathrm{mA/\,cm^2}$, which shows that efficient light trapping is a main prerequisite for these thin film approaches.

3.5.3 Results for finite mobilities

Up to now, I calculated the Shockley-Queisser limit from the absorption coefficients derived from first principles calculations. In the following, the model described in section 3.4 is used to calculate the radiative limit also for finite mobilities. Compared to the purely optical calculations in the Shockley-Queisser theory, the detailed balance model needs additional paramters, i.e. the mobility and the intrinsic carrier concentration n_{i} (see Eq. (3.5)).

The intrinsic carrier concentration follows from the effective density of states N_{C} and N_{V} of conduction and valence band and the band gap of the different ma-

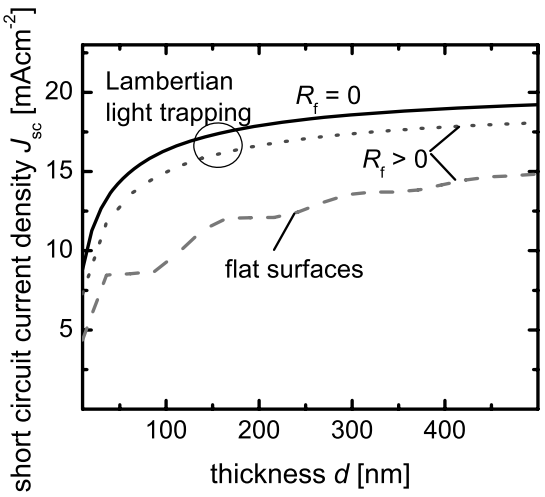

Fig. 3.11: *Short circuit current density displayed as a function of absorber thickness in the high mobility limit for the SiO_2/Si quantum well configuration ($w_{Si} = 1.08\,\mathrm{nm}$) for Lambertian light trapping with perfect antireflective coating, i.e. $R_f = 0$ (lines), for Lambertian light trapping and considering the reflections at an air/glass and glass/ZnO interface, i.e. $R_f > 0$ (dotted lines) and for flat surfaces (dashed line), where the same finite reflection at the front is included as for the dotted line. In case of the flat surfaces, the simulation includes coherent interference in all layers except the front glass. The difference between the flat surface (dashed line) and the Lambertian surface (dotted line) due to light trapping is tremendous, namely around $4\,\mathrm{mA/cm^2}$ at $d = 300\,\mathrm{nm}$, showing the large influence of light trapping for these thin devices.*

terials via the equation

$$n_\mathrm{i} = \sqrt{N_\mathrm{C} N_\mathrm{V}}\exp\left(-E_\mathrm{g}/2kT\right). \tag{3.16}$$

The band gaps follow from the onset of absorption as E_g (w_Si = 1.08 nm) = 1.76 eV, E_g (w_Si = 1.62 nm) = E_g (w_Si = 2.16 nm) = 1.74 eV, and E_g (ZnO/ZnS) = 1.88 eV (cf. Fig. (3.9)). The effective densities of states for the superlattices were

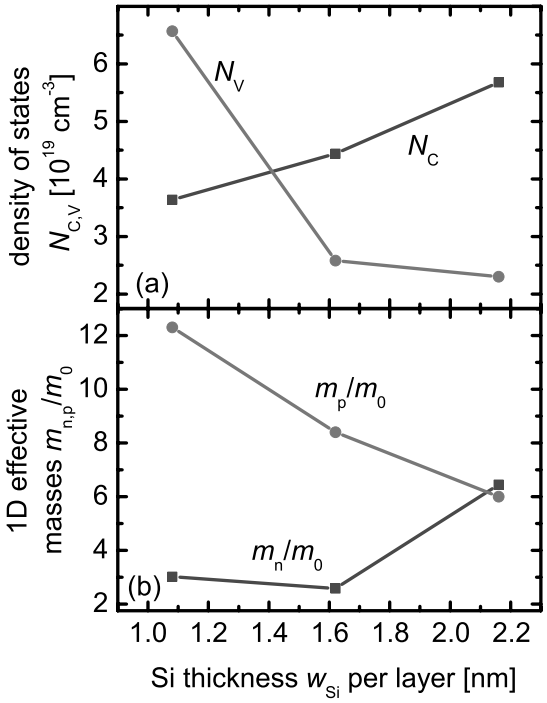

Fig. 3.12: *(a) Effective density of states for valence (circles) and conduction band (squares) as well as (b) one dimensional effective masses normalized to the electron mass in vacuum.*

calculated and are presented in Fig. 3.12a. The effective density of states for the nanowire is unknown and was set to an arbitrary value of $N_C = N_V = 10^{19}\,\mathrm{cm}^{-3}$.

The detailed balance model is designed in a way that for high mobilities of free carriers, the result is the same as in the generalized SQ-limit. Figure 3.13 shows the current/voltage curve of the three SiO_2/Si superlattices and the ZnO/ZnS nanowire in the radiative limit and for electron and hole mobilities $\mu_n = \mu_p = 10^3\,\mathrm{cm}^2(\mathrm{V\,s})^{-1}$. The J_{sc}, V_{oc} and efficiency are equal to those calculated with the radiation balance alone [Eqs. (2.37 - 2.39)], thus these mobilities are a good approximation of infinity.

The density of states and the effective masses of electrons and holes are not

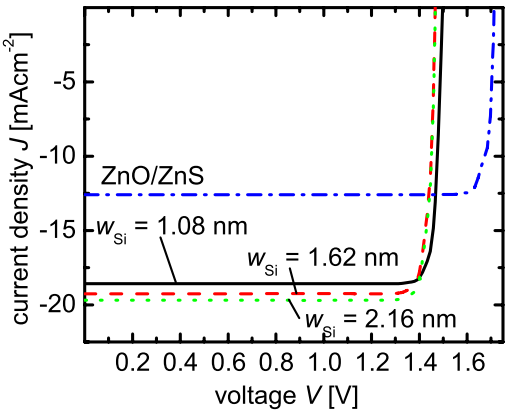

Fig. 3.13: *Current/Voltage curves in the radiative high mobility limit for 300 nm thick pin-devices for the four discussed theoretical absorber materials (three SiO_2/Si superlattices: $w_{Si} = 1.08\,\text{nm}$ - solid line, $w_{Si} = 1.62\,\text{nm}$ - dashed line, $w_{Si} = 2.16\,\text{nm}$ - dotted line; and the ZnO/ZnS nanowires - dash-dotted line). The efficiencies from these curves are the same that follow from the calculation of the SQ-limit.*

only relevant to calculate the intrinsic carrier concentration but they have also been used to estimate the mobilities of free charge carriers [67]. The Bloch mobility follows from [67]

$$\mu_{\text{n,p}} = \frac{q\tau_{\text{sc}}}{m_{\text{n,p}}}, \tag{3.17}$$

where τ_{sc} is the scattering time and $m_{\text{n,p}}$ are the effective masses for electrons and holes. In case of the SiO_2/Si superlattices, the mobility is expected to be strongly anisotropic. Since transport has to take place in direction normal to the interfaces, the relevant mobility is smaller than the mobility averaged over all directions. Thus, I have to determine the one dimensional effective mass of electrons and holes in z-direction. Figure 3.12b shows the result of this calculation normalized to the mass m_0 of electrons in vacuum. In order to calculate mobilities from the effective masses, I still need an estimate of the scattering time τ_{sc}. Jiang and Green [67] discuss this issue extensively for the case of Si quantum dots embedded in a dielectric and I

therefore use the same value, namely $\tau_{sc} = 30$ fs. This scattering time together with the effective masses in Fig. 3.12b yields the mobilities $\mu_n = 17.6\,\mathrm{cm^2(\,V\,s)^{-1}}$, $\mu_p = 4.3\,\mathrm{cm^2(\,V\,s)^{-1}}$ (for $w_{Si} = 1.08$ nm), $\mu_n = 20.5\,\mathrm{cm^2(\,V\,s)^{-1}}$, $\mu_p = 6.3\,\mathrm{cm^2(\,V\,s)^{-1}}$ (for $w_{Si} = 1.62$ nm) and $\mu_n = 8.2\,\mathrm{cm^2(\,V\,s)^{-1}}$, $\mu_p = 8.8\,\mathrm{cm^2(\,V\,s)^{-1}}$ (for $w_{Si} = 2.16$ nm).

For the case of the ZnO/ZnS nanowires, I don't have calculations of the effective masses needed for Eq. (3.17). Nevertheless, literature provides values for ZnO nanowires, which are however much thicker than our current nanowires. The reported values are in the range of [91–94] $10\,\mathrm{cm^2(\,V\,s)^{-1}} < \mu < 30\,\mathrm{cm^2(\,V\,s)^{-1}}$.

Figure 3.14 shows the short circuit current density as a function of the electron and hole mobility in the limit of solely radiative recombination. Here, the mobilities for electrons and holes are assumed to be equal. It is obvious that the critical mobility in the radiative limit is far below the values that have been calculated from the effective masses or have been taken from literature. For all four samples, again with a thickness of $d = 300$ nm, the critical mobility μ_c, where the short circuit current starts to drop below its high mobility limit, is in the range $10^{-5}\,\mathrm{cm^2(\,V\,s)^{-1}} \leq \mu \leq 10^{-4}\,\mathrm{cm^2(\,V\,s)^{-1}}$, i.e. 4 - 6 orders of magnitude below the estimated values. In the following, I need to investigate, whether this buffer is sufficient for high photocurrents also in the case of non-radiative recombination.

3.5.4 Results for non-radiative recombination

The last step from highly idealized devices to more realistic ones is the introduction of non-radiative recombination combined with the inclusion of parasitic absorption in the ZnO window layers. I assume a layer stack as shown in Fig. 3.15a, which is identical to the one used for Fig. 3.11. The layer stack consists of a thick glass layer on top and a 100 nm thick ZnO layer between the glass and the absorber layer. Optically below the absorber are 20 nm ZnO and 300 nm Ag. The optical properties of the layers are taken from Ref. [90]. Taking the same mobilities and densities of states that are given in Table 3.1, I receive the cell parameters presented in Fig. 3.16 for the three SiO_2/Si superlattices and for the ZnO/ZnS nanowire as a function of carrier lifetime. Non-radiative recombination is modeled with a recombination rate according to Shockley-Read-Hall statistics (see Eq. (3.1)). In the following, I

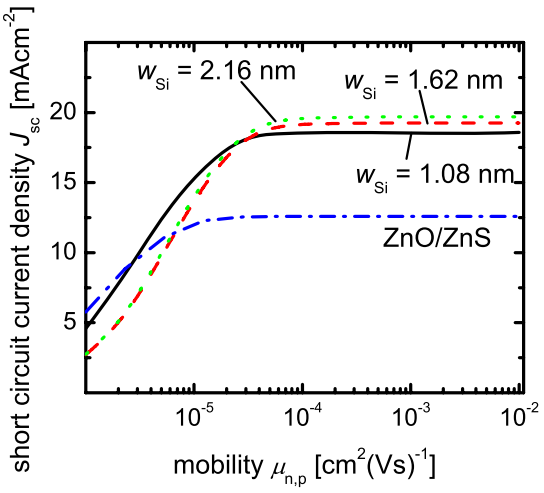

Fig. 3.14: *Short circuit current density J_{sc} as a function of electron and hole mobility $\mu = \mu_n = \mu_p$ for the three SiO_2/Si superlattices ($w_{Si} = 1.08\,\mathrm{nm}$ - solid line, $w_{Si} = 1.62\,\mathrm{nm}$ - dashed line, $w_{Si} = 2.16\,\mathrm{nm}$ - dotted line) and the ZnO/ZnS nanowires (dash-dotted line) in the limit of solely radiative recombination for a pin-type device with a thickness of $d = 300\,\mathrm{nm}$. For mobilities $\mu < 10^{-4}\,\mathrm{cm}^2/Vs$, the short circuit current density J_{sc} starts to drop rapidly below its high mobility limit. This critical mobility $\mu_c \approx 10^{-4}\,\mathrm{cm}^2/Vs$ is around five orders of magnitude below the estimated mobilities, which are in the range of $\mu \approx 10^{1}\,\mathrm{cm}^2/Vs$. Thus, I expect low mobilities to deteriorate device performance only for a considerable amount of non-radiative recombination.*

always set the lifetimes for electrons and holes equal, i.e. $\tau_\mathrm{n} = \tau_\mathrm{p} = \tau$.

Figure 3.16a shows that the efficiency increases monotonically with longer carrier lifetimes τ, however, the curves show two regions with different slopes. For lifetimes $\tau < 1$ ns, the increase is steeper than for higher lifetimes. The explanation for that is given by the different dependence of open circuit voltage V_{oc}, fill factor FF and short circuit current density J_{sc} on the lifetime. Figure 3.16b shows that the short circuit current density J_{sc} stays constant for $\tau > 1$ ns and starts to decay

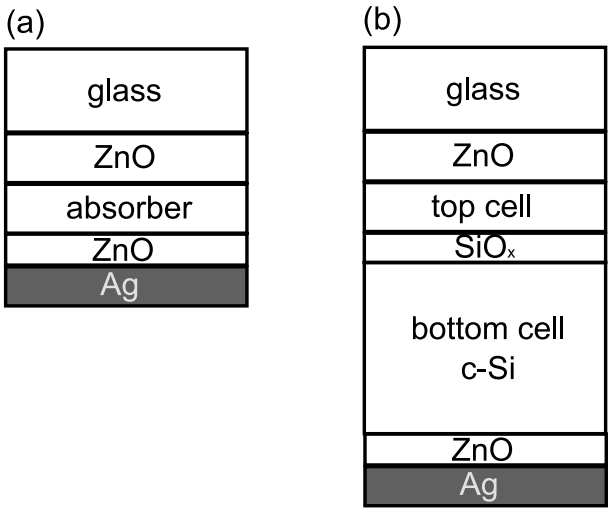

Fig. 3.15: *Scheme of the layer stacks used for the calculation of the efficiencies with non-radiative recombination. The stack shown in (a) is used for Fig. 3.16, while the tandem cell in (b) is used for Fig. 3.17. The absorber layer in (a) and the top cell in (b) represent the superlattice or nanowire layer.*

drastically once the lifetime drops below 1 ns. In contrast, the slope of the increase of open circuit voltage V_{oc} versus lifetime as shown in Fig. 3.16c does not vary much. The fill factor, which is presented in Fig. 3.16d, follows roughly the decay of the short circuit current density J_{sc}, with the only difference that the drop starts at slightly longer lifetimes $\tau \approx 10$ ns. This higher sensitivity of the fill factor compared to the short circuit current density J_{sc} to the lifetime is due to the collection of carriers being dependent on the built-in field in the pin-junction. Since the built in field is higher at zero voltage than at maximum power point voltage, the collection at short circuit is more efficient at a given mobility lifetime product $\mu\tau$. Collection at higher voltages and thus the fill factor will therefore suffer first, when the $\mu\tau$-product decreases.

It would now be interesting to estimate the carrier lifetimes one could expect from the superlattice structures and to compare them with the lifetimes required by Fig. 3.16. In order to calculate surface recombination velocities from lifetime

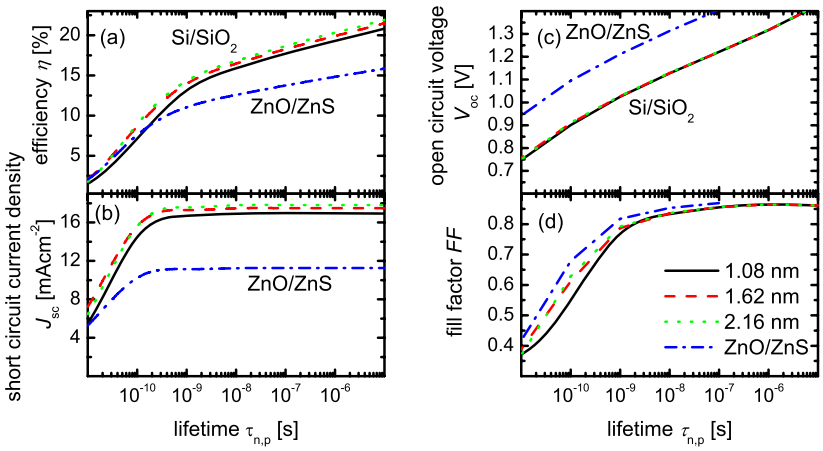

Fig. 3.16: *(a) Efficiency, (b) short circuit current density J_{sc}, (c) open circuit voltage V_{oc} and (d) fill factor FF as a function of electron and hole lifetime $\tau = \tau_n = \tau_p$ for the three SiO_2/Si superlattices ($w_{Si} = 1.08\,\mathrm{nm}$ - solid line, $w_{Si} = 1.62\,\mathrm{nm}$ - dashed line, $w_{Si} = 2.16\,\mathrm{nm}$ - dotted line) and the ZnO/ZnS nanowires (dash-dotted line). I assume a device thickness of $d = 300\,\mathrm{nm}$ and recombination following a Shockley-Read-Hall statistics with a recombination center in the middle of the device. While the open circuit voltage decreases with shorter lifetimes monotonously with a relatively constant slope, J_{sc} and FF have two regions with a different slope. Above a certain lifetime $\tau > 10\,\mathrm{ns}$ (for the FF) and $\tau > 1\,\mathrm{ns}$ (for the J_{sc}), the values are nearly constant, while they drop abruptly for lower lifetimes τ. These critical lifetimes depend linearly on the mobility μ and represent the critical $\mu\tau$-product up to which efficient extraction of the photocurrent is possible.*

measurements on passivated wafers, Sproul [95] developed an equation for the dependence of lifetime τ_S and surface recombination velocity given by

$$\tau_S = \frac{w}{2S} + \frac{w^2}{D\pi^2} \tag{3.18}$$

where w is the thickness of the whole wafer, S the surface recombination velocity

Tab. 3.1: *Values for the electron and hole mobilities μ_n and μ_p, the effective density of states N_V and N_C for valence and conduction band and the refractive index n for the SiO_2/Si-superlattices and the ZnO/ZnS nanowires used for the simulations if not stated otherwise. The effective density of states and the refractive index are used for Figs. 3.13, 3.14-3.17 and the mobilities for Figs. 3.16 and 3.17.*

	SiO_2/Si-superlattice			ZnO/ZnS
	$w_{Si} = 1.08$ nm	$w_{Si} = 1.62$ nm	$w_{Si} = 2.16$ nm	nanowires
μ_n [cm^2/Vs]	17.6	20.5	8.2	10
μ_p [cm^2/Vs]	4.3	6.3	8.8	10
N_C [cm^{-3}]	3.64×10^{19}	4.44×10^{19}	5.68×10^{19}	1×10^{19}
N_V [cm^{-3}]	6.57×10^{19}	2.58×10^{19}	2.30×10^{19}	1×10^{19}
refractive index n	2.37	2.57	2.71	2.5

of both surfaces and D the minority carrier diffusion constant. If the thickness w decreases, the second term describing the diffusion to the surface vanishes. If I now assume our superlattice to be made up of several Si-wells of thickness w that are well passivated with SiO_2, a crude approximation of the resulting lifetime would be to use $\tau_S = w/2S$ for the lifetime of a single well and $\tau_S = w/(2Sn_w)$ for a parallel connection of n_w wells. To estimate the order of magnitude of the lifetime, I assume $w = 2$ nm, $S = 10$ cm/s representing a very well passivated surface and about 100 wells. This leads to a lifetime of $\tau_S = 100$ ps, which is one or two orders of magnitude below the required lifetimes. It is therefore an important question, whether such simplistic calculations are admissible in quantum well solar cells or whether recombination in these devices behaves fundamentally different for extremely small feature sizes.

3.5.5 Tandem solar cells

As mentioned in the introduction, the long term goal of research on the presented absorber layers is the use as a top cell in a multijunction solar cell. In order to estimate the usefulness of the SiO_2/Si superlattices for the combination with e.g. crystalline silicon in a two terminal tandem device, I extended the layer stack used for

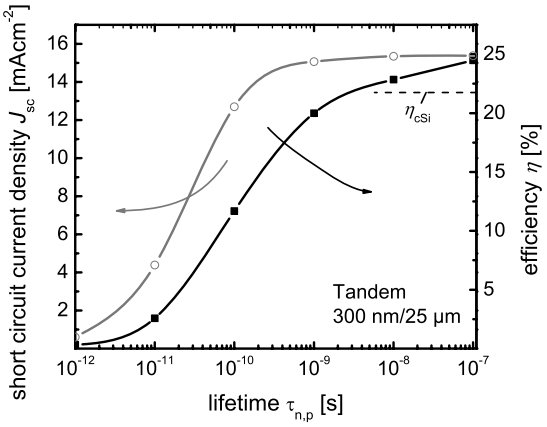

Fig. 3.17: *Short circuit current density J_{sc} and efficiency η of a two terminal tandem cell consisting of a pin-type SiO_2/Si superlattice (Si well thickness $w_{Si} = 1.62\,\mathrm{nm}$, intrinsic layer thickness $d_i = 300\,\mathrm{nm}$) as the top cell and a pn-type crystalline silicon bottom cell. The bottom cell thickness of $d_b = 25\,\mu\mathrm{m}$ was chosen such that the bottom cell is not current limiting. The carrier lifetime for the superlattice required for an efficiency $\eta = 20\%$ is roughly $\tau = 1$ ns. The efficiency of the bottom cell alone is $\eta_{cSi} = 21.8\%$*

Fig. 3.16 by adding a pn-junction made of crystalline silicon below the superlattice in pin-configuration. To enhance the photocurrent produced in the top cell, I added a thin, 20 nm thick intermediate reflector layer [96] with the refractive index of SiO_2. Thus, part of the light that hits the back surface of the top cell does not enter the bottom cell, but is reflected back. The thickness of the bottom cell was then chosen in a way that it is as thin as possible, but does not limit the current. Like for the calculations in Fig. 3.16, I assumed Lambertian light trapping also for the simulation of the tandem cell. The schematic drawing of the resulting layer stack is presented in Fig. 3.15b.

Figure 3.17 shows the short circuit current density and the efficiency of this tandem device as a function of the SRH lifetime of electrons and holes in the top

cell. The top cell is made up of the SiO_2/Si superlattices with the $w_{Si} = 1.62$ nm Si well thickness, since this absorber produced the highest photocurrents in a single junction configuration as shown in Fig. 3.16. It is obvious that the photocurrent of the tandem device is considerably below the $J_{sc} = 21.7$ mA/ cm^2 that were identified in Fig. 3.10 as the optimum value for a c-Si based tandem cell. That is due to the fact that the band gap of $E_g = 1.74$ eV is close to perfect in the SQ-limit for step-function like absorptances but not for our more realistic assumptions on device performance. Loss of photocurrent is due to finite absorption coefficients, imperfect light trapping in the tandem configuration (the top cell has no perfect back reflector), non-zero reflection, small amounts of parasitic absorption and imperfect collection of photogenerated carriers (at least for lifetimes $\tau < 10$ ns). In order to ensure current matching in a two terminal tandem cell, the band gap of the top cell should therefore be chosen considerably smaller than that given by the band gap in the SQ-limit.

The efficiency of the tandem cell just reaches the experimental efficiency limits of crystalline silicon solar cells of $\eta = 24.7\%$. Progress beyond that value would need a better adaptation of the two band gaps. However, high efficiencies in the tandem configuration are reached already at a low thickness of the total stack, which is around 25 μm and therefore much thinner than usual wafer based devices. Due to the difficulties of the top cell to reach a sufficiently high photocurrent, the use of tandem devices will therefore lead to the largest benefit for rather thin and lower quality bottom cells. Note that the efficiency of the c-Si bottom cell alone is $\eta_{cSi} = 21.8\%$, where I assumed a SRH-lifetime $\tau = 1$ ms and a surface recombination velocity $S = 10$ cm/s.

3.5.6 Conclusions

I have presented simulations of solar cells consisting of new types of absorber materials that use quantum effects to fine-tune their optical properties. These new absorber materials are SiO_2/Si superlattices with different Si well thicknesses and ZnO/ZnS coaxial nanowires. The optical and partly also electrical properties have been obtained by first principle calculations. Subsequently, these optical and electrical properties have been used to simulate complete devices. To determine meaningful

efficiency limits I have gone step by step from idealized systems as defined by the Shockley-Queisser theory to more realistic systems, where the efficiency limits are, however, less fundamental. These device simulations allow us to determine critical values for device properties as mobility and carrier lifetime that must be met to ensure efficient photovoltaic energy conversion. Simulations of complete tandem devices show that there is a considerable difference in photocurrent between the Shockley-Queisser theory and more realistic simulations. To ensure current matching albeit this difference in photocurrent one needs considerably lower band gaps for the top cell thereby increasing the part of the spectrum absorbed by the top cell.

Chapter 4

Detailed balance model for excitonic and bipolar charge transport

In most organic semiconductors, absorption of a photon first generates excitons, which then dissociate to form free carriers. The charge seperation process is thus a two step process: exciton dissociation followed by seperation of the free carriers. This chapter therefore includes this two step charge seperation process into the detailed balance model.

4.1 Introduction

The introduction of organic materials as photovoltaic absorbers in organic [6] or dye-sensitized [17] solar cells has raised questions whether or not these new types of devices can be described with the help of theories that initially have been developed for inorganic solid-state type devices usually provided with a pn-homo- or hetero-juncion. In addition, the nano-scale mixture of different organic materials [7, 8] has not only boosted the efficiencies of organic solar cells but also led to an apparent new type of solar cell, the bulk-heterojunction. Recently, it has been proposed to divide all solar cells into two classes, namely the classical inorganic solar cells and the 'excitonic' solar cells, embracing essentially all devices that use organic absorber materials [28, 29].

Thus, this chapter extends the bipolar detailed balance model presented in chapter 3 by including the transport and interaction of excitons to the model. The basic ingredients are (i) light absorption and creation of an exciton as well as radiative recombination and photon emission, (ii) exciton dissociation at an interface or in the bulk and the corresponding inverse process, the recombination of an electron/hole pair in an exciton, and (iii) drift-diffusion transport of electrons and holes as well as diffusive transport of excitons.

The compliance of our model with the principle of detailed balance ensures that for high mobilities and solely radiative recombination, I obtain the same photovoltaic performance of our device as the one following from the SQ-limit, no matter whether transport is predominantly excitonic or bipolar and no matter whether our device is pn-type or pin-type. Proceeding to devices with non-ideal transport, I identify differences between the cases of predominantly excitonic and predominantly bipolar transport in pin-type devices. Since the built in field in pin-type devices depends on the applied voltage, collection and injection of charged particles like electrons and holes will also be a function of voltage if mobilities are low. This voltage dependence is not only visible in simulated current/voltage curves but also in electroluminescence (EL) spectra. I show that the validity of the reciprocity [see Eq. (2.33)] between EL and solar cell quantum efficiency, directly correlates with the voltage dependence of carrier collection and injection. For the cases of either high mobilities or excitonic transport, no voltage dependence is visible and the reciprocity relation is valid. In addition to the cases of excitonic and bipolar solar cells, I also discuss how to incorporate the concept of bulk heterojunction solar cells into our model. Finally, I explain how the effects of band offsets at the heterointerface and the morphology of the blend in the bulk heterojunction cell are implicitly contained in the principle of detailed balance.

4.2 Model

4.2.1 Excitonic and bipolar solar cells

To be compatible with the detailed balance theory of Shockley and Queisser, the absorption of photons emitted by the device itself has to be taken into account [33].

This effect of optical coupling in the absorber is usually referred to as photon recycling and leads to a homogenization of the carrier distribution. Incorporation of the abovementioned processes in a numerical model results in four coupled differential equations to be solved, namely, the Poisson equation $\Delta\varphi = -\rho/\epsilon$ - relating the electrical potential φ to the space charge ρ and the dielectric constant ϵ - and three continuity equations, one for the exciton concentration χ given by

$$D_\chi \frac{d^2\chi}{dx^2} = \frac{\chi}{\tau_\mathrm{D}} + \frac{\chi}{\tau_\mathrm{r}} - R_\chi np - G_\chi \tag{4.1}$$

one for the electron concentration n

$$D_\mathrm{n} \frac{d^2n}{dx^2} + F\mu_n \frac{dn}{dx} = -\frac{\chi}{\tau_\mathrm{D}} + R_\chi np \tag{4.2}$$

and one for the hole concentration p

$$D_\mathrm{p} \frac{d^2p}{dx^2} - F\mu_p \frac{dp}{dx} = -\frac{\chi}{\tau_\mathrm{D}} + R_\chi np \tag{4.3}$$

Here, R_χ is the recombination rate of free carriers leading to the creation of excitons, τ_D is the bulk dissociation lifetime of the excitons, τ_r is the radiative lifetime of the excitons, F is the electric field, $\mu_{\chi/n/p}$ the mobilities and $D_{\chi/n/p} = \mu_{\chi/n/p}kT/q$ the diffusion constants according to Einstein's equation, where kT/q is the thermal voltage. Note that an electrical field is present only in case of a pin-junction as sketched in Fig. 4.1a whereas we have no electric field in the bulk of the absorber of a pn-junction device (Fig. 4.1b).

Equations (4.1-4.3) already contain the detailed balance relations between the different processes, meaning that the rates are connected to the equilibrium concentrations χ_0, n_0 and p_0 of excitons, electrons and holes by the fact that the probability of every process must equal that of its inverse process in thermodynamic equilibrium. Now, I again have to introduce the detailed balance relation between radiative recombination and photogeneration. For our case, namely the absorption of excitons, the van Roosbroeck-Shockley equation [48] yields

$$\chi_0/\tau_r = \int \alpha_\chi(E)\phi_\mathrm{bb}(E)dE, \tag{4.4}$$

where $\alpha_\chi(E)$ denotes the absorption coefficient resulting from the generation of excitons, E the photon energy, and $\phi_\mathrm{bb}(E)$ the black body radiation. Detailed

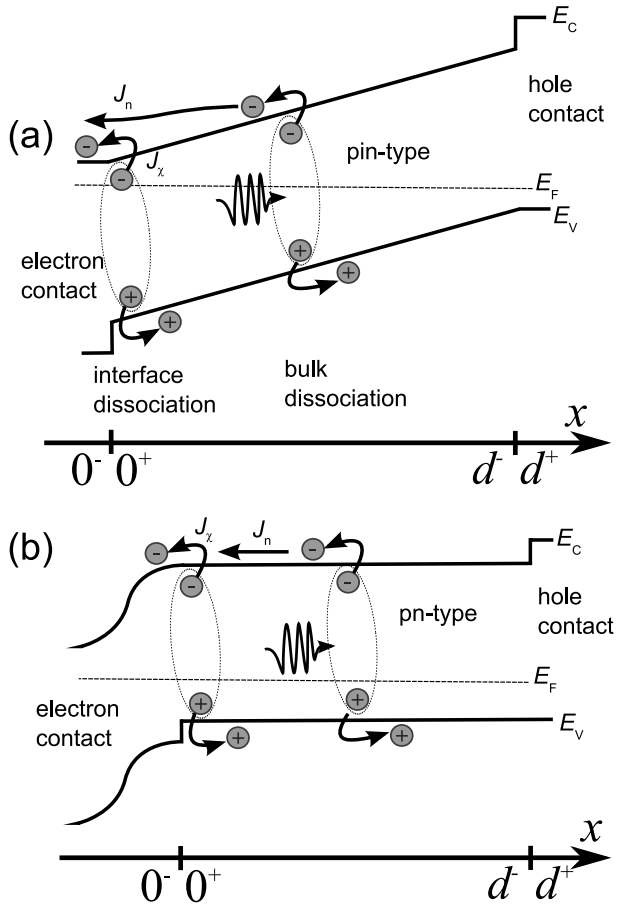

Fig. 4.1: *Scheme of the (a) pin-junction device and the (b) pn-junction device. For both types the photogenerated exciton can be either split in the bulk (bipolar case) or at the junction (excitonic case) of the device.*

balance between dissociation and recombination of excitons and electron/hole pairs leads to

$$R_\chi n_0 p_0 = \chi_0 / \tau_\mathrm{D} \tag{4.5}$$

Similarly, at the front or the back surface I allow for dissociation of an exciton into an electron in the respective junction and a hole that remains in the bulk of

the absorber, as well as the complementary process, dissociation into a hole in the junction and an electron in the bulk. The rates for this type of charge separation that is thought to be the dominant one in excitonic solar cells are determined by the detailed balance relations

$$H_{\mathrm{n}} n_{\mathrm{j0}} p_{\mathrm{b0}} = S_{\chi \mathrm{n}} \chi_0 \tag{4.6}$$

and

$$H_{\mathrm{p}} n_{\mathrm{b0}} p_{\mathrm{j0}} = S_{\chi \mathrm{p}} \chi_0 \tag{4.7}$$

where $H_{\mathrm{n/p}}$ are the cross recombination rates of electrons/holes in the junction with holes/electrons in the bulk of the absorber. The equilibrium concentrations of electrons and holes in the bulk/junction are denoted by $n_{\mathrm{b/j0}}$, $p_{\mathrm{b/j0}}$ and the dissociation velocities for the excitons by $S_{\chi n}$, $S_{\chi p}$. In the non-equilibrium situation, this interface dissociation/recombination process defines the boundary condition for the diffusion equation, Eq. (4.1). Assuming that at the left contact (see Fig. 4.1) the dissociation of an exciton leads to an electron in the junction and a hole in the bulk, the exciton current density j_χ reads

$$j_\chi = H_{\mathrm{n}} n_{\mathrm{j}} p_{\mathrm{b}} - S_{\chi \mathrm{n}} \chi \tag{4.8}$$

Accordingly, at the right contact only dissociation of an exciton into a hole in the junction and an electron in the bulk is allowed. Thus, we have

$$j_\chi = -H_{\mathrm{p}} n_{\mathrm{b}} p_{\mathrm{j0}} + S_{\chi \mathrm{p}} \chi \tag{4.9}$$

Since at the left contact the dissociation of an exciton leads to the generation of a hole in the bulk, we have here the boundary condition for holes

$$j_{\mathrm{p}} = -H_{\mathrm{n}} n_{\mathrm{j}} p_{\mathrm{b}} + S_{\chi \mathrm{n}} \chi \tag{4.10}$$

For electrons, I consider at this contact the possibility of extraction and injection to obtain

$$j_{\mathrm{n}} = S^*_{\mathrm{n}} n_{\mathrm{j}} - S_{\mathrm{n}} n_{\mathrm{b}} \tag{4.11}$$

where the rate constants S_{n}, S^*_{n} have the dimension of a (collection or injection) velocity and are interlinked by the requirements of detailed balance via

$$S^*_{\mathrm{n}} n_{\mathrm{j0}} = S_{\mathrm{n}} n_{\mathrm{b0}} \tag{4.12}$$

At the right contact we have the for symmetry reasons

$$j_{\mathrm{n}} = H_{\mathrm{p}} n_{\mathrm{b}} p_{\mathrm{j0}} - S_{\chi \mathrm{p}} \chi \tag{4.13}$$

and

$$j_{\mathrm{p}} = -S^{*}_{\mathrm{p}} p_{\mathrm{j}} + S_{\mathrm{p}} p_{\mathrm{b}} \tag{4.14}$$

with

$$S^{*}_{\mathrm{p}} p_{\mathrm{j0}} = S_{\mathrm{n}} p_{\mathrm{b0}} \tag{4.15}$$

Note that, for simplicity I assume throughout this chapter that only the electron contact at the left is active in dissociating excitons. Accordingly, I set $H_{\mathrm{p}} = 0$ and $S_{\chi p} = 0$ such that I get $j_{\chi} = j_{\mathrm{n}} = 0$ at the right contact because of Eqs. (4.9) and (4.13).

4.2.2 pn-type and pin-type solar cells

Figures 4.1a,b schematically show a pin-junction (a) and a pn-junction device (b) with a sketch of both, the excitonic as well as the bipolar photocurrent collection pathway. For the pin-junction device the absorber material is embedded between the p-type and the n-type contact. Thus, the fundamental capacitor that serves to electrostatically accommodate the open circuit voltage [63] is defined by the entire device. The built in potential difference between the electron and hole contact in the pin-type device is given by

$$V_{\mathrm{bi}} = V_{\mathrm{bi,0}} - V \tag{4.16}$$

where V is the applied voltage and $V_{\mathrm{bi,0}}$ is the equilibrium built in voltage. Equation (4.16) implies that application of a voltage V reduces the potential between the left and right edge of the absorber and the electrical field F in the absorber. The reduced field then leads to an injection of electrons via the left contact and of holes via the right contact without a change of n_{j} or p_{j} from their equilibrium values n_{j0} and p_{j0} in Eqs. (4.11) or (4.14). A part of the holes injected from the right contact arrive at the left contact where their increased concentration p_{b} triggers the generation of excitons [Eq. (4.8)].

In contrast, for the pn-junction the external voltage builds up across the space charge region which is here put outside the absorber (cf. Fig. 4.1b). The concentration n_j of electrons provided by the junction then follows the applied voltage V exponentially, i.e.,

$$n_\mathrm{j} = n_\mathrm{j0} \exp(qV/kT) \tag{4.17}$$

This increased number n_j of electrons provided by the junction triggers now both, the generation of excitons at the interface, via Eq. (4.8), as well as the injection of electrons, via Eq. (4.11).

4.3 Results

4.3.1 Excitonic and bipolar photocurrent

For all following simulations, I use a set of constant parameters, which are a thickness $d = 300\,\mathrm{nm}$, the absorption coefficient of ZnPc as a typical organic absorber material (taken from Fig. 4 in Ref. [97]), an optical generation profile and a photon recycling scheme calculated according to Ref. [33] that both result from a Lambertian cell surface, an intrinsic carrier concentration $n_\mathrm{i} = 10^3\,\mathrm{cm}^{-3}$ and an equilibrium built in voltage of $V_\mathrm{bi,0} = 1.3\,\mathrm{V}$. Assuming a radiative lifetime of $\tau_\mathrm{r} = 200\mu\,\mathrm{s}$, the equilibrium concentration of excitons follows from Eq. (4.4) as $\chi_0 = 4.4 \times 10^{-3}\,\mathrm{cm}^{-3}$. The other parameters, especially the mobilities and the dissociation lifetime are varied in the following simulations.

First, I want to show that a continuous transition from predominantly bipolar transport to predominantly excitonic transport is possible, when varying the coupling between excitons and free charge carriers defined by the dissociation lifetime τ_D. Since I am only interested in the dominant charge separation mechanism, I focus first on the short circuit situation. Because I assume only the left contact ($x = 0$) to be active in exciton dissociation, the total current equals the hole current $j_\mathrm{p}(d) = j_\chi(0) + j_\mathrm{n}(0)$ at the right contact ($x = d$) as defined by Eq. (4.14). In order to be able to distinguish between electron current and excitonic current, I need to define the currents at the absorber side of the electron contact, i.e. at $x = 0^+$. I distinguish between electrons injected into the contact from the reservoir of electrons in the absorber and electrons injected into contact, following a dissociation of an

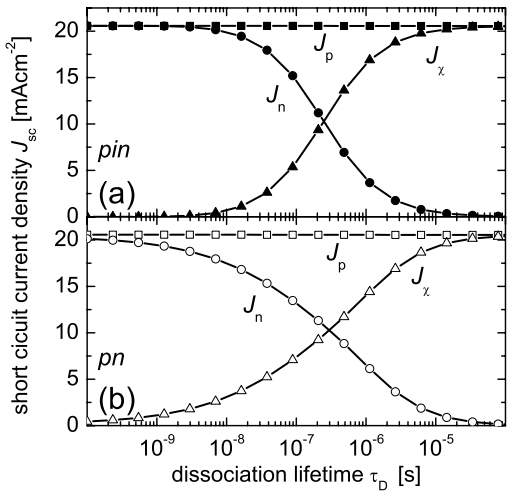

Fig. 4.2: *Short circuit current density as a function of the bulk dissociation lifetime τ_D for the case of a (a) pin-type and (b) pn-type device. Efficient coupling of excitons to charge carriers - i.e. low τ_D - leads to bipolar transport, while an inefficient coupling forces the current to be transported by excitons to the contact. Since the electron contact is the only interface active for dissociation of excitons, the sum of electron current J_n (flow of electrons injected from the absorber into the front contact) and the exciton current J_χ (flow of electrons injected from the absorber by interface dissociation of an exciton) always equals the hole current J_p (flow of holes injected from the absorber into the back contact). The parameters used are (a) $\mu_{\chi,\mathrm{n,p}} = 10^3\,\mathrm{cm^2\,V^{-1}\,s^{-1}}$, $S_n = S_{\chi n} = 10^6\,\mathrm{cm\,s^{-1}}$ and (b) $\mu_\chi = 10^{-1}\,\mathrm{cm^2\,V^{-1}\,s^{-1}}$, $\mu_n = \mu_p = 10^4\,\mathrm{cm^2\,V^{-1}\,s^{-1}}$, $S_n = 10^{10}\,\mathrm{cm\,s^{-1}}$ and $S_{\chi n} = 50\,\mathrm{cm\,s^{-1}}$.*

exciton. The former is denoted as electron current $j_\mathrm{n}(0^+) = S^*_\mathrm{n} n_\mathrm{j} - S_\mathrm{n} n_\mathrm{b}$ [see Eq. (4.11)] and the latter as exciton current $j_\chi(0^+) = H_\mathrm{n} n_\mathrm{j} p_\mathrm{b} - S_{\chi\mathrm{n}}\chi$ [see Eq. (4.8)].

Figure 4.2 shows how a variation of the dissociation lifetime in the range $10^{-4}\,\mathrm{s} > \tau_\mathrm{D} > 10^{-10}\,\mathrm{s}$ for the case of a pin-type cell (Fig. 4.2a) and a pn-type cell (Fig. 4.2b) affects the excitonic and bipolar contribution to the photocurrent.

Figure 4.2a shows that for a short dissociation lifetime $\tau_{\mathrm{D}} < 10^{-8}\,\mathrm{s}$, the solar cell behaves like a classical pin-type device, where the exciton is split into free carriers already in the volume of the absorber. These free carriers then travel via drift-diffusion transport to their respective contacts, where they contribute to $j_{\mathrm{n}}(0^{+})$ and $j_{\mathrm{p}}(d)$. In order to achieve this bipolar transport, exciton dissociation and transport of free carriers must be faster than exciton diffusion and interface dissociation and faster than exciton recombination. Since, I chose our equilibrium concentrations such that $n_{\mathrm{i}} >> \chi_0$ holds, for high mobilities $\mu_{\chi,n,p} = 10^{3}\,\mathrm{cm^2\,V^{-1}\,s^{-1}}$ and high interface dissociation and collection velocities S_{n}, $S_{\chi,n} > 10^{5}\,\mathrm{cm\,s^{-1}}$ of free carriers and excitons, free carriers will always be able to carry larger currents. In contrast, for dissociation lifetimes $\tau_{\mathrm{D}} > 10^{-5}\,\mathrm{s}$ interfacial exciton dissociation is responsible for the total current at the electron contact, i.e. energy transport via excitons is now more efficient than the slow bulk dissociation with subsequent fast bipolar transport. This limit corresponds to the situation of an 'excitonic' solar cell as defined by Refs. [28, 29].

The situation for the pn-type solar cell in Fig. 4.2b is qualitatively very similar. There is also a transition from the bipolar to the excitonic operation mode visible with an intersection between both contributions at dissociation lifetimes around $\tau_{\mathrm{D}} = 2 \times 10^{-7}\,\mathrm{s}$ just like for the pin case. However, there are two distinct differences: The first is the larger extension of the transition region and the second is that the mobilities had to be changed compared to the pin-type case. For equal and high mobilities of both excitons and free carriers, as was the case for Fig. 4.2a, the whole current would have been transported by excitons, no matter how fast they dissociate. This becomes obvious, when considering that although $n_{\mathrm{i}} >> \chi_0$ holds, the concentration of minority carriers $n_{\mathrm{i}}^2/N_{\mathrm{A}} = 1.2 \times 10^{-5}\,\mathrm{cm^{-3}} << \chi_0$, where N_{A} is the acceptor concentration. Note that I chose the doping for the pn-type cell such that the voltage, where minorities (electrons) become equal to the doping concentration, corresponds to the built-in voltage $V_{\mathrm{bi,0}} = 1.3\,\mathrm{V}$ for the pin-case, which was chosen to be just above the radiative open circuit voltage. Since there are more excitons than minority carriers available to transport the energy, I needed to make the mobilities and/or the interface dissociation velocities unequal to get a transition from excitonic to bipolar transport. Thus, I chose $\mu_{\chi} = 10^{-1}\,\mathrm{cm^2\,V^{-1}\,s^{-1}}$, $\mu_{\mathrm{n}} = \mu_{\mathrm{p}} = 10^{4}\,\mathrm{cm^2\,V^{-1}\,s^{-1}}$, $S_{\mathrm{n}} = 10^{10}\,\mathrm{cm\,s^{-1}}$ and $S_{\chi} = 50\,\mathrm{cm\,s^{-1}}$ in Fig. 4.2b. Note

that in case of the pin-type solar cell (Fig. 4.2a), the choice of the dissociation and collection velocities does not affect the photocurrent and its distribution into J_χ and J_n as long as S_n, $S_{\chi n} > 10^5\,\mathrm{cm\,s^{-1}}$.

Besides the coupling constant τ_D between excitons and free carriers, also the equilibrium concentrations of excitons and free carriers affect the dominant charge separation pathway. Note that the ratio between those equilibrium concentrations is determined by the binding energy E_B of the exciton. In order to keep the energy E_exc of the excitons and, therefore, the overall absorptance as well as the maximum short circuit current constant I shift the energy E_C by a relative amount δE_C as illustrated in Fig. 4.3a. A lowering of E_C at constant E_exc means that the binding energy of the exciton becomes E_B smaller and vice versa.

Figure 4.3b shows a simulation, where the conduction band edge and consequently the equilibrium concentration of electrons in the volume of the device varies. Note that the conduction band at the contact is not changed, in order to avoid intermixing of additional effects due to enhanced or deteriorated extraction of excitons and carriers at the contact. If the conduction band is lifted up, the equilibrium concentration of electrons is diminished and thus, the photocurrent becomes predominantly excitonic. In contrast, when the conduction band energy is lowered, there are more electrons in the absorber available to carry the current and thus, the balance shifts in direction of the bipolar current.

4.3.2 Current/voltage curves

Starting with the limit of high mobilities, I want to discuss how imperfect transport affects the shape of the J/V-curve and deteriorates solar cell parameters like short circuit current density J_sc and fill factor FF. Since our model describes both excitonic and bipolar solar cells, I will discuss both the excitonic as well as the bipolar limit defined by Fig. 4.2a. For our calculations, I will focus on the case of pin-type solar cells, since they show specific non-linear features that would be lost if I restricted myself to pn-type solar cells.

I will discuss two different combinations of parameters, as summarized in Table 4.1. Both configurations A and B are normal pin devices where both excitonic and bipolar transport is possible. Configuration A is a device with slow coupling between

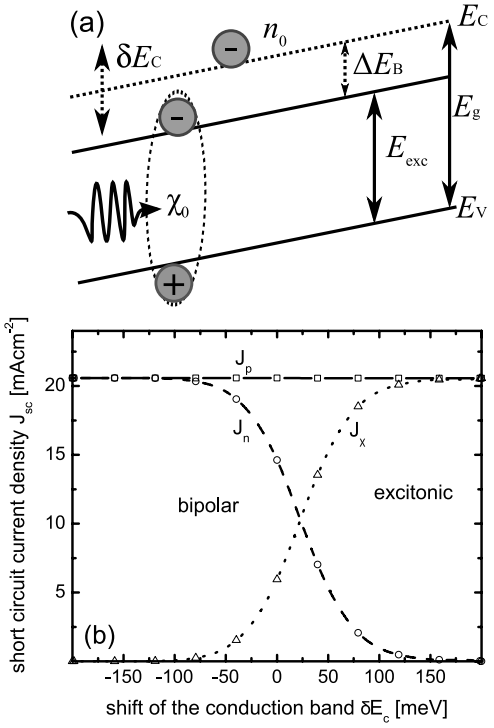

Fig. 4.3: *(a) Band diagram showing that a relative shift δE_C of the conduction band is equivalent to a change in exciton binding energy E_B. (b) Variations of the short circuit current density resulting from the relative shift δE_C of the conduction band for the free electrons in the volume for the case of a pin-type device. Shifting the conduction band leads to a change in electron equilibrium concentration n_0 and thus - for constant $R_\chi = 4.4 \times 10^{-2}\,\mathrm{cm}^3 s^{-1}$ and χ_0 - to a change in the dominating transport mechanism. Note that the choice of R_χ leads to $\tau_D = 10^{-7}\,\mathrm{s}$ for $\delta E_C = 0$, such that direct comparison is possible with Fig. 4.2a. Shifting the conduction band up, lowers n_0 and makes transport via excitons become more favorable. In order not to affect the extraction of excitons and carriers at the contacts and the built-in voltage, the equilibrium concentration in the contacts are not changed and mark the zero position in the δE_C-axis.*

Tab. 4.1: *Mobilities $\mu_{n,p}$ of free carriers and μ_χ of excitons as well as the bulk dissociation lifetime τ_D for the two discussed configurations of non-ideal solar cells.*

	cfg. A	cfg. B
carrier mobility $\mu_{\mathrm{n,p}}$ $[\mathrm{cm}^2(\mathrm{V\,s})^{-1}]$	10^3	$0.1 - 10^3$
exciton mobility μ_χ $[\mathrm{cm}^2(\mathrm{V\,s})^{-1}]$	$10^{-8} - 10^3$	10^{-5}
dissociation lifetime $\tau_{\mathrm{D}}[\mathrm{s}]$	10^{-4}	10^{-10}

excitons and free carriers ($\tau_{\mathrm{D}} = 10^{-4}\,\mathrm{s}$), where I want to focus on the effect of small exciton mobilities. Configuration B is a mainly bipolar device with an efficient coupling of excitons and free carriers, where I want to investigate the effect of low bipolar mobilities.

Figure 4.4 shows simulated current/voltage curves for configuration A, i.e. a solar cell with a fixed electron and hole mobility $\mu_{\mathrm{n/p}} = 10^3\,\mathrm{cm}^2(\mathrm{V\,s})^{-1}$ and a fixed dissociation lifetime $\tau_{\mathrm{D}} = 10^{-4}\,\mathrm{s}$. This long dissociation lifetime corresponds to a situation that is excitonic for high mobilities as shown in Fig 4.2a. The solid line corresponds to an exciton mobility $\mu_\chi = 10^{-5}\,\mathrm{cm}^2(\mathrm{V\,s})^{-1}$, while the dashed and the dotted line correspond to an exciton mobility $\mu_\chi = 10^{-1}\,\mathrm{cm}^2(\mathrm{V\,s})^{-1}$ (dashed) and $\mu_\chi = 10^{-7}\,\mathrm{cm}^2(\mathrm{V\,s})^{-1}$ (dotted). I.e., every absorbed photons contributes one elementary charge to the short circuit current and the radiative losses are given by the equation for $J_{0,\mathrm{SQ}}$ [Eq. (2.35)]. For lower mobilities, the decreased collection of excitons leads to the situation where the quantum efficiency becomes smaller than the absorptance and both $J_{0,\mathrm{rad}}$ and J_{sc} decrease. The open circuit voltage as well as the fill factor remain almost unaffected by the change of exciton mobility.

A more detailed analysis of the short circuit current density J_{sc} (solid line) and the contributions to the current density J_{n} and J_χ from electrons (dashed line) and excitons (dotted line) is depicted in the inset as a function of exciton mobility. Starting from the high mobility limit $\mu_\chi > 10^{-1}\,\mathrm{cm}^2(\mathrm{V\,s})^{-1}$, a decreasing exciton mobility leads to a decrease in J_χ, which is partly compensated by an increase in J_{n}, leading to a saturation of J_{sc} for low exciton mobilities μ_χ.

Figure 4.5 shows a simulation of configuration B, i.e. a pin-type device with a fixed exciton mobility $\mu_\chi = 10^{-5}\,\mathrm{cm}^2(\mathrm{V\,s})^{-1}$ and a fixed dissociation lifetime

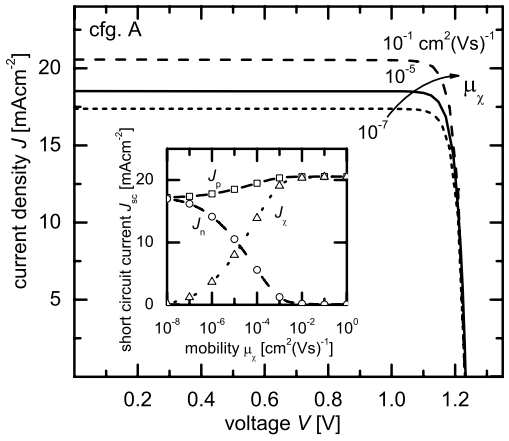

Fig. 4.4: *Simulation of current/voltage curves for a solar cell with a fixed electron and hole mobility* $\mu_{n,p} = 10^3\,\mathrm{cm}^2(\,\mathrm{V\,s})^{-1}$ *and a fixed dissociation lifetime* $D_\chi = 10^{-4}\,\mathrm{s}$ *(cfg. A in table 4.1). The parameter is the exciton mobility* $\mu_\chi = 10^{-1}$, 10^{-5}, $10^{-7}\,\mathrm{cm}^2(\,\mathrm{V\,s})^{-1}$, *which leads to a decrease in short circuit current, while keeping the fill factor the same. In the inset, the short circuit current density* J_{sc} *(solid line) and the contributions to the current density* J_n *and* J_χ *from electrons (dashed line) and excitons (dotted line) are depicted as a function of exciton mobility. Starting from the high mobility limit* $\mu_\chi > 10^{-1}\,\mathrm{cm}^2(\,\mathrm{V\,s})^{-1}$ *a decreasing exciton mobility leads to a decrease in* J_χ, *which is partly compensated by an increase in* J_n, *leading to a saturation of* J_{sc} *for low exciton mobilities* μ_χ.

$\tau_\mathrm{D} = 10^{-10}\,\mathrm{s}$. At high mobilities of free carriers ($\mu_{\mathrm{n,p}} \geq 10^3\,\mathrm{cm}^2(\,\mathrm{V\,s})^{-1}$), this fast dissociation lifetime corresponds to a bipolar photocurrent at short circuit as shown in Fig. 4.2a. Here, I vary the carrier mobility $\mu_{\mathrm{n,p}} = 10^0, 10^1, 10^3\,\mathrm{cm}^2(\,\mathrm{V\,s})^{-1}$. The decreasing carrier mobility $\mu_{\mathrm{n,p}}$, leads to a decay in fill factor and in short circuit current density J_{sc}. However, in contrary to configuration A (Fig. 4.4), the fill factor loss is by far more dominant than that in J_{sc}. This is because for low charge carrier mobilities in pin-type solar cells, the effect of the built-in field becomes decisive.

Since the charge carriers, unlike the excitons, react on the decrease of the built-in field resulting by application of forward bias voltage V, the photocurrent decreases with increasing V. The voltage dependence of carrier collection reduces the fill factor. Therefore, the fill factor is strongly influenced by the carrier mobilites $\mu_{\mathrm{n,p}}$ although the open circuit voltage is not dependent of $\mu_{\mathrm{n,p}}$ in. Fig. 4.5.

Figure 4.6 summarizes the effects of either low exciton or low electron and hole mobilities on the short circuit current density J_{sc} and fill factor FF of configurations A and B. Figures 7a,b show that the fill factor loss shows up at mobilities $\mu_{\mathrm{n,p}} < 10^2\,\mathrm{cm}^2(\,\mathrm{V\,s})^{-1}$, while a loss in J_{sc} starts only for much lower mobilities $\mu_{\mathrm{n,p}} < 10^0\,\mathrm{cm}^2(\,\mathrm{V\,s})^{-1}$. This is because the voltage dependence of the carrier collection probability from the 300 nm thick absorber layer shows up at high forward bias voltage V first (leading to FF losses) before at even lower $\mu_{\mathrm{n,p}}$ also carrier collection at $V = 0$ is diminished (leading to losses in J_{sc}).

Figures 4.6c,d show the effect of decreasing exciton mobility μ_χ, while keeping electron and hole mobilities at a high value of $\mu_{\mathrm{n,p}} = 10^3\,\mathrm{cm}^2(\,\mathrm{V\,s})^{-1}$. For the photocurrent of cfg. A as a function of exciton mobility, I obtain the result, which was already depicted in the inset of Fig. 4.4, namely a decrease of photocurrent for decreasing exciton mobilities $\mu_\chi < 10^{-3}\,\mathrm{cm}^2(\,\mathrm{V\,s})^{-1}$. This decline saturates at a level of about 83% of the maximum J_{sc}. This plateau results from the fact that the loss in excitonic current is partly compensated by an increase of electron and hole current. The fill factor as shown in Fig. 4.6d is independent from the exciton mobility. This finding is expected because changes in the electrical field cannot alter the collection of excitons. As a result the decline of photocurrent is voltage independent.

4.3.3 Electroluminescence and quantum efficiency

For the two different parameter configurations of Table 4.1, I investigate the validity of the reciprocity theorem defined by Eq. (2.33). Figure 4.7 illustrates the meaning of Eq. (2.33): The electroluminescence (EL) emission simulated with the model described above, allows us to derive the quantum efficiency via Eq. (2.33) from it. For the case of high mobilities the quantum efficiency derived from EL (solid line) agrees with the directly simulated quantum efficiency (open circles). Thus, for perfect transport both excitonic and bipolar solar cells follow the reciprocity

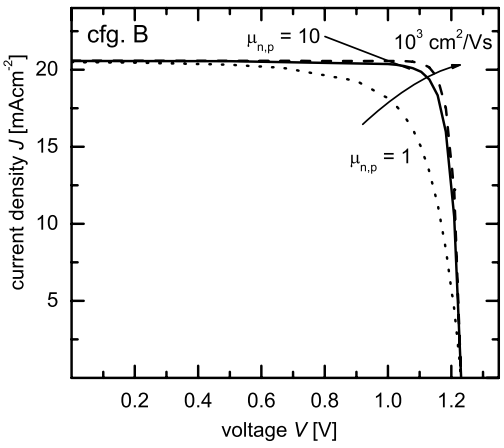

Fig. 4.5: *Simulation of current/voltage curves for a solar cell with a fixed exciton mobility* $\mu_\chi = 10^{-5}\,\mathrm{cm}^2(\,\mathrm{V\,s})^{-1}$ *and a fixed dissociation lifetime* $\tau_D = 10^{-10}\,\mathrm{s}$ *(cfg. B from table 4.1). The parameter is the carrier mobility* $\mu_{n,p} = 10^0, 10^1, 10^3\,\mathrm{cm}^2(\,\mathrm{V\,s})^{-1}$*, which leads to a decrease in fill factor, while keeping the short circuit current roughly the same. The solid line corresponds to the parameter configuration B from Table 4.1. In the inset, the fill factor FF is depicted as a function of the carrier mobility* $\mu_{n,p}$*.*

theorem, no matter whether the device is built as pin-type or pn-type device.

Proceeding now to less ideal devices, I investigate under which circumstances the reciprocity relation begins to loose its validity. Figure 4.7 also shows the EL spectrum (dotted line), the quantum efficiency calculated from the EL spectrum via the reciprocity theorem (dotted) and the quantum efficiency (open triangles) of the solar cell with parameter configuration A and a low exciton mobility ($\mu_{\mathrm{n,p}} = 10^3\,\mathrm{cm}^2(\,\mathrm{V\,s})^{-1}$, $\mu_\chi = 10^{-5}\,\mathrm{cm}^2(\,\mathrm{V\,s})^{-1}$, $\tau_{\mathrm{D}} = 10^{-4}\,\mathrm{s}$). Since this configuration leads to a relatively constant photocurrent and ideal recombination current, as shown by the mobility independent fill factor in Figs. 4.4 and 4.6d, also the reciprocity is valid.

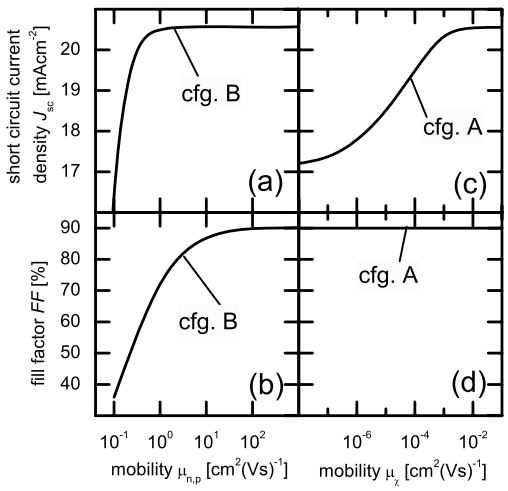

Fig. 4.6: *Summary of the effects of reduced bipolar and excitonic mobilities on short circuit current density J_{sc} and fill factor FF. In (a) and (b) I used the parameters for cfg. B except for the electron and hole mobility $\mu_{n,p}$ which is varied. I find a considerable decrease of fill factor for mobilities $\mu_{n,p} < 10^2\,\mathrm{cm}^2(\,\mathrm{V\,s})^{-1}$, while a loss in J_{sc} starts only for even lower mobilities $\mu_{n,p} < 10^0\,\mathrm{cm}^2(\,\mathrm{V\,s})^{-1}$. In (c) and (d), I used the parameters for cfg. A , except for the varied exciton mobility. For cfg. A, J_{sc} is reduced for exciton mobilities $\mu_\chi < 10^{-3}\,\mathrm{cm}^2(\,\mathrm{V\,s})^{-1}$, while the fill factor stays unaltered, since the electron and hole mobilities are high enough to warrant voltage independent collection.*

Figure 4.8 summarizes the validity of the reciprocity theorem by comparing the directly simulated quantum efficiency $Q_{\mathrm{e,dir}}$ (diamonds) and the quantum efficiency $Q_{\mathrm{e,EL}}$ calculated from the simulation of the EL (solid lines) for the case of configurations A and B. For cfg. A, as shown in Fig. 4.8a, the electron and hole mobilities are high and thus the reciprocity is valid, although the quantum efficiency is below unity in the saturation regime. Voltage-independent collection and injection of carriers at high bipolar mobilities thus implies both high and constant fill factors

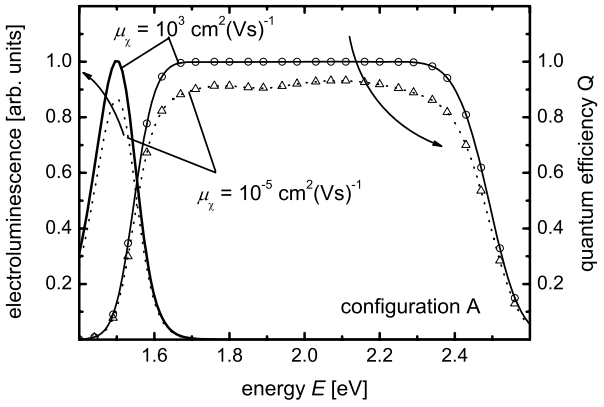

Fig. 4.7: *Quantum efficiency (symbols), EL spectrum and quantum efficiency calculated from the EL according to Eq. (2.33) for two cells that belong to cfg. A: an ideal cell with high carrier mobilities (solid lines) and a cell with a lower carrier mobility* $\mu_\chi = 10^{-5}\,\mathrm{cm}^2(\,\mathrm{V\,s})^{-1}$ *(dotted line). For both devices the reciprocity theorem is valid.*

(see Fig. 4.6d) and the validity of the reciprocity relation ($Q_{\mathrm{e,dir}} = Q_{\mathrm{e,EL}}$).

Figures 4.8b shows that for cfg. B, the reciprocity is no longer valid ($Q_{\mathrm{e,dir}} \neq Q_{\mathrm{e,EL}}$). We learned from Figs. 4.5 and 4.6b that a mobility of $\mu_{\mathrm{n,p}} = 10\,\mathrm{cm}^2(\,\mathrm{V\,s})^{-1}$ already leads to a small fill factor loss of around $\Delta FF = 3\%$ compared to the high mobility case. In consequence, I also find a small deviation of quantum efficiency $Q_{\mathrm{e,dir}}$ (diamonds) and quantum efficiency $Q_{\mathrm{e,EL}}$ from EL (solid line), as shown in Fig. 4.8b.

Note here that the voltage dependency of collection and thus injection makes the EL spectrum become a function of applied voltage. The voltage used for all EL spectra in Figs. 4.7 and 4.8 is $V = 1\,\mathrm{V}$. Using higher (lower) voltages would increase (decrease) the difference between direct quantum efficiency simulated at $V = 0\,\mathrm{V}$ and quantum efficiency calculated from EL.

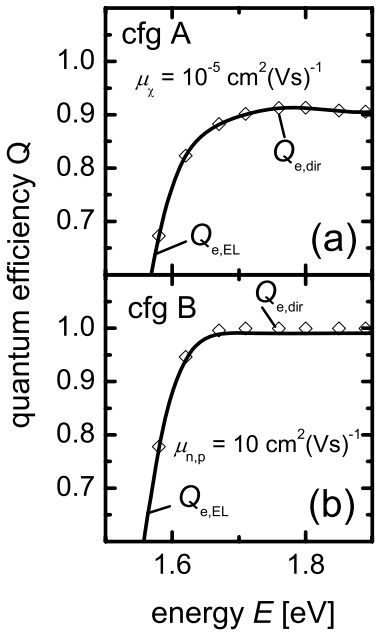

Fig. 4.8: *Simulation of the quantum efficiency $Q_{e,dir}$ (diamonds) compared with the simulation of the electroluminescence spectrum, from which the quantum efficiency $Q_{e,EL}$ (solid line) is calculated using Eq. (2.33), for the case of (a) configuration A and (b) configuration B. For case (a), the electron and hole mobility are high ($\mu_{n,p} = 10^3\,\mathrm{cm}^2(\mathrm{V\,s})^{-1}$) and thus collection and injection of carriers is voltage independent and the reciprocity is valid. For case (b), the low bipolar mobility leads to a small deviation between $Q_{e,dir}$ and $Q_{e,EL}$.*

Chapter 5

Detailed balance model for bulk heterojunction solar cells

The previous chapter 4 discussed excitonic solar cells, which mostly means that the absorber consists of a material with a high binding energy like an organic polymer or small molecule. In addition to the inclusion of excitons to the energy transport, organic solar cells usually have a different device geometry than standard inorganic solar cells. This device geometry is called bulk heterojunction. In this chapter, I will discuss how to implement such devices into my model.

5.1 Introduction

In recent years, several new technological approaches have emerged in the field of thin film photovoltaics, some of them, like the organic bulk heterojunction (bhj) cell [7–9, 12], using totally new types of device geometries. These new geometries require approaches for modeling and simulation of the devices that go beyond those used for standard inorganic device simulators. Consisting of a blend of two materials with different electron affinities, organic, inorganic [23] as well as hybrid [24, 25] bhj type devices require essentially two new aspects to be added to the standard ingredients of inorganic solar cell modeling: These are the incorporation of the multi-step charge separation process, starting with the creation of excitons rather than free electron/hole pairs [28, 29], as well as the network of donor/acceptor interfaces needed to split the photogenerated exciton. Incorporating these effects in

an electrical model either leads to complex and detailed microscopical models [98] or continuum approaches [99–101] that use effective parameters in order to be computationally more efficient. Some effective medium models, like the one proposed by Koster et al. [102], allow the description of generation and recombination of free charge carriers via excitons and bound electron/hole pairs as a modification of the standard generation and recombination rates, while not changing the form of the carrier continuity equations compared to the standard inorganic case.

Not only electrical but also optical modeling [103–105] has recently come to the focus of research on polymer cells, for instance leading to a better interpretation of quantum efficiencies [106, 107] or allowing the determination of design rules for optical spacers [108]. The requirements for optical simulations differ not much between inorganic and organic thin film solar cells. The most important aspect is the ability to consider interferences in thin layers, which is usually accomplished by a matrix transfer formalism.

This chapter introduces an effective electrical model for bhj solar cells that is compatible with the one dimensional continuity equations for electrons and holes and with the principle of detailed balance. The model takes into account exciton transport, dissociation as well as the field and temperature dependent dissociation of a bound electron/hole pair. The widely used [109–114] model of Koster et al., taking into account only the bound pair but not the exciton diffusion, is a special case of our model. I combine my model for the generation of free carriers in bhj-solar cells with the device simulator ASA , which is able to calculate the generation rate of excitons with a thin film optics approach. The result is an electro-optical simulation program able to calculate, e.g. current/voltage(J/V) curves, external and internal quantum efficiencies, reflectance and transmission spectra, as well as the band diagram, carrier concentrations and electric fields in the device. As an example for the applicability of our model, I show how to reproduce absorptance, quantum efficiency and current/voltage characteristics of a polymer/fullerene device described in literature [106].

5.2 Model

5.2.1 Charge separation scheme

An electrical model suitable for bulk heterojunction solar cells needs to consider a multi-step process of current generation. Figure 5.1 schematically shows the path leading from an absorbed photon to the final carrier separation at the contact. In contrast to the case of inorganic solar cells, where the generation of free carriers directly follows photon absorption, in an organic solar cell an exciton is created first. Since both the exciton diffusion length and the dissociation rate of excitons in free carriers are too low for efficient charge separation in a bilayer geometry , the organic devices must be built up of an intimate blend of two materials. Now, the exciton has to diffuse only to the next junction between the blended materials and not directly to one of the device contacts. At the junction, the exciton is split into an electron (e) and hole (h), which are now in different phases depending on the band offsets at the junction. In the example presented in Fig. 5.1, the hole remains in the absorber material, which may be a polymer, while the electron is injected into the material with the higher electron affinity, which is usually formed by a C_{60}-derivative. The electron and hole on either side of the interface are still coloumbically bound to each other. Only after this bound electron/hole (e/h) pair is split into free carriers, the bipolar drift-diffusion transport leads to the final charge separation at the contacts. Figure 5.2 shows how the mechanism, illustrated in Fig. 5.1, fits into the charge separation scheme of the complete device. At each point of the pin-type device, a heterojunction exists, where the processes in Fig. 5.1 lead to the creation of free carriers.

5.2.2 Differential equations for free carriers

The scheme in Fig. 5.1 shows that there are two steps of charge separation and two steps of transport necessary to achieve a photocurrent. Thus, a suitable model needs to include properties of excitonic and bipolar transport, as well as properties of the splitting of the exciton and bound e/h-pair and those relevant for the final charge separation. Let us start with those parts of the model I can adopt from inorganic photovoltaics.

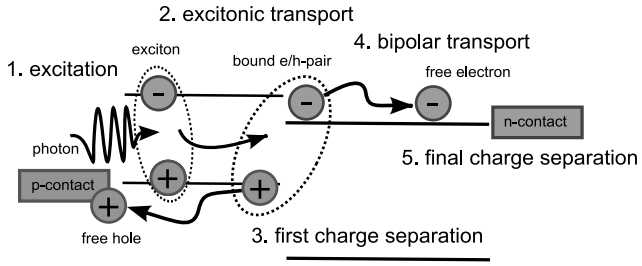

Fig. 5.1: *Sketch of the photoconversion process in bulk heterojunction solar cells. The photon creates an exciton, which has to diffuse to the next donor/acceptor interface, where it is split into a bound e/h-pair. This e/h-pair will then dissociate and form free charge carriers which are transported to the contacts.*

For the simplest case of direct band to band recombination, the drift diffusion equations for the electron concentration n and the hole concentration p are given by

$$-\frac{1}{q}\frac{dJ_\mathrm{n}}{dx} = -D_\mathrm{n}\frac{d^2n}{dx^2} - F\mu_n\frac{dn}{dx} = G - k_\mathrm{rec}np \tag{5.1}$$

$$\frac{1}{q}\frac{dJ_\mathrm{p}}{dx} = -D_\mathrm{p}\frac{d^2p}{dx^2} + F\mu_p\frac{dp}{dx} = G - k_\mathrm{rec}np \tag{5.2}$$

where J_n and J_p are the electrical electron and the hole current densities, $D_\mathrm{n,p} = \mu_{n,p}kT/q$ is the diffusion constant of the electrons and holes which depends on the electron and hole mobilities μ_n and μ_p and on the thermal voltage kT/q. For inorganic solar cells, the coupled solution of Eqs. (5.1, 5.2) is sufficient for obtaining the carrier concentrations and subsequently the currents. In bhj solar cells, however, the properties of the generation process of free carriers at each grid point, as depicted in Fig. 5.2, must be included to interpret the generation rate G and the recombination constant k_rec as quantities depending on exciton diffusion and dissociation.

5.2.3 Balance equation for bound carriers

Figure 5.3 depicts the transition rates from the four possible states, photon, exciton χ, bound e/h-pair ξ and free e/h-pair. The system consists of four pairs of rates that connect the states with each other. These are (i) the generation and

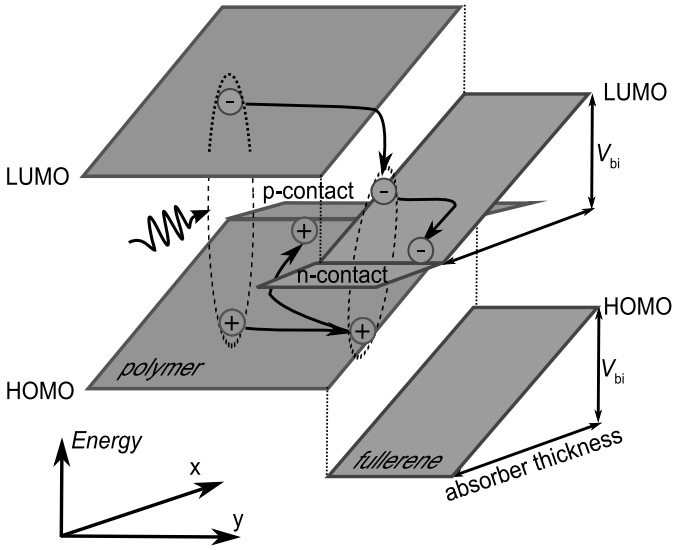

Fig. 5.2: *Sketch of the whole device to be simulated. At each grid point of a standard pin-junction solar cell, diffusion and dissociation of the exciton as well as dissociation of the bound e/h-pair precedes the creation of free e/h-pairs.*

recombination of excitons, (ii) the dissociation of excitons forming a bound e/h-pair and the recombination of bound pairs forming an exciton, (iii) the decay of bound pairs to the ground state and the creation of bound pairs, and (iv) the dissociation of bound pairs forming free carriers and the recombination of free carriers forming bound e/h-pairs. Due to the principle of detailed balance each process must be in equilibrium with its inverse process if the system is in thermodynamic equilibrium. This law allows us to eliminate one of the rate constants for each pair if I introduce the equilibrium concentrations for excitons χ_0, bound e/h-pairs ξ_0 and the intrinsic carrier concentration n_{i} for free e/h-pairs. For the generation and recombination of the exciton, the equilibrium generation $G_{\mathrm{opt}}^{\mathrm{eq}} = \chi_0/\tau_{\mathrm{r}}$, where τ_{r} is the lifetime. The coupling of excitons and bound pairs leads to the relation $S_D\chi_0 = S_R\xi_0$, where S_{D} is the dissociation and S_{R} the recombination velocity. Expressing the recombination velocity in terms of the dissociation velocity, allows us to write the net particle

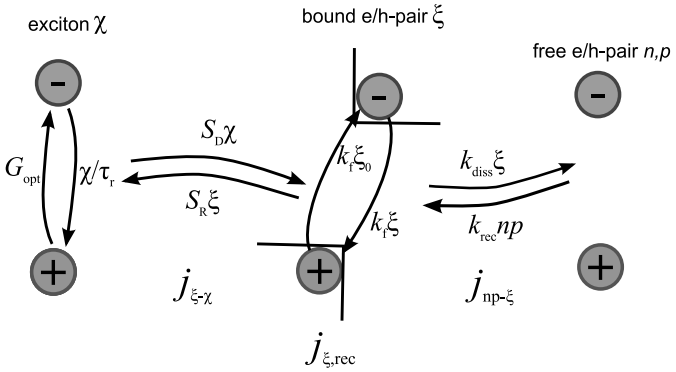

Fig. 5.3: *The model for modification of generation and recombination rates at each grid point in the devices includes three states of the excitation, the exciton, the bound e/h-pair and the free e/h-pair. All states are connected by detailed balance rates. In addition excitons may be optically generated and excitons and bound e/h-pairs may recombine.*

current density between excitons and bound pairs as

$$j_{\xi\leftrightarrow\chi} = S_{\mathrm{D}} \left(\frac{\xi}{\xi_0}\chi_0 - \chi_{\mathrm{hj}} \right), \tag{5.3}$$

where χ_{hj} is the concentration of excitons at the heterojunction between the donor and acceptor phase. The decay of bound pairs to the ground state must again lead to a zero net generation rate of bound pairs in thermodynamic equilibrium. Thus, the net recombination current density is

$$j_{\xi,\mathrm{rec}} = k_{\mathrm{f}}\xi_0 \left(\frac{\xi}{\xi_0} - 1 \right), \tag{5.4}$$

where k_{f} is the rate constant for the decay. The exchange between bound and free electron hole pairs leads to the balance between dissociation and recombination. I express the dissociation constant $k_{\mathrm{diss}} = k_{\mathrm{rec}} n_{\mathrm{i}}^2/\xi_0$ as a function of the recombination constant krec and receive for the net current density

$$j_{\mathrm{np}\leftrightarrow\xi} = k_{\mathrm{rec}} \left(np - \frac{\xi}{\xi_0} n_i^2 \right) \tag{5.5}$$

What we finally need, in order to compute the effective generation and recombination rates of the coupled processes shown in Fig. 5.3, is the result of Eq. (5.5), however

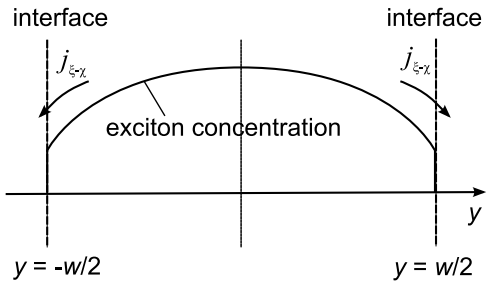

Fig. 5.4: *Scheme of the coordinate system used for the analytical solution of the exciton diffusion equation. The generation rate is assumed to be constant over the width w between two donor/acceptor interfaces.*

independent of the concentration of excitons χ and bound pairs ξ. In order to eliminate ξ in Eq. (5.5), I enforce current continuity between the current densities defined in Eqs. (5.3-5.5), leading to a balance equation

$$j_{\mathrm{np}\leftrightarrow\xi} - j_{\xi\leftrightarrow\chi} - j_{\xi,\mathrm{rec}} = k_{\mathrm{rec}}\left(np - \frac{\xi}{\xi_0}n_i^2\right) - S_D\left(\frac{\xi}{\xi_0}\chi_0 - \chi_{\mathrm{hj}}\right) - k_{\mathrm{f}}\xi_0\left(\frac{\xi}{\xi_0} - 1\right). \quad (5.6)$$

5.2.4 Differential equation for excitons

To obtain the effective generation and recombination rate of free carriers, I need to calculate the solution of Eq. (5.5), i.e. the net current $j_{\mathrm{np}\leftrightarrow\xi}$, which requires the knowledge of each component of Eq. (5.6). Let us start with the contribution from the excitons, i.e. $S_{\mathrm{D}}\chi_{\mathrm{hj}}$. In order to include exciton transport and dissociation I need to add another dimension to our originally one dimensional problem. Later, I will show that analytically solving the differential equation for excitons allows us to calculate effective modifications of the one-dimensional differential equations for free carriers, thereby circumventing the need for solving the coupled differential equations in two- or three dimensions.

To include exciton diffusion to the next interface, I solve the one dimensional diffusion equation for the exciton concentration χ

$$0 = D_\chi\frac{d^2}{dy^2}\chi - \frac{\chi}{\tau_{\mathrm{r}}} + G_{\mathrm{opt}} \quad (5.7)$$

in a new coordinate system as depicted in Figs. 5.2 and 5.4. The generation rate

$G_{\rm opt} = G_{\rm opt}^{\rm eq} + G_{\rm opt}^{\rm exc}$ is now the actual optical generation rate as calculated by a transfer matrix approach and consists of a contribution from the black body radiation of the environment and an contribution due to excess illumination. In addition, $\tau_{\rm r}$ is the lifetime of excitons and D_χ is the exciton diffusion constant. I assume that the generation rate is independent of the coordinate y, while interferences and damping are taken into account for the coordinate x. The boundary conditions for the particle currents at the interfaces are assumed to be symmetric

$$j_{\xi\leftrightarrow\chi} = \pm D_\chi \frac{d}{dy}\chi = S_{\rm D}\chi_0 \frac{\xi}{\xi_0} - S_{\rm D}\chi \tag{5.8}$$

for $y = \pm w/2$, where w is the distance between two interfaces. The solution for the exciton concentration is

$$\chi = (A_{\rm r} + A_{\rm g}) \left[\cosh\left(y/L_\chi\right)\right] + G_{\rm opt}\tau_{\rm r} \tag{5.9}$$

where $L_\chi = \sqrt{\mu_\chi \tau_{\rm r} kT/q}$. Equation (5.9) superimposes two contributions to the exciton population, namely the optical generation, proportional to the exciton generation rate $G_{\rm opt}$

$$A_g = \frac{-S_{\rm D} G_{\rm opt}\tau_{\rm r}}{S_\chi \cosh\left(w/2L_\chi\right) + D_\chi/L_\chi \sinh\left(w/2L_\chi\right)} \tag{5.10}$$

and the injection and extraction of excitons via the coupling to the bound e/h-pairs ?

$$A_r = \frac{S_{\rm D}\chi_0\xi/\xi_0}{S_\chi \cosh\left(w/2L_\chi\right) + D_\chi/L_\chi \sinh\left(w/2L_\chi\right)} \tag{5.11}$$

which is thus proportional to ξ/ξ_0.

Now, the solution for the exciton concentration as a function of y enables us to calculate the current $j_{\xi\leftrightarrow\chi}$, describing the exchange between bound pairs and excitons. For each domain with length $w/2$, the current $j_{\rm np\leftrightarrow\xi}$ is defined by Eq. (5.8). The current $j_{\xi\leftrightarrow\chi} = j_g + j_r$ consists of two contributions, one due to the photogeneration of excitons

$$j_{\rm g} = -S_{\rm D}\chi_{\rm g} = -S_{\rm D} G_{\rm opt}\tau_{\rm r}\beta \tag{5.12}$$

and one due to the injection of bound e/h-pairs

$$j_{\rm r} = S_{\rm D}\left(\frac{\xi}{\xi_0}\chi_0 - \chi_{\rm r}\right) = S_{\rm D}\chi_0\frac{\xi}{\xi_0}\beta \tag{5.13}$$

In Eqs. (5.12) and (5.13), I used the abbreviations

$$\beta = \frac{D_\chi}{L_\chi} \frac{\sinh\left(w/2L_\chi\right)}{S_\mathrm{D}\cosh\left(w/2L_\chi\right) + D_\chi/(L_\chi)\sinh\left(w/2L_\chi\right)} \tag{5.14}$$

the concentration of excitons at the interface due to photogeneration of excitons

$$\chi_\mathrm{g} = A_\mathrm{g}\cosh\left(\frac{w}{2L_\chi}\right) + G_\mathrm{opt}\tau_\mathrm{r} = G_\mathrm{opt}\tau_\mathrm{r}\beta \tag{5.15}$$

and the concentration due to injection of bound pairs

$$\chi_\mathrm{r} = A_\mathrm{r}\cosh\left(\frac{w}{2L_\chi}\right) = \chi_0\frac{\xi}{\xi_0}\left(1-\beta\right) \tag{5.16}$$

Finally, the result for the current defined in Eq. (5.3) is

$$j_{\xi\leftrightarrow\chi} = S_\mathrm{D}\left(\frac{\xi}{\xi_0}\chi_0 - \chi_\mathrm{hj}\right) = S_\mathrm{D}\beta\left(\frac{\xi}{\xi_0}\chi_0 - G_\mathrm{opt}\tau_\mathrm{r}\right) \tag{5.17}$$

5.2.5 Effective generation and recombination rates

In order to determine the current density and therewith the effective generation and recombination rate, I need to calculate the concentration of bound pairs. The balance equation for bound pairs, Eq. (5.6), leads to

$$\frac{\xi}{\xi_0} = \frac{S_\mathrm{D}\beta G_\mathrm{opt}\tau_\mathrm{r} + k_\mathrm{rec}np + k_\mathrm{f}\xi_0}{S_D\beta\chi_0 + k_\mathrm{rec}n_i^2 + k_\mathrm{f}\xi_0} \tag{5.18}$$

in steady state. Let us briefly discuss the meaning of Eq. (5.18) by considering the extreme cases: If either the coupling to the free e/h-pairs or the coupling to the excitons is dominant over the other and over the non-radiative decay, the Fermi-level - representing the ratio of concentration to equilibrium concentration - will be equal for the two strongly coupled states. Strong coupling means a sufficiently high rate or short lifetime that the other components of the two sums in numerator and denominator are negligible. That means if (i) the recombination constant k_rec is very high compared to the other rates, Eq. (5.18) will simplify to $\xi/\xi_0 = np/n_\mathrm{i}^2$, while (ii) a high dissociation velocity S_D leads to $\xi/\xi_0 = \chi_\mathrm{hj}/\chi_0 = G_\mathrm{opt}\tau_\mathrm{r}/\chi_0$. If (iii) the non-radiative decay channel is dominant, ξ will approach its equilibrium value ($\xi/\xi_0 = 1$). Now, I insert Eq. (5.18) into Eq. (5.3) and receive

$$\begin{aligned} j_{\mathrm{np}\leftrightarrow\xi} &= k_\mathrm{rec}\left(np - \tfrac{\xi}{\xi_0}n_i^2\right) = k_\mathrm{rec}\left(np - n_i^2\tfrac{S_\mathrm{D}\beta G_\mathrm{opt}\tau_r + k_\mathrm{rec}np + k_\mathrm{f}\xi_0}{S_\mathrm{D}\beta\chi_0 + k_\mathrm{rec}n_i^2 + k_\mathrm{f}\xi_0}\right) \\ &= k_\mathrm{rec}\left(\tfrac{k_\mathrm{f}\xi_0\left(np-n_i^2\right) + S_D\beta\left(\left[np-n_i^2\right]\chi_0 - n_i^2G_\mathrm{opt}^\mathrm{exc}\tau_r\right)}{S_\mathrm{D}\beta\chi_0 + k_\mathrm{rec}n_i^2 + k_\mathrm{f}\xi_0}\right) \end{aligned} \tag{5.19}$$

Note that I used the earlier derived relation $G_{\mathrm{opt}}^{\mathrm{eq}} = \chi_0/\tau_{\mathrm{r}}$ in order to obtain Eq. (5.19). In general, the derivation of the particle currents j_{x} in x-direction, i.e. the effective generation and recombination rates depend on the particle current in y-direction via

$$\frac{dj_{\mathrm{x}}}{dx} := \tilde{G} - \tilde{R} = \frac{j_{\mathrm{np}\leftrightarrow\xi}}{w/2} \tag{5.20}$$

since the particle current was defined as the current coming from one domain with width $w/2$. Thus, splitting the result of Eq. (5.20) in terms $\propto G_{\mathrm{opt}}^{\mathrm{exc}}$, yields the new effective generation rate to be inserted in Eqs. (5.1, 5.2) and those $\propto k_{\mathrm{rec}} np$, yields the new effective recombination rate to be inserted in Eqs. (5.1, 5.2). The new effective generation rate is then

$$\tilde{G} = G_{\mathrm{opt}}^{\mathrm{exc}} \frac{k_{\mathrm{rec}} n_{\mathrm{i}}^2}{S_D \beta \chi_0 + k_{\mathrm{rec}} n_{\mathrm{i}}^2 + k_{\mathrm{f}} \xi_0} \frac{S_D \beta \tau_{\mathrm{r}}}{w/2} \tag{5.21}$$

and the new effective recombination rate is

$$\tilde{R} = \frac{k_{\mathrm{rec}}}{w/2} \left(np - n_{\mathrm{i}}^2\right) \left(1 - \frac{k_{\mathrm{rec}} n_{\mathrm{i}}^2}{S_D \beta \chi_0 + k_{\mathrm{rec}} n_{\mathrm{i}}^2 + k_{\mathrm{f}} \xi_0}\right) \tag{5.22}$$

5.2.6 Equilibrium concentration of excitons

There still remain some open questions, especially how to choose the value of k_{rec} and how to determine the equilibrium concentrations χ_0, ξ_0 and n_{i} of the different particles. For efficient charge separation at the interface between donor and acceptor phase, band offsets are necessary. In our model, these band offsets are implicitly defined through the value of the equilibrium concentration of excitons χ_0. For a given density of states, the energy of the thermalized exciton is the only relevant parameter affecting the equilibrium concentration. Thus, a high energy difference ΔE between the LUMO (lowest unoccupied molecular orbital) of the donor and the LUMO of the acceptor leads to efficient charge separation, which is reflected in our model by a low χ_0 and subsequently to less back transfer of bound e/h-pairs in excitons. Since the exciton density of states is an unknown parameter, I cannot give quantitative values for χ_0 e.g. as a function of exciton energy in the polymer. Instead, for our simulations, I chose the value of χ_0 to be sufficiently low that the back transfer of bound e/h-pairs in excitons does not lead to an efficiency decrease. This is the case, when $S_{\mathrm{D}}\beta\chi_0 << k_{\mathrm{rec}} n_{\mathrm{i}}^2 + k_{\mathrm{f}}\xi_0$ is satisfied, since for this condition, the

mathematical expression for the recombination rate [Eq. (5.22)] is independent of $S_{\mathrm{D}}\chi_0$, meaning that the recombination of free carriers does not depend on injection and recombination of excitons.

5.2.7 Comparison with the model of Koster et al.

If I compare the results for the generation rate with the model of Koster, Smits, Mihailetchi and Blom, which I will refer to as the KSMB-model (see Ref. [102]), I notice that I have one factor dominated by the dissociation of the bound e/h-pair, which is equivalent to the dissociation probability p in Ref. [102], when I choose k_{rec} and χ_0 in a certain way. To make our model compatible with the KSMB-model, I choose

$$k_{\mathrm{rec}} = \frac{q \min\left(\mu_{\mathrm{n}}, \mu_{\mathrm{p}}\right)}{\varepsilon_0 \varepsilon_{\mathrm{r}}} (w/2) \tag{5.23}$$

according to a slightly modified Langevin recombination rate. I have to include the domain width $w/2$ to ensure that $[k_{\mathrm{rec}} n_{\mathrm{i}}^2] = \mathrm{cm}^{-2}\mathrm{s}^{-1}$. Since I fixed the dissociation rate via detailed balance considerations, I have to modify the equilibrium concentration for bound e/h-pairs instead, leading to

$$\xi_0 = \frac{4\pi z^3 n_{\mathrm{i}}^2 \exp\left(E_{\mathrm{B}}(z)/kT\right)}{3J_1\left(2\sqrt{-2b}\right)/\sqrt{-2b}} \tag{5.24}$$

where $J_1\left(2\sqrt{-2b}\right)/\sqrt{-2b} = 1+b+b^2/3+b^3/18+...$ is the first order Bessel function,

$$b = \frac{q^3 F}{8\pi\varepsilon_0\varepsilon_{\mathrm{r}}\left(kT\right)^2} \tag{5.25}$$

F is the electric field, $\varepsilon = \varepsilon_0\varepsilon_r$ is the dielectric constant, a is the separation distance between the bound electron and hole and $E_{\mathrm{B}}(a) = q^2/4\pi\varepsilon a$ is the binding energy of the bound e/h-pair. Note that the definitions in Eqs. (5.24, 5.25) imply a strong field and therefore bias dependence of bound e/h-pair dissociation, which has a considerable influence on the fill factor of the device. Using the definitions in Eqs. (5.23-5.25) and assuming $S_{\mathrm{D}}\beta\chi_0 << k_{\mathrm{rec}} n_{\mathrm{i}}^2 + k_{\mathrm{f}}\xi_0$, the dissociation probability

$$p_{\mathrm{diss}} = \frac{k_{\mathrm{rec}} n_{\mathrm{i}}^2}{S_{\mathrm{D}}\beta\chi_0 + k_{\mathrm{rec}} n_{\mathrm{i}}^2 + k_{\mathrm{f}}\xi_0} \tag{5.26}$$

appearing in Eqs. (5.21, 5.22) is the same as in the KSMB-model.The generation rate from Eq. (5.21) is now

$$\tilde{G} = G_{\mathrm{opt}} p_{\mathrm{diss}} 2\tau_{\mathrm{r}} S_{\mathrm{D}}/w = \tilde{G}_{\mathrm{KSMB}} 2\tau_{\mathrm{r}} S_{\mathrm{D}}/w =: \tilde{G}_{\mathrm{KSMB}} f_c \tag{5.27}$$

and thus being a series connection of the generation rate $\tilde{G}_{\mathrm{KSMB}}$ as defined by Ref. [102] and of a collection efficiency f_{c}, defined as the probability that a photogenerated exciton contributes to the current. Note that we omitted the integration over a distribution of separation distances, as carried out in Ref. 14, since it is incompatible with the principle of detailed. Thus, the generation rate $\tilde{G}_{\mathrm{KSMB}}$ represents the generation rate from Ref. 14, without this integration

Especially for the simulation of J/V curves, the recombination rate is of high importance. For all following simulations, I modify the recombination constant as defined in Eq. (5.22) in the same way as the generation rate. Using the dissociation probability for bound e/h-pairs, the recombination rate becomes

$$\tilde{R} = k_{\mathrm{rec}}/(w/2)(np - n_{\mathrm{i}}^2)\,(1 - p_{\mathrm{diss}})\,, \tag{5.28}$$

with P_{diss} defined by Eq. (5.26). Since I assume the back reaction of bound e/h-pairs into excitons to be weak, the recombination constant is identical to the one derived by Ref. [102].

The generation rate $\tilde{G}_{\mathrm{KSMB}}$, which takes the dissociation of the bound e/h-pair into account, has been extensively discussed in Refs. [102,109–113]. Therefore, I will concentrate here on the influence of f_{c}.

5.3 Fundamental aspects

5.3.1 Influence of the carrier mobilities and the surface recombination velocity

The KSMB-model has several implications for the J/V-curve and performance of the device. Among the most prominent are the temperature and field dependence of the photocurrent and the dependence of generation and recombination rate on the mobility of the free charge carriers. While the field and temperature dependence of the photocurrent have already been extensively discussed [102, 109], the influence of the mobility on the solar cell efficiency is still under debate. Marsh, Groves and Greenham [98], for instance, point out that high mobilities are of particular importance for organic solar cells, while Mandoc et al. [115] use the KSMB-model to show that solar cell efficiency has a maximum for finite mobilities and decreases for higher

mobilities. These findings lead to the question if and under which circumstances a high mobility deteriorates device performance - in our model and in general.

For this discussion on the charge carrier mobility, let us simplify our model in a way that the dependencies of generation and recombination rate on mobility become apparent. Let us therefore set the exciton collection efficiency $f_c = 1$ and let us neglect all field dependencies. Then the generation rate is

$$\tilde{G} = \frac{G_{\mathrm{opt}}^{\mathrm{exc}}}{w/2} \left(\frac{k_{\mathrm{rec}} n_{\mathrm{i}}^2}{k_{\mathrm{rec}} n_{\mathrm{i}}^2 + k_{\mathrm{f}} \xi_0} \right) \tag{5.29}$$

and the recombination rate is

$$\tilde{R} = \frac{(np - n_{\mathrm{i}}^2)}{w/2} \left(\frac{k_{\mathrm{rec}} k_{\mathrm{f}} \xi_0}{k_{\mathrm{rec}} n_{\mathrm{i}}^2 + k_{\mathrm{f}} \xi_0} \right) \tag{5.30}$$

It can be seen that both increase monotonically with k_{rec} and, thus, due to the Langevin equation (see Eq. (5.23)) with the mobility of the slowest carrier. Although the recombination rate increases with mobility, the ratio

$$\frac{\tilde{G}}{\tilde{R}} = \frac{G_{\mathrm{opt}}^{\mathrm{exc}}}{(np - n_i^2)} \frac{n_{\mathrm{i}}^2}{k_{\mathrm{f}} \xi_0} \tag{5.31}$$

is independent of k_{rec} and of carrier mobility and thus, one would not expect a decrease in open circuit voltage with increasing carrier mobility as reported in Ref. [115].

At this point it becomes important to consider the boundary conditions between absorber and contacts. An infinite surface recombination velocity S_{C} as assumed in Ref. [115] for the respective minorities will lead to strongly increased recombination at the surfaces if the mobilities are high. Thus, low mobilities act like a passivation for infinitely defective surfaces. However, infinte surface recombination is not a fundamental aspect of organic solar cells that is necessary for device functionality but instead an additional sink for minoriy carriers, which may become important for future device generations. Figure 5.5a shows the short circuit current density J_{sc} as a function of mobility for different surface recombination velocities $S_{\mathrm{C}} = 0$, 10^2, 10^4, $10^6\,\mathrm{cm/s}$ and $S_{\mathrm{C}} = \infty$ which corresponds to the case discussed in Ref. [115]. The short circuit current increases monotonically with mobility. The saturation level depends on surface recombination velocity since it affects the amount of recombination at short circuit.

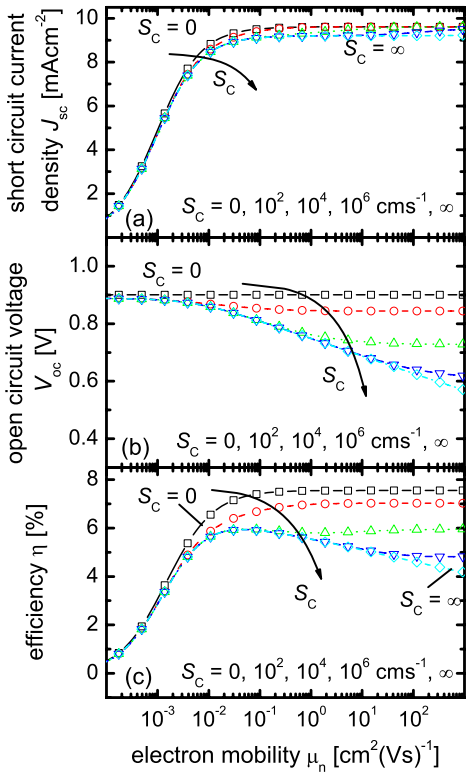

Fig. 5.5: *(a) Short circuit current, (b) open circuit voltage, and (c) solar cell efficiency as a function of electron mobility μ_n for different values of the recombination velocity S_C at the absorber/contact interface. For well passivated surfaces, the efficiency increases monotonically with mobility. Only for high recombination at the interface, the efficiency benefits from low mobilities, since they effectively passivate the defective surface regions. The parameters used are a constant generation rate $G_{opt}^{exc} = 6 \times 10^{21}$, an intrinsic carrier concentration $n_i = 3.5 \times 10^8\,\mathrm{cm}^{-3}$, the equilibrium decay rate $k_f \xi_0/(w/2) = 6 \times 10^6\,\mathrm{cm}^{-3}\,\mathrm{s}^{-1}$ for the bound pairs, a built in voltage $V_{bi,0} = 1.1\,\mathrm{V}$, a ratio of electron and hole mobility $\mu_n/\mu_p = 10$ and an absorber thickness $w = 100\,\mathrm{nm}$.*

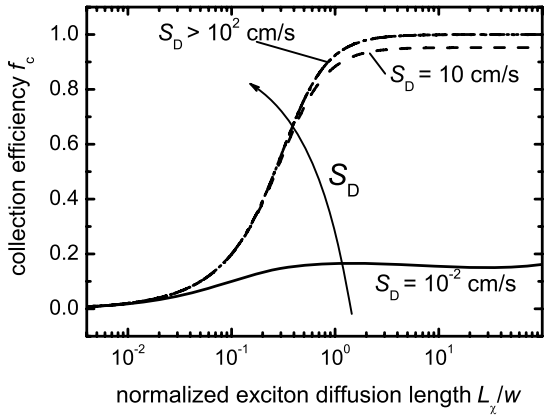

Fig. 5.6: *Collection efficiency f_c of excitons displayed as a function of the exciton diffusion length L_χ normalized to the distance w between two donor/acceptor interfaces using the exciton dissociation velocity S_D as parameter. The exciton recombination lifetime assumed for these simulations is $\tau_\mathrm{r} = 10\mu$s and the average distance between to hetero-interfaces is $w = 10\,$nm.*

Figure 5.5b shows the open circuit voltage, which decreases monotonically with mobility if the surface is not perfectly passivated ($S_\mathrm{C} = 0$). Figure 5.5c shows the efficiency as a function of mobility for different surface recombination velocities. The simulations with $S_\mathrm{C} = 0$ and $10^2\,\mathrm{cm/s}$ show a monotonous increase of efficiency with mobility. Very high surface recombination velocities of $S_\mathrm{C} = 10^6\,\mathrm{cm/s}$ lead to a dip in efficiency by around 1% absolute for very high mobilities. The parameters used for the simulation in Fig. 5.5 are a constant generation rate $G_\mathrm{opt}^\mathrm{exc} = 6 \times 10^{21}\mathrm{cm}^{-3}$, an intrinsic carrier concentration $n_\mathrm{i} = 3.5 \times 10^8\mathrm{cm}^{-3}$, the equilibrium decay rate $k_\mathrm{f}\xi_0/(w/2) = 6 \times 10^6\mathrm{cm}^{-3}\mathrm{s}^{-1}$ for the bound pairs, a built in voltage $V_\mathrm{bi,0} = 1.1\mathrm{V}$, a ratio of electron and hole mobility $\mu_\mathrm{n}/\mu_\mathrm{p} = 10$ and an absorber thickness $w = 100\,$nm.

In general, I conclude that a high mobility cannot be detrimental for the device performance as long as it only influences the charge seperation path crucial for the photovoltaic effect. Due to the principle of detailed balance, enhanced recombination

of free carriers to bound carriers will always imply more efficient dissociation, i.e. a better coupling between the free and the bound pairs. The higher the coupling the smaller the losses during charge separation will be, while the fact that this coupling also increases recombination can never lead to a performance loss.

However, increased mobilities can enhance recombination via additional (parasitic) pathways like high recombination at the absorber/contact interface. Thus, passivation of such defective regions is in theory also possible by making the transport towards these defective regions less likely, i.e. by decreasing the mobility. However, such an effect is neither caused by the Langevin type recombination rate nor is it a specific feature of organic and/or bulk heterojunction solar cells.

5.3.2 Influence of exciton diffusion on the photocurrent

Figure 5.6 shows the result of calculating $f_c = 2\tau_r S_D/w$ as a function of exciton diffusion length L_χ normalized to the average distance w between two interfaces and with the exciton dissociation velocity S_D as a parameter. In order to have an efficient collection of excitons, i.e. $f_c \approx 1$, the transport of excitons to the next hetero-interface between donor and acceptor phase as well as the dissociation velocity at this interface must be high. Thus, for sufficiently high $S_D > 10^2\,\mathrm{cm/s}$ and ratios $L_\chi/w >> 1$, the collection efficiency f_c in Fig. 5.6 approaches unity. That corresponds to the physical case, where each photogenerated exciton creates one bound e/h-pair. For low values of the dissociation velocity S_D the collection efficiency f_c saturates at a lower level for a high ratio $L_\chi/w >> 1$. For lower ratios $L_\chi/w << 1$, the excitons do not reach the next interface but recombine instead. The collection efficiency is then reduced below one even for high dissociation velocities. The exciton recombination lifetime assumed for these simulations is $\tau_r = 10\mu$s.

5.3.3 The role of band offsets

The open circuit voltage V_{oc} of most real solar cells is controlled by non-radiative recombination at defects and interfaces. In bhj solar cells especially the non-radiative recombination at the heterointerfaces between donor and acceptor phase is an important loss process. As a direct consequence, the band offset ΔE_C between conduction band of donor and acceptor molecule and the morphology [116], i.e. the average

distance w between two heterointerfaces, become decisive parameters for the efficiency of the bhj solar cell. Interestingly, both parameters bear a trade-off between optimizing dissociation of excitons, favored by low values of w and large band offsets ΔE_{C}, and the minimization of recombination losses, requiring large distances w and band offsets as small as possible. The following will provide a quantitative treatment of these effects. Since the existence of a bound electron/hole pair ξ at the heterointerface is not important for the following general considerations, I will only consider excitons and free carriers.

Nevertheless, a collection efficiency can be defined just like for the case with bound electron hole pairs. The collection efficiency depends on exciton diffusion length L_χ, interface dissociation lifetime S_χ and interface seperation w via

$$f_{\mathrm{c}} = \frac{2L_\chi S_\chi}{w} \frac{\sinh\left(w/2L_\chi\right)}{S_\chi \sinh\left(w/2L_\chi\right) + D_{\mathrm{x}}/L_\chi \cosh\left(w/2L_\chi\right)} \tag{5.32}$$

For very high exciton diffusion lengths $L_\chi >> w$, the collection efficiency saturates at its maximum. This maximum is usually $f_{\mathrm{c}} = 1$, if exciton dissociation at the interface is efficient ($S_\chi > 10^2\,\mathrm{cm/s}$). For ratios $w/2L_\chi < 1$, the collection efficiency decreases below its saturation level.

Let us first focus on the band offset ΔE_{C} at the interface and assume that the transport of excitons to the interface and the collection of electrons and holes are efficient. Then, the short circuit current density J_{sc} normalized to its maximum $J_{\mathrm{sc,SQ}}$ will be equal to the collection efficiency f_{c} in the limit of high exciton diffusion lengths $L_\chi >> w$. From Eq. (5.32) follows

$$\frac{J_{\mathrm{sc}}}{J_{\mathrm{sc,SQ}}} = \lim_{w/L_\chi \to 0} f_{\mathrm{c}} = \frac{1}{1 + w/(2S_\chi \tau_{\mathrm{r}})} \tag{5.33}$$

In thermal equilibrium, the recombination of electrons in the acceptor phase and holes in the donor phase equals the dissociation of excitons, leading to

$$H_\chi n_{0A} p_{0D} = S_\chi \chi_0 \tag{5.34}$$

where H_χ defines the recombination rate, S_χ the dissociation rate. Note that S_χ describes the interaction between excitons and free carriers just like S_{D} described the interaction between excitons and bound pairs. The equilibrium concentrations $n_{0\mathrm{A}}$ and $p_{0\mathrm{D}}$ of electrons in the acceptor and holes in the donor will depend on the

band gap of the respective material. Figure 5.7 shows a scheme of the heterojunction between donor and acceptor together with the equilibrium concentrations depending on the conduction and valence band energy E_{CA} and E_{VA} in the acceptor and E_{CD} and E_{VD} in the donor. If I now vary the conduction band energy E_{CA} in the acceptor, I will have to change the left hand side of Eq. (5.34), since $n_{0A} \propto \exp(\Delta E_C/kT)$, where $\Delta E_{\mathrm{C}} = E_{\mathrm{CD}} - E_{\mathrm{CA}}$ is the difference in conduction band energy between donor and acceptor. If everything else is kept constant, then a high band offset ΔE_{C} implies a low band gap of the acceptor and, thus, a high equilibrium concentration $n_{0\mathrm{A}}$. The validity of Eq. (5.34) requires that the dissociation rate S_χ also changes with the band offset, since χ_0 stays constant. The latter is a useful assumption since changing χ_0 would also mean that the band gap of the donor and therewith the absorption in the solar cell would change.

Thus

$$S_\chi = S_{00} \exp(\Delta E_C/kT) \tag{5.35}$$

holds, where S_{00} is a proportionality factor in units of a velocity. Equation (5.35) means that the dissociation is more efficient if the band offset is high. For the normalized short circuit current density, this exponential dependence of the dissociation velocity on the band offset implies that

$$\frac{J_{\mathrm{sc}}}{J_{\mathrm{sc,SQ}}} = \frac{1}{1 + \frac{w}{2S_{00}\tau_{\mathrm{r}}} \exp\left(-\Delta E_{\mathrm{C}}/kT\right)} \tag{5.36}$$

holds.

Now, I need to consider the dependence of the recombination current on the band offset. For a device with an extremely high amount of internal surfaces as is necessary in organic bhj solar cells, it is reasonable to assume the recombination at these interfaces determines the recombination current. Under this assumption, the saturation current density J_0 will be proportional to the equilibrium carrier concentrations. Since the hole concentration in the donor remains unchanged, I write

$$J_0 = J_{00} \exp(\Delta E_C/kT) \tag{5.37}$$

with J_{00} being a proportionality factor with the unit of a current density. Since a higher conduction band offset ΔE_{C} implies a smaller band gap E_{g} (as defined in Fig. 5.7), the recombination increases.

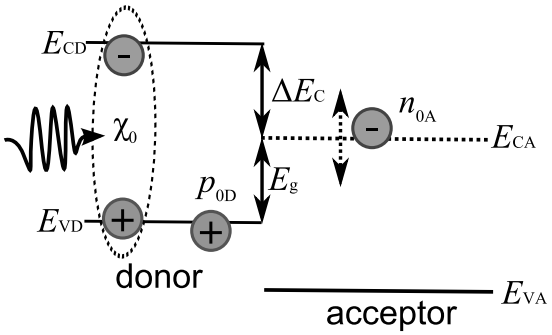

Fig. 5.7: *Schematic drawing of the heterointerface between donor and acceptor in a bhj solar cell. By varying the conduction band energy E_{CA} of the acceptor, the equilibrium concentration n_{0A} of electrons in the acceptor, the band gap E_g as well as the band offset ΔE_C in the conduction band between donor and acceptor are changed.*

Thus, the principle of detailed balance that led us arrive at Eqs. (5.33) and (5.35) predicts Eqs. (5.36) and (5.37) and thus a trade-off between photocurrent and recombination current. Figure 5.8 verifies our expectations, by showing the open circuit voltage V_{oc}, the normalized short circuit current density $J_{sc}/J_{sc,SQ}$ and the relative dependence of the product $V_{oc}J_{sc}/J_{sc,SQ}$ as a function of the conduction band offset ΔE_C. I have only two possible parameters, which change the result: The first parameter, which is varied in Fig. 5.8a, is the product $w/(2S_{00}\tau_r)$ and the second, being varied in Fig. 5.9b, is the prefactor J_{00} of the saturation current density. Both, Fig. 5.8a and b show that I obtain a maximum of the product $V_{oc}J_{sc}/J_{sc,SQ}$ with respect to the band offset ΔE_C. This maximum is in the range 0.3 eV $< \Delta E_C <$ 0.5 eV mostly depending on $w/(2S_{00}\tau_r)$.

5.3.4 The role of the blend morphology

The second parameter I study is the distance w between two heterointerfaces. For the short circuit current density, I now have to abandon the assumption of efficient transport to the interface, since the collection of excitons heavily depends on the

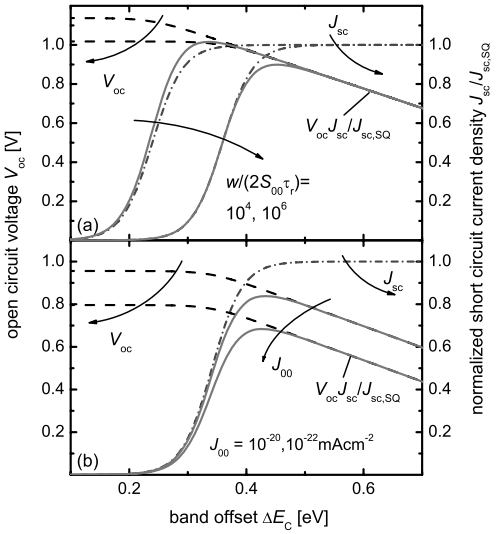

Fig. 5.8: *Simulation of short circuit current density J_{sc} (normalized to the maximum $J_{sc,SQ}$), open circuit voltage V_{oc} and the product $V_{oc}J_{sc}/J_{sc,SQ}$ as a function of the band offset Ec in a bhj-solar cell using the analytical equations (39, 40). The excitonic transport to the next heterointerface is assumed to be efficient $L/w >> 1$ and thus the only relevant parameters are (a) the ratio $w/(2S_{00}\tau_r) = 10^4$, 10^6 and (b) $J_{00} = 10^{-22}$, 10^{-20} mA cm^{-2}. A high band offset generally favors J_{sc}, since the exciton dissociation is made much more favorable than its inverse process (recombination of two free carriers forming an exciton). A low band offset favors V_{oc}, since the energy loss at the heterointerface is minimized and band gap (and minority carrier concentration) are kept as high (and low) as possible to ensure a low recombination current.*

distance to the next interface. For the normalized J_{sc}, then holds

$$\frac{J_{\mathrm{sc}}}{J_{\mathrm{sc,SQ}}} = f_{\mathrm{c}} = \frac{2L_\chi S_\chi}{w} \frac{\sinh\left(w/2L_\chi\right)}{S_\chi \sinh\left(w/2L_\chi\right) + \frac{D_\chi}{L_\chi}\cosh\left(w/2L_\chi\right)} \tag{5.38}$$

The recombination current density will scale linearly with the number of interfaces per surface area of the device. For high distances between the heterointerfaces, there

will be few recombination and vice versa. Thus, I rewrite Eq. (5.37) as

$$J_0 = J_{00} \exp(\Delta E_C / kT) \frac{w}{w_0} \tag{5.39}$$

where w_0 is an arbitrarily chosen thickness. Figure 5.9 shows the open circuit voltage V_{oc}, the normalized short circuit current density $J_{\mathrm{sc}}/J_{\mathrm{sc,SQ}}$ and the relative dependence of the product $V_{\mathrm{oc}}J_{\mathrm{sc}}/J_{\mathrm{sc,SQ}}$ as a function of the distance between two interfaces w. In order to make the values of J_{00} comparable between Figs. 5.8 and 5.9, I choose $w_0 = 10\,\mathrm{nm}$ and $\Delta E_{\mathrm{C}} = 0.4$ eV. Now, I have more free parameters than before, since I use a more complicated ansatz for the normalized short circuit current density. As parameters for Fig. 5.9, I chose the exciton diffusion length L_χ and the prefactor J_{00} of the saturation current density. The other parameters that were kept constant are the recombination lifetime $\tau_{\mathrm{r}} = 100\mu s$ and the prefactor $S_{00} = 1$ cm/s of the surface recombination velocity.

Figure 5.9a shows the variation of the exciton diffusion length L_χ leading to a varying optimum distance w for a maximum product $V_{\mathrm{oc}}J_{\mathrm{sc}}/J_{\mathrm{sc,SQ}}$. As shown in Fig. 5.9b, for a constant exciton diffusion length $L_\chi = 10$ nm and varying J_{00}, the optimum distance stays roughly the same. The optimum is rather broad and peaks at distances of around 5 nm, i.e. slightly smaller than the exciton diffusion length.

5.3.5 Optoelectronic reciprocity

Just like for the bipolar and excitonic pin-type solar cells, I want to discuss the connection between fill factor losses (voltage dependent collection and injection) and the reciprocity theorem also for the case of the bulk heterojunction solar cell. For the following simulations, I again neglect the effect of the bound electron/hole pair and use our complete model including photon recycling but without coherent optics.

In order to include exciton diffusion and dissociation at an interface into the model presented in chapter 4, I need to reinterpret the value of the dissociation lifetime τ_{D}. The derivation presented in chapter 5.2.4 leads to an effective generation rate for bound excitons and subsequently free carriers. Since the generation rate in the excitonic model from chapter 4 is $G = \chi/\tau_{\mathrm{D}}$, it is possible to include the effects of exciton diffusion and dissociation in the value for τ_{D}. The equation that follows

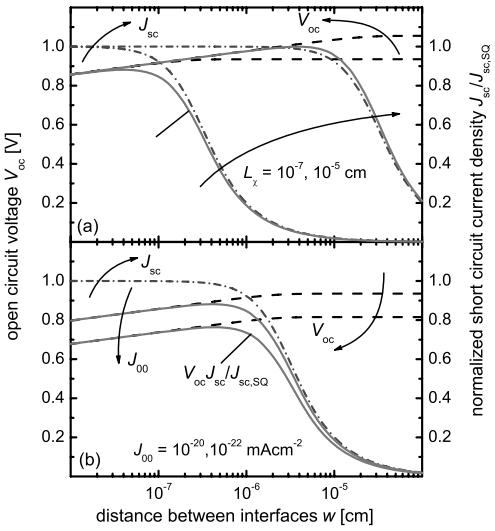

Fig. 5.9: *Simulation of short circuit current density J_{sc} (normalized to the maximum $J_{sc,SQ}$), open circuit voltage V_{oc} and the product $V_{oc}J_{sc}/J_{sc,SQ}$ as a function of the distance between two heterointerfaces in a bhj-solar cell using the analytical equations (41, 42). I vary (a) the exciton diffusion length $L_\chi = 10^{-7}$, $10^{-5}\,\mathrm{cm}$ and (b) $J_{00} = 10^{-22}$, $10^{-20}\,\mathrm{mA\,cm^{-2}}$. A high distance between interfaces generally favors V_{oc} since interface recombination is minimized, while a low distance favors J_{sc} due to more efficient diffusion of excitons to the next interface.*

is [117]

$$\tau_{\mathrm{D}} = \tau_{\mathrm{r}} \left[\frac{w}{2S_\chi \tau_{\mathrm{r}}} + \frac{w}{2L_\chi} \coth(w/2L_\chi) - 1 \right]. \tag{5.40}$$

In the following, I will compare the two parameter combinations A and B as introduced in Table 4.1 with two parameter combinations C and D that are bhj-devices. Bhj device means that no excitonic transport in the x-direction as defined by Fig. 5.10 is allowed and that the exciton mobility $\mu_\chi(y)$ in y-direction is inserted in Eq. (5.40) to determine the effective dissociation velocity τ_{D} which is used in the differential equations (4.1, 4.2, 4.3). Table 5.1 summarizes all four parameter combinations.

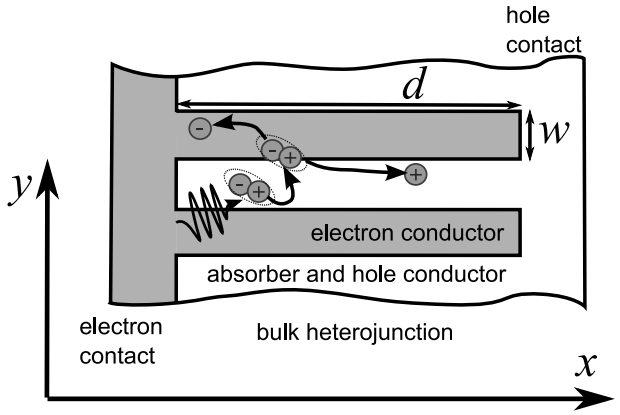

Fig. 5.10: *Scheme of a bulk heterojunction (bhj) solar cell. Bulk dissociation of excitons is interpreted in terms of bhj-devices as the combined process of diffusion to and subsequent dissociation at the nearest interface. The exciton diffusion to the interface is described by the mobility $\mu_\chi(y)$ in y-direction, while the mobility of excitons in x-direction is assumed to be zero. In terms of the model of chapter 4, the bhj solar cell is a device with purely bipolar transport in x-direction and with a dissociation lifetime that depends on the exciton transport in y-direction via Eq. (5.40)*

Figure 5.11 shows the same data as Fig. 4.6 and in addition the corresponding simulation results for the two bhj-configurations (C and D). Figure 5.11a,b shows that the dependence of short circuit current density and fill factor on the electron and hole mobility is the same for configurations B and D, i.e. for the bhj and the no-bhj case. Thus reducing bipolar mobilities in a bhj solar cells has the same effect as in any other bipolar pin-type device. Reducing the exciton mobilities, however, is different for the bhj and the no-bhj case. For cfg. A, the reduced exciton mobility in Fig. 5.11c,d is a mobility in x-direction. A reduction of $\mu_\chi(x)$ leads to a decrease in excitonic photocurrent being partly compensated by an increase in bipolar photocurrent. For the bhj case the interpretation of exciton mobility is different. Now I discuss the exciton mobilty $\mu_\chi(y)$ in y-direction towards the next interface. Thus the exciton mobility where the short circuit current density J_{sc} of the bhj solar cell (cfg. C) starts to fall below its maximum is at around

Tab. 5.1: *Mobilities $\mu_{n,p}$ of free carriers and μ_χ of excitons as well as the bulk dissociation lifetime τ_D for the (now) four discussed configurations of non-ideal solar cells. In case of configurations C and D, the dissociation lifetime τ_D is calculated via the equation for bulk heterojunction solar cells [Eq. (5.40)]. The parameters used to obtain these values are for cfg. C: a lifetime $\tau_r = 200\mu\,\mathrm{s}$, an interface dissociation velocity $S_\chi = 10^{10}\,\mathrm{cm/\,s}$ and an interface distance $w = 10\,\mathrm{nm}$. Furthermore, I assumed that the exciton diffusion length follows from $L_\chi = \sqrt{\mu\tau_\mathrm{r} kT/q}$. For cfg. D, I used $L_\chi = 10w = 100\,\mathrm{nm}$. All other parameters were the same as for cfg. C.*

	cfg. A	cfg. B	cfg. C	cfg. D
carrier mobility $\mu_{\mathrm{n,p}}$ $[\mathrm{cm}^2(\mathrm{V\,s})^{-1}]$	10^3	10	10^3	1
exciton mobility $\mu_\chi(x)$ $[\mathrm{cm}^2(\mathrm{V\,s})^{-1}]$	10^{-5}	10^{-5}	0	0
exciton mobility $\mu_\chi(y)$ $[\mathrm{cm}^2(\mathrm{V\,s})^{-1}]$	-	-	$10^{-8} - 10^{-1}$	2×10^{-5}
dissociation lifetime $\tau_\mathrm{D}[\mathrm{s}]$	10^{-4}	10^{-10}	3×10^{-11}	2×10^{-7}
			-3×10^{-4}	

$\mu_\chi = 10^{-6}\,\mathrm{cm}^2(\mathrm{V\,s})^{-1}$, i.e. three orders of magnitude below the value for the non-bhj cell (cfg. A). These three orders of magnitude stem from the ratio of distance w to the interface divided by the cell thickness d, which is $w/d = 1/30$. Since mobility enters the diffusion length via a squareroot-term, the factor of 30 in diffusion length normalized to the relevant geometrical quantity (either d or w) translates to a factor of $30^2 \approx 10^3$ in mobility.

Figure 5.12 shows the comparison of directly measured quantum efficiency $Q_{\mathrm{e,dir}}$ and the quantum efficiency $Q_{\mathrm{e,EL}}$ derived from the electroluminescence measurement via Eq. (2.33) for all cfgs. A-D. Figure 4.8 already discussed the non-bhj cases A and B. Now I add the two bhj cases C and D. The main result stays the same. As long as all bipolar mobilities are high, the fill factor will be high (cf. Fig. 5.11) and unaffected by excitonic mobility changes. In this case also the reciprocity will hold and $Q_{\mathrm{e,dir}} = Q_{\mathrm{e,EL}}$ as shown in Figs. 5.12a,c. If bipolar mobilities are low, the fill factor will be below its high mobility value and the reciprocity does not hold any more, i.e. $Q_{\mathrm{e,dir}} \neq Q_{\mathrm{e,EL}}$. This is the case for both cfgs. B and D and thus for Figs. 5.12b,d. For cfg D, the disagreement between $Q_{\mathrm{e,dir}}$ and $Q_{\mathrm{e,EL}}$ is larger than for cfg.

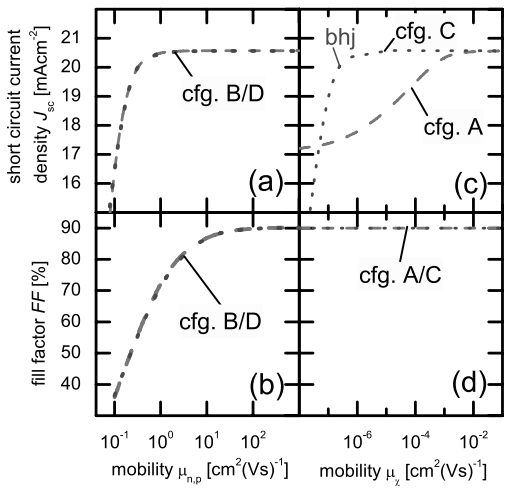

Fig. 5.11: *Summary of the effects of reduced bipolar and excitonic mobilities on short circuit current density J_{sc} and fill factor FF of configurations A-D. In (a) and (b) I used the parameters for cfg. B (dashed line) and cfg. D (dotted line) and varied the electron and hole mobility $\mu_{n,p}$. We find a considerable decrease of fill factor for mobilities $\mu_{n,p} < 10^2\,\mathrm{cm}^2(\,\mathrm{V\,s})^{-1}$, while a loss in J_{sc} starts only for even lower mobilities $\mu_{n,p} < 10^0\,\mathrm{cm}^2(\,\mathrm{V\,s})^{-1}$. Both, the bhj and the non-bhj solar cell show the same dependence of J_{sc} and FF on mobility. In (c) and (d), I used the parameters for cfgs. A (dashed line) and C (dotted line) and varied the exciton mobility. For cfg. A, J_{sc} is reduced for exciton mobilities $\mu_\chi < 10^{-3}\,\mathrm{cm}^2(\,\mathrm{V\,s})^{-1}$, while the fill factor stays unaltered, since the electron and hole mobilities are high enough to warrant voltage independent collection. For the bhj cell (cfg. D, dotted line) the decrease of J_{sc} starts only at $\mu_\chi < 10^{-6}\,\mathrm{cm}^2(\,\mathrm{V\,s})^{-1}$, where the exciton mobility is too low to reach the heterointerface.*

B simply because the bipolar mobility is smaller. On this level of abstraction, I see no differences between the bhj and the no-bhj case.

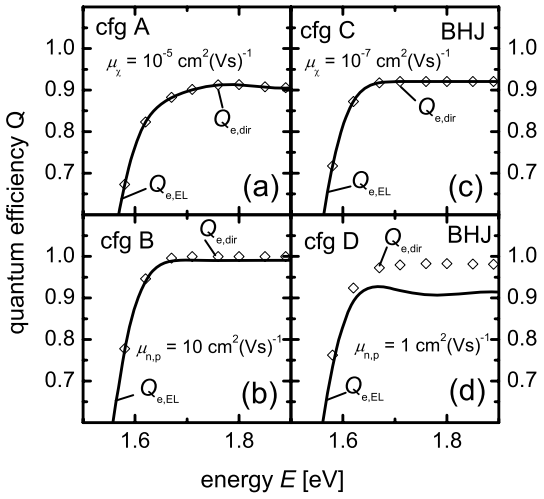

Fig. 5.12: *Simulation of the quantum efficiency $Q_{e,dir}$ (diamonds) compared with the simulation of the electroluminescence spectrum, from which the quantum efficiency $Q_{e,EL}$ (solid line) is calculated using Eq. (2.33), for the case of (a) configuration A, (b) configuration B, (c) configuration C and (d) configuration D. For case (a) and (c), the electron and hole mobility are high ($\mu_{n,p} = 10^3\,\mathrm{cm}^2(\mathrm{V\,s})^{-1}$) and thus collection and injection of carriers is voltage independent and the reciprocity is valid. For case (b), the low bipolar mobility leads to a small deviation between $Q_{e,dir}$ and $Q_{e,EL}$. For case (d), the even lower mobility leads to a clearly visible deviation between $Q_{e,dir}$ and $Q_{e,EL}$*

5.4 Comparison to experimental results

Recent investigations [106, 107] on the internal quantum efficiency Q_i in bulk heterojunction solar cells revealed different spectral regions with distinct differences in the internal quantum efficiency. The internal quantum efficiency has been defined by

$$Q_\mathrm{i}(E) = \frac{Q_e(E)}{a(E)}, \tag{5.41}$$

where Q_e is the measured external quantum efficiency and $a(E)$ the absorptance calculated with a matrix transfer formalism. For higher energies, the internal quantum efficiency was reported to be considerably higher than the internal one. The two suggested explanations [107] were that the change in Q_i is induced by the photons being absorbed in the fullerene phase which has either (i) a smaller domain size compared to the polymer phase [118, 119] or (ii) a higher exciton diffusion length, which can reach values of 40 nm in the fullerene [120] compared to 10 nm in the polymer.

In the framework of our model, both explanations have nearly the same effect. Under the assumption that the transfer of excitons at the interface into bound e/h-pairs at the interface is efficient ($S_D > 10^2\,\mathrm{cm/s}$), smaller domain sizes and higher exciton diffusion lengths both increase the ratio L_χ/w and subsequently the collection efficiency f_c. For exciton diffusion lengths as high as 40 nm, it is reasonable to assume that $L_\chi/w >> 1$ holds in the fullerene and, thus, that the collection efficiency in the fullerene $f_{c,F} \approx 1$. This finding helps to adjust the value of the generation rate $\tilde{G}_{KSMB}$ accounting for bound e/h-pair dissociation, which is the same for excitons created in the fullerene and in the polymer. The internal quantum efficiency for lower energies, corresponding to absorption in the polymer, then allows us to fix the collection efficiency in the polymer $f_{c,P} < 1$. The other parameters of the model, especially those entering in the dissociation probability P_{diss} for bound e/h-pairs have to be fixed by comparison between simulated and experimental current/voltage-curve.

Figure 5.13 shows an example for the application of our model to quantum efficiency data published in Ref. [106]. The open symbols represent the original data, I wanted to reproduce with our simulations (lines). The layer stack needed for the optical simulations consists of 1mm quartz superstrate, a total of 133 nm ITO, 68 nm of PEDOT:PSS, 186 nm of the absorber blend consisting of PF10TBT/PCBM (poly[9,9-didecanefluorene-alt-(bis-thienylene) benzothiadiazole]/ ([6,6]-phenyl C60 butyric acid methyl ester), 1 nm LiF and a 100 nm thick Al back reflector. The nk-data files used in our simulations were obtained from the authors of Ref. [106] leading to the absorptance represented by the solid line in Fig. 5.13. First I adjusted the parameters for the exciton dissociation in the fullerene ($\lambda < 420\,\mathrm{nm}$) to $L_\chi/w >> 1$ and in the polymer ($\lambda > 420\,\mathrm{nm}$) to $L_\chi/w = 0.78$. All other parameters had to

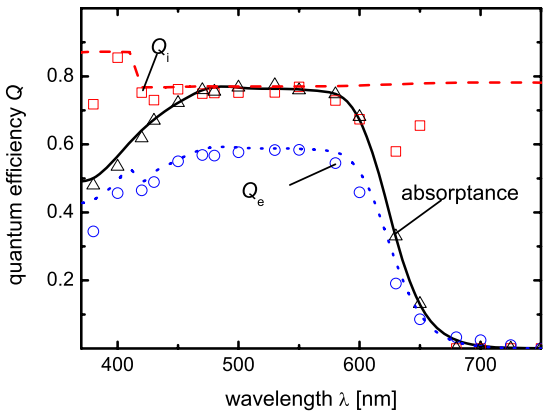

Fig. 5.13: *Internal and external quantum efficiency as well as absorptance of the cell presented in Ref. [106] (open symbols) compared to our simulations (lines). The parameters used for the simulations were a band gap* $E_g/q = 1.4\text{V}$*, a built in voltage* $V_{bi,0} = 1.4\text{V}$*, an effective density of states* $N_{C,V} = 2.5 \times 10^{-19}\,\text{cm}^{-3}$ *in valence and conduction band, a dielectric constant* $\epsilon_r = 3.4$ *of the blend, an electron mobility* $\mu_n = 1.2 \times 10^{-3}\,\text{cm}^2/\text{Vs}$*, a hole mobility* $\mu_p = 1.7 \times 10^{-4}\,\text{cm}^2/\text{Vs}$*, a decay constant for bound e/h-pairs* $k_f/(w/2) = 2.8 \times 10^5$ *and an average separation distance of bound e/h-pairs* $a = 1.8\,\text{nm}$*.*

be adjusted by both considering the quantum efficiency as well as the whole J/V-curve as shown in Fig. 5.14 (circles are the data from Ref. [106] and the solid line represents the simulation). Among the parameters relevant for electron hole transport as well as dissociation and recombination of bound pairs, some were kept constant or within close boundaries, while others were used to obtain a good fit of the J/V-curve. The effective density of states $N_{C,V} = 2.5 \times 10^{-19}\,\text{cm}^{-3}$ in valence and conduction band as well as the dielectric constant $\epsilon_r = 3.4$ were assumed to be the same as in Ref. [102]. The band gap $E_g = 1.4\,\text{eV}$, meaning the energy difference between the lowest unoccupied molecular orbital in the electron acceptor (PCBM) and the highest occupied molecular orbital in the electron donor (PF10TBT) was

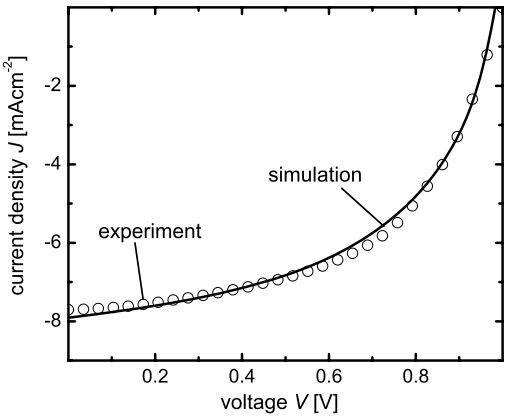

Fig. 5.14: *Experimental current/voltage curve from Ref. [106] (open circles) compared to our simulation (solid line) using the same parameters as for the quantum efficiency in Fig. 5.13.*

only varied slightly around the approximate value $E_\mathrm{g} = 1.3\,\mathrm{eV}$, given by Moet et al. [121] for the material system under investigation, in order to adjust the open circuit voltage precisely. For simplicity, the built in voltage was assumed to equal the band gap $V_{\mathrm{bi},0} = E_\mathrm{g}/q = 1.4\mathrm{V}$. The parameters that were obtained after fitting are an electron mobility $\mu_\mathrm{n} = 1.2\times10^{-3}\mathrm{cm}^2/\mathrm{Vs}$, a hole mobility $\mu_\mathrm{p} = 1.7\times10^{-4}\mathrm{cm}^2/\mathrm{Vs}$, a decay rate for bound e/h-pairs $k_\mathrm{f}/(w/2) = 2.8\times10^5\,\mathrm{s}^{-1}$ and an average separation distance of bound e/h-pairs $a = 1.8\,\mathrm{nm}$.

Chapter 6

Detailed balance model for solar cells with multiple exciton generation

The detailed balance model for quantum dot solar cells with quantum efficiencies above unity is extended to the case of non-ideal extraction of carriers from dots and finite mobilities of free carriers. For more realistic estimations of maximum efficiencies, I include experimental values for Auger lifetimes and absorption coefficients. Thus, for a given material, the model is capable of determining the critical values for the mobilities and extraction lifetimes in order to make the efficiency benefit from multiple exciton generation.

6.1 Introduction

While current single junction technologies are getting closer to the Shockley-Queisser (SQ) limit [30], there is a growing interest in mechanisms that can improve efficiencies above this limit [4, 122]. One such mechanism that overcomes the restrictions of the SQ-limit is the generation of more than one exciton or electron/hole-pair from a single photon with energy more than twice the band gap. Although first demonstrated in bulk silicon [123], the efficiency and threshold of multiple exciton generation (MEG) are strongly enhanced in quantum dots [26, 78, 124] made of, e.g., PbSe [125], CdSe [126], InAs [127], or even Si [128]. Up to now, the evidence

for MEG in these quantum dot layers stems from transient absorption and photoluminescence spectroscopy [129], and not from quantum efficiency measurements of finished solar cells. In addition, approaches to estimate the possible efficiency gain by MEG have been restricted to detailed balance calculations similar to the Shockley-Queisser approach that do not consider extraction of carriers [130–132]. However, although this is reasonable in many crystalline semiconductor cells, for quantum dot devices, extraction of photogenerated carriers is one of the most severe bottlenecks.

This chapter extends the radiative limits valid for perfect carrier collection to the case of a finite extraction lifetime of excitons from the quantum dot and a finite mobility of the free carriers. We use measured absorption coefficients for films of coupled PbSe quantum dots [133] to calculate the absorptance and different configurations for the quantum yield of MEG as a function of energy. Quantum yield and absorptance directly yield the generation rates for mono-, bi-, and triexcitons separately. Considering the two bottlenecks for charge carrier extraction, the (i) extraction of multiexcitons on a time-scale faster than the Auger-recombination and (ii) transport of free carriers to the contacts, I use two different models, where the respective other parameter is kept sufficiently high that it does not limit the result.

6.2 Model

Figure 6.1a shows the processes taking place in a quantum dot upon absorption of a high energy photon (adapted from Ref. [134]). First, the absorbed photon transfers its energy to a hot monoexciton with an energy much higher than the band gap on a time scale of $\approx$ 0.1 ps. By impact ionization, a hot biexciton is created, which then thermalizes ($\approx$ 2 ps) to form a relaxed biexciton. This biexciton is the useful state for a solar cell with quantum efficiency above unity. If no extraction of the biexciton happens, the biexciton forms a hot monoexciton again by Auger recombination taking around 20 - 130 ps [133,134]. Since several thermalization steps have happened during the process from the initial hot monoexciton, this second hot monoexciton has considerably less energy, i.e. not enough energy to start the cycle from the beginning and form a biexciton again. Thus, after a last thermalization step ($\approx$ 2 ps), we are left with a single relaxed exciton. This scheme shows the

processes that happen in a sample of quantum dots under irradiation with high energy photons. Now, I have to consider the case, when these quantum dots are part of the absorber of a solar cell.

In order to calculate time constants relevant for quantum dot solar cells, we need to agree on a solar cell geometry useful for such quantum dot solar cells. Nozik [77] suggested in principal three geometries: (i) a version of the dye-sensitized solar cell with quantum dots instead of dyes, (ii) a bulk heterojunction approach with quantum dots in close proximity to a hole- and an electron-conducting polymer, and (iii) an array of quantum dots forming the intrinsic region of a pin-junction solar cell. We will focus on the two configurations, depicted in Fig. 6.1. Figure 6.1b shows the scheme of a bulk-heterojunction type cell, where the absorber layer - the dots - are separated from the electron- and hole-transporting layer (ETL and HTL). This configuration has a conceptual advantage since it reduces the problem to a zero-dimensional one if the transport in the ETL and HTL is efficient. The second configuration shown in Fig. 6.1c is an array of quantum dots, serving for carrier absorption and collection. Solar cells of this type have already been fabricated [135], however without reaching quantum efficiencies above unity. From a modeling perspective, this type of cell needs finite mobility effects to be considered, since quantum dot arrays are usually low mobility materials.

The simplest starting point for a detailed balance model is thus the bulk heterojunction cell from Fig. 6.1b, where I only consider extraction of carriers from one quantum dot and keep the concentration of electrons n and holes p constant over the thickness of the device, i.e. I assume high mobilities for free carriers in the ETL and HTL.

Since, I won't consider thickness dependencies, the model will be an extension of the discrete two state model introduced in the fundamentals chapter 2.3.1. The simple two state model described the interaction between minority carriers and photons, phonons and the contact. The basic difference is that the present model has mono-, bi-, and triexcitons instead of minority carriers and it has to include the interactions between the excitons. To compute the interaction of mono-, bi-, and triexcitons with each other, with the incoming photons and with the free carriers in the ETL and HTL, I define rate equations, which strictly obey the principle of detailed balance. The simplest example is the detailed balance between photogener-

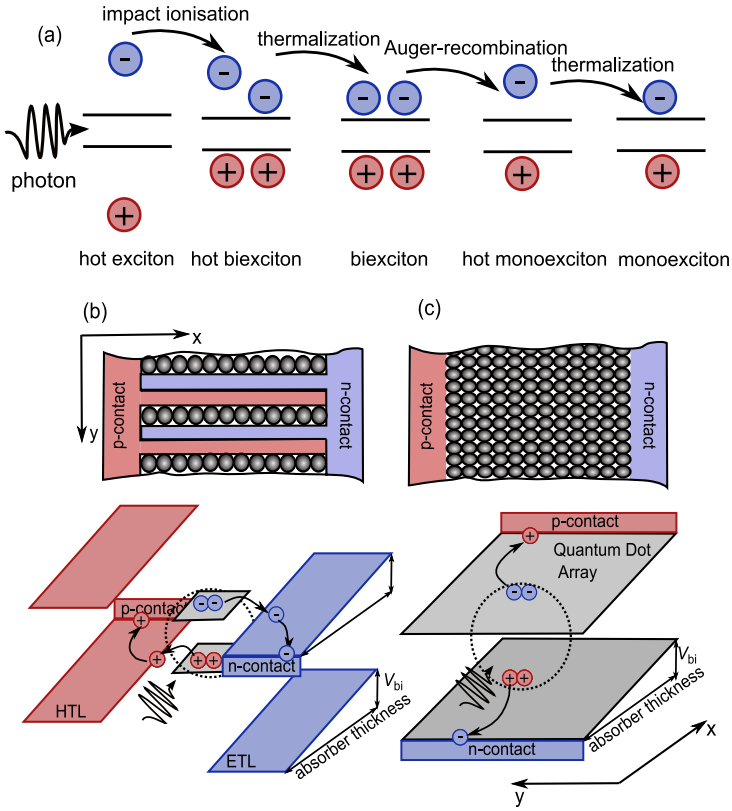

Fig. 6.1: *(a) Scheme of the processes in a quantum dot upon absorption of a high energy photon without any extraction of the excitons from the dot. Schemes of two different configurations of a quantum dot cells. (b) Bulk heterojunction configuration, where the absorption in the quantum dot is separated from the electron and hole transporting layers. (c) Quantum dot array as intrinsic region of a pin-junction solar cell.*

ation and radiative recombination. Let us define the concentration of monoexcitons normalized to the equilibrium value as x_1 and the photon flux normalized to its equilibrium value and already multiplied with the quantum yield for monoexcitons as ϕ_1; then the detailed balance requires that

$$a_1 x_1 = a_1^* \phi_1 \tag{6.1}$$

holds in thermodynamic equilibrium. In Eq. (6.1), a_1 and a_1^* are the rate constants for radiative recombination and photogeneration of a monoexciton. This, however, means that Eq. (6.1) holds, when both x_1 and ϕ_1 are one, i.e. equal to their equilibrium value, which in term leads to the requirement $a_1 = a_1^*$. Thus, if I normalize all exciton and carrier concentrations as well as photon fluxes, I write the three rate equations for the normalized concentration x_i of i-excitons (where $i = 1$ denotes mono-, $i = 2$ bi-, and $i = 3$ triexcitons) always with the same rate constant for each process and its corresponding inverse process. The resulting matrix equation in steady state is

$$\mathbf{M}\begin{pmatrix} x_1 \\ x_2 \\ x_3 \end{pmatrix} + \begin{pmatrix} a_1\phi_1 \\ a_2\phi_2 \\ a_3\phi_3 \end{pmatrix} + \begin{pmatrix} c_1 np/n_\mathrm{i}^2 + b_1 \\ 0 \\ 0 \end{pmatrix} = 0 \tag{6.2}$$

with the matrix $\mathbf{M}$ defined as

$$\mathbf{M} = \begin{pmatrix} -a_1 - b_1 - b_2 - c_1 - c_2 np/n_\mathrm{i}^2 & b_2 + c_2 & 0 \\ b_2 + c_2 np/n_\mathrm{i}^2 & -a_2 - b_2 - b_3 - c_2 - c_3 np/n_\mathrm{i}^2 & b_3 + c_3 \\ 0 & b_3 + c_3 np/n_\mathrm{i}^2 & -a_3 - b_3 - c_3 \end{pmatrix} \tag{6.3}$$

and with n_i as the intrinsic carrier concentration. The rate constants in units of $[\,\mathrm{cm}^{-2}\,\mathrm{s}^{-1}]$ for radiative interactions - absorption and radiative recombination - are denoted as ai for i excitons per dot. The factor $a_\mathrm{i}\phi_\mathrm{i}$ is the generation rate for the i-exciton, thus, a_i itself is the generation rate under ambient black body radiation in equilibrium. Note at this point, that a_i is the generation rate per unit surface, since we don't need to consider any depth dependence of the generation rate as long as we keep the concentration of free carriers independent of depth. From a_i, I calculate the equilibrium concentration $x_{0\mathrm{i}}$ of i-excitons with the help of

$$a_\mathrm{i} = \frac{x_{0\mathrm{i}}}{\tau_{\mathrm{rad,i}}} \tag{6.4}$$

in units $[\,\mathrm{cm}^{-2}]$.

The rate constants for non-radiative interactions are denoted as b_i and describe the non-radiative recombination of x_i creating a $x_{\mathrm{i}-1}$. For instance, b_2 describes the strength of the non-radiative recombination of a biexciton thereby creating a

monoexciton. In practice, the b_i are determined by the equilibrium concentrations $x_{0\mathrm{i}}$ and the Auger lifetimes $\tau_{\mathrm{Auger,i}}$ as

$$b_\mathrm{i} = \frac{x_{0\mathrm{i}}}{\tau_{\mathrm{Auger,i}}} \tag{6.5}$$

for bi- and triexcitons and $b_1 = 0$ for the radiative limit. That means, I want to include all intrinsic recombination processes, i.e. radiative recombination for the monoexciton and Auger-recombination for all higher numbers of excitons confined to one dot. The value of the Auger lifetime for the i-exciton is assumed to be $\tau_{\mathrm{Auger,i}} = 120 \times 4/i^2\mathrm{ps}$ [136].

Finally, the coupling constants of excitons to the free carriers are denoted as c_i and can again be expressed in terms of a lifetime τ_x for extraction of excitons as

$$c_\mathrm{i} = \frac{x_{0\mathrm{i}}}{\tau_{\mathrm{x,i}}} \tag{6.6}$$

I assume that one free e/h-pair is created by one extraction process, e.g. the extraction of one e/h-pair from a biexciton also creates one monoexciton. To calculate the current density J for a given voltage $V = kT/q \ln(np/n_\mathrm{i}^2)$, where kT is the thermal energy and q the elementary charge, I evaluate

$$J = qc_1 \left(np/n_\mathrm{i}^2 - x_1\right) \tag{6.7}$$

6.3 Generation of multiexcitons

There is currently a strong debate [134, 137, 138] about the origin of the ultrafast ($\tau < 200$ fs) creation [138] of multiexcitons in quantum dots. Since, we are only investigating the extraction of carriers, we assume that photons with a certain energy have a certain probability to create a multiexciton, i.e. more than one exciton confined in the same dot. The timescale for the creation of a multiexciton is assumed to be smaller than the timescales relevant for the extraction and recombination (Auger lifetime $\tau_{\mathrm{Auger}} \approx 100$ ps) of the excitons.

The quantum yield, defined as the average number of excitons per dot created by one photon has been experimentally determined for quantum dots made from different materials. For the case of PbSe, which will be discussed throughout this chapter, Schaller et al. [9] reported a threshold energy $E_\mathrm{th} = 2.85E_\mathrm{g}$ and a slope

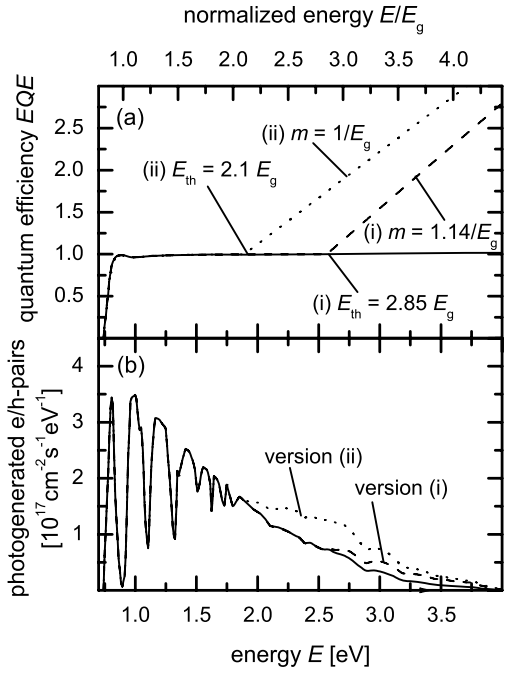

Fig. 6.2: *(a) Quantum efficiency as a function of energy E for the case of multiple exciton generation (MEG) with (i) energy threshold $E_{th} = 2.85E_g$ and slope $m = 1.14/E_g$ and (ii) with $E_{th} = 2.1E_g$ and $m = 1.0/E_g$. The band gap corresponding to the absorption coefficient is $E_g = 0.9\,\mathrm{eV}$. (b) From the external quantum efficiency, the number of photogenerated carriers per energy interval for the two configurations is calculated and compared with the case without MEG.*

$m = 1.14/E_\mathrm{g}$, both relative to the band gap E_g. This quantum yield was also used by Klimov [131] as well as Hanna and Nozik [132] to calculate the maximum power conversion efficiency for quantum dot solar cells with MEG as a function of band gap. Theoretical calculations of Franceschetti et al. [134] as well as experimental results of Ellingson et al. [137], however, showed threshold energies for MEG as low as $E_\mathrm{th} = 2.1E_\mathrm{g}$ for PbSe quantum dots. Thus, I will make our calculations for two versions of the quantum yield as a function of energy: (i) the version according

to [125, 131, 132] with $E_{\mathrm{th}} = 2.85E_{\mathrm{g}}$ and a slope $m = 1.14/E_{\mathrm{g}}$, and (ii) a version with a threshold energy $E_{\mathrm{th}} = 2.1E_{\mathrm{g}}$ according to [134, 137] and a linear slope $m = 1.0/E_{\mathrm{g}}$. Figure 6.2a shows the maximum possible external quantum efficiencies Q_{e} as a function of energy for the two versions. The external quantum efficiency in Fig. 6.2 follows via

$$Q_{\mathrm{e}}(E) = a(E)QY(E) \tag{6.8}$$

as a function of absorptance $a(E)$ and quantum yield $QY(E)$.

The absorptance, which corresponds to the external quantum efficiency without MEG (solid line) in Fig. 6.2a, follows from the absorption coefficient for a film of coupled PbSe quantum dots (Eg = 0.9 eV), calculated from the optical density and photoluminescence data presented in Ref. [133]. The photoluminescence data was used to determine the absorption coefficient in the weakly absorbing spectral range [139], which is of paramount importance if one wants to calculate the radiative recombination current (see Equation (2.38)) needed for the computation of radiative efficiency limits. The absorptance and the generation rate are calculated from the absorption coefficient under the assumption of perfect Lambertian light trapping with a limiting pathlength enhancement of $4n^2$ according to Yablonovitch [140]. The refractive index n, which is thus of high relevance for the absorptance, is chosen as $n = 4.7$ according to values for bulk PbSe [141]. For the case of perfectly isotropically scattering surfaces, which I assume to be a reasonable approximation to the optimum absorptance, the absorptance and generation rate are calculated according to Refs. [142]. The thickness d chosen for the absorber layer is $d = 150\,\mathrm{nm}$.

Figure 6.2b shows the quantum efficiency from Fig. 6.2a multiplied with the AM 1.5g spectrum [47] and, thus, the number of photogenerated electron/hole (e/h)-pairs per energy interval. For a detailed balance model, I need to be able to calculate the generation rate for mono-, bi- and triexcitons under illumination with the solar spectrum as well as under illumination with the black body spectrum at ambient temperature. These calculations require that the quantum yield is split into the parts that account for creation of mono-, bi- and triexcitons, respectively. Figure 6.3 shows such a distribution of the quantum yield QY. For energies just above the threshold energy, the $1 < QY < 2$ holds and thus, there is a certain probability for the creation of mono- and a certain probability for the creation of biexcitons. If I

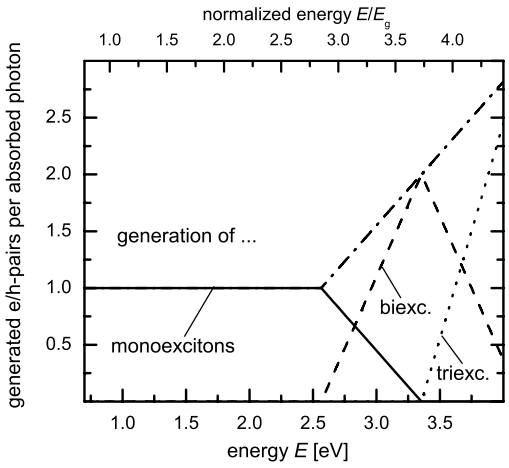

Fig. 6.3: *Distribution of the total quantum yield on the generation rate of mono-, bi- and triexcitons.*

denote the probability for the creation of monoexcitons with β,

$$QY(E) = (1 - \beta) \times 2 + \beta \times 1 \tag{6.9}$$

must hold, since $0 < \beta < 1$. Now, the value of β is fixed automatically, since QY is known. For energies $E > 3E_g$, the creation of triexcitons becomes possible, as well. Then, I would need to introduce a new parameter that regulates how much of the light directly creates triexcitons. This makes the solution of Eq. (6.9) be no longer unique. Thus, I assume that creation of triexcitons is only relevant, when $QY > 2$ holds. At the corresponding energy, the generation rate for monoexcitons is zero and the distribution of the photons to the generation rates for mono-, bi- and triexciton becomes unique again.

6.4 Results

Figure 6.4a shows the current/voltage (J/V) curves resulting from the solution of Eq. (6.7) with varying values of $\tau_x = \tau_{x,1} = \tau_{x,2} = \tau_{x,3}$ and an assumed radiative

lifetime $\tau_{\mathrm{rad}} = 10$ ns . The quantum yield chosen for the J/V-curves corresponds to version (i) in Fig. 6.2, while the dotted line is the reference without MEG. It is obvious from Fig. 6.4a that an increase in τ_{x} does only affect the short circuit current and not the fill factor. This is due to the fact that the equilibrium concentration of multiexcitons is so low that the recombination current does not depend on creation of multiexcitons by injection of free carriers and that the photocurrent is not dependent on the applied voltage. However, in general Eqs. (6.2, 6.3) allow for a non-linear recombination as well as photocurrent, provided the parameters are chosen such that the np-product in the off-diagonal coefficients of the matrix $\mathbf{M}$ starts to matter.

Figure 6.4b shows the short circuit current density J_{sc} as a function of extraction lifetime τ_{x} for the two quantum yields in Fig. 6.2 and for the case of no MEG. As expected, the short circuit current density J_{sc} decreases strongly, when the extraction lifetime becomes longer than the Auger lifetime.

Now, I want to briefly discuss the issue of finite mobilities of the free charge carriers. We presented a model [see Chapter 4], capable of calculating the radiative efficiency limits for pin-junction cells with finite mobilities based on the photon-recycling scheme developed in Ref. [33, 142]. If I assume that the extraction of carriers is very efficient, that photon recycling is only relevant for the monoexcitons and that the finding of ideal recombination currents and constant photocurrents from Fig. 6.4 is reasonable, the mobility dependent J/V-curves are calculated only requiring modifications of the generation rate according to Fig. 6.3. Figure 6.5a shows the J/V-curves as a function of electron and hole mobility $\mu_{\mathrm{n}} = \mu_{\mathrm{p}}$. In contrast to the change in extraction lifetime, the change in mobility instantaneously leads to losses in both fill factor and short circuit current density J_{sc}. Figure 6.5b shows the change in short circuit current density J_{sc} as a function of electron and hole mobility, again for the two versions of the quantum yield as in Fig. 6.4b and for the case without MEG.

6.5 Summary

We presented models to simulate the extraction of multiexcitons created by high energy photons from quantum dots. The two possible electronic bottlenecks are (i) the extraction of excitons from a dot on a time scale faster than the respective

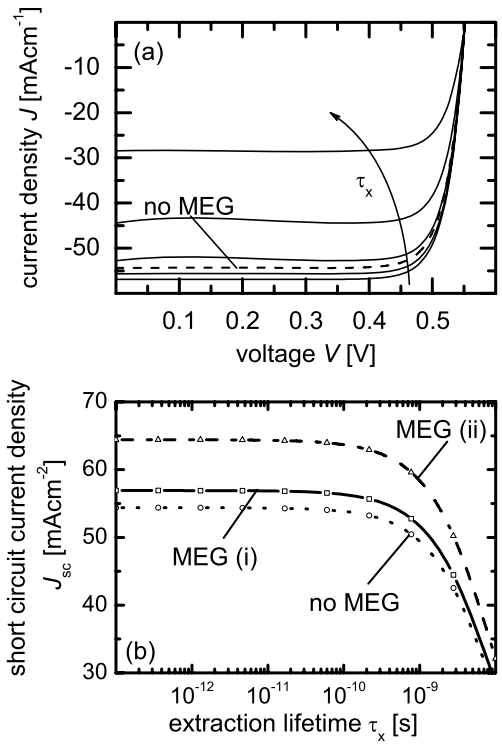

Fig. 6.4: *(a) Current/voltage-curves for the quantum yield version (i) for different values of the extraction lifetime ($\tau_x = 10^{-8}, 2.8\times10^{-9}$, 7.7×10^{-10}, 6.0×10^{-11}, 10^{-13} s) compared to the case without MEG. (b) Short circuit current density as a function of extraction lifetime for both versions of the quantum yield depicted in Fig. 6.2a ((i): solid line with open squares, (ii) dashed line with open triangles) and for the case without MEG (dotted line with open squares).*

radiative and non-radiative lifetime and (ii) the finite mobility of free carriers. We show how the short circuit current depends on both extraction lifetime and finite mobilities.

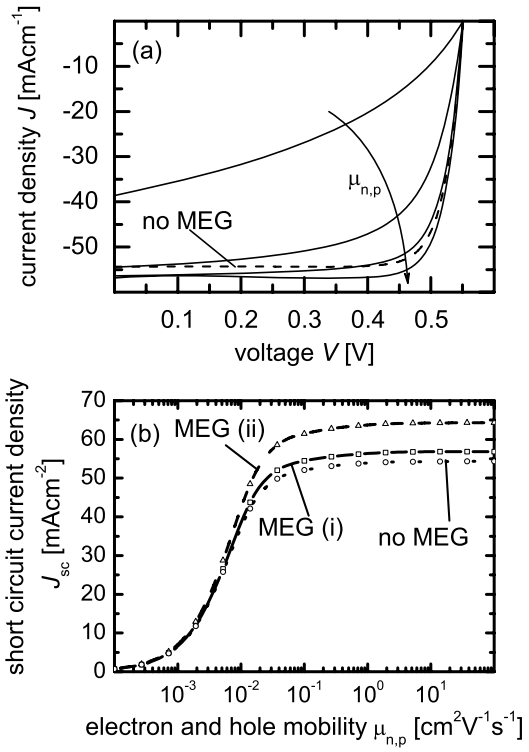

Fig. 6.5: *(a) Current/voltage-curves for the quantum yield version (i) for different values of the electron and hole mobility ($\mu_{n,p} = 10^{-2}, 10^{-1}, 100, 10^{3}\,\mathrm{cm}^2(\mathrm{V\,s})^{-1}$) compared to the case without MEG. (b) Short circuit current density as a function of electron and hole mobility for both versions of the quantum yield depicted in Fig. 6.2a ((i): solid line with open squares, (ii) dashed line with open triangles) and for the case without MEG (dotted line with open squares).*

Chapter 7

Experimental applications of the reciprocity relation

This chapter discusses the electroluminescence measurements of c-Si, Cu(In,Ga)Se_2 and GaInP/GaInAs/Ge triple-junction solar cells and shows how the interpretation of these measurements is simplified by the reciprocity relation introduced and discussed in the fundamentals chapter.

7.1 Introduction

In the fundamentals chapter 2, I introduced two optoelectronic reciprocity relations that connect the light absorbing with the light emitting situation in a solar cell. In chapters 3, 4 and 5, I discussed the validity range of the reciprocity relation between electroluminescence and photovoltaic quantum efficiency [Eq. (2.33)] in different types of solar cells. In the following, I will show how Eqs. (2.33) and (2.41) help to better interpret EL measurements used for solar cell characterization.

Depending on the material under investigation, EL can help to characterize different physical properties of a solar cell. I will start with the example of crystalline silicon, where the detection of optical and electronical properties, like the quality of the back side reflector or the effective diffusion length, is of major interest. I start with the description of the spectrally resolved EL before I proceed to the even more relevant case of spatially resolved EL.

Electroluminescence imaging has become an important topic for characterisa-

tion of solar cells and modules in the last years. This is mostly due to the fact that it is a fast spatially resolved method that is in addition cheap and easy to implement. The necessary prerequisites are merely a silicon CCD camera, with a PC for data processing and a protection agains ambient light to ensure a low noise level of the picture. The time needed for one image varies from milliseconds to few minutes depending on the applied current and the quality of the cell. Similar methods that provide a comparable amount of information like the LBIC (light beam induced current) method need to scan the sample and thus take several hours.

The major advantage of EL is at the same time its major drawback. It is sensitive to a large variety of different influences. That means that when something is wrong in the device, it will most likely show up as a dark spot in the EL image. However, when something dark shows up in the EL image, you will most likely not know for sure what it is. Sound interpretation of EL image is thus both challenging and of high importance. The main drawback of spatially resolved EL imaging is the fact that for every pixel the information is a scalar, where no spectral information is contained. Thus, I present simulations showing how to add the spectral component to EL imaging and how to interpret the images easily. The crystalline silicon chapter ends with a short section, dedicated to the question of Si based LEDs [57, 143–147] and how their performance relates to the open circuit voltage.

In the case of Cu(In,Ga)Se_2 solar cells, I discuss the EL as a function of the photon energy and the sample temperature but neglect the issue of spatial information. I focus on the different radiative recombination paths in the solar cell and how they evolve over temperature. In addition, I quantify the amount of band gap inhomogeneity inside highly efficient Cu(In,Ga)Se_2 solar cells from the electroluminescence in several ways. The main tendency is a rather low amount of band gap inhomogeneities that could be explained with the intentional band gap grading alone.

The last device, I characterize with EL, is a III/V-based multijunction solar cell on Ge substrate. For multijunction cells, the main advantage of EL is the access to information about individual subcells. I analyze electroluminescence spectra of a GaInP/GaInAs/Ge triple-junction solar cell at different injection currents. Using again the reciprocity theorem between electroluminescent emission and external quantum efficiency [Eq. (2.33)] allows me to derive the current/voltage curves and

the diode quality factors of all individual subcells.

7.2 Crystalline Silicon

In terms of internal quantum efficiency Q_i and front side reflectance R_f, Eq. (2.33) reads as

$$\phi_\mathrm{em}(\mathbf{r}_\mathrm{s}, E) = [1 - R_\mathrm{f}(\mathbf{r}_\mathrm{s}, E)]Q_\mathrm{i}(\mathbf{r}_\mathrm{s}, E)\phi_\mathrm{bb}(E)\left[\exp\left(\frac{qV(\mathbf{r}_\mathrm{s})}{kT}\right) - 1\right], \tag{7.1}$$

where $\mathbf{r}_\mathrm{s} = (x, y)$ is the spatial coordinate on the surface of the device. It is important to note that in Eq. (7.1) the dependence of $\phi_\mathrm{em}(\mathbf{r}_\mathrm{s}, E)$ on the coordinate $\mathbf{r}_\mathrm{s}$ shows up in (i) the reflectance R_f, (ii) in the local internal quantum efficiency $Q_\mathrm{i}(\mathbf{r}_\mathrm{s}, E)$, and (iii) in the local junction voltage $V(\mathbf{r}_\mathrm{s})$ that might be different at different coordinates along the junction area. Thus, the three different terms in Eq. (2.33) correspond to the classical loss mechanisms in solar cells: (i) optical losses, (ii) recombination losses, and (iii) resistive losses [148].

In the following, I will discuss mainly optical losses and recombination losses and show how to derive them from both spectrally as well as spatially resolved EL measurements.

7.2.1 Spectrally resolved EL

In order to measure the EL of mono-crystalline silicon solar cells a liquid nitrogen cooled Ge-detector attached to a single stage monochromator is used. A function generator applies a rectangularly shaped voltage to the sample and amplifies the signal of the Ge-detector with lock-in technique.

Figure 7.1 shows the detected room temperature EL (filled circles) of a textured sample in arbitrary units. By applying Eq. (2.33), I determine the external quantum efficiency $Q_\mathrm{e,EL}$ (filled triangles) from the EL spectrum (in arbitrary units). A calibrated quantum efficiency measurement (open squares) allows to adjust the $Q_\mathrm{e,EL}$ in the overlap region. Combining two totally different measurements, I finally receive a quantum efficiency spanning nine orders of magnitude and revealing a good agreement of both measurements in the overlap region.

In principle it is possible to extract parameters like the effective diffusion length from the EL measurement, as it is a standard procedure for quantum efficiency

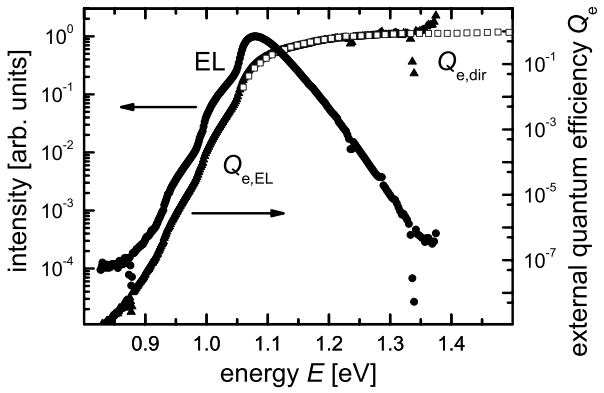

Fig. 7.1: *Electroluminescence spectrum, external quantum efficiency calculated from the EL spectrum, and directly measured quantum efficiency as a function of the photon energy. The quantum efficiency $Q_{e,EL}$ from EL is scaled to the directly measured $Q_{e,dir}$. The increased signal of the EL for energies $E > 1.35\,\mathrm{eV}$ is due to stray light.*

measurements. The interesting spectral region, however, covers penetration depths $d_e << L_\alpha < d/4$, where d is the cell thickness and d_e the emitter thickness. For cell thicknesses $d = 250\,\mu\mathrm{m}$ this inequality corresponds approximately to an energy range 1.31 eV $< E <$ 1.59 eV, where luminescence emission is already much lower than it is at the peak. Stray light does not allow correctly evaluating the EL spectrum with our setup, as can be seen by in Fig. 7.1 featuring an additional signal due to stray light starting at around 1.35 eV. Future investigations using a double stage monochromator will allow more detailed investigation of the high energy part of the spectrum, due to enhanced stray light suppression.

In contrast to electronic properties of the device, which affect mainly the high energy part of the spectrum, the optical properties of the device are visible in the low energy regime. Thus, EL spectra nicely reveal the effect of increased light trapping, usually caused in crystalline silicon cells by textured front surfaces and highly reflective back surfaces. In order to quantify the quality of light trapping in our samples with EL, we need a useful mathematical description for the low energy

part of the quantum efficiency. For low absorption coefficients, the exponential decay of the light intensity due to Lambert-Beer's law becomes smaller, leading to a nearly constant photon flux at these low photon energies everywhere in the device. Thus, for weakly absorbed light the generation rate is homogeneous over the depth of the device, and the external quantum efficiency becomes

$$Q_\mathrm{e} = (1 - R_\mathrm{f})\alpha k_\mathrm{eff} \int_0^d f_\mathrm{c}\,(x)\,dx = (1 - R_\mathrm{f})\alpha k_\mathrm{eff} d\overline{f}_\mathrm{c} \tag{7.2}$$

and, thus, proportional to the absorption coefficient α times an effective pathlength enhancement factor k_eff. The pathlength enhancement k_eff describes the path weakly absorbed light travels in the cell before it leaves the cell as a multiple of the cell thickness. Summarized in the quantity k_eff are the properties of the front texture, which diffracts light into oblique angles, and the quality of the back reflector. In Eq. (7.2), R_f denotes the reflectance at the front surface, while $f_\mathrm{c}(x)$ is the collection efficiency of photogenerated carriers.

Since photogeneration is homogeneous for low absorption coefficients as discussed above, I use the average collection efficiency

$$\begin{aligned} \overline{f_\mathrm{c}} &= \frac{1}{d}\int_0^d f_\mathrm{c}\,(x)\,dx \\ &= \frac{L}{d}\frac{S\,(\cosh\,(d/L) - 1) + D/L\sinh(d/L)}{S\sinh(d/L) + D/L\cosh(d/L)}. \end{aligned} \tag{7.3}$$

The second equality follows from the dark carrier distribution, which equals the collection efficiency in pn-junction solar cells according to the Donolato's theorem [34]. The average collection efficiency depends on the bulk diffusion length L, the diffusion coefficient D and the back surface rembination velocity S. From Eq. (7.2) now follows the pathlength enhancement as

$$k_\mathrm{eff} = \lim_{\alpha\to 0} \frac{Q_\mathrm{e}}{\alpha d\overline{f}_\mathrm{c}\,(1 - R_\mathrm{f})} \tag{7.4}$$

Figure 7.2 shows the result of plotting $k_\mathrm{eff} = Q_\mathrm{e}/\alpha d\overline{f}_\mathrm{c}\,(1 - R_\mathrm{f})$ as a function of the absorption coefficient. The collection efficiency used for these results was calculated assuming a high diffusion length $L = 2\,\mathrm{mm}$ appropriate for these monocrystalline floatzone cells, a surface recombination velocity of $S = 100\,\mathrm{cm/\,s}$ and an electron

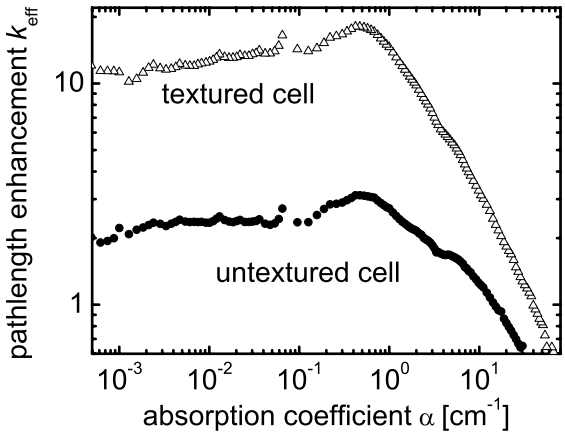

Fig. 7.2: *Pathlength enhancement factor k_{eff} as a function of the absorption coefficient for two different samples, one with a random texture and one without texture.*

diffusion constant $D = 27\,\mathrm{cm}^2/\mathrm{s}$ (corresponding to a doping concentration $N_\mathrm{A} = 10^{16}\,\mathrm{cm}^{-3}$). The values for the collection efficiency are then $\overline{f_\mathrm{c}} = 0.90$ for the $550\,\mu$m thick untextured cell and $\overline{f_\mathrm{c}} = 0.95$ for the $250\,\mu$m thick textured cell. Note that according to the definition in Eq. (7.4), the pathlength enhancement in Fig. 7.1 has to be taken for small absorption coefficients, where it saturates. For high absorption coefficients, the light is absorbed before it reaches the back side of the absorber and thus, the influence of light trapping on the spectrum vanishes and the value of $k_\mathrm{eff} = Q_\mathrm{e}/\alpha d\overline{f}_\mathrm{c}\,(1 - R_\mathrm{f})$ is below unity.

I display the results of a textured and an untextured mono-crystalline solar cell for comparison of the effect of a random pyramids obtained by a KOH etching. The textured cell with random pyramids has a pathlength enhancement of roughly 12, while the nominally flat solar cell has a pathlength enhancement of around 2. Although the effect of the texture is clearly visible, the resulting value of 12 is still much lower than the maximum possible value of $k_\mathrm{eff} = 4n^2 \approx 50$ [140], where $n \approx 3.5$ is the refractive index of silicon.

Note that the pathlength enhancement as defined in Eq. (7.4) is not necessarily

a good measure for the increase of the photocurrent. As shown by Brendel [149], not only a high *average* pathlength is important for increased photocurrent but also the distribution of pathlengths. The present method only quantifies the average path length as shown in Fig. 3.

7.2.2 Spatially resolved EL

Since solar cells are thin ($\approx 200\,\mu$m for wafer based silicon) but large area devices, spatial inhomogeneities and their characterization are of high importance for photovoltaics. The simplest approach to spatially resolved measurements is to measure the quantum efficiency two-dimensionally. However, recording the spectrum for each point on a cell would be extremely time-consuming. Thus, a common method, the so called Light Beam Induced Current (LBIC) measurement, uses only a few different laser diodes or light emitting diodes. These nearly monochromatic light sources induce a certain short circuit current which is measured while scanning the cell with the light spot. In the following, this LBIC measurement will be compared to electroluminescence imaging.

Figure 7.3a shows an LBIC scan (10 mm × 10 mm) of a monocrystalline silicon solar cell with a step size of 50 μm and with an LED with $\lambda \approx 950\,$nm used as the light source. The LBIC scan clearly reveals a horizontal band with a lower LBIC signal. This feature stems from the Al being directly in contact with the silicon base while the rest of the back surface is passivated with thermally grown SiO_2. The contacts through the SiO_2 are realized through lithographically defined point contacts, which are also visible in the LBIC scan as small spots with decreased signal. This sample has the advantage of providing macroscopic regions of different back surface recombination velocity on the same cell. Those parts of the cell, where the back surface of the absorber is in direct contact with the metal, have a rather high surface recombination velocity and thus a decreased quantum efficiency and EL, while the parts passivated with SiO_2 have a lower surface recombination velocity and thus an increased quantum efficiency and thus also an increased LBIC signal. In the following, we will refer to the regions, where the metal is in direct contact with the absorber as the "unpassivated regions" (the point contacts and the dark horizontal band in Fig. 7.3), and we will refer to the parts of the absorber, where

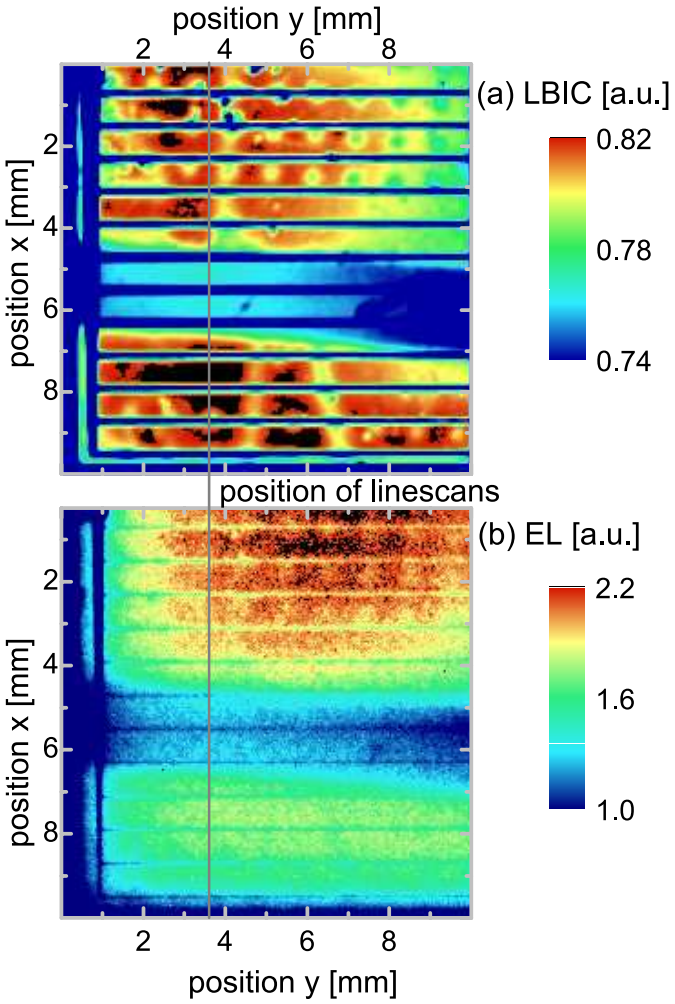

Fig. 7.3: *Comparison of (a) an LBIC scan (excitation wavelength $\lambda = 950\,\mathrm{nm}$) and (b) EL image of one part of a monocrystalline silicon solar cell with different back surfaces. The dark horizontal band in both images stems from an unpassivated metal surface, while the rest of the back is passivated with a SiO_2 layer with small point contacts. The y-position, which is later used for the linescans in Fig. 7.5, is indicated by a vertical line.*

the Si is in contact with the SiO_2 layer, as the passivated region.

Figure 7.3b shows the corresponding EL image of the same region on the solar cell. The image was taken with an injection current $J_{\mathrm{inj}} = 7.5\,\mathrm{mA\,cm^{-2}}$ and an integration time of 300 s. Qualitatively, the image looks similar to the LBIC image. However, superimposed to the intensity variation between the passivated and unpassivated regions due to different surface recombination is an intensity variation depending on the distance to the contact located in the upper left corner of the image. This additonal feature arises because the internal voltage decreases with increasing distance from the contacts due to resistive voltage losses of the emitter and gridfingers.

In order to explain, in which way both images depend quantitatively on the local solar cell quantum efficiency $Q_{\mathrm{e}}(\mathbf{r}_{\mathrm{s}})$, I perform a series of quantum efficiency measurements at different positions close to the transition region between passivated and unpassivated back side. Theoretically, the quantum efficiency $Q_{\mathrm{e}}(\mathbf{r}_{\mathrm{s}}, \lambda \approx 950\,\mathrm{nm})$ should be proportional to the LBIC intensity values I_{LBIC}, i.e.

$$I_{\mathrm{LBIC}}(E, \mathbf{r}_{\mathrm{s}}) \propto Q_{\mathrm{e}}(E, \mathbf{r}_{\mathrm{s}}) \tag{7.5}$$

Since the LBIC measurement setup has no absolute calibration, I have to use the proportionality sign in Eq. (7.5), while for a calibrated setup $I_{\mathrm{LBIC}}(E, \mathbf{r}_{\mathrm{s}}) = Q_{\mathrm{e}}(E, \mathbf{r}_{\mathrm{s}})$. For the EL measurement, the photon flux emitted by the solar cell is given by Eq. (7.1), while the spectrally resolved intensity ϕ_{cam} of the camera signal is then

$$\phi_{\mathrm{cam}}(E, \mathbf{r}_{\mathrm{s}}) \propto Q_{\mathrm{e}}(E, \mathbf{r}_{\mathrm{s}}) \phi_{\mathrm{bb}}(E) Q_{\mathrm{cam}}(E) \tag{7.6}$$

where Q_{cam} is the quantum efficiency of the camera. The EL image as shown in Fig. 7.3b is a scalar value for each pixel. The intensity of the camera signal Φ_{cam} follows from Eq. (7.6) via integration over energy, i.e.

$$\Phi_{\mathrm{cam}}(E, \mathbf{r}_{\mathrm{s}}) = \int \phi_{\mathrm{cam}}(E, \mathbf{r}_{\mathrm{s}}) dE \tag{7.7}$$

Figure 7.4 shows the result of performing the operation in Eq. (7.6) on the two quantum efficiency spectra. The solid lines represent both, the external quantum efficiency Q_{e}, as well as the spectrally resolved EL signal $\phi_{\mathrm{cam}}(E)$ from the camera for the measurement on the passivated region, while the dashed lines represent the same

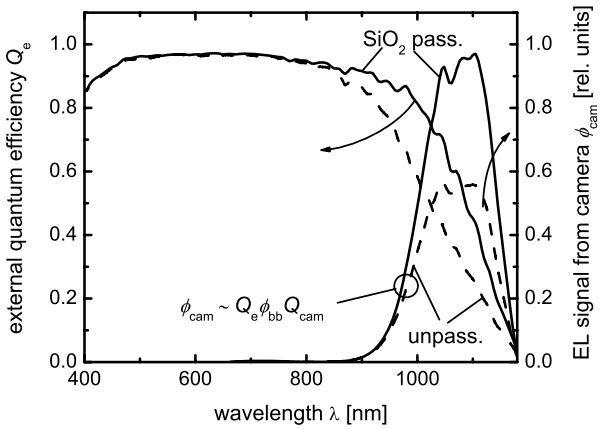

Fig. 7.4: *Quantum efficiency measured on the unpassivated region (the dark band in Fig 7.3; dashed lines) and on the passivated region (solid lines) and the resulting wavelength resolved intensity of the camera signal, calculated with Eq. (7.6) and normalized to the peak of the spectra on the passivated region.*

two quantities for the measurement on the unpassivated back side. The integral over the resulting curves for $\phi_{\mathrm{cam}}(E)$ then gives the camera signal $\Phi_{\mathrm{cam}}(E)$.

In order to check, whether the above stated proportionalities [Eqs. (7.5) and (7.6)] really hold in experiment, I evaluate line scans of the LBIC and the EL image in Fig. 7.3 and compare those with the quantum efficiencies $Q_{\mathrm{e}}(\lambda \approx 950\,\mathrm{nm})$ and the camera signals calculated from the quantum efficiency according to Eq. (7.6).

Figure 7.5a shows the comparison between the LBIC linescan and quantum efficiencies taken at different positions and with different spot sizes. I made three sets of measurements, where I varied the x-coordinate in each of the three cases in order to get quantum efficiency measurements on the passivated and unpassivated region. The three sets of measurements are distinguished by different symbols that indicate different positions on the sample (squares, triangles: $y \approx 5$ mm, circles $y \approx$ 10 mm) for which the Q_{e} measurements were made and different spot sizes (squares: 1 mm × 3 mm; circles, triangles: 2 mm × 5 mm). The qualitative agreement between LBIC and Q_{e} is quite good, although the contrast between the quantum

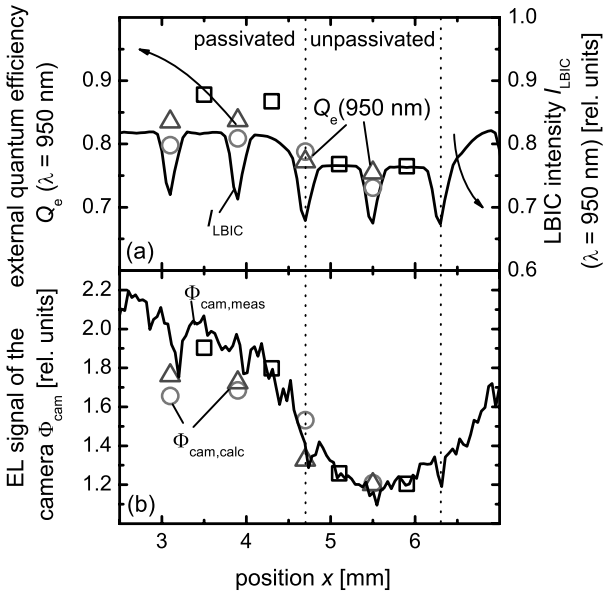

Fig. 7.5: *(a) Comparison of LBIC linescan of the image in Fig. 7.3a with quantum efficiencies taken at 950 nm. (b) Comparison of the linescan of the EL image in Fig. 7.3b with EL intensities calculated from quantum efficiency measurements as shown in Fig. 7.4. The y-position of both linescans is indicated by the vertical line in Fig. 7.3 ($y \approx 3.6\,\mathrm{mm}$). The quantum efficiencies are taken in different y-ranges (squares, triangles: $y \approx 5\,\mathrm{mm}$, circles $y \approx 10\,\mathrm{mm}$) and with different spot sizes (squares: $1\,\mathrm{mm} \times 3\,\mathrm{mm}$; circles, triangles: $2mm \times 5\,\mathrm{mm}$)*

efficiency measurements on the passivated and the unpassivated regions seems to be higher than that of the LBIC linescan. Reasons for this discrepancy are the fact that I approximated the LED spectrum by a single wavelength and compare that with only one point of quantum efficiency measurement. Thus, noise in the quantum efficiency date has a strong influence since no averaging is done here.

Figure 7.5b shows the EL linescan compared with the values calculated from the same quantum efficiencies as used for comparison with the LBIC. Now, we have to consider that there is a superposition of the effects of the quantum efficiency and

the internal voltage on the shape of the EL-linescan. Low values of x are equivalent to low distances from the contact, which is situated roughly at x = 0. Thus, for increasing x, the intensity of the EL signal goes down slightly even for constant Q_e. Considering this fact, Fig. 7.5b shows a quite good correspondence between the values $\Phi_{cam,calc}$ calculated according to the reciprocity relation between EL and quantum efficiency and the EL intensity $\Phi_{cam,meas}$ itself.

Thus, I have shown that the reciprocity relation [Eqs. (2.33, 7.1)] is not only of relevance for spectrally resolved EL measurements but also describes EL images very well. However, this finding does not immediately lead to a good method to quantify cell parameters in a spatially resolved way. Due to the intermixing of different influences in an EL image, quantitative interpretation of data and, thus, determination of more than one unknown, always requires an increase of the number of equations. This has been done to get access to the diffusion length [150] and to the series resistance [151], while the reciprocity helps us to better interpret the results [58, 59, 152].

7.2.3 Interpretation of EL images taken with filters

Theory

A quantitative interpretation of the spectral component of the EL emission requires an accurate model of all unknown spectral parts of Eq. (2.33). Since the black body spectrum

$$\phi_{bb}(E) = \frac{2\pi E^2/(h^3c^2)}{\exp(E/kT) - 1} \approx \frac{2\pi E^2}{h^3c^2} \exp\left\{\frac{-E}{kT}\right\} \tag{7.8}$$

is a known factor that depends basically on the photon energy, I only have to model the quantum efficiency and later multiply it by ϕ_{bb}. In Eq. (7.8), h is the Planck constant and c is the speed of light. To obtain the quantum efficiency, one can either use device simulators like ASA, AFORS-HET or PC1D, which have been developed for use with solar cells, or apply analytical equations, which is feasible in pn-junction solar cells under low level injection. In the following, I will discuss these analytical equations, which were also used for all our simulations.

Modeling the quantum efficiency requires knowledge of the generation of charge carriers in the device as well as knowledge of the collection of photogenerated carriers. It is useful to write the internal quantum efficiency Q_i as a function of generation

rate $g(x)$ and collection efficiency $f_c(x)$ as

$$Q_{\mathrm{i}}(E) = \int_0^d g(x)\, f_c(x)\, dx \tag{7.9}$$

where the generation rate $g(x)$ is defined normalized to the photon flux entering the cell; i.e. for the simplest case of flat surfaces and no back reflections $g(x) = \alpha \exp(-\alpha x)$.

Equation (2.33) is valid for the case of low level injection, where minorities can be clearly defined. The validity of Eq. (2.33) requires the validity of the Donolato theorem [34] relating the collection efficiency $f_c(x)$ of photogenerated carriers with the normalized dark carrier concentration. Thus, I obtain the collection efficiency from the solution of the diffusion equation for minorities in the dark as

$$f_{\mathrm{c}}(x) = \cosh(x/L) - \frac{L}{L_{\mathrm{eff}}} \sinh(x/L) \tag{7.10}$$

The calculation of the generation rate $g(x)$ depends on the optical properties of the device. For flat surfaces and multiple reflections at front and back surface, the generation rate is

$$g(x) = \frac{\alpha(1-R_{\mathrm{f}})\left(\mathrm{e}^{-\alpha x} + R_{\mathrm{b}}\mathrm{e}^{\alpha(x-2w)}\right)}{1 - R_{\mathrm{f}}R_{\mathrm{b}}\mathrm{e}^{-2\alpha d}} \tag{7.11}$$

For textured surfaces, the generation rate is either calculated with a ray tracing program or the texture is approximated with perfectly Lambertian surfaces. An analytical solution of the generation in a cell with a Lambertian front surface and a specular back surface follows from [142] as

$$g(x) = 2\alpha(1-R_{\mathrm{f}}) \frac{\left[Ei_2(\alpha x) + R_{\mathrm{b}} Ei_2(\alpha(2d-x))\right]}{1 - t_{\mathrm{cell}}(1 - t_{\mathrm{lamb}})} \tag{7.12}$$

with $t_{\mathrm{lamb}} = (1-R_{\mathrm{f}})/n^2$, where n is the index of refraction. Equation (7.12) uses the definition

$$t_{\mathrm{cell}} = R_{\mathrm{b}}\left(e^{-2\alpha d}(1-2\alpha d) + (2\alpha d)^2 Ei(2\alpha d)\right) \tag{7.13}$$

for the angle-integrated transmission of the cell from the front with one reflection at the back side to the front. For the definition of the functions Ei and Ei_2 see Eqs. (3.13) and (3.14). Note that the defintions in Eqs. (7.12) and (7.13) are equivalent to Eqs. (3.11) and (3.12) except for the consideration of back side reflectances $R_{\mathrm{b}} < 1$ in the present case.

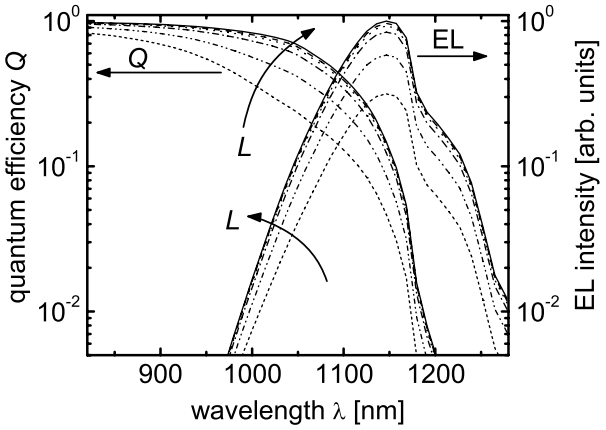

Fig. 7.6: *Simulation of quantum efficiency and electroluminescence versus wavelength for different values of the bulk diffusion length* $L = 50, 100, 200, 300, 400$*, and* $800\,\mu$m.

Results and discussion

As already mentioned, the spectral shape of the EL emission depends on both recombination in bulk and interfaces as well as the optical properties of the device. First, I will only concentrate on recombination and assume the optical properties to be known. In a second step, I will show how to distinguish between both optical and electrical properties. For all cases, I will concentrate on the following relevant parameters: bulk diffusion length L, surface recombination velocity S of the back side, reflection coefficient R_b of the back side and thickness d of the base, which is assumed to be identical to the total optical thickness. For simplicity, I assume for all simulations that the front side reflectance is zero for all wavelengths and, thus, do no longer distinguish between internal and external quantum efficiency. In the following, I will thus speak of the quantum efficiency $Q = Q_\mathrm{i} = Q_\mathrm{e}$. For interpretation of real measurements, the front side reflectance has to be measured separately and must be taken into account for simulations.

Figure 7.6 shows the simulated quantum efficiency and EL for different values

of the bulk diffusion length $L = 50$, 100, 200, 300, 400, and 800 μm, respectively. The other parameters used are $S = 1000\,\mathrm{cm\,s^{-1}}$, $d = 200\,\mu$m, $R_\mathrm{b} = 0.8$. The curves for the EL follow from the application of Eq. (2.33), i.e. the quantum efficiencies are first multiplied by the black body spectrum and then normalized to the peak for the highest diffusion length. We see a wavelength dependence of the influence the diffusion length has on both Q and EL. We also notice the dramatic decrease of EL intensity for the shorter wavelengths. For instance around 900 nm, where the quantum efficiency is usually evaluated to extract the effective diffusion length, the total intensity is around four orders of magnitude below the peak. Using the spectral information in the low wavelength regime will thus always have the downside of longer data acquisition times.

To access the spectral information with a camera, I have to use a limited number of filters and evaluate the contrast of measurements with and without a certain filter or combination of filters. I define the contrast C_s obtained from the ratio of two images taken with different step-function like short pass filters as

$$C_\mathrm{s}\left(E_\mathrm{cut,1} = \frac{hc}{\lambda_\mathrm{cut,1}}, E_\mathrm{cut,2} = \frac{hc}{\lambda_\mathrm{cut,2}}\right) = \frac{\int\limits_{hc/\lambda_\mathrm{cut,2}}^{\infty} \phi_\mathrm{em} Q_\mathrm{CCD} dE}{\int\limits_{hc/\lambda_\mathrm{cut,1}}^{\infty} \phi_\mathrm{em} Q_\mathrm{CCD} dE} \tag{7.14}$$

where Q_CCD is the sensitivity of the camera and $\lambda_\mathrm{cut,i}$ is the cut wavelength for the i^{th} filter.

Figure 7.7 shows how the information about the different diffusion lengths influences the contrast as defined in Eq. (7.14). Figure 7.7a depicts the EL spectra of the highest - $L = 800\,\mu$m - and lowest - $L = 50\,\mu$m - diffusion length from Fig. 7.6 but now normalized to their respective peaks. The spectrum for $L = 800\,\mu$m (solid line) has a steeper slope on the low wavelength side than the spectrum for $L = 50\,\mu$m (dashed lines). It is this difference in slope that I want to detect with a filter. The absolute difference between the curves with different diffusion lengths, which was depicted in Fig. 7.6, cannot be used, since it affects the absolute EL emission just like changes in voltage. In addition, Fig. 7.7a shows the camera sensitivity, which is (taken from Ref.) and extrapolated with an absorptance of flat crystalline silicon to have data also for longer wavelengths.

However, it is not the EL spectrum in Fig. 7.7a that determines the output

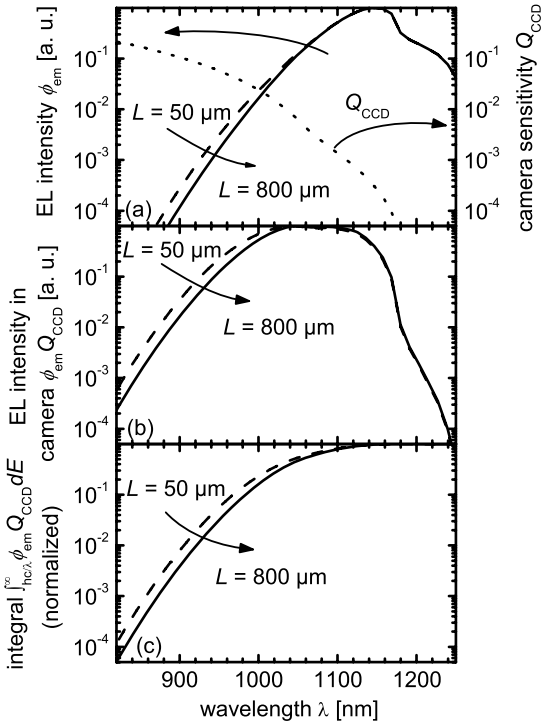

Fig. 7.7: *(a) EL spectra for the diffusion lengths $L = 50\,\mu$m (dashed line) and $L = 800\,\mu$m (solid line), both normalized to their respective peak. The relative difference in slope on the short wavelength side needs to be detected by the use of filters. Camera sensitivity as a function of wavelength (dotted line). (b) Multiplication of EL spectra with the camera sensitivity. (c) Integration of EL spectra in (b) from short wavelengths up to the cut wavelength of a filter as a function of this cut wavelength. The result is normalized to the integral over the total spectrum (without filter) and thus the normalized integral approaches unity for high wavelengths. The filter is assumed to have a step-function-like transmission (i.e. all wavelengths $\lambda = \lambda_{cut}$ pass the filter).*

of the camera, but instead the multiplication of the spectra in Fig. 7.7a with the camera sensitivity Q_{CCD} in the same figure. Figure 7.7b shows the result of this multiplication. Due to the decreased camera sensitivity for long wavelengths, the resulting spectra pronounce the short wavelength part stronger compared to the original spectra.

If I now introduce a short pass filter with cut wavelength λ_{cut}, the actual signal of the camera, will be the integral $\int_{hc/\lambda_{cut}}^{\infty} \phi_{\mathrm{em}} Q_{\mathrm{CCD}} dE$. Figure 7.7c shows this integral as a function of cut wavelength normalized to the integral over the whole spectrum from Fig. 7.7b. According to the definition of the contrast in Eq. (7.14), the curves in Fig. 7.7c are equivalent to the inverse contrast for the case where one short pass filter is used for the first image and the other image is taken without filters, i.e. for the case $C_{\mathrm{s}}(hc/\lambda_{\mathrm{cut,1}}, 0)$. Note here that the contrast is defined in a way that it is always larger than one and thus in the same way as in Ref. [150].

Figure 7.8a shows the contrast as a function of the cut wavelength $\lambda_{\mathrm{cut,1}}$ for the EL spectra in Fig. 7.6. The most obvious result of Fig. 7.8a is the steep increase of the absolute contrast for decreasing wavelength. This implies that the denominator of Eq. (7.14) becomes very small for short cut wavelengths and thus the signal to noise ratio for the filtered image becomes very low. However, I am not interested in the absolute contrast C_{s} but instead in the relative change in contrast induced by the change in diffusion length.

In order to better highlight these relative changes, I introduce the normalized contrast C_{sn}. Figure 7.8b shows C_{sn}, normalized to the absolute contrast of the cell with the highest diffusion length $L = 800$ mm. The normalized contrast is more sensitive to changes in diffusion length, when the cut wavelength gets shorter; i.e. a compromise must be made between signal to noise ratio and selectivity.

The right choice of the cut wavelength will depend on the signal to noise ratio and the tolerable duration of the measurement. A shorter measurement time with a filter with a higher cut wavelength will lead to less accuracy in the determination of the recombination parameters. Thus, I cannot give a general answer to the question for the perfect filter wavelength; however, I show how to estimate or simulate the effects, which may help to find the optimal filter for a given sample and setup.

Now, I will consider two unknowns, the bulk diffusion length and the back side reflection and assume a Lambertian generation profile. I choose a matrix of two bulk

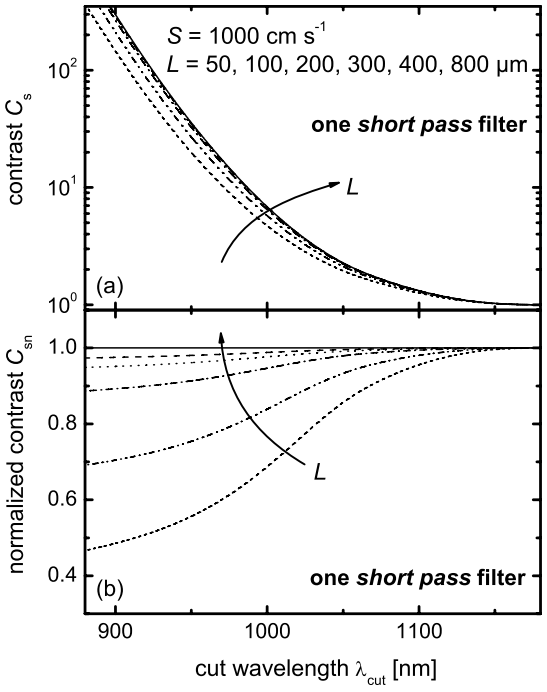

Fig. 7.8: *Simulation of (a) contrast and (b) normalized contrast of two images, where one is taken without filter and the other with a short pass filter with a cut wavelength λ_{cut}. The filter is assumed to have a step-function-like transmission (i.e. all wavelengths $\lambda = \lambda_{cut}$ pass the filter). Parameters are a diffusion length $L = 50$, $100, 200, 300, 400$, and $800\,\mu$m, a surface recombination velocity $S = 1000\,$cm/ s, a back reflectance $R_b = 0.8$ and a thickness $d = 200\,\mu$m.*

diffusion lengths $L = 200\,\mu$m and $L = 400\,\mu$m as well as two back side reflections $R_{\mathrm{b}} = 0.6$ and 0.8, while keeping $S = 1000\,\mathrm{cm\,s^{-1}}$ and the thickness $d = 200\,\mu$m constant. Figure 7.9a shows the corresponding situation for the normalized contrast with only one short pass filter. Figure 7.9a clearly reveals that it is challenging to distinguish between optics and recombination with only one filter.

This situation greatly improves if I follow the scheme of Ref. [150] and use a

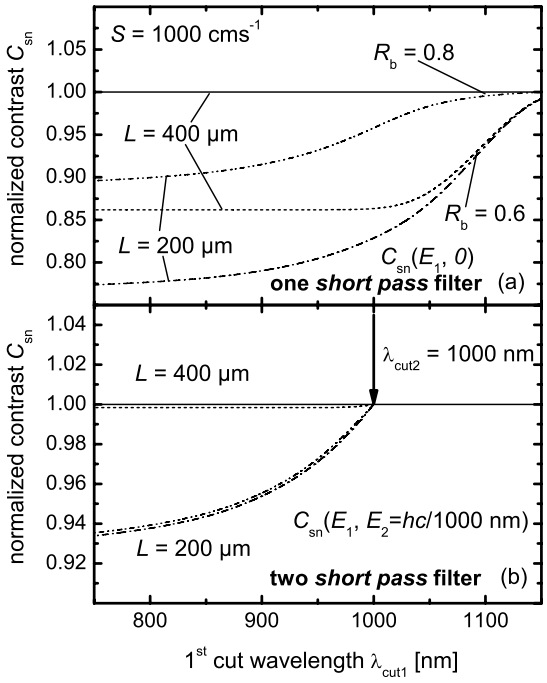

Fig. 7.9: *Normalized contrast for the case of variable diffusion length L and back side reflectance R_b for the case of (a) one short pass filter or (b) two short pass filters with the higher wavelength filter being used for both measurements. The effect of the second filter makes the result nearly independent of the back side reflectance. Parameters are a diffusion length $L = 200$ and $400\,\mu$m, a back reflectance $R_b = 0.6$ and 0.8, a surface recombination velocity $S = 1000\,$cm/ s and a thickness $d = 200\,\mu$m.*

second short pass filter around 1000 nm for the measurement that was done without filter before. Figure 7.9b shows this situation for a variable value of the first cut wavelength, keeping the cut wavelength of the second filter constant at 1000 nm. The effect of the different back side reflections vanishes. However, the selectivity -i.e. the change in normalized contrast between two diffusion lengths - decreases

considerably with the introduction of the second filter.

Thus, I again have the need to make a compromise in choosing the second filter. The cut wavelength should be high enough for a good contrast and low enough for a sufficient suppression of light trapping effects. The value $\lambda_{\mathrm{cut}} = 1000\,\mathrm{nm}$, which is chosen here, corresponds to a penetration depth L_α roughly 1.3 times the cell thickness d. Simulations with other cell thicknesses and reflection coefficients R_{b} showed that a value of $L_\alpha/d = 1$ to 1.5 is quite reasonable for a wide range of thicknesses and nearly independent of the value of R_{b}.

Since I am able to simulate the EL emission for all wavelengths, I also try to exploit any information about light trapping, contained in the spectrum. For this purpose, it is helpful to choose long pass filters, instead of short pass filters. I define the contrast C_{l} obtained from the ratio of two images, where one is taken with a long pass filter as

$$C_{\mathrm{l}}\left(E_{\mathrm{cut}} = \frac{hc}{\lambda_{\mathrm{cut,1}}}\right) = \frac{\int_0^\infty \phi_{\mathrm{em}} Q_{\mathrm{CCD}} dE}{\int_0^{hc/\lambda_{\mathrm{cut}}} \phi_{\mathrm{em}} Q_{\mathrm{CCD}} dE} \tag{7.15}$$

where λ_{cut} is the cut wavelength for the long pass filter.

How does the contrast C_{l} give information about the light trapping? To answer this question, I again go step by step from the spectra to the contrast. Figure 7.10a shows EL spectra for two back reflectances $R_{\mathrm{b}} = 0.6$ (dashed line) and $R_{\mathrm{b}} = 0.8$ (solid line). The other parameters are $L = 400\,\mu\mathrm{m}$, $S = 1000\,\mathrm{cm\,s^{-1}}$ and the thickness $d = 200\,\mu\mathrm{m}$. In contrast to Fig. 7.7a the spectra are now not normalized to the peak. Multiplication of the spectra in Fig. 7.10a with the camera sensitivity in Fig. 7.10a gives the spectra in Fig. 7.10b that control the camera signal. It is obvious that the difference between the two spectra with difference back side reflectances affects the spectra on their high wavelength sides. Thus, in order to detect these differences with a filter, I need to choose filters with higher wavelengths and inverse behaviour, i.e. long pass filters.

Figure 7.10c shows the result of solving the integral $\int_0^{hc/\lambda_{\mathrm{cut}}} \phi_{\mathrm{em}} Q_{\mathrm{LED}} dE$ as a function of λ_{cut} and normalizing it to the integral over the whole spectrum. It is obvious that the differences between the spectra in Fig. 7.10b are still visible after the integration carried out by the camera pixels if a long pass filter with cut

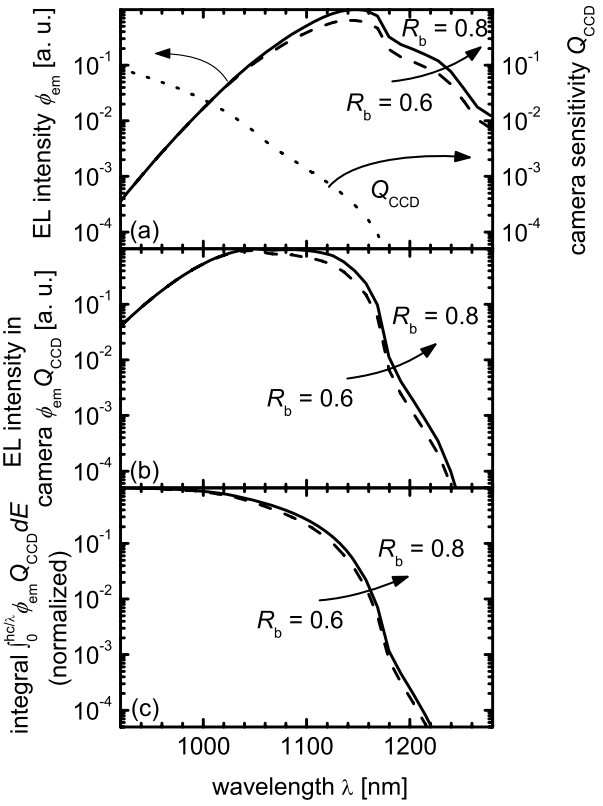

Fig. 7.10: *(a) EL spectra for two back reflectances $R_b = 0.6$ (dashed line) and $R_b = 0.8$ (solid line). The other parameters are $L = 400\,\mu$m, $S = 1000\,$cm/s and the thickness $d = 200\,\mu$m. In contrast to Fig. 7.7a the spectra are now not normalized to the peak. (b) Multiplication of the spectra in (a) with the camera sensitivity in (a). (c) Result of solving the integral $\int_0^{hc/\lambda_{\rm cut}} \phi_{\rm em} Q_{\rm CCD} dE$ as a function of λ_{cut} and normalizing it to the integral over the whole spectrum.*

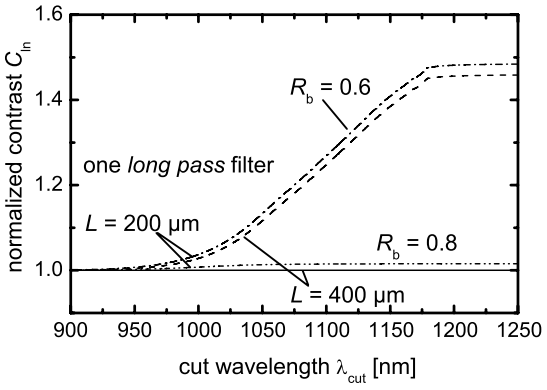

Fig. 7.11: *Normalized contrast for the case of a long pass filter with varying cut wavelength. In this case, different values of the back surface reflectance R_b lead to a pronounced contrast for cut wavelengths $\lambda_{cut} > 1150\,\mathrm{nm}$ whereas different values of the effective diffusion length L_{eff} have no influence.*

wavelengths above 1000 nm is used. The inverse of the spectra in Fig. 7.10c gives the contrast C_1 (not shown) and from that the normalized contrast follows in the same way as for short pass filters.

Figure 7.11 shows this normalized contrast for the four parameter combinations also used in Fig. 7.9: $R_b = 0.6$ and 0.8 and $L = 200\,\mu\mathrm{m}$ and $400\,\mu\mathrm{m}$. Since I have defined the contrast in a way that it is always larger than one, the curve with high R_b and L is now at the bottom and a decreasing quality of light trapping, i.e. a smaller R_b, leads to higher absolute contrast. The difference between $R_b = 0.6$ and 0.8 becomes pronounced already at cut wavelengths $\lambda_{cut} = 1050\,\mathrm{nm}$, which is around the typical peak position in detected emission of Si CCD cameras. Thus, the evaluation of light trapping will not require long data acquisition times.

Up to now, I only considered variations of the bulk diffusion length and back side reflection. However, as for the quantum efficiency, the effects of surface and bulk recombination are closely intermixed. Thus, Fig. 7.12 shows the meaning of the absolute contrast for the example of one short pass filter with the cut wavelength $\lambda_{cut} = 900\,\mathrm{nm}$ in terms of possible combinations of surface recombination velocity S

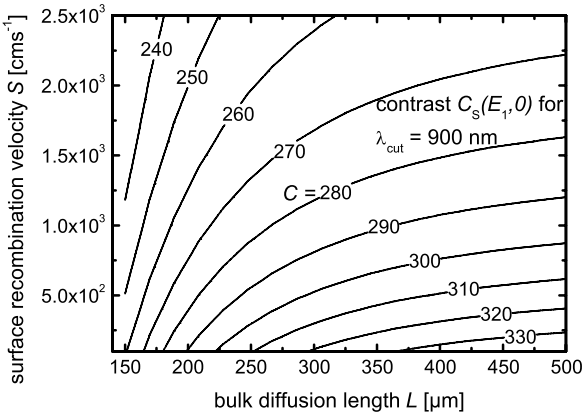

Fig. 7.12: *Possible combinations of surface recombination velocity S and diffusion length L that lead to a certain contrast when applying a short pass filter with a cut wavelength $\lambda_{cut} = 900\,\mathrm{nm}$.*

and bulk diffusion length L leading to the same contrast value. It is obvious that rather large variations of both S and L are possible. Only for high quality bulk material ($L >> d$), S is determined accurately.

The question remains, whether a combination of measurements can help us to distinguish between recombination in the bulk and at the surface. For quantum efficiency measurements this is possible, when comparing the first and second linear regime in the plot of inverse internal quantum efficiency versus penetration depth [153, 154]. The first linear regime gives information about L_{eff} defined by

$$L_{\mathrm{eff}} = L\frac{S\sinh(d/L) + D/L\cosh(d/L)}{S\cosh(d/L) + D/L\sinh(d/L)} \tag{7.16}$$

while the spectral region for longer absorption lengths depends on the average collection probability (cf. Eq. (7.3))

$$\overline{f_{\mathrm{c}}} = \frac{1}{d}\int_0^d f_{\mathrm{c}}(x)\,dx = \frac{L}{d}\frac{S\left(\cosh(d/L) - 1\right) + D/L\sinh(d/L)}{S\sinh(d/L) + D/L\cosh(d/L)} \tag{7.17}$$

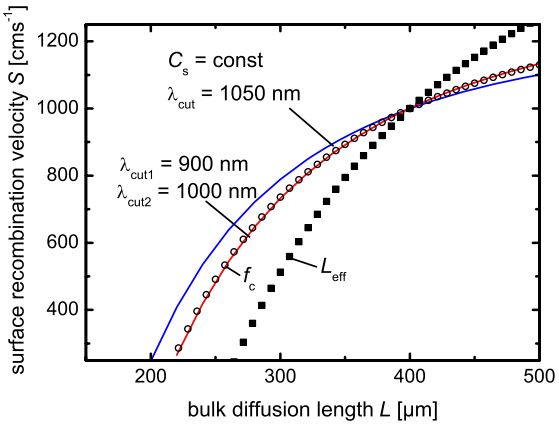

Fig. 7.13: *Lines of equal L_{eff} and $\overline{f_c}$ for the case of $L = 400\,\mu$m and $S = 1000\,$cm/ s as well as two lines of equal contrast for two different combinations of short pass filters. Independent determination of S and L is more difficult with EL than with quantum efficiency measurements since the angle between the curves with different filters is much smaller than the one between L_{eff} and $\overline{f_c}$.*

For high absorption lengths, the photogeneration becomes uniform and the collection probability of the generated charge carriers independent of thickness. The two different combinations of S and L as defined by Eqs. (7.16) and (7.17) allow to distinguish S and L if both L_{eff} and $\overline{f_c}$ have an intersection in the (S, L)-plane. A similar approach is in principle possible, combining the EL measured with different filters with each other.

Figure 7.13 shows both the intersection of L_{eff} and $\overline{f_c}$ and of the EL with two different combinations of short pass filters. For the chosen parameter combination $S = 1000\,\text{cm}\,\text{s}^{-1}$ and $L = 400\,\mu\text{m} = 2d$, it is difficult to find two filter-combinations that do not lead to nearly parallel curves. Although the intersection is clearly visible in the simulation, for experimental purposes the curves are probably not linearly independent enough. Both EL curves resemble the case for $\overline{f_c}$. Thus the approach of Bothe et al. [155] to use light beam induced current (LBIC) measurements for getting

local values for L_{eff} will lead to clearer results, if the injection level dependence of recombination is not too strong.

7.2.4 Absolute EL emission and the LED quantum efficiency

The reciprocity theorem, Eq. (2.33), does not only contain information about photovoltaic properties, following from the emission, but also information about the quality of a solar cell if operated as LED. The reciprocity theorem constitutes a connection between EL emission and the short circuit situation of a solar cell. This leads to a more general question that was already mentioned in chapter 2.4: Is a good solar cell necessarily a good LED? Green et al. [156] showed that the same device geometry gives both the highest efficiency solar cells and the best silicon LEDs. Of course, the long radiative lifetimes of the indirect semiconductor silicon are a severe problem for the application as light source but no obstacle for photovoltaic use. However, as the quantum efficiency and thus the short circuit situation gives information about the EL spectrum, the open circuit situation is linked to the absolute intensity of the emitted light. I quantify the latter by the LED quantum efficiency as defined by Eq. (2.42) i.e. the ratio of radiative J_{rad} to total - i.e. radiative and non-radiative - recombination currents $J_{\text{nr}} + J_{\text{rad}}$. The link between the LED quantum efficiency and the open circuit voltage of a solar cell has already been introduced in Eq. (2.41). The link between the radiative saturation current density $J_{0,\text{rad}}$ and the solar cell quantum efficiency directly results from the spectral reciprocity, Eq. (2.33), if one considers that the radiative recombination current must equal - as a particle current - the emission of light from the solar cell under applied bias, i.e. $J_{0,\text{rad}}/q = \phi_{\text{em}}/(\exp(qV/kT) - 1)$ (see also Eq. (2.38)).

To predict the LED performance from solar cell properties, I need the actual and the radiative open circuit voltage. For high quality silicon solar cells, the pathlength enhancement is the most important factor determining the quantum efficiency around the band gap and thus the radiative recombination current density and the radiative open circuit voltage. I therefore approximate the solar cell quantum efficiency by the absorptance [68, 157]

$$a(E) = \frac{1}{1 + \frac{1}{\alpha k_{\text{eff}} d}} \tag{7.18}$$

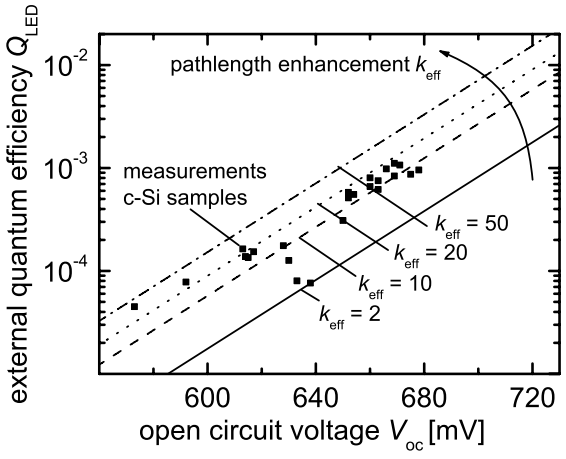

Fig. 7.14: *External LED quantum efficiency as a function of the open circuit voltage. The measurements (squares) of randomly textured mono-crystalline silicon solar cells are compared with the predictions (lines) for different pathlength enhancement factors k_{eff}. Most of the devices with higher V_{oc} show agree with the theoretical prediction when pathlength enhancement factors $10 < k_{eff} < 20$ are assumed, which is agreement with the finding of Fig. 7.2 where the shown randomly textured device had a $k_{eff} \approx 13$.*

using an approximation for textured surfaces. Inserting the absorptance given by Eq. (7.18) instead of the solar cell quantum efficiency into Eq. (2.40) leads to a radiative open circuit voltage as a function of the light trapping properties. Subsequently, I measure both open circuit voltages and LED quantum efficiencies of several textured mono-crystalline solar cells and compare them to the predictions for different pathlength enhancement factors.

Figure 7.14 shows the relation between experiment and theory. The high quality samples are all within the typical range of $k_{\text{eff}} = 10$ to 20 that corresponds to our investigations with the EL spectra. Some of the lower quality samples seem to have even better light trapping. However, this effect is caused by strongly decreased quantum efficiencies, implying that our initial assumption $Q_{\text{e}}(E) = a(E)$ is no longer

valid. Overestimations of the solar cell quantum efficiencies thus lead to underestimations of the radiative open circuit voltages and consequently to overestimations of the LED quantum efficiencies.

Figure 7.14 also shows, which LED quantum efficiencies can be reached with solar cell technology. The crystalline silicon solar cells with the highest open circuit voltages $V_{\mathrm{oc}} = 712\,\mathrm{mV}$ [158] are the HIT cells from Sanyo. According to the calculations in Fig. 7.14, solar cells with such a V_{oc} and a perfect light trapping scheme approaching the Yablonovitch limit of $k_{\mathrm{eff}} = 4n^2 \approx 50$ have the potential to reach a quantum efficiency of $Q_{\mathrm{LED}} = 1.3\%$.

7.3 Cu(In,Ga)Se$_2$

7.3.1 Introduction

Solar cells made from the quaternary alloy Cu(In,Ga)Se$_2$ have achieved efficiencies $\eta > 19\%$ [159]; i. e. more than any other thin film approach despite of the polycrystallinity of the material. One commonly used characterization tool for photovoltaic absorber materials is the analysis of the photoluminescence, e. g., for the study of defect related properties. Photoluminescence measurements are mostly performed as a function of the position on the sample, i.e. spatially resolved [160–163], or as a function of the energy of the emitted photons [162–170]. Photoluminescence allows characterizing deposited films as well as completed solar cells in a contactless manner. Bauer et al. [164] even showed how to extract the maximum attainable open circuit voltage from absolute photoluminescence measurements. The electroluminescence (EL) of CuInSe$_2$ has been subject to fundamental studies in the 1970s [167, 171–173], where the material was considered for application as emitter and detector in optical communication.

However, as shown for crystalline silicon before, EL measurements are a valuable tool also for solar cell characterization. The experimental part starts with discussion of EL-spectra recorded in the temperature range $100\,\mathrm{K} < T < 300\,\mathrm{K}$. They help to investigate, how the dominant radiative recombination path changes over temperature. Injection level dependent measurements allow to identify the character of the peaks in the spectrum. In a second step, I show that the temperature

dependence of the band to band peaks reveals information about the inhomogeneity of the band gap. These inhomogeneities are partly due to an intentional grading of the band gap versus depth, aiming at a better carrier collection, and partly due to lateral changes in the Ga-content which strongly influence the local band gap. Mattheis et al. [174] have developed a theory, describing the influence of a Gaussian distribution of band gaps on the emission spectrum. I show that with small refinements to this theory, the standard deviation σ_{g} of the band gap inhomogeneities follows from the electroluminescence spectra. The extracted values are low, i.e. in the range of $15\,\mathrm{meV} < \sigma_{\mathrm{g}} < 27\,\mathrm{meV}$. These values are comparable to those expected from band gap gradings [174], which indicates that the lateral inhomogeneity might actually be rather low in these high-efficiency devices. In a third step, I apply the reciprocity theorem between electroluminescent emission and quantum efficiency of a solar cell [35] to the room temperature measurements. I define an experimental, radiative open circuit voltage, considering the actual radiative recombination current - as measured with electroluminescence - and compare it to both, the actual open circuit voltage as well as the ideal, Shockley-Queisser (SQ) open circuit voltage [30]. The difference between the SQ-limit and the radiative open circuit voltage is the loss due to a broadened band edge [175], while the difference between the radiative and actually measured open circuit voltage gives information on the light emitting diode (LED) quantum efficiency. I show how to connect the LED quantum efficiency with the open circuit voltage of the solar cell. It turns out that the Cu(In,Ga)Se_2 solar cells have LED quantum efficiencies approaching $Q_{\mathrm{LED}} = 0.1\%$.

7.3.2 Experiments

The investigated samples are high efficiency Cu(In,Ga)Se_2 solar cells, fabricated by a three stage process [176] that enables efficiencies $\eta > 19\%$ (on a cell area of 0.5 cm^2) [177]. In the following, I will briefly outline the three stage process used for these samples: After evaporation of the 1.5 μm thick Mo back contact on a glass substrate, the absorber depostion starts with the first stage, namely the evaporation of In, Se, and Ga at a substrate temperature $T = 400^\circ\,\mathrm{C}$. At the end of the first stage, the substrate temperature is increased to $T \approx 610^\circ\,\mathrm{C}$ and the Cu evaporation is started. The evaporation of In and Ga is slightly decreased while the Se rate is

kept constant throughout the whole process. At the end of stage two, the substrate temperature stays constant, the Cu evaporation decreases again, and the In and Ga evaporation increases to a level slightly below stage one. After stage three, the Se rate stays constant until the substrate has cooled down to 300° C. Reference [177] describes further details of the processing.

The three samples investigated in this article have a comparable band gap but strongly different open circuit voltages and efficiencies, which are reflected in different EL spectra. The values of the band gap E_g, as extrapolated from quantum efficiency measurements, the Ga-content $x = [\mathrm{Ga}]/[\mathrm{In} + \mathrm{Ga}]$ obtained from energy dispersive X-ray analysis (EDX), and cell parameters are given in Table 7.1. Note that both, band gap energy E_g and Ga-content x are not constant throughout the depth and over the sample area. Therefore the values given in Table 7.1 need to be interpreted with regard to the method used to determine them [178]. As described in Ref. [177] the Ga-content is determined by EDX with penetration depths around 1 μm at cell thicknesses around 2.5 μm. Due to the strong grading of the band gap versus cell depth, the minimum band gap at a point in the cell volume will be considerably smaller than that corresponding to the extracted Ga-content. Hence the band gap energy in Table 7.1 yields a value similar to the spatially averaged minimum band gap where absorption starts while the Ga-content is an average over the volume.

The electroluminescence is recorded with a liquid nitrogen cooled Ge-detector attached to a monochromator with a 600 lines/mm-grating blazed at $\lambda = 1000$ nm. The sample is mounted into an Oxford Cryodrive cryostat, while a Hewlett Packard pulse generator applies a rectangular shaped periodic voltage to the sample enabling the use of a lock-in amplifier.

7.3.3 Temperature dependent measurements

Results

Among the three investigated solar cells, sample A has the highest values for efficiency and open circuit voltage, followed by sample B, while sample C has the lowest performance as a solar cell. However, all three can be regarded as highly efficient polycrystalline thin film solar cells. The device quality is reflected in the

Tab. 7.1: *Band gap energy E_g (extrapolated from the quantum efficiency), Ga content from EDX measurements, and the Shockley-Queisser-values under AM 1.5 G illumination for the saturation current density $J_{0,SQ}$, short circuit current density $J_{sc,SQ}$, and open circuit voltage $V_{oc,SQ}$. These values are compared to the measured values J_{sc}, V_{oc} and to the parameters $J_{0,rad}$, $V_{oc,rad}$ for radiative recombination in the device as extracted from the combined electroluminescence and Q_e analysis. The LED external quantum efficiencies Q_{LED} refer to injected current densities of* 200 cm^{-2}. *The cell area of all samples is* $A = 0.5\,\mathrm{cm}^2$.

	sample A	sample B	sample C
E_g [eV]	1.21	1.19	1.24
Ga-content x	0.40	0.39	0.43
$J_{0,\mathrm{SQ}}[\,\mathrm{A\,cm^{-2}}]$ at E_g	3.0×10^{-18}	6.2×10^{-18}	9.7×10^{-19}
$J_{\mathrm{sc,SQ}}[\,\mathrm{mA\,cm^{-2}}]$ at E_g	38.8	39.8	37.3
$V_{\mathrm{oc,SQ}}[\,\mathrm{mV}]$ at E_g	959	941	987
$J_{0,\mathrm{rad}}[\,\mathrm{A\,cm^{-2}}]$ exp.	3.5×10^{-18}	7.5×10^{-18}	2.3×10^{-18}
$V_{\mathrm{oc,rad}}[\,\mathrm{mV}]$ exp.	955	935	964
$J_{\mathrm{sc}}[\,\mathrm{mA\,cm^{-2}}]$ measured	31.2	31.6	29.0
$V_{\mathrm{oc}}[\,\mathrm{mV}]$ measured	739	719	700
efficiency η[%]	18.2	17.4	16.1
$Q_{\mathrm{LED}}[10^{-4}]$ at 200 $\mathrm{mA\,cm^{-2}}$	4.4	3.3	0.49

temperature dependence of the electroluminescence spectra, which are recorded in the temperature range $100\,\mathrm{K} < T < 300\,\mathrm{K}$.

In a first step, I present the measured spectra and discuss all obvious observations. Then, I look closer at the position of the peaks as a function of temperature and identify the physical character of the recombination process by excitation current dependent measurements. Finally, I discuss the differences between the samples.

For simplicity, Figure 7.15 shows the electroluminescence at four temperatures ($T = 120\,\mathrm{K}, 180\,\mathrm{K}, 240\,\mathrm{K}$, and $300\,\mathrm{K}$). As a general trend, all samples exhibit a transition from lower peak energies at lower temperatures to higher peak energies at higher temperatures. The differences between the samples become apparent in the

extent of the transition range and the number of visible peaks. Figure 7.15a shows that sample A exhibits one peak at $E_{\text{low T}} \approx 1.09\,\text{eV}$ for temperature $T = 120\,\text{K}$ and one peak around $E_{\text{high T}} \approx 1.17\,\text{eV}$ for higher temperatures $T = 240$, and 300 K. Only at $T = 180\,\text{K}$, two contributions are distinguishable.

Figure 7.15b shows the spectra at the same temperatures ($T = 120\,\text{K}, 180\,\text{K}, 240\,\text{K}$, and 300 K) for sample B. For temperatures $T = 120, 240$, and 300 K, the spectra are again dominated by one peak, while at $T = 180\,\text{K}$, two distinct peaks are visible. However, a closer look reveals that even at the energy of the low temperature peak dominant at $T = 120\,\text{K}$, a smaller shoulder remains up to room temperature. For all temperatures, there are more than two peaks visible in the spectra.

Figure 7.15c shows that sample C has a variety of radiative transitions up to room temperature. The low energy peak dominating the spectrum at $T = 120\,\text{K}$ stays the most dominant up to $T = 240\,\text{K}$ and is still clearly visible at room temperature. Due to the three different peaks at room temperature, the spectrum is very broad.

For a detailed analysis, I determinded the peak energies of the spectra. Where more than one peak is visible, I fitted those spectra to determine the peak energies. Figure 7.16a shows the evolution of peak position versus temperature for sample A. Below $T = 120\,\text{K}$, the only peak is around $E_{\text{low T}} \approx 1.09\,\text{eV}$, between 160 K and 180 K two peaks are distinguishable and fitted by two Gaussians to determine the peak positions, while above 200 K only the high energy peak is left. To identify the character of the radiative recombination process responsible for a certain peak, I performed injection level dependent measurements. The reason for this is the dependence of the peak position of donor-acceptor pair recombination on injection level [179]. The excitation level dependent measurements presented in Fig. 7.16b show a strong blue shift of 60 meV/decade below the transition range, at $T = 140\,\text{K}$. Above the transition no peak shift with increasing temperature is visible. This leads to the conclusion that the low energy transition, dominating at low temperatures, is a donor-acceptor pair (DAP) transition, while the high energy peak is the band to band (BB) transition.

Figure 7.17 shows the equivalent measurements for the case of sample B. The temperature dependent peak positions presented in Fig. 7.17a show the existence of up to four different peaks. The spectra were fitted with Lorentian peak shapes

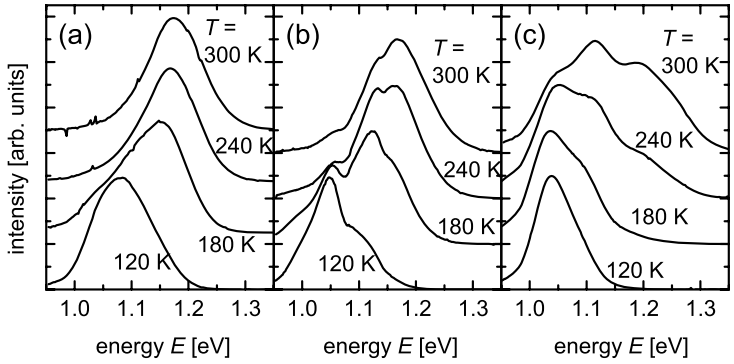

Fig. 7.15: *Electroluminescence spectra from samples A, B, and C at the temperatures* $T = 120\,\mathrm{K}, 180\,\mathrm{K}, 240\,\mathrm{K}$*, and* $300\,\mathrm{K}$*. All samples show a clear transition from lower peak energies at low temperatures to higher energies at high temperatures. The intensity axis is roughly proportional to the number of photons per time and energy interval. The spectra are offset for clarity.*

instead of Gaussians to achieve a better fit. The excitation dependent measurements shown in Fig. 7.17b were performed at $T = 100, 200$ and $300\,\mathrm{K}$ and show that the low energy peak around features a blue shift with increasing injection current only for the lowest temperature. This blue shift is considerably smaller than that of sample A. Since only one peak shows a clear shift at low temperatures, unambiguous identification of the other peaks becomes impossible with the methods used here. The most probable interpretation is that the high energy peak is the band to band peak (marked with BB in Fig. 7.17a), the second peak is a free to bound peak (marked with FB in Fig. 7.17a) and the third is the donor-acceptor pair peak (marked with DAP). The origin of the lowest energy peak being only visible at low temperatures is not yet understood.

Figure 7.18a shows that sample C features only three peaks, which I could fit well with Gaussians. The excitation level dependent measurements in Fig. 7.18b show a small blue shift for the low energy peak at $T = 140\,\mathrm{K}$ and $T = 200\,\mathrm{K}$. Thus,

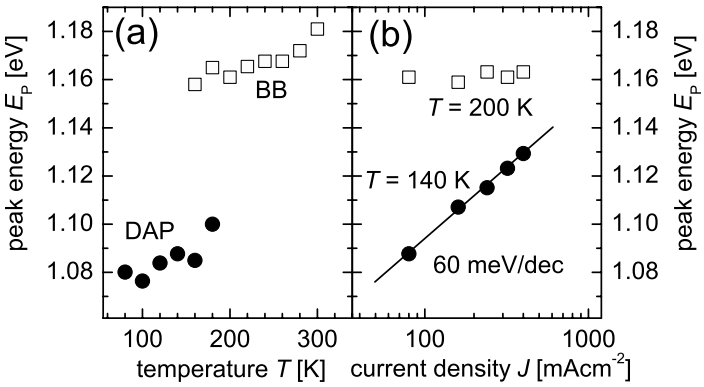

Fig. 7.16: *(a) Dependence of the peak position in the Cu(In,Ga)Se_2 electroluminescence of sample A on temperature T showing a transition between donor-acceptor pair (DAP) recombination at energies $E \approx 1.08\,\mathrm{eV}$ and band-to-band (BB) recombination at $E \approx 1.16 - 1.17\,\mathrm{eV}$. The data points in the transition range $160\,\mathrm{K} \leq T \leq 180\,\mathrm{K}$ are obtained by fitting two Gaussians to the experimental data. (b) At $T = 200\,\mathrm{K}$ the peak position of the BB recombination does not depend on excitation current density, whereas at $T = 140\,\mathrm{K}$ I observe the characteristic blue shift (60 meV/decade) of a donor-acceptor pair transition.*

the interpretation of the peaks as band to band, free to bound and donor-acceptor pair follows the abovementioned suggestion for sample B.

Comparing all three samples leads to three conclusions: (i) The less efficient cells show more peaks and especially broader spectra at room temperature. I extracted the full width at half maximum $FWHM$ of the room temperature spectra, which amounts to $FWHM = 107, 123, 231\,\mathrm{meV}$ for samples A, B, and C, respectively. Hence, especially sample C has a strongly broadened room temperature spectrum with several peaks leading to a FWHM being more than two times that of sample A. (ii) All spectra are considerably broader than one would expect from a direct semiconductor. For low temperatures this broadening is a result of a donor-

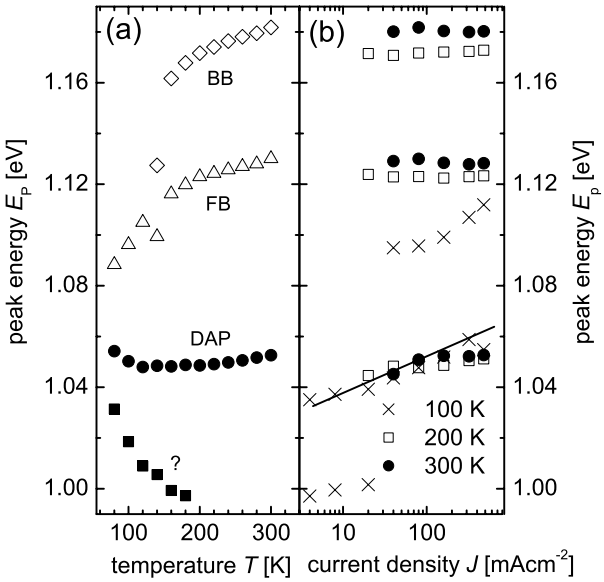

Fig. 7.17: *(a) Dependence of the peak position in the electroluminescence of sample B on temperature T showing up to four peaks at the different temperatures. The data points are obtained by fitting two up to four Lorentzians to the experimental data. In contrast to sample A, sample B has a contribution from sub-band-gap transitions up to room temperature. (b) Excitation current dependent measurements only identify the peak around* $E \approx 1.05\,\mathrm{eV}$ *as a DAP transition at the lowest temperature investigated (*$T = 100\,\mathrm{K}$*). For all other temperatures and energies, there is no clear blue shift visible. The labels DAP and FB (for free to bound transitions) are therefore suggestions rather than proven facts.*

acceptor pair (DAP) transition, broadened due to potential fluctuations [180–182], whereas at higher temperatures the broadening of a band-to-band (BB) transition is due to lateral band gap fluctuations [174, 175, 183] and the intentional band gap grading. (iii) The blue shift with increasing injection current is visible for all samples for the low energy peak at low temperatures. However the DAP peaks of both

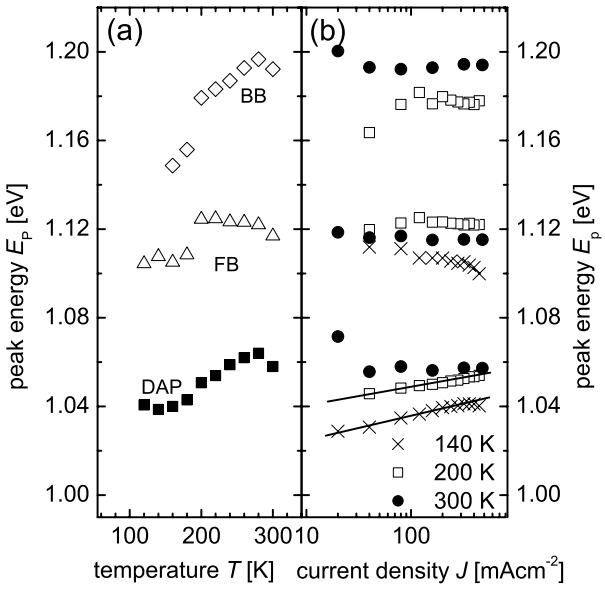

Fig. 7.18: *(a) Dependence of the peak position in the electroluminescence of sample C on temperature T showing three peaks, which are identified as donor-acceptor pair (DAP), free to bound (FB) and band to band (BB) in order of increasing energy. The data points are obtained by fitting up to three Gaussians to the experimental data. The spectrum of sample C shows a contribution of several sub-band-gap transitions up to room temperature. (b) Similar as for sample B, the excitation current dependent measurements only identify the lowest energy peak at* $T = 140\,\mathrm{K}$ *and* $200\,\mathrm{K}$ *as a DAP transition, while all other transitions do not show a blue shift.*

sample B and C have much smaller blue shifts (15 meV/decade for sample B and 12 meV/decade for sample C) than sample A. Explaining the exact strength of the blue shift is an issue still to be solved.

Interpretation in terms of compositional inhomogeneities

The temperature dependent measurements show that all samples have a very broad luminescence at room temperature because of band gap fluctuations. Furthermore, samples B and C have an additionally broadened luminescence, since a contribution of sub-band-gap recombination remains up to room temperature.

The Ga-content of these Cu(In,Ga)Se_2 solar cells is changed intentionally over depth to achieve a better charge collection. In addition also lateral changes in composition may occur, both together leading to a dependence of the band gap on all three spatial coordinates. Since the band gap determines the peak positions of the band to band transitions, the amount of inhomogeneity may be accessible by electroluminescence. As introduced in Refs. [174, 175], I assume a Gaussian distribution of band gaps centered around an average band gap $\overline{E}_{\mathrm{g}}$ with a standard deviation σ_{g}. The first order approach of a step-function-like local absorptance $a_{\mathrm{loc}}(E) = 0$ for energies $E < E_{\mathrm{g}}$ and $a_{\mathrm{loc}}(E) = 1$ for $E > E_{\mathrm{g}}$, as assumed in Refs. [174,175], leads to an error-function-like global absorptance

$$a_{\mathrm{glob}}\left(E, \overline{E}_{\mathrm{g}}\right) = \int_0^{\infty} a_{\mathrm{loc}}\left(E_{\mathrm{g}}\right) \exp\left(-\left[\frac{E_g - \overline{E}_g}{\sqrt{2}\sigma_{\mathrm{g}}}\right]^2\right) \frac{dE_{\mathrm{g}}}{\sqrt{2\pi}\sigma_{\mathrm{g}}} = \frac{1}{2}\mathrm{erfc}\left(\frac{\overline{E}_g - E}{\sqrt{2}\sigma_{\mathrm{g}}}\right) \tag{7.19}$$

The emission spectrum follows from Kirchhoff's law, i.e. the multiplication of the global absorptance with the black body spectrum at the temperature of the sample. This simple approach already reveals that the standard deviation σ_{g} is contained twofold in the dependence of the peak energies of the band to band transition on temperature. First, the distance between band gap and electroluminescence peak becomes larger with larger standard deviation σ_{g} and the slope of the peak positions versus temperature becomes steeper with higher σ_{g}. However, in order to get a decent fit for the spectra, I needed to refine the model. For the absorption, I used a square root-like absorption coefficient a above the band gap E_{g} and an Urbach-tail below the band gap. The Urbach-tail was allowed to have a linearly temperature dependent Urbach-energy E_{U}. The two parts of the absorption coefficient were chosen in a way that they are continuously differentiable. Considering these boundary

conditions the absorption coefficient follows as

$$\alpha = \begin{cases} \alpha_0 \sqrt{\frac{E-E_\mathrm{g}}{kT}} & \text{for } E > E_\mathrm{g} + E_\mathrm{U}/2 \\ \alpha_0 \exp\left(E - E_\mathrm{g}/E_\mathrm{U}\right) \sqrt{\frac{E_U}{2\exp(1)kT}} & \text{for } E < E_\mathrm{g} + E_\mathrm{U}/2 \end{cases} \tag{7.20}$$

where k is the Boltzmann constant. The local absorptance a_loc is approximated as $a_\mathrm{loc} = [1 - \exp(-\alpha d_\mathrm{eff})]$, where d_eff is an effective optical thickness. The effect that the optical path of insufficiently absorbed light is increased by light trapping above the cell thickness is considered by the effective thickness. The global absorptance a_glob is then

$$a_\mathrm{glob}\left(E, \overline{E}_\mathrm{g}\right) = \int_0^\infty a_\mathrm{loc}\left(E_\mathrm{g}\right) \exp\left(-\left[\frac{E_g - \overline{E}_g}{\sqrt{2}\sigma_g}\right]^2\right) \frac{dE_\mathrm{g}}{\sqrt{2\pi}\sigma_g} \tag{7.21}$$

According to Eq. (2.33), the quantum efficiency and not the absorptance is responsible for the shape of the electroluminescence spectrum. However, in the present case, using the absorptance given in Eq. (7.21) and applying Kirchhoff's law is a good approximation. Given the fact, that the band to band peaks, as shown in Figs. 7.16a, 7.17a, 7.18a are all well below the band gap as presented in Table 7.1, the peak shape and position of electroluminescence spectra are mostly determined by optical effects and not by an energy dependent collection efficiency. This is due to the fact that for small absorption coefficients the generation rate becomes small as well as independent of depth. The collection efficiency being a function of depth is now independent of energy and simply a constant factor, not changing the shape of the spectrum.

Discussion

Figure 7.19 shows the EL spectra of sample A for temperatures of $T = 200\,\mathrm{K}$ (circles), 240 K (triangles) and 300 K (squares) together with the fits following Eq. (7.21. The band gap was fixed at $E_\mathrm{g} = 1.21\,\mathrm{eV}$ and the fit-parameters were the standard deviation σ_g, the linearly dependent Urbach-tail E_U(T) and the prefactor of the absorption coefficient times the effective thickness $\alpha_0 d_\mathrm{eff}$. I fitted the spectra at $T = 200\,\mathrm{K}$ and 300 K at once and added the spectrum at $T = 240\,\mathrm{K}$ to show that the shape of this spectrum is still well approximated. The resulting values are $\sigma_\mathrm{g} = 26.6\,\mathrm{meV}$, $E_\mathrm{U}(T) = (0.034T + 7.4)\,\mathrm{meV}$, and $\alpha_0 d_\mathrm{eff} = 1.043$.

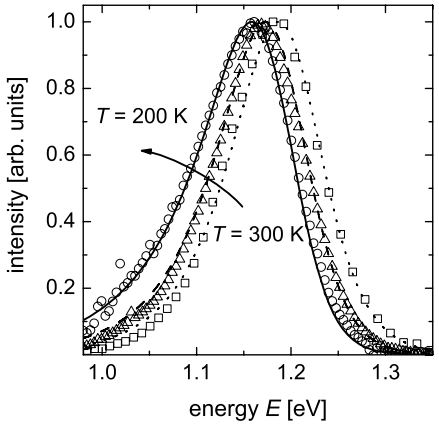

Fig. 7.19: *The electroluminescence spectra of sample A at temperatures* $T = 200\,\mathrm{K}$ *(circles),* $240\,\mathrm{K}$ *(triangles), and* $300\,\mathrm{K}$ *(squares). The experimental spectra are fitted with an absorptance following Eq. (7.21) multiplied by a black body spectrum. The resulting values for the fit parameters are* $\sigma_g = 26.6\,\mathrm{meV}$ *for the standard deviation,* $E_U(T) = (0.034T + 7.4)\,\mathrm{meV}$ *for the Urbach energy, and* $\alpha_0 d_{eff} = 1.043$ *for the prefactor of the absorption coefficient times the effective thickness of the device.*

As shown in Figs. 7.15b,c the room temperature spectra of samples B and C do not only consist of the single band to band peak. A fit of the whole spectra to obtain the standard deviation of the band gap distribution is therefore not possible. Instead, I use the information of the peak positions of the band to band peak as a function of temperature, which were already shown in Figs. 7.16a, 7.17a, 7.18a. In order to fit the peak positions to extract the standard deviation, I used a simpler approach for the absorption coefficient neglecting Urbach tails. The results are shown in Figure 7.20 together with the band to band transitions of samples A, B, and C. The standard deviations resulting from the fit of the peak positions and the fit of the whole spectra are nearly the same (comparing $\sigma_\mathrm{g} = 26.4$ from fitting the peak positions to $\sigma_\mathrm{g} = 26.6$ from the fit of the spectra shown in Fig. 7.19). Hence, I conclude that (i) the standard deviation σ_g is a rather robust parameter and (ii) that the method of determining σ_g must somehow consider the fact that the band

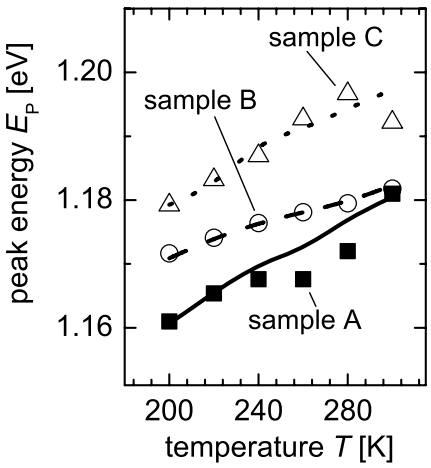

Fig. 7.20: *Peak positions of the band to band transitions of samples A, B, and C as a function of temperature. The standard deviation σ_g = 26.6 meV resulting from the fit of the spectra of sample A shown in Fig. 7.19 corresponds to that ($\sigma_g = 26.4\,\mathrm{meV}$) obtained from fitting only the peak positions (solid line). For samples B and C, where the existence of sub-band-gap transitions makes the fit of the spectra difficult, I can only use the information of the peak positions versus temperature. The resulting standard deviations are $\sigma_g = 16.6\,\mathrm{meV}$ (sample B) and $\sigma_g = 25.0\,\mathrm{meV}$ (sample C).*

to band peaks are several tens of meV below the band gap. From the two results of a high standard deviation of the band gap distribution, the distance between band gap and peak positions as well as the temperature dependence of the peaks, only the temperature dependence of the peaks is suited for the determination of the standard deviation.

The sub-band gap absorption, however, has to be considered by a suitably modelled absorption coefficient. Although only a slightly more sophisticated model with Urbach tails is capable of describing the peak shapes, a simple model already yields a similar result, when only considering the peak positions. Due to the presence of more than one peak in the room temperature spectra for samples B and C, only

the simpler model is applicable. Just regarding the peak positions, the resulting standard deviations of sample B and sample C are $\sigma_g = 16.5\,\mathrm{meV}$ and $\sigma_g = 25.0\,\mathrm{meV}$, respectively.

The low standard deviations for the three cells are of the order of the standard deviations caused by a band gap grading as calculated in Ref. [174]. The lateral inhomogeneity of the samples might therefore be small and the fact that the most efficient cell (sample A) has the highest standard deviation may be only an indication of a large, intentional grading that is a useful feature to increase carrier collection.

7.3.4 Reciprocity between electroluminescence and photovoltaic quantum efficiency

Theory

Again we need the two optoelectronic reciprocity relations (Eqs. (2.33) and (2.41)) for the interpretation of the EL spectra. The application of these relations in samples with graded band gaps requires additional care. Are they still valid in this case? The reciprocity relation (Eq. (2.33)) relies on the validity of the Donolato theorem connecting the carrier concentration in the dark under applied bias with the collection efficiency of photogenerated charge carriers under illumination [cf. Eq. (2.46)]. As shown in Ref [50], Donolato's theorem is valid for a generalized diffusive transport [184] of minority carriers with spatially fluctuating band gaps, lifetimes, mobilities and equilibrium minority carrier concentrations. Thus, the Donolato theorem as well as Eq. (2.33) also hold for Cu(In,Ga)Se_2 solar cells. where the Ga-content and hence the band gap change as a function of depth.

Discussion

From the band gaps as listed in Table 7.1 the cell parameters ($J_{0,\mathrm{SQ}}$, $J_{\mathrm{sc,SQ}}$, $V_{\mathrm{oc,SQ}}$) of a Shockley-Queisser-cell are calculated and presented in Table 7.1. The cell in the Shockley-Queisser limit is a cell with step function like absorptance and exclusively radiative recombination. The saturation current of real solar cells is different in two respects, (i) the absorptance is not step-function like, and (ii) non-radiative recombination exists. To distinguish, which part of the total open circuit voltage

difference $\Delta V_{\mathrm{oc}}^{\mathrm{tot}} = V_{\mathrm{oc,SQ}} - V_{\mathrm{oc}}$ between the open circuit voltage in the Shockley-Queisser limit $V_{\mathrm{oc,SQ}}$ and the actually measured open circuit voltage V_{oc} is due to which effect, I introduce the experimental radiative open circuit voltage $V_{\mathrm{oc,rad}}$. The experimental radiative open circuit voltage answers the question of how large V_{oc} would be if there was only radiative recombination but the quantum efficiency was the same as for the actual device (i.e. no step function). To determine $V_{\mathrm{oc,rad}}$, I need to calculate the radiative saturation current density $J_{0,\mathrm{rad}}$ from Eq. (2.38). The radiative saturation current density is the integral over the properly scaled electroluminescence spectrum. The scaling is accomplished by using the reciprocity theorem of Eq. (2.33). The quantum efficiency calculated from the electroluminescence spectrum is compared with the directly measured quantum efficiency as shown in Fig. 7.21 for the samples A, B, and C. Since the directly measured solar cell quantum efficiency is calibrated (lines) I can adjust the quantum efficiency from electroluminescence (squares) and subsequently determine J_0^{rad}. Note that although I can calculate the product $Q_{\mathrm{e}}(E)\phi_{\mathrm{bb}}(E)$ in absolute units, I cannot measure $\phi_{\mathrm{em}}(E) = Q_{\mathrm{e}}(E)\phi_{\mathrm{bb}}(E)\left[\exp\left(qV/kT\right) - 1\right]$ with this approach, since the internal voltage V is not directly accessible.

Since I know the short circuit currents from current/voltage measurements under AM 1.5 G illumination, I am now able to compute the experimental, radiative open circuit voltages. Table 7.1 presents the resulting values. This allows us to define two open circuit voltage differences, namely $\Delta V_{\mathrm{oc}}^{*} = V_{\mathrm{oc,SQ}} - V_{\mathrm{oc,rad}}$ and $\Delta V_{\mathrm{oc}} = V_{\mathrm{oc,rad}} - V_{\mathrm{oc}}$, the latter being identical to the definition of Eq. (2.41). The broadened luminescence leads to a broadened absorption edge and subsequently causes the experimental radiative saturation current density to be higher than without the broadening. This loss is measured with $\Delta V_{\mathrm{oc}}^{*} = V_{\mathrm{oc,SQ}} - V_{\mathrm{oc,rad}}$. For samples A and B, which feature only one dominant peak, this loss is only $\Delta V_{\mathrm{oc}}^{*} = 4\mathrm{mV}$ (sample A) and $\Delta V_{\mathrm{oc}}^{*} = 6\mathrm{mV}$ (sample B). But for the strongly broadened luminescence of sample C, the loss is $\Delta V_{\mathrm{oc}}^{*} = 23\mathrm{mV}$. As long as the spectrum is dominated by the band to band transition, the determination of the standard deviation of inhomogeneous band gaps, as carried out in section B, is in principle also possible only using $\Delta V_{\mathrm{oc}}^{*}$. Reference [175] gives a simple equation for the voltage loss $\Delta V_{\mathrm{oc}}^{\mathrm{inhom}} = \sigma_{\mathrm{g}}^2/2kTq$ caused by an inhomogeneous band gap with standard deviation σ_{g} as compared to a sample with a homogeneous band gap. I assume that the broadening of the

room temperature spectra is due to the inhomogeneity of the band gap - and hence, broadening of the band to band transition - and in addition due to transitions via levels in the band gap. Under this assumption, the open circuit voltage difference $\Delta V_{\mathrm{oc}}^{*}$ will be an upper limit for the voltage loss $\Delta V_{\mathrm{oc}}^{\mathrm{inhom}}$. Hence I find upper limits for the standard deviation, namely $\sigma_{\mathrm{g}} = 14.4\,\mathrm{meV}$ for sample A, 17.7 meV for sample B and 34.6 meV for sample C. Sample B and C behave as expected, since the value is larger than that from the temperature dependence. The difference is small for sample B (17.7 meV to 16.5 meV) while it is significantly larger for sample C (34.6 meV to 25.0 meV). This is in accordance with the fact that the broadening due to additional sub band gap peaks is small for sample B and pronounced for sample C. For sample A however, the true standard deviation of the inhomogeneities as obtained from the fits in Fig. 7.19 is $\sigma_{\mathrm{g}} = 26.6\,\mathrm{meV}$, which is larger than the value extracted from $\Delta V_{\mathrm{oc}}^{*}$ as explained above. This reminds us of the fact that the band gap determination via an extrapolation of α^2 versus energy E is not accurate enough to determine the band gap with meV resolution. Therefore, I conclude that the method of determining the standard deviation σ_{g} of the band gap inhomogeneities via the voltage difference $\Delta V_{\mathrm{oc}}^{*} = V_{\mathrm{oc,SQ}} - V_{\mathrm{oc,rad}}$ is in principle possible but much more error prone than the determination via the temperature dependence. However, the value of $\Delta V_{\mathrm{oc}}^{*}$ is even more general than the value of the standard deviation σ_{g}, since it also considers other sources of emission broadening that cause the radiative open circuit voltage to decrease.

Obviously, the largest part of the total loss in open circuit voltage is caused by non-radiative recombination, namely $\Delta V_{\mathrm{oc}} = 216\mathrm{mV}$ for samples A and B and $\Delta V_{\mathrm{oc}} = 264\mathrm{mV}$ for sample C. This loss solely determines the efficiency of the device as LED. According to Eq. (2.41) we can calculate the external LED quantum efficiency Q_{LED} at an injection current $J_{\mathrm{inj}} = J_{\mathrm{sc}}$ from the voltage loss . Figure 7.22 compares these predictions with measured values of the external LED quantum efficiency. For absolute optical power measurements I used a calibrated low power optical sensor from Coherent, equipped with a Ge-detector. To calculate the optical power from the number of detected photons, the spectrum is assumed to be monochromatic. The Ge detector has not sufficient sensitivity to measure the optical power from the solar cells for injection currents as low as $J = 30\ \mathrm{mA\,cm^{-2}}$ corresponding to one sun conditions (i.e corresponding to the measured J_{sc}). There-

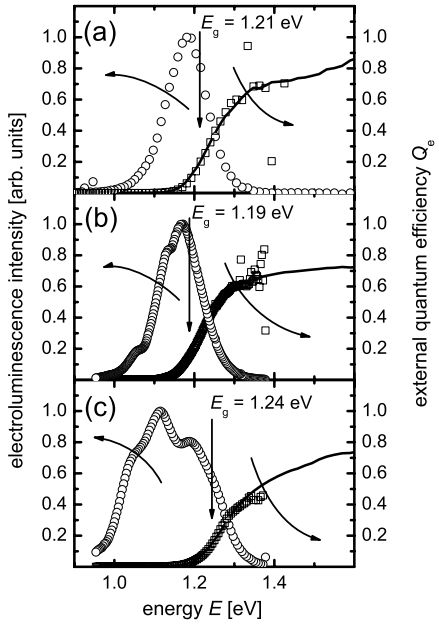

Fig. 7.21: *The electroluminescence spectra at T = 300 K (open circles) yield a recalculated external quantum efficiency $Q_{e,EL}$ (open squares), which is in good agreement with the measured photovoltaic external quantum efficiency $Q_{e,dir}$ (lines). The scaling of the electroluminescence with the quantum efficiency enables the calculation of the radiative saturation current densities $J_{0,rad}$ and the radiative open circuit voltages $V_{oc,rad}$ for the three cells.*

fore the prediction cannot be directly checked. However, the predicted values fit well to the measured data. Considering the uncertainties, when measuring absolute optical power, the agreement is excellent.

It is obvious from the measurements of all three samples shown in Fig. 7.22 that the maximum LED efficiency is far above one sun conditions. The maximum room temperature LED quantum efficiency approaches $Q_{\mathrm{LED}} = 0.1\%$ at injection current densities around $J = 1\,\mathrm{A\,cm^{-2}}$.

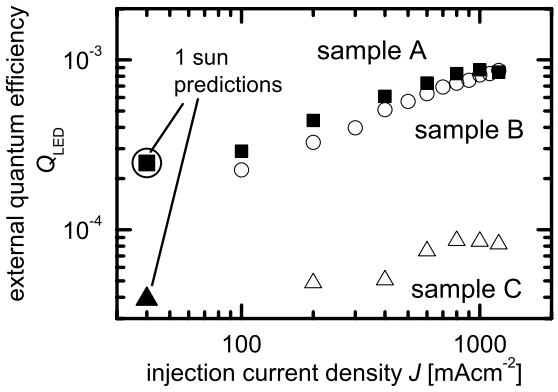

Fig. 7.22: *External LED quantum efficiency as a function of injection current for samples A, B, and C. The experimental values begin at current densities corresponding to 2 or more suns due to the limited sensitivity of the setup for absolute measurements. Nevertheless, the one sun predictions, derived from the open circuit voltage and the room temperature electroluminescence spectrum, correspond well to the experimental data. The maximum room temperature LED quantum efficiency approaches* 0.1% *at injection current densities around* $J = 1\,\mathrm{A\,cm^{-2}}$.

7.3.5 Summary

I have compared the electroluminescence of three polycrystalline Cu(In,Ga)Se_2 heterojunction solar cells with similar bandgaps but different open circuit voltages and consequently efficiencies, indicating a difference in the electronic quality of the absorber. Temperature dependent electroluminescence measurements have revealed that all cells feature transitions from donor-acceptor pair recombination at lower temperature to band to band recombination at higher temperatures. However, the less efficient cells show a longer transition range with donor-acceptor pair recombination still apparent at room temperature, while the best cell has a shallow transition range $160\,\mathrm{K} < T < 180\,\mathrm{K}$. The amount of compositional fluctuations causing an inhomogeneity of the band gap is extracted from the temperature dependence of

the band to band peaks. The resulting values for the standard deviation are between 16.5 and 26.6 meV. These values are comparable to the ones predicted for strong band gap gradings, indicating that the influence of lateral inhomogeneities may indeed be small. I use reciprocity relations between electroluminescent and photovoltaic action of solar cells to identify the losses in open circuit voltage due to broadened luminescence and to non-radiative recombination. Finally I am able to predict the external LED quantum efficieny and verify our calculations experimentally. The measurements show that Cu(In,Ga)Se_2 solar cells reach external LED efficiencies around .

7.4 GaInP/GaInAs/Ge-multijunction solar cells

Multi-junction solar cells based on III-V semiconductors on Ge substrate have the highest efficiency among today's solar cell technologies [56]. The possibility to grow high quality semiconductor layers epitaxially on top of each other allows a better adaptation of the absorber materials to the solar spectrum [69]. Characterization of these devices, however, is challenging, especially for multijunction cells designed for use in concentrator systems. For instance, the experimental access to information about individual subcells as well as the device characteristics at high illumination conditions is of interest yet difficult to assess with common methods.

This section introduces a method to derive the individual current/voltage curves of all subcells in a stacked multi-junction cell by combining electroluminescence (EL) and quantum efficiency measurements. I measure the EL spectra of a lattice mismatched $Ga_{0.35}In_{0.65}P$/ $Ga_{0.83}In_{0.17}As$/Ge solar cell at currents ranging from 100 μA to 150 mA and over a range of wavelengths λ from 600 nm to 1800 nm. The solar cell of an area $A = 0.032$ cm^2 was prepared by metal organic vapor phase epitaxy [185]. The current is applied with a DC current source and the EL emission is chopped in order to allow the use of lock-in amplifiers. The spectra are then recorded with a Ge detector attached to a single stage monochromator and are subsequently corrected for the relative sensitivity of the setup. Figure 7.23a shows three exemplary EL measurements at currents $I = 2, 20$, and 150 mA. The spectra feature two pronounced peaks of the direct semiconductors GaInAs ($E \approx 1.20\,\mathrm{eV}$) and GaInP ($E \approx 1.72\,\mathrm{eV}$). The Ge peak is hardly visible since the sensitivity of the

Ge detector is already low at the peak around $E \approx 0.70\,\mathrm{eV}$.

The basic theoretical ingredient for our analysis is the spectral reciprocity relation (RR) between solar cell and light emitting diode (LED) as described in Ref. [35]. The RR relates the external solar cell quantum efficiency $Q_\mathrm{e}(E)$ to the spectral emission ϕ_em via

$$\phi_\mathrm{em}(E) = Q_\mathrm{e}(E)\phi_\mathrm{bb}(E)\left[\exp\left(\frac{qV}{kT}\right) - 1\right], \tag{7.22}$$

where ϕ_bb is the black body photon flux, V is the internal voltage applied to the pn-junction, and kT/q is the thermal voltage. Equation (7.22) connects the spectral EL emission with two quantities of high relevance for photovoltaics: with the quantum efficiency $Q_\mathrm{e}(E)$ and the junction voltage V. In the following, I determine the three junction voltages $V_\mathrm{j}(j = 1, 2, 3)$ of the three individual subcells of our GaInP/GaInAs/Ge stack. Therefore, I use directly measured external quantum efficiencies $Q_\mathrm{e,dir}$ to scale EL emission of each subcell with the help of Eq. (2.33).

Figure. 7.23b shows $Q_\mathrm{e,dir}$ of the three subcells measured directly (using the method described in Ref. [186]) in comparison to the quantum efficiency $Q_\mathrm{e,EL}$ extracted from the EL spectrum taken using Eq. (7.22). For the GaInAs and GaInP solar cells, I find a good agreement of the respective low-energy portions of $Q_\mathrm{e,dir}$ and $Q_\mathrm{e,EL}$ including a part of the region where the quantum efficiency saturates. At higher photon energies $Q_\mathrm{e,EL}$ becomes noisy because of the low intensity of the underlying EL signal (Fig. 7.24a). For the Ge cell, the spectral region, where $Q_\mathrm{e,dir}$ and $Q_\mathrm{e,EL}$ correspond to each other is restricted to the low-energy slope whereas at higher photon energies ($E > 0.76\,\mathrm{eV}$) the original EL is distorted by small amounts of stray light. Due to the exponential energy dependence of the black body spectrum in Eq. (7.22), the increased luminescence signal strongly affects the $Q_\mathrm{e,EL}$ leading to the discrepancy to $Q_\mathrm{e,dir}$, visible in Fig. 7.23b.

In order to determine the internal junction voltages, I have to consider the fact that the EL intensity is measured in arbitrary units, and thus reformulate Eq. (7.22) using the Boltzmann approximation for ϕ_bb as

$$\phi_\mathrm{em}(E) = CQ_\mathrm{e}(E)E^2 \exp\left(\frac{-E}{kT}\right)\exp\left(\frac{qV}{kT}\right) \tag{7.23}$$

with C being an unknown energy independent proportionality factor. Solving for

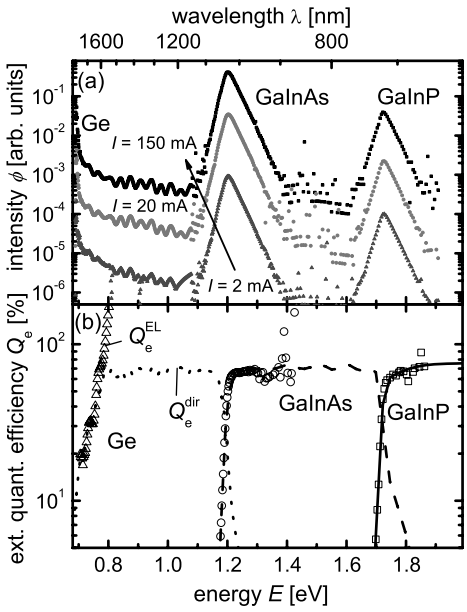

Fig. 7.23: *(a) Electroluminescence (EL) spectra of the multijunction cell at three different injection currents. (b) Comparison of the directly measured quantum efficiency (lines) to the quantum efficiencies derived from the EL spectrum (symbols) using Eq. (7.22).*

the internal voltage V_j at any of the three junctions $j = 1, 2, 3$ leads to

$$V_\mathrm{j} = V_\mathrm{T} \ln(\phi_\mathrm{em}) + E/q - 2V_\mathrm{T} \ln(E) - V_\mathrm{T} \ln\left(Q_\mathrm{e}^\mathrm{j}\right) - V_\mathrm{T} \ln(C) \tag{7.24}$$

with $V_\mathrm{T} = kT/q$. Except for the constant additive term $\delta V = V_\mathrm{T} \ln(C)$, Eq. (7.24) enables us to determine the voltage that internally drops over each of the three pn-junctions.

Figures 7.24a-c show the result of performing the operation given by Eq. (7.24) on the measured spectra of Fig. 7.24. The three spectral regions highlighted by vertical lines in Figs. 7.24a-c correspond to the ranges, where the EL of each subcell yields a maximum signal and where $Q_\mathrm{e,dir,j} \approx Q_\mathrm{e,EL,j}$ in Fig. 7.23b. Since the internal voltages are the quasi Fermi-level splittings at the three internal junctions,

the application of Eq. (7.24) in these regions must lead to a result for V_j being independent of energy. This is verified by Figs. 7.24a-c.

The constant offset voltage δV is determined from a separately measured current/voltage (J/V) curve under about 25 suns illumination as depicted in Fig. 7.24d. Then I adjust the sum ΣV_j of the junction voltages (measured at a dark current density J_D) to the open circuit voltage V_{oc} at the illumination condition leading to the corresponding short circuit current density $J_{sc} = J_D$. Note that this scaling must only be performed once for the total series of EL measurements because the offset voltage δV is the same for all spectra. Adjusting the voltages to V_{oc} and not to an arbitrary voltage is necessary since neither the internal voltages from EL nor the V_{oc} contain resistive effects as any other directly measured voltages do.

Having determined the offset voltage, I can rescale the voltage axis in Figs. 7.24a-c and finally receive the internal voltages of the individual subcells, shown in Fig. 7.24d for a wide range of injection currents. From the semilogarithmic slope of the J/V-curves, I determine the diode quality factors n_{id} with the relation $n_{id} = q/kTdV/d\ln(J)$, receiving the values $n_{id} = 1.14, 1.61$, and 1.37 for the Ge, GaInAs, and GaInP cell, respectively. Summing up the individual voltages leads to ΣV_j as a function of injection current. This curve nicely corresponds to the directly measured J/V-curve over the whole range and not only at the point $V = V_{oc}$ (which is the case by design).

Apart from measuring the internal voltages, I can also rate the quality of the subcells from the difference between these internal voltages and their respective radiative limits. The saturation value of the radiative recombination current of cell j follows directly from Eq. (7.22) via [58, 59]

$$J^j_{0,rad} = q \int Q^j_e(E)\phi_{bb}(E)dE \tag{7.25}$$

Defining the radiative open circuit voltage by $V^j_{oc,rad} = V_T \ln(J_{sc}/J^j_{0,rad})$ allows us to determine $V^j_{oc,rad}$ for each subcell. The difference $\Delta V_{oc} = V^j_{oc,rad} - V_j(J = J_{sc})$ is then a measure for non-radiative recombination losses in the subcell. The resulting values at the injection current of the J/V-measurement (25 suns) are $\Delta V_{oc} = 226$ mV, 132 mV, and 210 mV for the Ge, GaInAs, and GaInP cell, respectively. Hence, the GaInAs cell comes by far closest to its radiative limit.

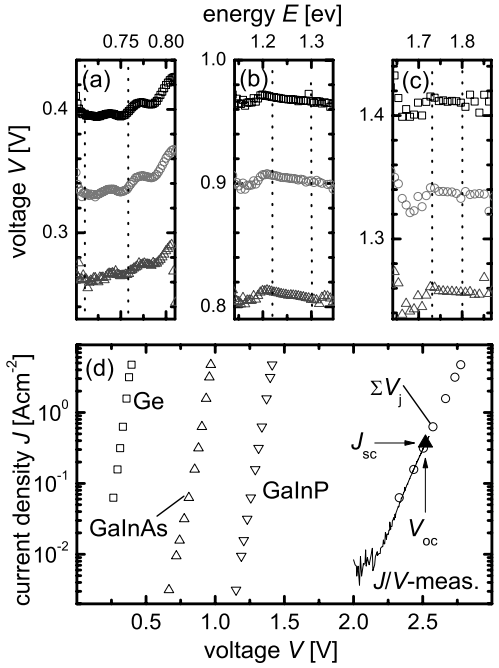

Fig. 7.24: *(a, b, c) Relative internal voltage derived from the EL spectra of Fig. 7.23 according to Eq. (7.24) for currents $I = 2$ mA (open triangles), 20 mA (circles), 150 mA (squares). The dotted vertical lines indicate the spectral intervals, where the voltages have been determined. (d) These voltages (open circles) are adjusted to the open circuit voltage V_{oc} (full triangle) of a current/voltage (J/V)-curve under 25 suns illumination. The solid line represents this J/V curve shifted by the short circuit current density J_{sc}. I finally receive the J/V-curves of the three individual subcells (open squares) with a correctly scaled voltage axis.*

Summary

In summary, the present method allows us by combining EL and quantum efficiency measurements not only to determine the internal voltages of stacked multi-junction solar cells but also to evaluate the performance of each subcell with respect to the

respective radiative limit.

Chapter 8

Conclusions and Outlook

All different types of solar cells, be it wafer based silicon, inorganic thin films or organic bulk heterojunction solar cells, are fundamentally limited by the Shockley-Queisser limit, which is based on the principle of detailed balance. In contrast to the claim [28] that organic, excitonic solar cells are fundamentally different from inorganic, bipolar devices, this thesis shows that a single detailed balance model can be designed that encompasses both excitonic and bipolar solar cells. The model starts with the idea behind the Shockley-Queisser limit, namely to balance all processes in equilibrium according to the principle of detailed balance. The fundamental character of the Shockley-Queisser theory stems from idealizing transport and charge separation, which are exactly those aspects of solar cells, where excitonic and bipolar devices differ conceptionally from each other. By including transport, my model is able to account for the device specific aspects of a variety of solar cells and provides a means to determine fundamental efficiency limits as well as to simulate practical devices with one common model.

The devices that were modelled in this thesis include all types of inorganic solar cells, quantum dot and quantum well solar cells with some simplifications and organic bulk heterojunction solar cells. One important candidate for future work is the dye-sensitized solar cell. In this device, the absorbing layer is a dye attached to a porous TiO_2 layer, which acts as the electron transporting layer. The positive charge is carried by ions in an electrolyte. Thus exchanging the continuity equation for holes with one for ions, which may have more than one positive elementary charge per particle, should be the main change required for the detailed balance model to

cover also dye-sensitized solar cells.

The experimental part of this thesis prooved the usefulness of electroluminescence measurements for characterization of different solar cells and for the determination of a variety of different parameters. In crystalline silicon solar cells, the spatially resolved characterization of recombination and light trapping is of high relevance. Quantum efficiency measurements provide this information. To obtain spatial information will however be very time consuming with quantum efficiency measurements. If one reduces the number of different wavelengths at which the quantum efficiency is measured, light beam induced current measurements provide spatial information with measurement times of hours. Due to the reciprocal relation between electroluminescence and quantum efficiency, similar information is also contained in electroluminescence images that take seconds or few minutes for data acquisition. In Cu(In,Ga)Se_2 solar cells the characterization of compositional inhomogeneities is crucial, since a change in composition implies a change in band gap, which strongly affects recombination and photocurrents. Temperature resolved electroluminescence measurement showed that inhomogeneities in the high efficiency cells under investigation are small and can be explained by intentional band gap gradings over the depth of the device and not by unintentional lateral variations. Finally electroluminescence spectra yielded the internal voltages of the individual subcells of a multijunction solar cell. Thus, luminescence is a suitable method to characterize cells within a stack of cells that cannot be contacted separately.

All experimentally investigated solar cells have in common that they are inorganic pn-junction solar cells, where band to band recombination is dominates EL emission at room temperature. Future investigations should therefore extend these luminescence studies to pin-type solar cells, where the reciprocity is no longer directly applicable, to solar cells where recombination via band tails dominates emission (e.g. amorphous and microcrystalline Si solar cells) and to organic solar cells. Especially interesting is the case of organic solar cells, where photoluminescence quenching is regarded as a means to efficiently dissociate the photogenerated exciton. However, this thesis shows a clear relationship between luminescence intensity and open circuit voltage. Thus, organic solar cells sacrifice the high luminescence yield for enhanced exciton dissociation, due to the addition of electron accepting materials like PCBM. Thus, electroluminescence measurements should be able to

characterize these non-radiative recombination losses effectively.

Appendix A

List of Publications

A.1 Publications in Journals

1. P. J. Rostan, U. Rau, V. X. Nguyen, T. Kirchartz, M. B. Schubert, and J. H. Werner, *Low-temperature a-Si:H/ZnO/Al back contacts for high-efficiency silicon solar cells*, Sol. Energy Mat. Sol. Cells **90**, 1345 (2006)

2. T. Kirchartz, U. Rau, M. Kurth, J. Mattheis, J. H. Werner, *Comparative study of electroluminescence from Cu(In,Ga)Se_2 and Si solar cells*, Thin Solid Films **515**, 6238 (2007).

3. T. Kirchartz and U. Rau, *Electroluminescence analysis of high efficiency $Cu(In,Ga)Se_2$ solar cells*, J. Appl. Phys. **102**, 104510 (2007)

4. T. Kirchartz, U. Rau, M. Hermle, A. W. Bett, A. Helbig, and J. H. Werner, *Internal voltages in GaInP/GaInAs/Ge multi-junction solar cells determined by electroluminescence measurements*, Appl. Phys. Lett. **92**, 123502 (2008)

5. S. Fahr, C. Ulbrich, T. Kirchartz, U. Rau, C. Rockstuhl, F. Lederer, *Rugate filter for light-trapping in solar cells*, Optics Express **16**, 9332 (2008)

6. T. Kirchartz and U. Rau, *Charge separation in excitonic and bipolar solar cells- a detailed balance approach*, Thin Solid Films **516**, 7144 (2008)

7. T. Kirchartz, A. Helbig and U. Rau, *Note on the interpretation of electroluminescence images using their spectral information*, Sol. Energy Mat. Sol. Cells

92, 1621 (2008)

8. T. Kirchartz, B. E. Pieters, K. Taretto, and U. Rau, *Electro-optical modeling of bulk heterojunction solar cells*, J. Appl. Phys. **104**, 094513 (2008)

9. T. Kirchartz and U. Rau, *Reciprocity and detailed balance in solar cells*, phys. stat. solidi a **205**, 2737 (2008)

10. C. Ulbrich, S. Fahr, J. Üpping, M. Peters, T. Kirchartz, C. Rockstuhl, R. Wehrspohn, A. Gombert, F. Lederer and U. Rau, *Directional selectivity and ultra-light-trapping in solar cells*, phys. stat. solidi a **205**, 2831 (2008)

11. T. Kirchartz and U. Rau, *Modeling charge carrier collection in multiple exciton generating PbSe quantum dots*, Thin Solid Films **517**, 2438 (2009)

12. T. Kirchartz, J. Mattheis, and U. Rau, *Detailed balance theory of excitonic and bulk heterojunction solar cells*, Phys. Rev. B **78**, 235320 (2008)

13. T. Kirchartz, A. Helbig, W. Reetz, M. Reuter, J. H. Werner, and U. Rau, *Reciprocity between electroluminescence and quantum efficiency used for the characterization of silicon solar cells*, Prog. Photovolt. Res. Appl., DOI: 10.1002/pip.895

14. T. Kirchartz, K. Seino, J.-M. Wagner, U. Rau, and F. Bechstedt *Efficiency limits of Si/SiO_2 quantum well solar cells from first-principles calculations*, J. Appl. Phys., in print

A.2 Peer reviewed conference proceedings

1. T. Kirchartz, J. Mattheis, and U. Rau, *Electroluminescence from $Cu(In,Ga)Se_2$ thin-film solar cells*, MRS Res. Soc. Symp. Proc. **1012**, 115 (2007)

2. T. Kirchartz, A. Helbig, and U. Rau, *Quantification of Light Trapping Using a Reciprocity Between Electroluminescent Emission and Photovoltaic Action in a Solar Cell* MRS Res. Soc. Symp. Proc. **1101E**, KK01-04 (2008)

3. C. Ulbrich, T. Kirchartz, and U. Rau, *Enhanced Light-trapping in Solar Cells by Directional Selective Optical Filters* MRS Res. Soc. Symp. Proc. **1101E**, KK08-03 (2008)

A.3 Conference proceedings (not reviewed)

1. P. J. Rostan, U. Rau, V. X. Nguyen, T. Kirchartz, M. B. Schubert, and J. H. Werner, *21 % efficient Si solar cell with a low-temperature a-Si:H/ZnO back contact*, in Techn. Digest 15th International Photovoltaic Science and Engineering Conference, Shanghai (2005), pp. 214

2. T. Kirchartz and U. Rau, *Charge separation in bipolar, excitonic and bulk heterojunction solar cells*, Proc. of the 22nd PVSEC Milan, (WIP Renewable Energies, Munich, 2007) p. 196

3. P. J. Rostan, J. Maier, T. Kirchartz, U. Rau, F. Einsele, R. Merz, M. B. Schubert and J. H. Werner, *a-Si:H/c-Si Heterojunction Solar Cells on p-type c-Si Wafers*, Techn. Digest of the 17th Internat. Photovolt. Sol. En. Conf., Fukuoka (2007)

4. C. Ulbrich, S. Fahr, M. Peters, J. Üpping, T. Kirchartz, C. Rockstuhl, J. C. Goldschmidt, P. Löper, R. Wehrspohn, A. Gombert, F. Lederer and U. Rau, *Directional selectivity and light-trapping in solar cells*, Proc. SPIE **7002**, 70020A (2008)

5. S. Fahr, C. Ulbrich, T. Kirchartz, U. Rau, C. Rockstuhl, F. Lederer, *Optimization of Rugate filters for ultra light-trapping in solar cells* Proc. SPIE, **7002**, 70020B (2008)

6. T. Kirchartz, A. Helbig, M. Hermle, U. Rau, and A. W. Bett, *Characterisation of GaInP/GaInAs/Ge solar cells with electroluminescence*, Proc. of the 23rd PVSEC Valencia (WIP Renewable Energies, Munich, 2008) p. 86

7. A. Helbig, T. Kirchartz, and U. Rau, *Quantitative information of electroluminescence images*, Proc. of the 23rd PVSEC Valencia (WIP Renewable Energies, Munich, 2008) p. 426

Appendix B

Curriculum vitae

Thomas Kirchartz	born January 14th, 1982 in Karlsruhe, Germany
Education	
1988-1989	Ernst-Reuter Schule, Karlsruhe
1989-1992	Schalksburgschule, Albstadt
1992-2001	Gymnasium Ebingen
6/2001	Abitur
10/2001-6/2006	Studies of Electrical Engineering and Information Technology at the University Stuttgart
9/2003	Vordiplom
10/2003-6/2006	Hauptstudium, main subject: micro- and optoelectronics
12/2005-6/2006	Diploma thesis at the Institute of Physical Electronics Title: "Reciprocity between electroluminescent emission and photovoltaic action in solar cells"
6/2006	Diploma at the University Stuttgart
Internships	
7/2001-9/2001	Internship at effeff Fritz Fuss GmbH in Albstadt
6/2005-11/2005	Internship at RWE Schott Solar in Alzenau, Germany, Billerica, Massachussetts, and Tampa, Florida
Professional Experience	
7/2006-6/2007	PhD student at the Institute of Physical Electronics
7/2007-now	PhD student at the IEF5-Photovoltaics

Bibliography

[1] D. M. Chapin, C. S. Fuller, and G. L. Pearson, J. Appl. Phys. **25**, 676 (1954).

[2] M. A. Green, *Solar Cells - Operating Principles, Technology and System Applications* (University of New South Wales, Sydney, 1986). p. 103.

[3] D. Ginley, M. A. Green, and R. Collins, MRS Bulletin **33**, 355 (2008).

[4] N. S. Lewis, Science **315**, 798 (2007).

[5] R. F. Service, Science **319**, 718 (2008).

[6] C. W. Tang, Appl. Phys. Lett. **48**, 183 (1986).

[7] G. Yu, J. Gao, J. C. Hummelen, F. Wudl, and A. J. Heeger, Science **270**, 1789 (1995).

[8] N. S. Sariciftci, L. Smilowitz, A. J. Heeger, and F. Wudl, Science **258**, 1474 (1992).

[9] H. Hoppe and N. S. Sariciftci, J. Mater. Res. **19**, 1924 (2004).

[10] C. J. Brabec, N. S. Sariciftci, and J. C. Hummelen, Adv. Funct. Mater. **11**, 15 (2001).

[11] F. Yang, M. Shtein, and S. R. Forrest, Nat. Mater. **4**, 37 (2005).

[12] P. W. M. Blom, V. D. Mihailetchi, L. J. A. Koster, and D. E. Markov, Adv. Mater. **19**, 1551 (2007).

[13] Y. Kim, S. Cook, S. M. Tuladhar, S. A. Choulis, J. Nelson, J. R. Durrant, D. D. C. Bradley, M. Giles, I. McCulloch, C.-S. Ha, and M. Ree, Nat. Mater. **5**, 197 (2006).

[14] J. Y. Kim, K. Lee, N. E. Coates, D. Moses, T.-Q. Nguyen, M. Dante, and A. J. Heeger, Science **317**, 222 (2007).

[15] J. Peet, J. Y. Kim, N. E. Coates, W. L. Ma, D. Moses, A. J. Heeger, and G. C. Bazan, Nat. Mater. **6**, 497 (2007).

[16] S. Bertho, G. Janssen, T. J. Cleij, B. Conings, W. Moons, A. Gadisa, J. D'Haen, E. Goovaerts, L. Lutsen, J. Manca, and D. Vanderzande, Sol. Energy Mat. Sol. Cells **92**, 753 (2008).

[17] B. O'Regan and M. Grätzel, Nature **353**, 737 (1991).

[18] M. Grätzel, Nature **414**, 338 (2001).

[19] P. Wang, S. M. Zakeeruddin, J. E. Moser, M. K. Nazeeruddin, T. Sekiguchi, and M. Grätzel, Nat. Mater. **2**, 402 (2003).

[20] M. Law, L. E. Greene, J. C. Johnson, R. Saykally, and P. Yang, Nat. Mater. **4**, 455 (2005).

[21] L. Schmidt-Mende, U. Bach, R. Humphry-Baker, T. Horiuchi, H. Miura, S. Ito, S. Uchida, and M. Grätzel, Adv. Mater. **17**, 813 (2005).

[22] J. Schrier, D. O. Demchenko, L.-W. Wang, and A. P. Alivisatos, Nano Lett. **7**, 2377 (2007).

[23] I. Gur, N. A. Fromer, M. L. Geier, and A. P. Alivisatos, Science **310**, 462 (2005).

[24] W. U. Huynh, J. J. Dittmer, and A. P. Alivisatos, Science **295**, 2425 (2002).

[25] W. J. E. Beek, M. M. Wienk, M. Kemerink, X. N. Yang, and R. A. J. Janssen, J. Phys. Chem. B **109**, 9505 (2005).

[26] R. D. Schaller and V. I. Klimov, Phys. Rev. Lett. **92**, 186601 (2004).

[27] U. Bach, D. Lupo, P. Comte, J. E. Moser, F.Weissörtel, J. Salbeck, H. Spreitzer, and M. Grätzel, Nature **395**, 583 (1998).

[28] B. A. Gregg and M. C. Hanna, J. Appl. Phys. **93**, 3605 (2003).

[29] B. A. Gregg, J. Phys. Chem. B **107**, 4688 (2003).

[30] W. Shockley and H. J. Queisser, J. Appl. Phys. **32**, 510 (1961).

[31] L. Onsager, Phys. Rev. **37**, 405 (1931).

[32] W. Shockley, Bell. Syst. Tech. J. **28**, 435 (1949).

[33] J. Mattheis, J. H. Werner, and U. Rau, Phys. Rev. B **77**, 085203 (2008).

[34] C. Donolato, Appl. Phys. Lett. **46**, 270 (1985).

[35] U. Rau, Phys. Rev. B **76**, 085303 (2007).

[36] K. Seino, J.-M. Wagner, and F. Bechstedt, Appl. Phys. Lett. **90**, 253109 (2007).

[37] G. N. Lewis, Proc. Nat. Acad. Sci. **11**, 179 (1925).

[38] R. C. Tolman, Proc. Nat. Acad. Sci. **11**, 436 (1925).

[39] O. E. Richardson, Proc. Roy. Soc. Lon. **36**, 392 (1924).

[40] E. O. Lawrence, Phys. Rev. **27**, 555 (1926).

[41] P. W. Bridgman, Phys. Rev. **31**, 101 (1928).

[42] M. Planck, *Vorlesungen über die Theorie der Wärmestrahlung* (Barth, Leipzig, 1906).

[43] G. Kirchhoff, Ann. Physik **19**, 275 (1860).

[44] P. Würfel, J. Phys. C **15**, 3967 (1982).

[45] S. Bose, Z. Phys. **26**, 178 (1924).

[46] A. Einstein, Sitzungsb. K. Preuss. Akad. Wiss. **22**, 261 (1924).

[47] R. Hulstrom, R. Bird, and C. Riordan, Sol. Cells **15**, 365 (1985).

[48] W. van Roosbroeck and W. Shockley, Phys. Rev. **94**, 1558 (1954).

[49] U. Rau and R. Brendel, J. Appl. Phys. **84**, 6412 (1998).

[50] M. A. Green, J. Appl. Phys. **81**, 269 (1997).

[51] K. Misiakos and F. A. Lindholm, J. Appl. Phys. **58**, 4743 (1985).

[52] T. Markvart, IEEE Trans. Elec. Dev. **ED-43**, 1034 (1996).

[53] R. H. Friend, R. W. Gymer, A. B. Holmes, J. H. Burroughes, R. N. Marks, C. Taliani, D. D. C. Bradley, D. A. D. Santos, J. L. Bredas, M. Logdlund, and W. R. Salaneck, Nature **397**, 121 (1999).

[54] C. Adachi, M. A. Baldo, S. R. Forrest, and M. E. Thompson, Appl. Phys. Lett. **77**, 904 (2000).

[55] M. A. Green, J. Zhao, A. Wang, and S. R. Wenham, IEEE Trans. Elec. Dev. **46**, 1940 (1999).

[56] M. A. Green, K. Emery, Y. Hisikawa, and W. Warta, Prog. Photovolt.: Res. Appl. **15**, 425 (2007).

[57] M. A. Green, J. Zhao, A. Wang, P. J. Reece, and M. Gal, Nature **412**, 805 (2001).

[58] T. Kirchartz, U. Rau, M. Kurth, J. Mattheis, and J. H. Werner, Thin Solid Films **515**, 6238 (2007).

[59] T. Kirchartz and U. Rau, J. Appl. Phys **102**, 104510 (2007).

[60] G. Dennler, M. C. Scharber, and C. J. Brabec, Adv. Mater. (2008).

[61] W. Shockley and W. T. Read, Phys.Rev. **87**, 835 (1952).

[62] R. N. Hall, Phys.Rev. **87**, 387 (1952).

[63] U. Rau, G. Kron, and J. H. Werner, J. Phys. Chem. B **107**, 13547 (2003).

[64] P. A. Basore and D. A. Clugston (1997), PC1D Version 5.1.

[65] S. J. Robinson, A. G. Aberle, and M. A. Green, J. Appl. Phys. **76**, 7920 (1994).

[66] P. J. Rostan, U. Rau, V. X. Nguyen, T. Kirchartz, M. B. Schubert, and J. H. Werner, Sol. Energy Mat. Sol. Cells **90**, 1345 (2006).

[67] C.-W. Jiang and M. A. Green, J. Appl. Phys. **99**, 114902 (2006).

[68] T. Tiedje, E. Yablonovitch, G. C. Cody, and B. G. Brooks, IEEE Trans. Elec. Dev. **ED-31**, 711 (1984).

[69] F. Dimroth and S. Kurtz, MRS Bull. **32**, 230 (2007).

[70] T. Trupke, M. A. Green, and P. Würfel, J. Appl. Phys. **92**, 4117 (2002).

[71] A. Shalav, B. S. Richards, T. Trupke, K. W. Kramer, and H. U. Gudel, Appl. Phys. Lett. **86**, 013505 (2005).

[72] T. Trupke, M. A. Green, and P. Würfel, J. Appl. Phys. **92**, 1668 (2002).

[73] D. Timmerman, I. Izeddin, P. Stallinga, I. N. Yassievich, and T. Gregorkiewicz, Nat. Photon. **2**, 105 (2008).

[74] R. T. Ross and A. J. Nozik, J. Appl. Phys. **53**, 3813 (1982).

[75] P. Wuerfel, Sol. Energy Mat. Sol. Cells **46**, 43 (1997).

[76] M. Neges, K. Schwarzburg, and F. Willig, Sol. Energy Mat. Sol. Cells **90**, 2107 (2006).

[77] A. J. Nozik, Physica E **14**, 115 (2002).

[78] P. Guyot-Sionnest, Nat. Mater. **4**, 653 (2005).

[79] F. Meillaud, A. Shah, C. Droz, E. Vallat-Sauvain, and C. Miazza, Sol. Energy Mat. Sol. Cells **90**, 2952 (2006).

[80] G. Conibeer, M. A. Green, R. Corkish, Y. Cho, E.-C. Cho, C.-W. Jiang, T. Fangsuwannarak, E. Pink, Y. Huang, T. Puzzer, T. Trupke, B. Richards, A. Shalav, and K. Lin, Thin Solid Films **511**, 654 (2006).

[81] G. Conibeer, M. A. Green, E.-C. Cho, D. König, Y.-H. Cho, T. Fangsuwannarak, G. Scardera, E. Pink, Y. Huang, T. Puzzer, S. Huang, D. Song, C. Flynn, S. Park, X. Hao, and D. Mansfield, Thin Solid Films **516**, 6748 (2008).

[82] T. Mchedlidze, T. Arguirov, S. Kouteva-Arguirova, M. Kittler, R. Rölver, B. Berghoff, D. L. Bätzner, and B. Spangenberg, Phys. Rev. B **77**, 161304 (2008).

[83] R. Rölver, B. Berghoff, D. L. Bätzner, B. Spangenberg, and H. Kurz, Appl. Phys. Lett. **92**, 212108 (2008).

[84] B. Stegemann, A. Schöpke, and M. Schmidt, J. Non-Cryst. Sol. **354**, 2100 (2008).

[85] L. V. Dao, J. Davis, P. Hannaford, Y.-H. Cho, M. A. Green, and E.-C. Cho, Appl. Phys. Lett. **90**, 081105 (2007).

[86] D. Song, E.-C. Cho, G. Conibeer, Y. Huang, and M. A. Green, Appl. Phys. Lett. **91**, 123510 (2007).

[87] D. Song, E.-C. Cho, G. Conibeer, Y. Huang, C. Flynn, and M. A. Green, J. Appl. Phys. **103**, 083544 (2008).

[88] C. Meier, A. Gondorf, S. Lüttjohann, A. Lorke, and H. Wiggers, J. Appl. Phys. **101**, 103112 (2007).

[89] T. Kirchartz, K. Seino, J.-M. Wagner, U. Rau, and F. Bechstedt (2009), In preparation.

[90] M. Zeman, R. A. C. M. M. van Swaaij, J. W. Metselaar, and R. E. I. Schropp, J. Appl. Phys. **88**, 6436 (2000).

[91] J. B. Baxter and C. A. Schmuttenmaer, J. Phys. Chem. **110**, 25229 (2006).

[92] K. Keem, D.-Y. Jeong, S. Kim, M.-S. Lee, I.-S. Yeo, U.-I. Chung, and J.-T. Moon, Nano Lett. **6**, 1454 (2006).

[93] Y.-Y. Noh, X. Cheng, H. Sirringhaus, J. I. Sohn, M. E. Welland, and D. J. Kang, Appl. Phys. Lett. **91**, 043109 (2007).

[94] D.-I. Suh, S.-Y. Lee, J.-H. Hyung, T.-H. Kim, and S.-K. Lee, J. Phys. Chem. **112**, 1276 (2008).

[95] A. B. Sproul, J. Appl. Phys. **76**, 5 (1994).

[96] P. Buehlmann, J. Bailat, D. Domine, A. Billet, F. Feltrin, and C. Ballif, Appl. Phys. Lett. **91**, 143505 (2007).

[97] J. Rostalski and D. Meissner, Sol. Energy Mat. Sol. Cells **63**, 37 (2000).

[98] R. A. Marsh, C. Groves, and N. C. Greenham, J. Appl. Phys. **101**, 083509 (2007).

[99] S. Lacic and O. Inganäs, J. Appl. Phys. **97**, 124901 (2005).

[100] C. M. Martin, V. M. Burlakov, and H. E. Assender, Sol. Energy Mat. Sol. Cells **90**, 900 (2006).

[101] C. M. Martin, V. M. Burlakov, H. E. Assender, and D. A. R. Barkhouse, J. Appl. Phys. **102**, 104506 (2007).

[102] L. J. A. Koster, E. C. P. Smits, V. D. Mihailetchi, and P. W. M. Blom, Phys. Rev. B **72**, 085205 (2005).

[103] L. A. A. Pettersson, L. S. Roman, and O. Inganäs, J. Appl. Phys. **86**, 487 (1999).

[104] L. A. A. Pettersson, L. S. Roman, and O. Inganäs, J. Appl. Phys. **89**, 5564 (2001).

[105] H. Hoppe, N. Arnold, N. S. Sariciftci, and D. Meissner, Sol. Energy Mat. Sol. Cells **80**, 105 (2003).

[106] L. H. Slooff, S. C. Veenstra, J. M. Kroon, D. J. D. Moet, J. Sweelsen, and M. M. Koetse, Appl. Phys. Lett. **90**, 143506 (2007).

[107] G. Dennler, K. Forberich, M. C. Scharber, C. J. Brabec, I. Tomis, K. Hingerl, and T. Fromherz, J. Appl. Phys. **102**, 054516 (2007).

[108] J. Gilot, I. Barbu, M. Wienk, and R. A. J. Janssen, Appl. Phys. Lett. **91**, 113520 (2007).

[109] V. D. Mihailetchi, L. J. A. Koster, J. C. Hummelen, and P. W. M. Blom, Phys. Rev. Lett. **93**, 216601 (2004).

[110] D. W. Sievers, V. Shrotriya, and Y. Yang, J. Appl. Phys. **100**, 114509 (2006).

[111] H. H. P. Gommans, M. Kemerink, J. M. Kramer, and R. A. J. Janssen, Appl. Phys. Lett. **87**, 122104 (2005).

[112] L. J. A. Koster, V. D. Mihailetchi, R. Ramaker, and P. W. M. Blom, Appl. Phys. Lett. **86**, 123509 (2005).

[113] L. J. A. Koster, V. D. Mihailetchi, and P. W. M. Blom, Appl. Phys. Lett. **88**, 093511 (2006).

[114] J. D. Kotlarski, P. W. M. Blom, L. J. A. Koster, M. Lenes, and L. H. Slooff, J. Appl. Phys. **103**, 084502 (2008).

[115] M. M. Mandoc, L. J. A. Koster, and P. W. M. Blom, Appl. Phys. Lett. **90**, 133504 (2007).

[116] H. Hoppe and N. S. Sariciftci, J. Mat. Chem. **16**, 45 (2006).

[117] T. Kirchartz, J. Mattheis, and U. Rau, Phys. Rev. B **78**, 235320 (2008).

[118] X. Yang, J. K. van Duren, R. A. J. Janssen, M. A. J. Michels, and J. Loos, Macromolecules **37**, 2151 (2004).

[119] X. Yang, J. Loos, S. C. Veenstra, W. J. H. Verhees, M. M. Wienk, J. M. Kroon, M. A. J. Michels, and R. A. J. Janssen, Nano Lett. **5**, 579 (2005).

[120] P. Peumans, A. Yakimov, and S. R. Forrest, J. Appl. Phys. **93**, 3693 (2003).

[121] D. J. D. Moet, L. H. Slooff, J. M. Kroon, S. S. Chevtchenko, J. Loos, M. M. Koetse, J. Sweelssen, and S. C. Veenstra, Mater. Res. Soc. Symp. Proc. **974**, CC03 (2007).

[122] M. A. Green, *Third Generation Photovoltaics* (Springer, Berlin, 2003).

[123] S. Kolodinski, J. H. Werner, T. Wittchen, and H. J. Queisser, Appl. Phys. Lett **63**, 2405 (1993).

[124] A. Luque, A. Marti, and A. J. Nozik, MRS Bull. **32**, 236 (2007).

[125] R. D. Schaller, M. Sykora, J. M. Pietryga, and V. I. Klimov, Nano Lett. **6**, 424 (2006).

[126] R. D. Schaller, M. A. Petruska, and V. I. Klimov, Appl. Phys. Lett. **87**, 253102 (2005).

[127] R. D. Schaller, J. M. Pietryga, and V. I. Klimov, Nano Lett. **7**, 3469 (2006).

[128] M. C. Beard, K. P. Knutsen, P. R. Yu, J. M. Luther, Q. Song, W. K. Metzger, R. J. Ellingson, and A. J. Nozik, Nano Lett. **7**, 2506 (2007).

[129] R. D. Schaller, M. Sykora, S. Jeong, and V. I. Klimov, J. Phys. Chem. B **110**, 25332 (2006).

[130] J. H. Werner, S. Kolodinski, and H. J. Queisser, Phys. Rev. Lett **72**, 3851 (1994).

[131] V. I. Klimov, Appl. Phys. Lett. **72**, 123118 (2006).

[132] M. C. Hanna and A. J. Nozik, J. Appl. Phys. **100**, 074510 (2006).

[133] J. M. Luther, M. C. Beard, Q. Song, M. Law, R. J. Ellingson, and A. J. Nozik, Nano Lett. **7**, 1779 (2007).

[134] A. Franceschetti, J. M. An, and A. Zunger, Nano Lett. **6**, 2191 (2006).

[135] J. M. Luther, M. Law, M. C. Beard, Q. Song, M. O. Reese, R. J. Ellingson, and A. J. Nozik, Nano Lett. (2008), Published online, doi: 10.1021/nl802476m.

[136] V. I. Klimov, J. Phys. Chem. B **110**, 16827 (2006).

[137] R. J. Ellingson, M. C. Beard, J. C. Johnson, P. Yu, O. I. Micic, A. J. Nozik, A. Shabaev, and A. L. Efros, Nano Lett. **5**, 865 (2005).

[138] R. D. Schaller, V. A. Agranovich, and V. I. Klimov, Nat. Phys. **1**, 189 (2005).

[139] E. Daub and P. Würfel, Phys. Rev. Lett. **74**, 1020 (1995).

[140] E. Yablonovitch, J. Opt. Soc. Am. **72**, 899 (1982).

[141] W. Theiss, Hard- and Software, Dr.-Bernhard-Klein-Str. 110, D-52078 Aachen, Germany.

[142] J. Mattheis, *Mobility and homogeneity effects on the power conversion efficiency of solar cells*, Ph.D. thesis, Universität Stuttgart (2007), p. 142.

[143] L. Pavesi, L. D. Negro, C. Mazzoleni, G. Franzo, and F. Priolo, Nature **408**, 440 (2000).

[144] R. J. Walters, G. I. Bourianoff, and H. A. Atwater, Nature Mat. **4**, 143 (2005).

[145] J. Linnros, Nature Mat. **4**, 117 (2005).

[146] W. L. Ng, M. A. Lourenco, R. M. Gwilliam, S. Ledain, G. Shao, and K. P. Homewood, Nature **410**, 192 (2001).

[147] T. Trupke, J. Zhao, A. Wang, R. Corkish, and M. A. Green, Appl. Phys. Lett. **82**, 2996 (2003).

[148] A. Goetzberger, B. Voss, and J. Knobloch, *Sonnenenergie: Photovoltaik - Physik und Technologie der Solarzelle* (Teubner, Stuttgart, 1984). p. 99.

[149] R. Brendel, Prog. Photovolt.: Res. Appl. **3**, 25 (1995).

[150] P. Würfel, T. Trupke, T. Puzzer, E. Schäffer, W. Warta, and S. W. Glunz, J. Appl. Phys. **101**, 123110 (2007).

[151] D. Hinken, K. Ramspeck, K. Bothe, B. Fischer, and R. Brendel, Appl. Phys. Lett. **91**, 182104 (2007).

[152] T. Kirchartz, U. Rau, M. Hermle, A. W. Bett, A. Helbig, and J. H. Werner, Appl. Phys. Lett. **92**, 123502 (2008).

[153] N. D. Arora, S. G. Chamberlain, and D. J. Roulston, Appl. Phys. Lett. **37**, 325 (1980).

[154] P. A. Basore, in *Proc. of the 23rd IEEE Photovoltaic Specialists Conference* (IEEE, New York, 1993), p. 147.

[155] K. Bothe, D. Hinken, K. Ramspeck, B. Fischer, and R. Brendel, in *Proc. of the 22nd European Photovoltaic Solar Energy Conference in Milan* (WIP Renewable Energies, 2007), p. 1673.

[156] M. A. Green, Prog. Photovolt. **9**, 123 (2001).

[157] T. Trupke, E. Daub, and P. Würfel, Sol. Energy Mat. Sol. Cells **53**, 103 (1998).

[158] M. Taguchi, A. Terakawa, E. Maruyama, and M. Tanaka, Prog. Photovolt.: Res. Appl. **13**, 481 (2005).

[159] M. A. Contreras, B. Egaas, K. Ramanathan, J. Hiltner, A. Swartzlander, F. Hasoon, and R. Noufi, Prog. Photovolt.: Res. Appl. **7**, 311 (1999).

[160] M. J. Romero, C.-S. Jiang, R. Noufi, and M. M. Al-Jassim, Appl. Phys. Lett. **86**, 143115 (2005).

[161] M. J. Romero, C.-S. Jiang, J. Abushama, H. R. Moutinho, M. M. Al-Jassim, and R. Noufi, Appl. Phys. Lett. **89**, 143120 (2006).

[162] L. Gütay and G. H. Bauer, Thin Solid Films **515**, 6212 (2007).

[163] K. Bothe, G. H. Bauer, and T. Unold, Thin Solid Films **403**, 453 (2002).

[164] G. H. Bauer, R. Brüggemann, S. Tardon, S. Vignoli, and R. Kniese, Thin Solid Films **480**, 410 (2005).

[165] G. Dagan, F. Abou-Elfotouh, D. J. Dunlavy, R. J. Matson, and D. Cahen, Chem. Mater. **2**, 287 (1990).

[166] G. Massé and E. Redjai, Chem. Mater. **56**, 1154 (1984).

[167] P. Migliorato, J. L. Shay, H. M. Kasper, and S. Wagner, J. Appl. Phys. **46**, 1777 (1975).

[168] S. Shimakawa, K. Kitani, S. Hayashi, T. Satoh, Y. Hashimoto, Y. Takahashi, and T. Negami, phys. stat. solid. (a) **203**, 2630 (2006).

[169] S. Zott, K. Leo, M. Ruckh, and H. W. Schock, Appl. Phys. Lett. **68**, 1144 (1996).

[170] S. Zott, K. Leo, M. Ruckh, and H. W. Schock, J. Appl. Phys. **82**, 356 (1997).

[171] P. W. Yu, Y. S. Park, S. P. Faile, and J. E. Ehret, Appl. Phys. Lett. **26**, 717 (1975).

[172] P. Migliorato, B. Tell, J. L. Shay, and H. M. Kasper, Appl. Phys. Lett. **24**, 227 (1974).

[173] P. M. Bridenbaugh and P. Migliorato, Appl. Phys. Lett. **26**, 459 (1975).

[174] J. Mattheis, U. Rau, and J. H. Werner, J. Appl. Phys. **101**, 113519 (2007).

[175] U. Rau and J. H. Werner, Appl. Phys. Lett. **84**, 3735 (2004).

[176] A. M. Gabor, J. R. Tuttle, D. S. Albin, M. A. Contreras, R. Noufi, and A. M. Herrmann, Appl. Phys. Lett **65**, 198 (1994).

[177] P. Jackson, R. Würz, U. Rau, J. Mattheis, M. Kurth, T. Schlötzer, G. Bilger, and J. H. Werner, Progr. Photov.: Res. Appl. **15**, 507 (2007).

[178] T. Dullweber, U. Rau, M. A. Contreras, R. Noufi, and H.-W. Schock, IEEE Trans. Electron. Devices **47**, 2249 (2000).

[179] E. Zacks and A. Halperin, Phys. Rev. B **6**, 3072 (1972).

[180] I. Dirnstorfer, M. Wagner, D. M. Hoffmann, M. D. Lampert, F. Karg, and B. K. Meyer, phys. stat. sol. (a) **168**, 163 (1998).

[181] A. Bauknecht, S. Siebentritt, J. Albert, and M. C. Lux-Steiner, J. Appl. Phys. **89**, 4391 (2001).

[182] S. Siebentritt, N. Papathanasiou, and M. C. Lux-Steiner, Physica B **376-377**, 831 (2001).

[183] J. H. Werner, J. Mattheis, and U. Rau, Thin Solid Films **480-481**, 399 (2005).

[184] J. A. del Alamo and R. M. Swanson, IEEE Trans. Electron Devices **ED-31**, 1878 (1984).

[185] F. Dimroth, phys. stat. solid. (c) **3**, 373 (2006).

[186] M. Meusel, C. Baur, G. Létay, A. W. Bett, W. Warta, and E. Fernandez, Prog. Photovolt.: Res. Appl. **11**, 499 (2003).

Acknowledgements

During my time in Stuttgart and Jülich a large number of people helped and supported me and made me enjoy the whole time of my PhD thesis. I would like to thank

Prof. Dr. Uwe Rau for being able to learn from him most of what I know about semiconductors and about writing a paper, for his ingenious ideas and his criticism, for his confidence in me and for several conferences I could attend with him,

Prof. Dr. Heinrich Kurz for kindly accepting to report on my thesis,

Prof. Dr. Jürgen H. Werner for his continuous support during my whole studies, for his excellent advice, and for his lectures, which have created my interest in solid state electronics and photovoltaics,

Prof. Arthur J. Nozik for discussions on multiple exciton generating quantum dot solar cells,

Dr. Reinhard Carius for long discussions and for his advice about everything concerning spectroscopy,

Dr. Julian Mattheis for being my ingenious predecessor in my work and for being a good friend in the time we spent together in Stuttgart,

Bart Pieters for always knowing an answer about computers and simulations, when I get to my limits,

Dr. Daniel Abou-Ras for allowing me to contribute to his Young-Scientist Tutorial,

Dr. Kurt Taretto for reading everything carefully, I wrote since I know him, and for his interest in my ideas,

Prof. Martijn Kemerink and Dr. Carsten Deibel for discussions about modelling of organic solar cells,

Dr. Lenneke Slooff and Prof. Joshua Schrier for providing nk-files used in this work and for disscussions about optical modeling and first principles calculations

Dr. Steve Reynolds for many sincere as well as funny discussions,
Florian Einsele for being a friend and colleague from our Studienarbeit until our PhD thesis,
Liv Prönneke, Carolin Ulbrich and Shiwei Ku for being my roommate for some time and not to complain too much about me
Carolin Ulbrich and Anke Helbig for continuing some of my work that would otherwise probably have died
Sandra Schicho and Jorj Owen for help whenever help was needed
Josef Klomfass, Markus Hülsbeck and Wilfried Reetz for giving me the possibility to work with professionals at least once in a lifetime
all colleagues in Stuttgart and Jülich
project members from the "Quanten"-project, the "Nanosun"-project and the "Nanovolt"-project, especially Derk Bätzner, Bernd Spangenberg, Birger Berghoff, Robert Rölver, Bert Stegemann, Manfred Schmidt, Andreas Schöpke, Kaori Seino, Friedhelm Bechstedt, Jan-Martin Wagner, Martin Kittler, Teimuraz Mchedlize, Tzvanimir Arguirov, Marius Peters, Philip Löper, Stephan Fahr, Christian Helgert, Carsten Rockstuhl, Florian Hallermann, Johannes Üpping, Andreas Bielawny, and Florian Heidemann for the good collaboration and the nice discussions during the project meeting (especially those discussions later in the evening)
Yael Augarten for her brave attempt to introduce me to everybody on the Q-Cells party
Lucie Castens for never complaining about that all-you-can-eat restaurant in Strasbourg
and Deborah Adkins for her interest in my work.

1. **Einsatz von multispektralen Satellitenbilddaten in der Wasserhaushalts- und Stoffstrommodellierung – dargestellt am Beispiel des Rureinzugsgebietes**
   von C. Montzka (2008), XX, 238 Seiten
   ISBN: 978-3-89336-508-1

2. **Ozone Production in the Atmosphere Simulation Chamber SAPHIR**
   by C. A. Richter (2008), XIV, 147 pages
   ISBN: 978-3-89336-513-5

3. **Entwicklung neuer Schutz- und Kontaktierungsschichten für Hochtemperatur-Brennstoffzellen**
   von T. Kiefer (2008), 138 Seiten
   ISBN: 978-3-89336-514-2

4. **Optimierung der Reflektivität keramischer Wärmedämmschichten aus Yttrium-teilstabilisiertem Zirkoniumdioxid für den Einsatz auf metallischen Komponenten in Gasturbinen**
   von A. Stuke (2008), X, 201 Seiten
   ISBN: 978-3-89336-515-9

5. **Lichtstreuende Oberflächen, Schichten und Schichtsysteme zur Verbesserung der Lichteinkopplung in Silizium-Dünnschichtsolarzellen**
   von M. Berginski (2008), XV, 171 Seiten
   ISBN: 978-3-89336-516-6

6. **Politikszenarien für den Klimaschutz IV – Szenarien bis 2030**
   hrsg.von P. Markewitz, F. Chr. Matthes (2008), 376 Seiten
   ISBN 978-3-89336-518-0

7. **Untersuchungen zum Verschmutzungsverhalten rheinischer Braunkohlen in Kohledampferzeugern**
   von A. Schlüter (2008), 164 Seiten
   ISBN 978-3-89336-524-1

8. **Inorganic Microporous Membranes for Gas Separation in Fossil Fuel Power Plants**
   by G. van der Donk (2008), VI, 120 pages
   ISBN: 978-3-89336-525-8

9. **Sinterung von Zirkoniumdioxid-Elektrolyten im Mehrlagenverbund der oxidkeramischen Brennstoffzelle (SOFC)**
   von R. Mücke (2008), VI, 165 Seiten
   ISBN: 978-3-89336-529-6

10. **Safety Considerations on Liquid Hydrogen**
    by K. Verfondern (2008), VIII, 167 pages
    ISBN: 978-3-89336-530-2

11. **Kerosinreformierung für Luftfahrtanwendungen**
    von R. C. Samsun (2008), VII, 218 Seiten
    ISBN: 978-3-89336-531-9

12. **Der 4. Deutsche Wasserstoff Congress 2008 – Tagungsband**
    hrsg. von D. Stolten, B. Emonts, Th. Grube (2008), 269 Seiten
    ISBN: 978-3-89336-533-3

13. **Organic matter in Late Devonian sediments as an indicator for environmental changes**
    by M. Kloppisch (2008), XII, 188 pages
    ISBN: 978-3-89336-534-0

14. **Entschwefelung von Mitteldestillaten für die Anwendung in mobilen Brennstoffzellen-Systemen**
    von J. Latz (2008), XII, 215 Seiten
    ISBN: 978-3-89336-535-7

15. **RED-IMPACT**
    Impact of Partitioning, Transmutation and Waste Reduction Technologies on the Final Nuclear Waste Disposal
    SYNTHESIS REPORT
    ed. by W. von Lensa, R. Nabbi, M. Rossbach (2008), 178 pages
    ISBN 978-3-89336-538-8

16. **Ferritic Steel Interconnectors and their Interactions with Ni Base Anodes in Solid Oxide Fuel Cells (SOFC)**
    by J. H. Froitzheim (2008), 169 pages
    ISBN: 978-3-89336-540-1

17. **Integrated Modelling of Nutrients in Selected River Basins of Turkey**
    Results of a bilateral German-Turkish Research Project
    project coord. M. Karpuzcu, F. Wendland (2008), XVI, 183 pages
    ISBN: 978-3-89336-541-8

18. **Isotopengeochemische Studien zur klimatischen Ausprägung der Jüngeren Dryas in terrestrischen Archiven Eurasiens**
    von J. Parplies (2008), XI, 155 Seiten, Anh.
    ISBN: 978-3-89336-542-5

19. **Untersuchungen zur Klimavariabilität auf dem Tibetischen Plateau - Ein Beitrag auf der Basis stabiler Kohlenstoff- und Sauerstoffisotope in Jahrringen von Bäumen waldgrenznaher Standorte**
    von J. Griessinger (2008), XIII, 172 Seiten
    ISBN: 978-3-89336-544-9

20. **Neutron-Irradiation + Helium Hardening & Embrittlement Modeling of 9%Cr-Steels in an Engineering Perspective (HELENA)**
by R. Chaouadi (2008), VIII, 139 pages
ISBN: 978-3-89336-545-6

21. **Messung und Bewertung von Verkehrsemissionen**
von D. Klemp, B. Mittermaier (2009), ca. 230 Seiten, erscheint in Kürze
ISBN: 978-3-89336-546-3

22. **Verbundvorhaben APAWAGS (AOEV und Wassergenerierung) – Teilprojekt: Brennstoffreformierung – Schlussbericht**
von R. Peters, R. C. Samsun, J. Pasel, Z. Porš, D. Stolten (2008), VI, 106 Seiten
ISBN: 978-3-89336-547-0

23. **FREEVAL**
Evaluation of a Fire Radiative Power Product derived from Meteosat 8/9 and Identification of Operational User Needs
Final Report
project coord. M. Schultz, M. Wooster (2008), 139 pages
ISBN: 978-3-89336-549-4

24. **Untersuchungen zum Alkaliverhalten unter Oxycoal-Bedingungen**
von C. Weber (2008), VII, 143, XII Seiten
ISBN: 978-3-89336-551-7

25. **Grundlegende Untersuchungen zur Freisetzung von Spurstoffen, Heißgaschemie, Korrosionsbeständigkeit keramischer Werkstoffe und Alkalirückhaltung in der Druckkohlenstaubfeuerung**
von M. Müller (2008), 207 Seiten
ISBN: 978-3-89336-552-4

26. **Analytik von ozoninduzierten phenolischen Sekundärmetaboliten in *Nicotiana tabacum* L. cv Bel W3 mittels LC-MS**
von I. Koch (2008), III, V, 153 Seiten
ISBN 978-3-89336-553-1

27. **IEF-3 Report 2009. Grundlagenforschung für die Anwendung**
(2009), ca. 230 Seiten erscheint in Kürze
ISBN: 978-3-89336-554-8

28. **Influence of Composition and Processing in the Oxidation Behavior of MCrAlY-Coatings for TBC Applications**
by J. Toscano (2009), 168 pages
ISBN: 978-3-89336-556-2

29. **Modellgestützte Analyse signifikanter Phosphorbelastungen in hessischen Oberflächengewässern aus diffusen und punktuellen Quellen**
von B. Tetzlaff (2009), 149 Seiten
ISBN: 978-3-89336-557-9

30. **Nickelreaktivlot / Oxidkeramik – Fügungen als elektrisch isolierende Dichtungskonzepte für Hochtemperatur-Brennstoffzellen-Stacks**
von S. Zügner (2009), 136 Seiten
ISBN: 978-3-89336-558-6

31. **Langzeitbeobachtung der Dosisbelastung der Bevölkerung in radioaktiv kontaminierten Gebieten Weißrusslands – Korma-Studie**
von H. Dederichs, J. Pillath, B. Heuel-Fabianek, P. Hill, R. Lennartz (2009), Getr. Pag.
ISBN: 978-3-89336-532-3

32. **Herstellung von Hochtemperatur-Brennstoffzellen über physikalische Gasphasenabscheidung**
von N. Jordán Escalona (2009), 148 Seiten
ISBN: 978-3-89336-532-3

33. **Real-time Digital Control of Plasma Position and Shape on the TEXTOR Tokamak**
by M. Mitri (2009), IV, 128 Seiten
ISBN: 978-3-89336-567-8

34. **Freisetzung und Einbindung von Alkalimetallverbindungen in kohlebefeuerten Kombikraftwerken**
von M. Müller (2009), 155 Seiten
ISBN: 978-3-89336-568-5

35. **Kosten von Brennstoffzellensystemen auf Massenbasis in Abhängigkeit von der Absatzmenge**
von J. Werhahn (2009), 242 Seiten
ISBN: 978-3-89336-569-2

36. **Einfluss von Reoxidationszyklen auf die Betriebsfestigkeit von anodengestützten Festoxid-Brennstoffzellen**
von M. Ettler (2009), 138 Seiten
ISBN: 978-3-89336-570-8

37. **Großflächige Plasmaabscheidung von mikrokristallinem Silizium für mikromorphe Dünnschichtsolarmodule**
von T. Kilper (2009), XVII, 154 Seiten
ISBN: 978-3-89336-572-2

38. **Generalized detailed balance theory of solar cells**
von T. Kirchartz (2009), IV, 198 Seiten
ISBN: 978-3-89336-573-9

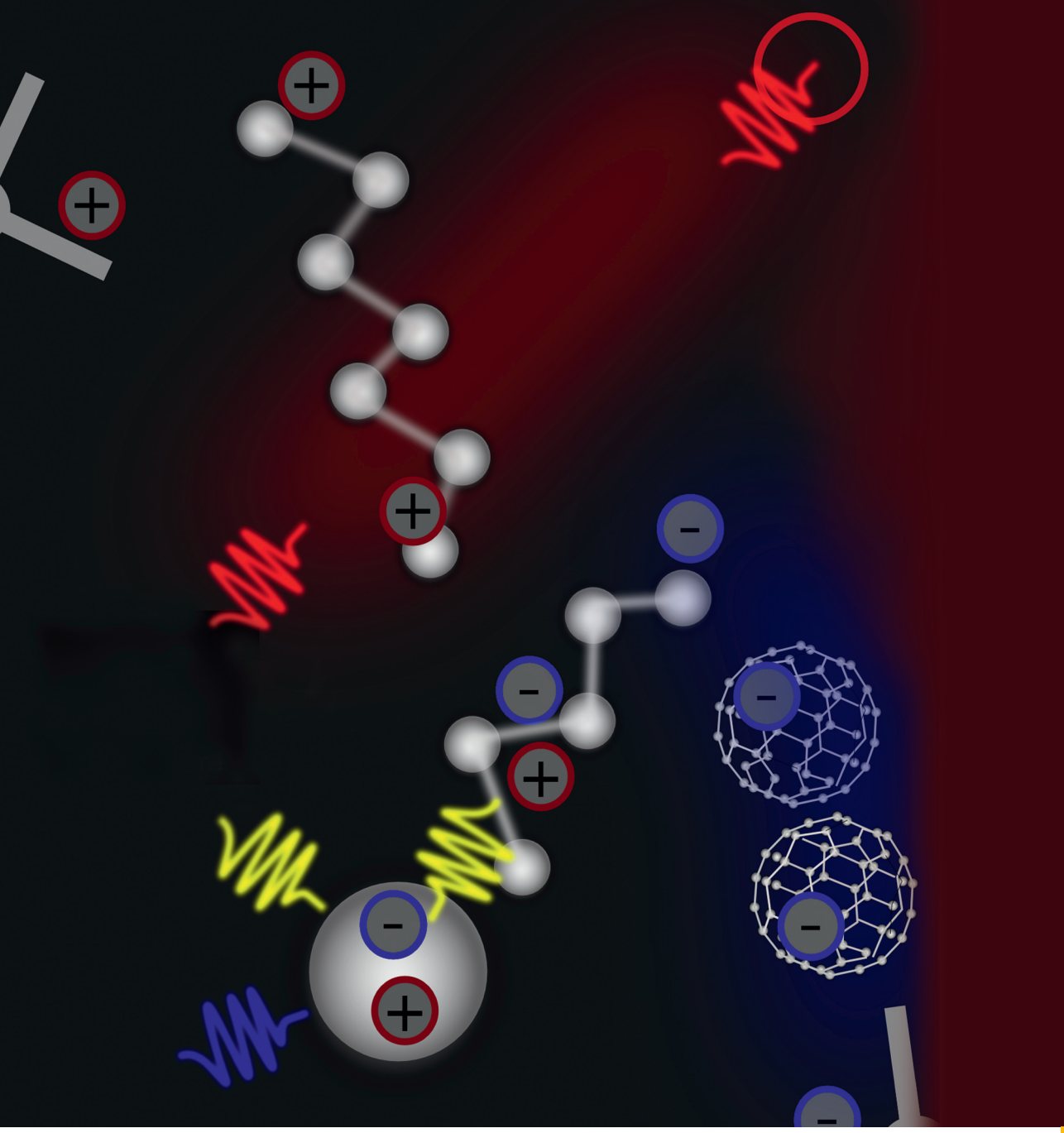

Band | Volume 38
ISBN 978-3-89336-573-9

JÜLICH
FORSCHUNGSZENTRUM